The Single-Boson Exchange Formalism and its Application to the Functional Renormalization Group

Dissertation

der Mathematisch-Naturwissenschaftlichen Fakultät

der Eberhard Karls Universität Tübingen

zur Erlangung des Grades eines

Doktors der Naturwissenschaften

(Dr. rer. nat.)

vorgelegt von

Sarah Elisabeth Heinzelmann

aus Reutlingen

Tübingen

2023

Gedruckt mit Genehmigung der Mathematisch-Naturwissenschaftlichen Fakultät der Eberhard Karls Universität Tübingen.

Tag der mündlichen Qualifikation:	27.11.2023
Dekan:	Prof. Dr. Thilo Stehle
1. Berichterstatter/-in:	Prof Dr Sabine Andergassen
2. Berichterstatter/-in:	Prof Dr Michael Scherer

Abstract:

The recently introduced single-boson exchange (SBE) decomposition of the two-particle vertex classifies diagrams in terms of single- and multiboson exchange processes in the different channels. Providing a physically intuitive and also computationally efficient description of the relevant fluctuations, the SBE allows for the development of new approximation schemes that overcome the limitations of current implementations.

Here we apply the SBE to the functional renormalization group (fRG). In this formulation, the effective bosonic interaction can be represented by bosonic propagators and fermion-boson couplings determined from the vertex asymptotics, while the multiboson processes are shown to be irrelevant. They become important only in the vicinity of the pseudo-critical transition observed in the one-loop approximation. Since only these depend on three independent frequency and momentum variables, neglecting them drastically reduces the computational complexity of the problem compared to the purely fermionic one-loop fRG.

On the methodological side, we generalise the SBE decomposition to the treatment of non-local interactions, providing a numerically feasible fRG-based computation scheme. This includes the derivation of the self-energy flow based on the Schwinger-Dyson equation which is crucial to capture the pseudogap opening and the multiloop extension that allows to recover the parquet approximation. For the latter, we also provide an alternative formulation that does not resort to the expansion in loop orders. We determine the effects induced by the presence of a nearest-neighbour interaction and explore the physics arising from the interplay between local and non-local degrees of freedom.

Finally, we investigate the two-dimensional Hubbard model with a local Coulomb interaction for a wide range of dopings. For this analysis we compute the magnetic, density, and superconducting, susceptibilities at weak coupling and present a detailed analysis of their evolution with temperature, interaction strength, and loop order.

The SBE provides greater algorithmic flexibility, leading to higher accuracy at lower cost, as well as better physical understanding of relevant processes and thereby paves access to new parameter regimes. Future developments include multiboson extensions of fRG-based algorithms.

Zusammenfassung:
Die kürzlich eingeführte "single-boson exhange" (SBE) Zerlegung des Zwei-Teilchen-Vertex klassifiziert Diagramme in Bezug auf Ein- und Multiboson-Austauschprozesse in den verschiedenen Kanälen. Die SBE ermöglicht eine physikalisch intuitive sowie rechnerisch effiziente Beschreibung der relevanten Fluktuationen in Quantenvielteilchensystemen. Insbesondere ergibt sich daraus auch ein Entwicklungsfeld für neue Näherungsansätze, die über derzeitige Einschränkungen hinausgehen.

Hier wenden wir die SBE auf die funktionale Renormierungsgruppe (fRG) an. In der SBE Formulierung kann die effektive bosonische Wechselwirkung durch bosonische Propagatoren und Fermion-Boson Kopplungen dargestellt werden, die aus der Vertex-Asymptotik bestimmt werden, während sich die Multiboson-Prozesse als irrelevant erweisen. Letztere werden nur in der Nähe der pseudokritischen Temperatur wichtig, die in der 1-loop Näherung auftritt. Da nur die Multiboson-Prozesse von drei unabhängigen Frequenz- und Impulsvariablen abhängen, wird durch ihre Vernachlässigung der Rechenaufwand im Vergleich zu einer rein fermionischen fRG drastisch reduziert.

Auf der methodischen Seite verallgemeinern wir die SBE-Zerlegung auf die Behandlung nichtlokaler Wechselwirkungen und etablieren ein numerisch praktikables fRG-basiertes Berechnungsschema. Dazu gehört die Herleitung des Selbstenergieflusses über die Schwinger-Dyson-Gleichung, die für die theoretische Beschreibung des Pseudogaps entscheidend ist, sowie der sogenannten Multiloop-Erweiterung der fRG. Für diese präsentieren wir auch eine alternative Formulierung, die nicht auf der Entwicklung in loop-Ordnungen beruht. Zudem bestimmen wir die Effekte, die durch die Nächst-Nachbar-Wechselwirkung induziert werden, und erforschen die Physik, die sich aus dem Zusammenspiel zwischen lokalen und nicht-lokalen Freiheitsgraden ergibt.

Wir untersuchen das zweidimensionale Hubbard Modell mit einer lokalen Coulomb-Wechselwirkung über einen breiten Füllungsbereich. Wir berechnen die magnetischen, dichte- und supraleitenden Suszeptibilitäten bei schwacher Kopplung und präsentieren eine detaillierte Analyse ihrer Abhängigkeit von Temperatur, Wechselwirkungsstärke und loop-Ordnung.

Zusammenfassend bietet die SBE eine größere algorithmische Flexibilität, die zu höherer Genauigkeit bei geringerem numerischen Aufwand führt und damit den Zugang zu neuen Parameterregimes ermöglicht. Gleichzeitig vermittelt sie ein besseres physikalisches Verständnis der relevanten Prozesse. Zukünftige Entwicklungen umfassen Multiboson-Erweiterungen von fRG-basierten Algorithmen.

Acknowledgements:

First I would like to express my gratitude to my supervisor Sabine Andergassen for the opportunity to dive headfirst into the fascinating and mysterious world of strongly correlated electrons. Your experienced input and guidance - while giving me the space and time to come up with my own solutions - have helped me grow as a physicist. As co-supervisor I am also very grateful to Alessandro Toschi for opening my eyes to new concepts and helping me see the wider context as well as offering concrete advice on my work. I would like to thank Michael Scherer for the time and effort it takes to be the second 'Berichterstatter'.

My work builds on the advancements made by the members of the AG Andergassen that came before me. In particular, I would like to thank Cornelia Hille for taking me under her wings: She introduced me to the code with great patience, always made time to discuss any question I had, and became a friend along the way. Being a part of a wider community of scientist seeking answers to related questions has been a rewarding aspect of the PhD student experience and I would like to thank Pietro Bonetti, Demetrio Vilardi, and Friedrich Krien in particular for the valuable discussions.

Collaborating with my colleagues, Aiman and Kilian, has been a great pleasure. I knew I could always count on you to discuss any idea, bug, or confusing factor of $4\pi^2$. And of course thank you, Manfred, for being the perfectly fluffy group mascot. Thanks are due to Franiska Stief and Patricia Heinzelmann for catching all the commas (many, many commas) and typos I missed.

Last but certainly not least I would like to thank Simon for every cup of tea you brought me, every word of encouragement you gave when motivation ran low, and always believing that I would successfully complete this PhD.

Contents

1 Introduction

The physics of strongly correlated electrons is among the most active fields in condensed matter research, featuring both novel discoveries and long-standing open questions. A material is said to exhibit strong electronic correlations when descriptions based on single particles break down and fail to make even qualitatively correct predictions. This is the case in presence of narrow bands and consequently more localized electrons [1], as for example is the case in many transition metal oxides [2]. In these materials, a whole new world of exotic phases and phenomena is revealed at low temperatures, such as unconventional superconductivity [3], the (fractional) quantum Hall effect [4], Mott insulators [5], colossal magneto resistance (GMR) [6], magic angle graphene [7], and quantum spin liquids [8]. These macroscopic manifestations of quantum mechanics result from the complex interplay between different degrees of freedom (charge, spin, lattice, orbital) and competing ordering tendencies. Despite the differences in the physical properties, these phenomena can all be interpreted as systems condensing into a state with coherent collective excitations, that have no equivalent in a free particle description. In this sense one speaks of an emergent collective behaviour.

Besides the intriguing questions related to the understanding of the fundamental mechanisms controlling the physics of strongly correlated electron systems, their high tunability lends themselves to technical applications. Examples include the GMR effect used in read-write devices [9] and superconductors employed to generate the strong magnetic fields necessary for magnetic resonance imaging. Room temperature superconductors and quantum computing devices based on correlation effects are envisioned for future applications, with the potential to revolutionize technology.

A common strategy to go beyond single-particle descriptions is to work with model Hamiltonians that incorporate correlation effects to varying degrees of sophistication. The most widely used model Hamiltonian in the context of high T_c superconductors is the Hubbard model [1], where electrons hop between neighbouring sites of a two-dimensional square lattice and interact with one another only when they find themselves on the same site. A plethora of methods have been used to attack it from various angles, see [10] for a recent review. Among them, Quantum Monte Carlo methods are particularly suited to half filling where numerically exact data is available both for the ground state as well as at finite temperatures [11]. For the strong coupling regime, DMFT[1] is often the method of choice as it incorporates all local correlations non-perturbatively. Many more methods with complementary strengths and weaknesses have been developed including exact diagonalization [13], dual fermion approaches [14], and the fluctuation exchange approximation [15].

Quantum field-theoretic approaches based on the diagrammatic resummation of the one- and two-particle vertices such as parquet solvers [16] and functional renormalization group (fRG) approaches are well suited to investigate the interplay between competing instabilities in the weak to intermediate coupling regime. In particular, the fRG provides exact flow equations which describe the evolution of a generating functional for all many-particle vertices as a function of a regularizing cutoff. The flow allows to interpolate smoothly between the uncorrelated system and the effective low-energy description that encodes possibly complex emergent phenomena. Its strength lies in the unbiased approach to all excitation channels as well as in the flexibility in its application. Recent algorithmic advancements [17] have brought the fRG to a quantitatively reliable level. In particular, it has also been shown to recover the parquet approximation within the multiloop extension of the fRG.

However, the treatment of the full momentum and frequency dependence of the two-particle vertex is numerically too expensive to allow for a systematic analysis. Here, the recently introduced single-boson exchange (SBE) decomposition of the two-particle vertex [18] offers a promising alternative. Based on the classification in terms of U-reducibility, the bosonization of the vertex accounts for the key collective excitations by construction, thereby linking diagrammatic properties directly to physical observables.

[1] DMFT is exact for the limit of infinite dimensions [12].

As a consequence, approximations can be motivated both from diagrammatic arguments and physical understanding [19]. Originally, the SBE has been introduced to a parquet solver of the Anderson impurity model, where it has been shown to improve the numerical implementation [20]. It followed the extension to the treatment of lattice models [21, 22], also within dual fermions [19, 23] and the DMF^{2}RG [24]. Approaches similar in spirit have also been previously applied to the fRG [25, 26]. More recently, a formal rederivation of the multiloop equations [27] in the SBE formalism has been put forward in [28].

The goal of this work is to extend the SBE formalism to the fRG for general models demonstrating the advantages of its implementation. In particular, we focus on deriving and testing physically motivated approximations thereby opening the route towards new parameter regions yet to explore, paving the way for the treatment of more realistic models. This work is structured as follows. In Chapter 2 we introduce the Hubbard Model (2.1) and the N-particle vertex functions (2.2). The flavour of fRG serving as starting point for this work has already been developed to a high level of sophistication capable of quantitatively correct results for the Hubbard model in the weak coupling regime [17]. The frequency and momentum treatment [29], as well as the extensions allowing us to venture beyond the common one-loop (1ℓ) truncation [30] that made quantitative accuracy possible, are summarized in Section 2.3. Chapter 3 forms the theoretical heart piece of this work. First we present the SBE decomposition in Sections 3.1 and 3.2 and then adapt it to the fRG formalism in Section 3.3, where we discuss possible approximations and extensions beyond the 1ℓ truncation. We also derive a natural expression for the Schwinger-Dyson equation in the SBE framework, in Section 3.4. Subsequently, the previous sections are generalised to include non-local interactions in the extended Hubbard model in Section 3.5. The results are presented in Chapter 4. After a short description of the implementation in Section 4.1, the effect of neglecting multiboson processes in the Hubbard model is analysed at half filling (Section 4.2) and at finite doping (in Section 4.3). Further approximation schemes arising within the SBE are investigated in Section 4.4. The data for the extended Hubbard model are provided Section 4.5. Chapter 5 is dedicated to presenting a fluctuation diagnostics of the leading susceptibilities in the Hubbard model, both at half filling and finite doping. From the postprocessing computation described in Section 5.1, the contributions of the individual channels are determined in the various parameter regions in Section 5.2. The results for the magnetic, superconducting, and density susceptibilities are discussed in detail in Sections 5.3, 5.4, and 5.5, respectively. We conclude with a summary and an outlook to promising future directions in the final Chapter 6.

2 Model and Method

Capturing the full behaviour of correlated electrons in realistic two-dimensional materials by solving the Schrödinger equation, is completely out of reach from a numerical stand point, [1] and even if possible, would not contribute much to our understanding of the system. Instead, it is imperative to find the relevant degrees of freedom which allow us to move from the picture of single-particle wave functions to that of collective excitations and order parameters. Likewise, finding a simple Hamiltonian that reproduces the relevant physics can tell us more about the underlying processes and competing phases than one with a dozen terms. The latter may give more accurate, yet possibly over-fitted, results at the cost of not understanding how one arrives at these numbers.

2.1 The Hubbard model

The two-dimensional Hubbard model [1] is graphically illustrated in Fig. 2.1. It describes electrons hopping between neighbouring sites on a square lattice while experiencing an energy penalty when occupying the same site. Despite its conceptual simplicity, it is complex enough to capture interesting physics of competing magnetic, superconducting, and charge order on the one hand, yet simple enough to make progress numerically [10]. One reason the Hubbard model has been studied so intensively is its connection to the cuprates. Here the physics relevant to superconductivity mainly plays out in two-dimensional square layers, and cuprates exhibit many of the same phases observed in the Hubbard model [1, 32, 33]. Thus, many methods have been developed to attack this model from various angles [10, 11, 13, 34, 35]. One particularly suited to explore the subtleties of the interplay between different fluctuations is the *functional renormalization group* (fRG) [36, 37], which will be introduced in Section 2.3. A derivation of the Hubbard model is given in the following section and possible extensions are discussed in Section 2.1.3.

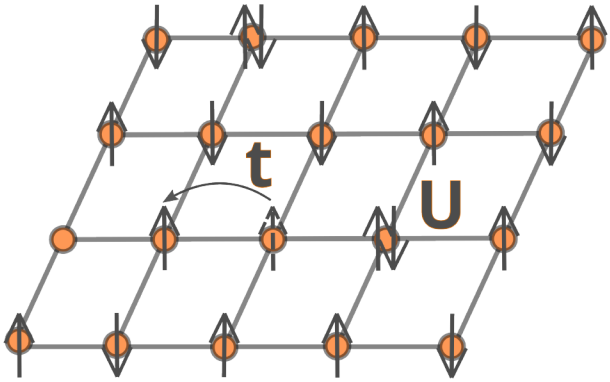

Figure 2.1: Graphical illustration of the two-dimensional Hubbard model, where electrons tunnel between neighbouring sites and an energy penalty U is to be payed for double occupation.

2.1.1 From the many-body Schrödinger equation to the Hubbard model

Here a short overview is given of the approximations and assumptions that transform the full condensed matter Hamiltonian into the Hubbard Hamiltonian. The full Hamiltonian of electrons in the presence of

[1] The dimension of the Hilbert space of n interacting fermions grows as 2^n. Already for $n = 250$ this exceeds the number of hadrons in the universe[31]!

an external potential $V(r)$ reads

$$\mathcal{H} = \sum_\sigma \int \mathrm{d}^3 r \Psi_\sigma^\dagger(r) \left[-\frac{\hbar^2}{2m}\Delta + V(r) \right] \Psi_\sigma(r) - \mu \underbrace{\sum_\sigma \int \mathrm{d}^3 r \Psi_\sigma^\dagger(r)\Psi_\sigma(r)}_{N} + \frac{1}{2}\sum_\sigma \int \mathrm{d}^3 r \mathrm{d}^3 r' \Psi_\sigma^\dagger(r)\Psi_{\sigma'}^\dagger(r')\frac{1}{|r-r'|}\Psi_{\sigma'}(r')\Psi_\sigma(r), \tag{2.1}$$

where $\Psi_\sigma^{(\dagger)}(r)$ (creates) annihilates an electron at position r and spin σ. The first term represents a free electron in an external potential, the second allows for the addition/subtraction of electrons in the framework of the grand canonical ensemble controlled by the chemical potential μ, and the third term incorporates the interaction between the electrons. The system of interest for this work is a two-dimensional square lattice at finite temperatures which allows the use of Bloch's theorem, Wannier functions, and the Matsubara frequency formalism. The intermediate steps are presented in [38], here only the result is stated to be

$$\mathcal{H} = \sum_\sigma \sum_{ijmn} (-t_{ij}^{mn} - \mu\delta_{ij}\delta_{mn}) c_{im\sigma}^\dagger c_{jn\sigma} + \sum_{\sigma\sigma'}\sum_{ijkl}\sum_{mnop} U_{ijkl}^{mnop} c_{im\sigma}^\dagger c_{jn\sigma'}^\dagger c_{ko\sigma'} c_{lp\sigma} \tag{2.2}$$

with lattice site indices i, j, k, and l, Wannier orbital indices m, n, o, and p, spin indices σ and σ', and

$$t_{ij}^{mn} = -\int \mathrm{d}^3 r \varphi_m^*(r - R_i)\left(\frac{\hbar^2}{2m}\Delta + V(r)\right)\varphi_n^*(r - R_j)$$

$$U_{ijkl}^{mnop} = \frac{1}{2}\int \mathrm{d}^3 r \int \mathrm{d}^3 r' \varphi_m^*(r - R_i)\varphi_n^*(r' - R_j)\frac{e^2}{|r-r'|}\varphi_o^*(r' - R_k)\varphi_p^*(r - R_l)$$

where $\varphi_m(r)$ denotes the Wannier functions. By considering the low temperature regime, only bands around the Fermi surface need to be taken into account, and it is assumed that there is only one band crossing the Fermi level, so no orbital indices are used in the following. For highly localised d- and f-orbitals the Wannier functions are strongly localized around the atomic nuclei thus limiting hybridization, aka hopping t, to neighbouring sites which gives $t_{ij} = 0$, unless i and j label neighbouring sites. For a small overlap between Wannier functions of neighbouring sites and none for sites that are further apart, the electron-electron interaction simplifies to a momentum independent on-site interaction $U_{ijkl} = U$ for $i = j = k = l$ and vanishes otherwise.

2.1.2 Hubbard Hamiltonian

Using the assumption stated in the previous section, the exact equation of interacting electrons on a lattice Eq. (2.2) simplifies to the Hubbard Hamiltonian

$$H = -t \sum_{<ij>\sigma} c_{i\sigma}^\dagger c_{j\sigma} + \frac{U}{2}\sum_{i\sigma} n_{i\sigma} n_{i-\sigma} - \mu \sum_{i\sigma} n_{i\sigma}, \tag{2.3}$$

where $c_{i\sigma}^{(\dagger)}$ creates an electron (hole) of spin σ at site i, $n_{i\sigma} = c_{i\sigma}^\dagger c_{i\sigma}$ is the number operator, $< ij >$ a pair of neighbouring sites, t the hopping parameter between neighbouring sites, U the effective on-site interaction, and μ the chemical potential of the system. As such it describes the interplay and competition between the kinetic and potential energy of a particle on a lattice and is able to capture (at least qualitatively correctly) phenomena associated with strong electronic correlations [39, 40]. The combination of its conceptual simplicity and rich phase diagram has made it a popular toy model for Mott insulators and unconventional superconductors [32, 33, 41, 42, 43]. However, the model's simplicity is deceptive and exact solutions are known only for a few special cases such as in 1D [40, 44]. The main obstacle to solving it is the hopping term being diagonal in momentum space whereas the interaction term is diagonal in real space. In momentum space the Hubbard Hamiltonian reads

$$H = \frac{1}{N}\sum_{\mathbf{k}\sigma} \xi_{\mathbf{k}} c_{\mathbf{k}\sigma}^\dagger c_{\mathbf{k}\sigma} + \frac{1}{2N^3}\sum_{\sigma\sigma'}\sum_{\mathbf{k}\mathbf{k}'\mathbf{q}} U c_{\mathbf{k}\sigma}^\dagger c_{\mathbf{k}+\mathbf{q}\sigma} c_{\mathbf{k}'+\mathbf{q}\sigma'}^\dagger c_{\mathbf{k}'\sigma'}, \tag{2.4}$$

where $c_{\mathbf{k}\sigma}^{(\dagger)}$ creates (annihilates) an electron of momentum k and spin σ, and the dispersion is given by $\xi_{\mathbf{k}} = t_k - \mu = -2t(\cos k_x + \cos k_y) - \mu$. All energies are given in units of the nearest-neighbour hopping $t \equiv 1$.

2.1.3 Extensions to the Hubbard model

For many systems of interest the assumptions and approximations made in the derivation of the Hubbard model are too severe. They can, however, be relaxed somewhat by adding further terms to the Hamiltonian.

Next-nearest-neighbour hopping t'

In addition to the hybridization of nearest-neighbour sites, it is common to allow for a diagonal next-nearest-neighbour hopping t' changing the dispersion to

$$\xi_{\mathbf{k}} = t_k - \mu = -2t(\cos k_x + \cos k_y) - 4t' \cos k_x \cos k_y - \mu. \tag{2.5}$$

Next-nearest-neighbour hopping breaks particle-hole symmetry and introduces frustration into an antiferromagnetically ordered system by adding a link across the diagonal. A next-nearest-neighbour hopping t' of order unity would effectively turn diagonal sites into nearest neighbours, thereby changing the lattice geometry.

Nearest-neighbour interaction V

Given the long-range nature of the Coulomb interaction, a purely local interaction cannot be expected to describe realistic materials correctly. For an arbitrarily long-ranged interaction the Hubbard Hamiltonian reads

$$H = -t \sum_{<ij>\sigma} c^\dagger_{i\sigma} c_{j\sigma} \frac{1}{2} \sum_{ij\sigma\sigma'} V_{ij} n_{i\sigma} n_{j\sigma'} - \mu \sum_{i\sigma} n_{i\sigma}. \tag{2.6}$$

In a dense cloud of charges in a lattice of atoms and electrons, the interaction is screened on larger length scales. Therefore non-local short range interactions are a promising first step beyond the classic Hubbard model towards more realistic systems. For the particular case of on-site interactions complemented by a nearest-neighbour interaction, the Hamiltonian reads

$$\begin{aligned} H &= -t \sum_{<ij>\sigma} c^\dagger_{i\sigma} c_{j\sigma} + \frac{U}{2} \sum_{i\sigma} n_{i\sigma} n_{i-\sigma} + \frac{V}{2} \sum_{<ij>\sigma\sigma'} n_{i\sigma} n_{j\sigma'} - \mu \sum_{i\sigma} n_{i\sigma} \\ &= \frac{1}{N} \sum_{\mathbf{k}\sigma} \xi_{\mathbf{k}} c^\dagger_{\mathbf{k}\sigma} c_{\mathbf{k}\sigma} + \frac{1}{2N^3} \sum_{\sigma\sigma'} \sum_{\mathbf{k}\mathbf{k}'\mathbf{q}} (U + V_{\mathbf{q}}) c^\dagger_{\mathbf{k}\sigma} c_{\mathbf{k}+\mathbf{q}\sigma} c^\dagger_{\mathbf{k}'+\mathbf{q}\sigma'} c_{\mathbf{k}'\sigma'}, \end{aligned} \tag{2.7}$$

where $V_{\mathbf{q}} = 2V(\cos q_x + \cos q_y)$ and V is an effective interaction between particles on neighbouring sites. On-site interactions make the avoidance of double occupancy energetically favourable, leading to an evenly spread out charge configuration, an effect which increases with the interaction strength. A nearest-neighbour interaction adds a directly opposing influence where a configuration of evenly spread out particles maximizes the energy penalty from the non-local part of the interaction. In this case a checkerboard pattern of one doubly occupied site, neighboured by four empty ones, comes at no additional potential energy cost at half filling.

In the atomic limit where $t = 0$, it can be inferred from Fig. 2.2 that at $V = \frac{U}{4}$ the advantage of spreading out particles to avoid the cost of double occupancy is counterbalanced exactly by the cost of particles on neighbouring sites interacting. The factor of four is a reflection of the square lattice geometry where every lattice point has four nearest neighbours. Early analytical calculations for the extended Hubbard model predicted the transition to occur at values of $V \gtrsim \frac{U}{4}$ [45, 46], which has been confirmed by exact numerical simulations of quantum Monte Carlo (QMC) [47], the Hartree-Fock approximation and the dynamical mean-field theory (DMFT) [48], the extended DMFT (EDMFT) [49], the dynamical cluster approach (DCA) [50, 51, 52, 53], the dual-boson approach [43, 54, 55], the parquet approximation [56], as well as the determinantal QMC (DQMC) [57].

2.2 Vertices

Though originally developed in the context of quantum electrodynamics, Feynman diagrams have proven their value also in condensed matter physics [58] as a mathematical tool providing deep physical insight

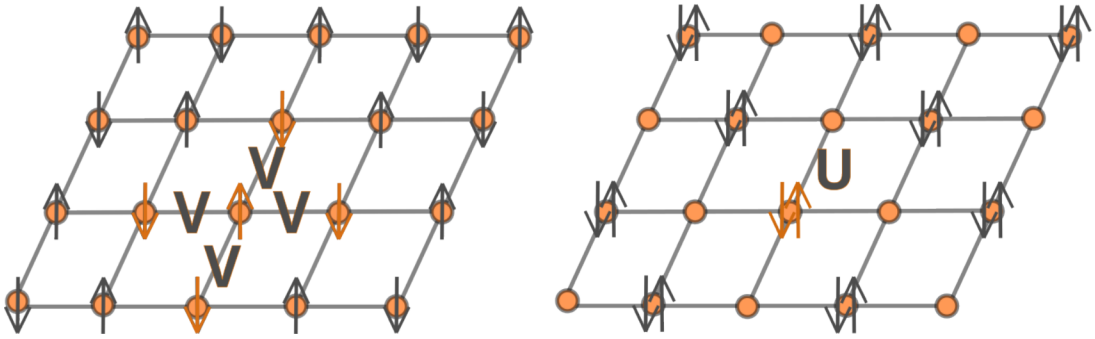

Figure 2.2: The energy cost of the orange configuration on the left is $4V$ per particle and U on the right with a transition between the two configurations to be expected around $V = \frac{U}{4}$.

into the nature of particle interactions. In this thesis the formalism is used extensively to calculate and understand one- and two-particle vertices - the sum of all connected diagrams with two/four external amputated legs respectively - from which physical quantities such as the susceptibilities are obtained. This section is dedicated to introducing their properties relevant to this work's main body.

2.2.1 Self-energy

The one-particle vertex or, more commonly the *self-energy*, Σ is the sum of all one-particle reducible diagrams with amputated external legs. This comprises all diagrams that cannot be separated into two distinct diagrams by cutting one internal Green's function, as illustrated in Fig. 2.3, where the dashed lines represent bare Green's functions G_0 and dots the bare interaction U [58]. As the name suggests, the self-energy can be interpreted as a correction to the free propagator, accounting for the influence of interactions on a single particle's propagation [59]. The self-energy is related to the full - or interacting -

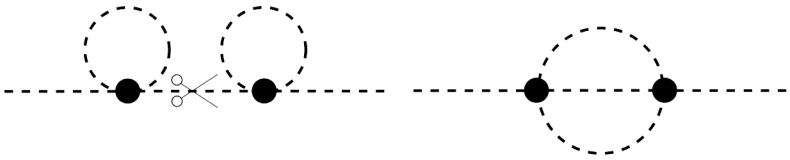

Figure 2.3: One-particle reducibility: examples of a one-particle reducible diagram on the left and an irreducible diagram on the right. The dashed line represents the bare Green's function G_0 and the filled circles stand for the bare interaction U.

Green's function, which is the sum of all diagrams with one incoming and one outgoing leg by the Dyson equation [59]

$$G = G_0 + G_0 \Sigma G \qquad \leftrightarrow \qquad G = (G_0^{-1} - \Sigma)^{-1}. \tag{2.8}$$

2.2.2 Two-particle reducibility and parquet decomposition

The most common criterion of classifying two-particle vertex diagrams based on a notion of reducibility is that of two-particle reducibility. A vertex diagram is said to be *two-particle reducible* if it can be split into two separate parts by cutting two internal lines which are full Green's functions. Likewise, if this is not possible the diagram is termed *two-particle irreducible* (2PI). The two-particle reducible diagrams can be further subdivided based on whether the two lines cut are parallel(/particle-particle), horizontal anti-parallel(/particle-hole crossed), or vertical anti-parallel(/particle-hole) internal lines, as illustrated in Fig. 2.4. Any two-particle reducible diagram falls into exactly one of these three categories, referred to as particle-particle (pp), particle-hole crossed ($\overline{ph}$) and particle-hole (ph) *channel*. The sum of all diagrams of the same channel is denoted by the *two-particle reducible vertices* $\phi_{pp/\overline{ph}/ph}$ [2]. All two-particle irreducible diagrams are collected into $\mathcal{I}^{\mathrm{2PI}}$. Together this yields an exact decomposition of

[2] There may be multiple options of cutting internal lines for one diagram, however they are always of the same type.

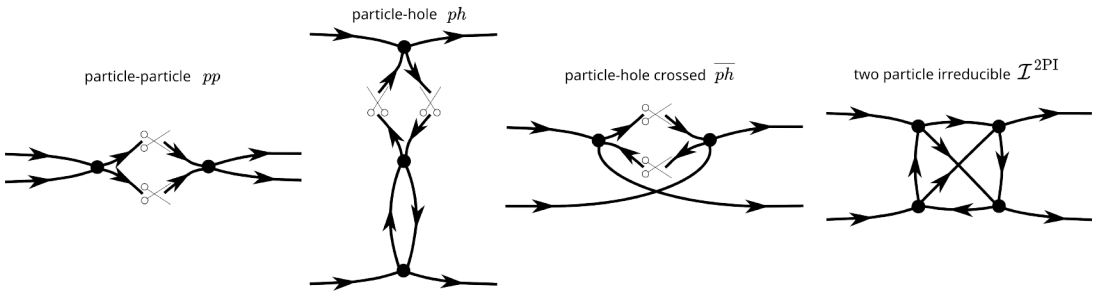

Figure 2.4: Two-particle reducibility: lowest order diagrams of $\phi_{\overline{ph}/ph/pp}$. Right most diagram: lowest order contribution to $\mathcal{I}^{2\mathrm{PI}}$ beyond the bare interaction.

the vertex

$$V = \phi_{pp} + \phi_{ph} + \phi_{\overline{ph}} + \mathcal{I}^{2\mathrm{PI}} \tag{2.9}$$

termed the *parquet decomposition* [60, 61]. The common approximation of limiting the two-particle irreducible vertex $\mathcal{I}^{2\mathrm{PI}}$ to the bare interaction U is referred to as *parquet approximation*, thus confining the method to the weak coupling regime.

2.2.3 Bethe-Salpeter equations

The channel-based classification can be further exploited to yield a set of self-consistent equations, the so-called *Bethe-Salpeter equations* [62]. To this end, we introduce the sum of all diagrams irreducible in a given channel r as

$$\mathcal{I}_r = V - \phi_r = \sum_{r' \neq r} \phi_{r'} + \mathcal{I}^{2\mathrm{PI}} \tag{2.10}$$

and the bubble

$$\Pi_r = \int (GG)_r \tag{2.11}$$

where the channel dependence lies in the summation and integration of internal arguments, which will be given explicitly in the following section. The Bethe-Salpeter equation then reads

$$\phi_r = \int V \Pi_r \mathcal{I}_r. \tag{2.12}$$

For simplicity, the momentum and frequency dependence is suppressed at this stage.

2.2.4 Vertex parametrisation based on bosonic and fermionic arguments

So far, the dependence on external, and summation over internal, arguments has been suppressed to keep the equations and diagrams easily readable. In general, a two-particle vertex diagram depends on four Matsubara frequencies and four momenta, as well as spin indices $V_{\sigma_1\sigma_2\sigma_3\sigma_4}(k_1, k_2, k_3, k_4)$, where the spin quantum number is given by σ_i, and the four-vector $k_i = (\mathbf{k}_i, \nu_i)$ includes both the momentum and frequency. The time and translational invariance of the square lattice $k_4 = k_1 + k_3 - k_2$ can be exploited to reduce the number of independent arguments to three frequencies and momenta respectively and $SU(2)$ symmetry is employed to eliminate the spin dependence [63]

$$V_{\sigma_1\sigma_2\sigma_3\sigma_4}(k_1, k_2, k_3, k_4) = V(k_1, k_2, k_3)\delta_{\sigma_1\sigma_3}\delta_{\sigma_2\sigma_4} - V(k_2, k_1, k_3)\delta_{\sigma_1\sigma_4}\delta_{\sigma_2\sigma_3}. \tag{2.13}$$

Due to symmetries of the vertex, it is sufficient to calculate only $V_{\uparrow\downarrow} \equiv V_{\uparrow\uparrow\downarrow\downarrow}$ [64], and therefore spin indices are dropped to lighten the notation unless needed.

Instead of parametrising the vertex by the two incoming and one outgoing momenta (k_1, k_3 and k_2 respectively), it is advantageous, both for implementations as well as the understanding of the most

important mechanisms at work, to cleverly choose linear combinations of the three. As an example, the dependence of ϕ_{pp} on its arguments is examined:

$$\phi_{pp}(k_1,k_2,k_3,k_4) = \int \mathrm{d}p_1 \int \mathrm{d}p_2\, V(k_1,p_1,k_3,p_2)G(p_1)G(p_2)\mathcal{I}_{pp}(p_1,k_2,p_2,k_4) \tag{2.14}$$

Conservation of momentum and frequencies yields $k_3 = p_1 + p_2 - k_1$ and $k_4 = p_1 + p_2 - k_2$. It turns out that ϕ_{pp} depends most strongly on the transfer momentum $q = k_1 + k_3 = p_1 + p_2$ [65]. Keeping this in mind, Eq. (2.14) is rewritten using $k_1 = k, k_2 = k'$ and $p_1 = p$ as

$$\phi_{pp}(k,k',q-k,q-k') = \int \mathrm{d}p\, V(k,p,q-k,q-p)G(p)G(q-p)\mathcal{I}_{pp}(p,k',q-p,q-k'). \tag{2.15}$$

The analogous expressions for the ph- and $\overline{ph}$-channel read

$$\phi_{ph}(k,k+q,k'+q,k') = \int \mathrm{d}p\, V(k,k+q,p,p+q)G(p)G(p+q)\mathcal{I}_{ph}(p+q,p,k'+q,k') \tag{2.16}$$

$$\phi_{\overline{ph}}(k,k',k'+q,k+q) = \int \mathrm{d}p\, V(k,p,p+q,k+q)G(p)G(p+q)\mathcal{I}_{\overline{ph}}(p,k',k'+q,p) \tag{2.17}$$

where $\mathcal{I}_r = V - \phi_r$ is the two-particle irreducible vertex in channel r. The two four-vectors k and k' are referred to as *fermionic* in contrast to the *bosonic* four-vector q. Which combination of in- and outgoing indices adds up to yield the bosonic transfer four-vector q depends on the channel. Instead of writing $\phi_{pp}(k_1,k_2,k_3,k_4)$, a channel specific notation denoted by an upper index is introduced as

$$\phi_{pp}(k,k',q-k,q-k') \equiv \phi_{pp}^{pp}(q,k,k') \tag{2.18a}$$

$$\phi_{ph}(k,k+q,k'+q,k') \equiv \phi_{ph}^{ph}(q,k,k') \tag{2.18b}$$

$$\phi_{\overline{ph}}(k,k',k'+q,k+q) \equiv \phi_{ph}^{\overline{ph}}(q,k,k') \tag{2.18c}$$

shown in Fig. 2.5. Note that any object, irrespective of its channel, may be expressed in the notation of any (other) channel. To avoid an unnecessary doubling of indices, objects are assumed to be expressed

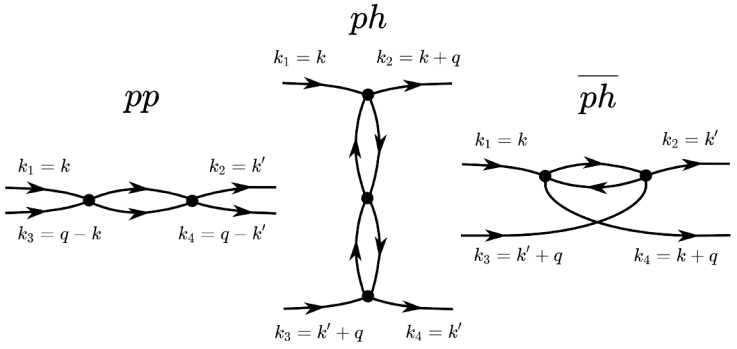

Figure 2.5: Channel dependent notation. The three independent momenta are chosen to be the transfer four-vector q and one incoming and one outgoing fermionic four-vectors k and k' respectively.

in their natural notation unless stated otherwise. Note that objects like the vertex, that have no natural notation, may be expressed in channel notation nonetheless

$$V^r = \phi_{pp}^r + \phi_{ph}^r + \phi_{\overline{ph}}^r + U. \tag{2.19}$$

2.2.5 Form factors

As already mentioned, the two-particle reducible vertices depend weakly on the two fermionic momenta and strongly on the bosonic one [65]. This observation is the basis for the expansion in *form factors* of the fermionic momenta [25, 65, 66, 67]. The practice was formalized and coined ***truncated unity*** fRG (TUfRG) in [68]. The two-particle vertices expanded in form factors are given by

$$\phi_r(q,k,k') = \sum_{n,n'} f_n(\mathbf{k})\Phi_r(\mathbf{q},\Omega,\nu,n,\nu',n')f_{n'}(\mathbf{k}') \tag{2.20}$$

and reversed

$$\Phi_r(\mathbf{q},\Omega,\nu,n,\nu',n') = \frac{1}{4\pi^2}\int_{\mathrm{BZ}} \mathrm{d}\mathbf{k}\mathrm{d}\mathbf{k}' f_n(\mathbf{k})\phi_r(\mathbf{q},\Omega,n,\nu,n',\nu')f_{n'}(\mathbf{k}') \tag{2.21}$$

which is exact for any complete set of functions f_n. For the square lattice Hubbard model the set of choice are orthonormal functions based on bond distances in real space. They are listed in Table 2.1 alongside their momentum space equivalents obtained by Fourier transformation. The constant form factor f_0

Real space	Momentum space
$\tilde{f}_0(\mathbf{R}) = \delta_{R_x,0}\delta_{R_y,0}$	$f_0(\mathbf{k}) = \frac{1}{2\pi}$
$\tilde{f}_1(\mathbf{R}) = \frac{1}{\sqrt{2}}(\delta_{R_x,-1}+\delta_{R_x,1})$ or $\tilde{f}_1(\boldsymbol{R}) = \frac{1}{2}\delta_{R_y,0}(\delta_{R_x,-1}+\delta_{R_x,1}) + \frac{1}{2}\delta_{R_x,0}(\delta_{R_y,-1}+\delta_{R_y,1})$	$f_1(\mathbf{k}) = \frac{1}{\sqrt{2\pi^2}}\cos(k_x)$ or $f_1(\mathbf{k}) = \frac{1}{\sqrt{4\pi^2}}(\cos(k_x)-\cos(k_y))$
$\tilde{f}_2(\mathbf{R}) = \frac{1}{\sqrt{2}}(\delta_{R_y,-1}+\delta_{R_y,1})$ or $\tilde{f}_2(\boldsymbol{R}) = \frac{1}{2}\delta_{R_y,0}(\delta_{R_x,-1}+\delta_{R_x,1}) - \frac{1}{2}\delta_{R_x,0}(\delta_{R_y,-1}+\delta_{R_y,1})$	$f_2(\mathbf{k}) = \frac{1}{\sqrt{2\pi^2}}\cos(k_y)$ or $f_2(\mathbf{k}) = \frac{1}{\sqrt{4\pi^2}}(\cos(k_x)+\cos(k_y))$
$\tilde{f}_3(\mathbf{R}) = \frac{i}{\sqrt{2}}(\delta_{R_x,-1}-\delta_{R_x,1})$	$f_3(\mathbf{k}) = \frac{1}{\sqrt{2\pi^2}}\sin(k_x)$
$\tilde{f}_4(\mathbf{R}) = \frac{i}{\sqrt{2}}(\delta_{R_y,-1}-\delta_{R_y,1})$	$f_4(\mathbf{k}) = \frac{1}{\sqrt{2\pi^2}}\sin(k_y)$
$\tilde{f}_5(\mathbf{R}) = \frac{1}{\sqrt{2}}(\delta_{R_x,-1}\delta_{R_y,1}+\delta_{R_x,1}\delta_{R_y,-1})$	$f_5(\mathbf{k}) = \frac{1}{\sqrt{2\pi^2}}\cos(k_x+k_y)$

Table 2.1: Form factors of the square lattice based on real space bonds in real space and momentum space. It is common to linearly combine the bond distance based form factors 1 and 2 to yield the so-called 'd-wave' and 'extended s-wave' form factors.

is often called 's-wave'. Instead of $f_{1/2}$ as listed in Table 2.1 linear combinations of the two are more common with $f_1(\mathbf{k}) = \frac{1}{\sqrt{2\pi^2}}(\cos(k_x)-\cos(k_y))$ ('d-wave') and $f_2(\mathbf{k}) = \frac{1}{\sqrt{2\pi^2}}(\cos(k_x)+\cos(k_y))$ ('extended s-wave'). The weak dependence on fermionic momenta allows for the use of only a handfull of form factors [68]. Translations between the channels are no longer accomplished by a shift in the momentum arguments, instead the dependence of fermionic momenta is handled using so-called '*projection matrices*' $P^{r\to r'}$, reported in Appendix A.1.1. Note that the projection matrices also shift the frequency dependence and bosonic momentum dependence in addition to 'projecting' the form factor dependence.

2.2.6 Physical and diagrammatic channels

So far, the idea of a channel was based on shared diagrammatic properties. These diagrammatic channels are useful in the context of Feynman diagram's properties, such as two-particle or U-reducibility. Other diagrammatic properties include the high-frequency behaviour of the two-particle vertices and the form of the extended bare interaction in channel dependent notation. However, in most cases the questions of the greatest interest are not about properties of diagrams, but physical observables motivating the use of the so-called *physical channels*. They are based on the superconducting, magnetic, and density fluctuations. The physical channels are closely related to the diagrammatic ones by

$$\phi^{\mathrm{SC}} = \phi_{pp} \tag{2.22a}$$
$$\phi^{\mathrm{D}} = 2\phi_{ph} - \phi_{\overline{ph}} \tag{2.22b}$$
$$\phi^{\mathrm{M}} = -\phi_{\overline{ph}}. \tag{2.22c}$$

Unless specified otherwise, SC/D/M quantities are expressed in $pp/ph/\overline{ph}$ notation, respectively. The vertex can also be translated to physical channels

$$V^{\mathrm{SC}} = V^{pp} \tag{2.23a}$$
$$V^{\mathrm{D}} = 2V^{ph} - V^{\overline{ph}} \tag{2.23b}$$
$$V^{\mathrm{M}} = -V^{\overline{ph}}. \tag{2.23c}$$

Diagrammatic channels are labelled by r, and η is used for physical channels. There is only one vertex when working in diagrammatic channels which can, however, be expressed in the different channel notations, indicated by an upper rather than a lower channel label. In contrast, the vertices in physical channels contain different information and cannot be transformed into one another by a change of notation only. More detailed relations between the physical and diagrammatic channels in form factor expanded form can be found in Appendix A.2.

2.3 The functional Renormalization Group

Interacting Fermi systems in low dimensions exhibit complicated competing instabilities, with the relevant energy scales spanning multiple orders of magnitude, while simultaneously being plagued by infrared divergences. The fRG expands on perturbation theory in a way that avoids the infrared divergences and is capable of treating competing fluctuation tendencies on equal footing. It can be derived by replacing the free propagator by a propagator depending on an infrared cutoff Λ, and taking the derivative of the generating functional with respect to this cutoff, resulting in an infinite hierarchy of coupled differential flow equations [36]. The equations' solutions are the exact N-particle vertices. In practice, solving an infinite hierarchy of differential equations is impossible; the approximations made in this specific work are detailed in the following sections.

2.3.1 1ℓ flow equations

An excellent and extensive derivation of the fRG flow equations is presented in [36] and will not be repeated here. The flow equations for the different vertex quantities are given by an infinite hierarchy of flow equations where the flow of the N-particle vertex depends on the higher order vertices. In this section the flow equations for the one- and two-particle vertices are reported and linked to the vertex objects introduced in Section 2.2.

Self-energy

The one-particle vertex' or self-energy's flow equation after exploiting SU(2) symmetry [69] reads

$$\dot{\Sigma}(k) := \partial_\Lambda \Sigma^\Lambda(k) = \sum_p (2V^\Lambda(k,k,p) - V^\Lambda(p,k,k)) S^\Lambda(p), \tag{2.24}$$

with the cut-off parameter Λ and single-scale propagator

$$S^\Lambda(k) = \partial_\Lambda G^\Lambda(k)|_{\Sigma=\text{const}}. \tag{2.25}$$

The self-energy flow equation (2.24) exhibits a strong dependence on internal momenta and requires the two-particle vertex V without form factor expansion as input. To construct the vertex in this expression, the expansion in form factors is reversed to yield data on a momentum grid, and then the momentum and frequency arguments are translated from the channel specific notation to the purely fermionic notation (see Appendix B.1 for details). In physical channels the equation of the vertex thus reads

$$\begin{aligned} V(k_1,k_2,k_3,k_4) = \phi^{\mathrm{SC}}(k_1+k_3,k_1,k_2) + \frac{1}{2}\left(\phi^{\mathrm{D}}(k_2-k_1,k_1,k_4) - \phi^{\mathrm{M}}(k_2-k_1,k_1,k_4)\right) \\ -\phi^{\mathrm{M}}(k_3-k_2,k_1,k_2) + U. \end{aligned} \tag{2.26}$$

where

$$\phi^{\mathrm{SC}}(k_1+k_3,k_1,k_2) = \sum_{n,n'} f_n(\mathbf{k}_1) f_{n'}(\mathbf{k}_2) \phi^{\mathrm{SC}}(\nu_1+\nu_3, \mathbf{k}_1+\mathbf{k}_3, \nu_1, n, \nu_2, n') \tag{2.27}$$

and the other channels follow analogously. Due to the information loss of the form factor expansion, the conventional self-energy flow equation is unfortunately not well suited to capture the momentum dependence of the self-energy, leading to a considerably worse convergence in form factors than for the two-particle vertex itself [70]. As increasing the number of form factors for the vertex quantities is not feasible, an alternative flow equation for the self-energy is needed to resolve the momentum structure of the self-energy correctly.

The adverse effect of the form factor truncation on the self-energy can be cured by using the derivative of the Schwinger-Dyson equation (SDE) [71]

$$\begin{aligned}\dot{\Sigma}(k_1) &:= -\partial_\Lambda \left(\sum_{k_2,k_3,k_4} V(k_1,k_2,k_3,k_4) G(k_2) G(k_3) G(k_4) \delta_{k_1+k_3-k_2,k_4} U \right) \\ &= - \sum_{k_2,k_3,k_4} \partial_\Lambda \left(V(k_1,k_2,k_3,k_4) \right) G(k_2) G(k_3) G(k_4) \delta_{k_1+k_3-k_2,k_4} U \\ &\quad - \sum_{k_2,k_3,k_4} V(k_1,k_2,k_3,k_4) \partial_\Lambda \left(G(k_2) G(k_3) G(k_4) \right) \delta_{k_1+k_3-k_2,k_4} U \end{aligned} \tag{2.28}$$

as a flow equation for the self-energy instead [17, 70]. In addition, the SDE contains all diagrams without the need for multiloop corrections (see Section 2.3.2). While the numerical effort is higher for the SDE-based flow equation due to the many terms, it does not require a reversal of the form factor expansion and therefore completely eliminates the issue discussed above. Differences due to information loss when using the TUfRG aside, the conventional flow equation and SDE flow equation do not yield the same results; only at multiloop convergence do they agree. Further details on the implementation, effect of TUfRG, and relation between the two schemes can be found in Cornelia Hille's excellent PhD thesis [69] and will not be repeated here. Instead, in Section 3.4 we demonstrate how the SDE can be adapted to the SBE framework.

Two-particle vertex

The flow equation of the two-particle vertex V at the 1ℓ level are given by [30]

$$\begin{aligned}\partial_\Lambda V^\Lambda(k_1,k_2,k_3,k_4) =& \dot{\phi}^{\mathrm{SC},(1)}(k_1+k_3,k_1,k_2) - \dot{\phi}^{\mathrm{M},(1)}(k_3-k_2,k_1,k_2) \\ &+ \frac{1}{2}\left(\dot{\phi}^{\mathrm{M},(1)}(k_2-k_1,k_1,k_4) - \dot{\phi}^{\mathrm{D},(1)}(k_2-k_1,k_1,k_4) \right) \end{aligned} \tag{2.29}$$

where

$$\begin{aligned}\dot{\phi}^{\eta,(1)}(q,k,k') &:= \partial_\Lambda \phi^{\Lambda,\eta,(1)}(q,k,k') \\ &= \int \mathrm{d}p \; V^\eta(q,k,p) \dot{\Pi}^\eta(q,p) V^\eta(q,p,k'). \end{aligned} \tag{2.30}$$

The derivative of the bubbles is given by

$$\dot{\Pi}^{\mathrm{SC}}(q,k) = \dot{\Pi}_{pp}(q,k) = S^\Lambda(q-k) G^\Lambda(k) + G^\Lambda(q-k) S^\Lambda(k) \tag{2.31a}$$

$$\dot{\Pi}^{\mathrm{M/D}}(q,k) = -\dot{\Pi}_{ph}(q,k) = -\left(S^\Lambda(q+k) G^\Lambda(k) + G^\Lambda(q+k) S^\Lambda(k) \right). \tag{2.31b}$$

Equivalent equations in diagrammatic channels and the expansion in form factors are provided in Appendix A.3 and A.4, respectively. These equations are incomplete as contributions from the six-particle vertex (and higher orders) are lacking. As a consequence, the Mermin Wagner theorem is not fulfilled, instead the incomplete inter-channel feedback leads to divergent behaviour at finite temperature.

Susceptibilities

The susceptibilities or linear response functions χ^η can also be calculated from flow equations [72]

$$\dot{\gamma}^{3,\eta}(q,k,k') = -\int \mathrm{d}p \; V^\eta(q,k,p) \dot{\Pi}^\eta(q,p) \gamma^{3,\eta}(q,p,k') \tag{2.32}$$

$$\dot{\chi}^\eta(q,k,k') = \frac{1}{2} \int \mathrm{d}p \; \gamma^{3,\eta}(q,k,p) \dot{\Pi}^\eta(q,p) \gamma^{3,\eta}(q,p,k'). \tag{2.33}$$

with the fully screened three-point vertex $\gamma^{3,\eta}$. The physical vertices and susceptibilities are closely related by the '*postprocessing relation*'

$$\chi^\eta = \chi^{\eta,0} + \chi^{\eta,0} V^\eta \chi^{\eta,0} \tag{2.34}$$

with bare bubbles

$$\chi^{\eta,0}(\Omega,\mathbf{q},\mathbf{k},\mathbf{k}') = \sum_\nu \Pi^\eta(\Omega,\mathbf{q},\nu,\mathbf{k},\mathbf{k}'). \tag{2.35}$$

2.3.2 Multiloop extension

The influence of the six-particle vertex on the flow of Σ and V may be recovered by iterative extensions to the flow equations [27, 73, 74]. The first correction is the Katanin substitution [75], where the single-scale propagator $S^\Lambda = \partial_\Lambda G^\Lambda$ is replaced by the full derivative of the Green's function

$$\mathrm{d}_\Lambda G^\Lambda(k) = S^\Lambda(k) + G^\Lambda(k)\dot{\Sigma}(k)G^\Lambda(k). \tag{2.36}$$

Multiloop corrections of this type are illustrated in Fig. 2.6 by the first diagram in the series. The second

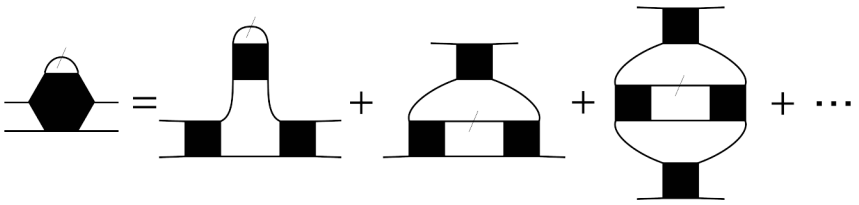

Figure 2.6: Six-particle vertex contribution to the flow of the two-particle vertex. The first diagram represents the Katanin substitution, the second a two-loop correction and the third a correction at the 3ℓ level.

diagram represents two-loop (2ℓ) corrections which introduce extra feedback between the channels. In physical channels the 2ℓ flow equations are [75]

$$\dot{\phi}^{\eta,(2),L}(q,k,k') = \int \mathrm{d}p\, \dot{\mathcal{I}}^{\eta,(1)}(q,k,p)\Pi^\eta(q,p)V^\eta(q,p,k') \tag{2.37a}$$

$$\dot{\phi}^{\eta,(2),R}(q,k,k') = \int \mathrm{d}p\, V^\eta(q,k,p)\Pi_{pp}(q,p)\dot{\mathcal{I}}^{\eta,(1)}(q,p,k'), \tag{2.37b}$$

where $\dot{\mathcal{I}}^{\eta,(\ell)}$ is given by

$$\dot{\mathcal{I}}^{\mathrm{SC},(\ell)} = \frac{1}{2}\left(P^{ph\to pp}[\dot{\phi}^{\mathrm{D},(\ell)}] - P^{ph\to pp}[\dot{\phi}^{\mathrm{M},(\ell)}]\right) + P^{\overline{ph}\to pp}[\dot{\phi}^{\mathrm{M},(\ell)}] \tag{2.38a}$$

$$\dot{\mathcal{I}}^{\mathrm{M},(\ell)} = -\frac{1}{2}\left(P^{ph\to \overline{ph}}[\dot{\phi}^{\mathrm{D},(\ell)}] - P^{ph\to \overline{ph}}[\dot{\phi}^{\mathrm{M},(\ell)}]\right) - P^{pp\to \overline{ph}}[\dot{\phi}^{\mathrm{SC},(\ell)}](q,k,k') \tag{2.38b}$$

$$\dot{\mathcal{I}}^{\mathrm{D},(\ell)} = +2P^{pp\to ph}[\dot{\phi}^{\mathrm{SC},(\ell)}] - P^{pp\to \overline{ph}}[\dot{\phi}^{\mathrm{SC},(\ell)}] - 2P^{\overline{ph}\to ph}\left[\dot{\phi}^{\mathrm{M},(\ell)}\right] - P^{ph\to \overline{ph}}\left[\frac{1}{2}\dot{\phi}^{\mathrm{D},(\ell)} - \frac{1}{2}\dot{\phi}^{\mathrm{M},(\ell)}\right]. \tag{2.38c}$$

Beginning at the 3ℓ level also central corrections enter [30] which are represented by the third diagram in Fig. 2.6. They read

$$\dot{\phi}^{\mathrm{SC},(3),C}(q,k,k') = \int \mathrm{d}p\, \dot{\phi}^{\eta,R,(1)}(q,k,p)\Pi^\eta(q,p)V^\eta(q,p,k'). \tag{2.39}$$

Corrections of the type $\dot{\phi}^{\eta,(\ell),L} = \int \dot{\mathcal{I}}^{\eta(\ell-1)}\Pi^\eta V^\eta$ and $\dot{\phi}^{\eta,(\ell),R} = \int V^\eta \Pi^\eta \dot{\mathcal{I}}^{\eta(\ell-1)}$ are referred to as *left* and *right corrections* of order ℓ, respectively. The diagrams of the type $\dot{\phi}^{\eta,C,(\ell)} = \int \dot{\phi}^{\eta,(\ell-2),R}\Pi^\eta V^\eta$ are called *central corrections*. For general $l \geqq 3$ the derivative is given by [30]

$$\dot{\phi}^{\eta,(\ell)} = \dot{\phi}^{\eta,(1)} + \dot{\phi}^{\eta,(2),L} + \dot{\phi}^{\eta,(2),R} + \sum_{\ell'>2}^{\ell'\leqq\ell} \dot{\phi}^{\eta,(\ell'),L} + \dot{\phi}^{\eta,(\ell'),R} + \dot{\phi}^{\eta,(\ell'),C} \tag{2.40}$$

with

$$\dot{\phi}^{\eta,(\ell),L}(q,k,k') = \int \mathrm{d}p\, \dot{\mathcal{I}}^{\eta,(\ell-1)}(q,k,p)\Pi^\eta(q,p)V^\eta(q,p,k') \tag{2.41}$$

$$\dot{\phi}^{\eta,(\ell),R}(q,k,k') = \int \mathrm{d}p\, V^\eta(q,k,p)\Pi^\eta(q,p)\dot{\mathcal{I}}^{\eta,(\ell-1)}(q,p,k') \tag{2.42}$$

$$\dot{\phi}^{\eta,C,(\ell)}(q,k,k') = \int \mathrm{d}p\, \dot{\phi}^{\eta,(\ell-2),R}(q,k,p)\Pi^\eta(q,p)V^\eta(q,p,k'). \tag{2.43}$$

At $\ell \to \infty$ the contributions from the six-point vertex are restored, the inter-channel feedback completed, the parquet equation recovered, and the latter guarantees that the Mermin Wagner theorem is fulfilled.

At the 2ℓ level the vertex is already correct up to $\mathcal{O}(U^3)$. There are also multiloop corrections to the conventional flow equation of the self-energy [74], however, in this work the derivative of the SDE is used when venturing beyond the 1ℓ truncation which is inherently a multiloop quantity and requires no additional corrections. For the susceptibilities the multiloop corrections are

$$\dot{\gamma}^{3,\eta,(\ell),R}(q,k) = -\int \mathrm{d}p\ \dot{\mathcal{I}}^{\eta,(\ell-1)}(q,k,p)\Pi^{\eta}(q+p,p)\gamma^{3,\eta}(q,p) \tag{2.44}$$

$$\dot{\gamma}^{3,\eta,(\ell),C}(q,k) = \int \mathrm{d}p\ V^{\eta}(q,k,p)\Pi^{\eta}(q+p,p)\dot{\gamma}^{3,\eta,(\ell-1),R}(q,p) \tag{2.45}$$

$$\dot{\chi}^{\eta,(\ell),C}(q,k,p) = -\frac{1}{2}\int \mathrm{d}p\ \gamma^{3,\eta}(q,p)\Pi^{\eta}(q+p,p)\dot{\gamma}^{3,\eta,(\ell-1),R}(q,p). \tag{2.46}$$

At finite ℓ the results from the flow of χ^{η} and results obtained using the postprocessing relation Eq. (2.34) in general do not agree, however, agreement is restored for $\ell \to \infty$ [74].

2.3.3 Cutoff schemes

One of the advantages of the fRG is its flexibility with respect to the path through parameter space that is chosen for the integration by means of the exact form of Green's function's cutoff dependence [36]. The choice can be exploited to avoid infrared divergencies by integrating out the unproblematic degrees of freedom first and then carefully approaching the Fermi surface or the low-frequency regime at the end of the flow. Unless stated otherwise, a frequency cutoff referred to as 'Ω−flow' [65] is used for all data in the following chapters, which corresponds to a Green's function of the form

2.3.4 Algorithmic implementation

When using channel-based notation the strongest dependence is on the bosonic momentum, which is implemented on a square grid with the option of adding a finer grid around $\mathbf{q} = (\pi, \pi)$. The weaker dependence on the fermionic momenta is treated by expansion in form factors. Switching between channel notations is complicated by the expansion in form factors, necessitating the introduction of the projection matrices listed in Appendix A.1.1. The imaginary time Matsubara frequency formalism is used. Analogous to the momenta, frequencies are divided into a bosonic transfer frequency Ω and secondary fermionic frequencies ν, ν'. However, a symmetrized notation is chosen for the fermionic frequencies to centre them around Ω in contrast to the non-symmetrized notation favourable for the form factor expansion

$\overline{ph}$-notation	ph-notation	pp-notation
$k_1 = (\nu - \Omega/2, \mathbf{k})$	$k_1 = (\nu - \Omega/2, \mathbf{k})$	$k_1 = (\nu + \Omega/2, \mathbf{k})$
$k_2 = (\nu' - \Omega/2, \mathbf{k}')$	$k_2 = (\nu + \Omega/2, \mathbf{k} + \mathbf{q})$	$k_2 = (\nu' + \Omega/2, \mathbf{k}')$
$k_3 = (\nu' + \Omega/2, \mathbf{k}' + \mathbf{q})$	$k_3 = (\nu' + \Omega/2, \mathbf{k}' + \mathbf{q})$	$k_3 = (\Omega/2 - \nu, \mathbf{q} - \mathbf{k})$
$k_4 = (\nu + \Omega/2, \mathbf{k} + \mathbf{q})$	$k_4 = (\nu' - \Omega/2, \mathbf{k}')$	$k_4 = (\Omega/2 - \nu', \mathbf{q} - \mathbf{k}')$.

The solver routine is outlined in Fig. 2.7. After initializing a 'state vector' that contains all the flowing objects initialized to their respective values, the single-scale propagator S^{Λ} and Green's function G^{Λ} are calculated at the current scale Λ. Next they are fed into the conventional flow equation for the self-energy (Eq. 2.24), which in turn is inputted into the self-energy iteration. The self-energy is treated on a considerably finer grid and uses a vertex in purely fermionic notation as input. Within a self-energy iteration step, the Katanin substitution (Eq. 2.36) is performed, followed by the evaluation of the 1ℓ-loop flow equations (Eq. A.4), and then higher loop order corrections (Eq. A.5c) are added. Finally, the self-energy is re-evaluated with the updated vertex using the derivative of the Schwinger-Dyson equation (Eq. 2.28), before the next self-energy iteration begins. When using the SBE formalism, ϕ is replaced by λ, w and M. The results in Sections 4.2 to 4.5 are obtained with a simpler routine, where no Katanin substitution, no self-energy and multiloop iterations are performed, and only the conventional flow equation for the self-energy is used.

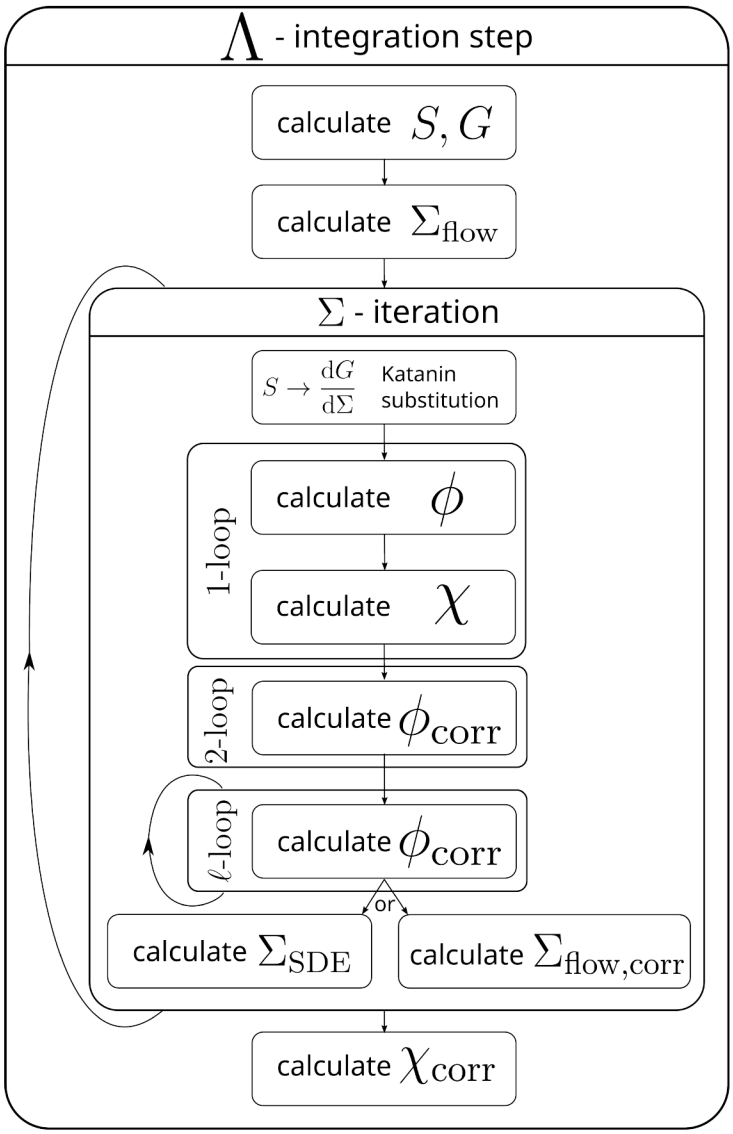

Figure 2.7: Schematic overview of the individual solver steps.

3 The single-boson exchange decomposition and fRG formulation

Treating the two-particle vertex accurately in all its complexities is a notoriously challenging task [76]. Countless methods and approximations have been put forward to tackle the problem [35]. This work details the advantages and applicability of a recent development in this field [18], the single-boson exchange (SBE) decomposition of the two-particle vertex function, in the context of the fRG. The motivation behind the SBE is to express the vertex in terms of different flavours of collective excitations, represented by effective exchange bosons [18]. On top of the physically intuitive picture of the vertex this provides, gathering the diagrams that are part of the same collective excitation in one object limits divergences to this one object. Multiple divergences then occur only if there are actual competing physical instabilities [18]. In this chapter the concept of the SBE is presented in detail and applied to the fRG. First, the somewhat abstract idea underlying the SBE is translated into a set of diagrammatic properties based on the *bare interaction* reducibility in Section 3.1. Then the vertex-like quantities of the SBE are introduced in Section 3.2 followed by the flow equations in Section 3.3. In Section 3.4 a self-energy flow equation is derived from the Schwinger-Dyson equation. Finally, we generalize the SBE formalism to the extended Hubbard model in Section 3.5 Data demonstrating the value of the SBE for the fRG is provided in Chapter 4.

3.1 Bare interaction reducibility

Previously, in Section 2.2.2, the concept of two-particle reducibility was discussed. Recently, an alternative notion of reducibility, the bare interaction or *U-reducibility*, was introduced [18]. This alternative takes the observation that the strongest dependence is on the bosonic arguments (see Section 2.2.4), further. Diagrams are interpreted as the exchange of a single boson depending only on the bosonic four-vector q or if the structure of the diagram does not allow it, of multiple bosons. Diagrams in the first category are termed U-reducible, i.e., they can be split into two separate parts by cutting a bare interaction, and diagrams that cannot, are U-irreducible. Analogous to the two-particle reducibility, these U-reducible diagrams can be further subdivided depending on whether the two lines attached to the bare interaction are two particle-particle, particle-hole crossed, or particle-hole lines. While, therefore, a U-reducible diagram is also two-particle reducible with the exception of the bare interaction itself (considered to be U-reducible in all three channels), the reverse is not true. In this sense, U-reducibility can be seen as a further subdivision of two-particle reducible diagrams (bare interaction excluded), instead of an alternative notion of reducibility. Figure 3.1 showcases examples of a U-reducible diagram, where the fermions interact via the exchange of a single bosonic propagator w, mediated by a fermion-boson coupling λ, and a U-irreducible diagram that features the exchange of multiple bosonic objects.

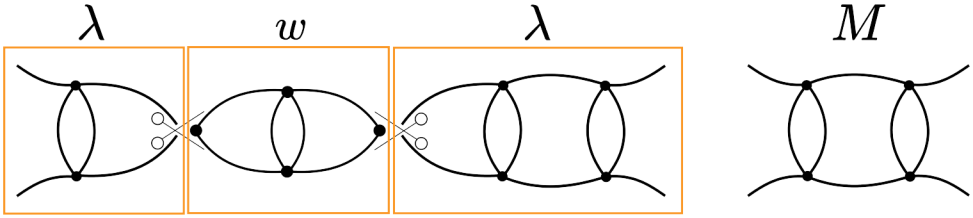

Figure 3.1: Example of a U-(ir)reducible diagram on the left and right, respectively.

3.2 SBE quantities

In this section the idea of interpreting diagrams as the exchange of a single or multiple bosons will be made concrete and translated to equations for the special case of the parquet approximation with a local interaction. We use diagrammatic channels for this introduction, as they are best suited to the discussion of diagrammatic properties; equivalent expressions translated to physical channels are reported in Appendix B.2.

The sum of all U-reducible diagrams in a given channel r, including the bare interaction, is denoted by ∇_r and represents the exchange of a single bosonic propagator w_r between two fermion-boson couplings λ_r

$$\begin{aligned}\nabla_r(q,k,k') \equiv \nabla_r^{\uparrow\downarrow}(q,k,k') &= [\sum_{\sigma,\sigma'} \lambda_r^{\uparrow\sigma}(q,k) w_r^{\sigma\sigma'}(q) \bar{\lambda}_r^{\sigma',\downarrow}(q,k')]^{\uparrow\downarrow} \\ &\equiv \lambda_r(q,k) \bullet w_r(q) \bullet \bar{\lambda}_r(q,k') \end{aligned} \tag{3.1}$$

where we use the natural notation for r introduced in Section 2.2.4 and the filled circle represents a summation over spins [28, 77]. Spin dependence is suppressed to lighten the notation and given explicitly only when strictly necessary. In the ph−channel particular care is due, as

$$\begin{aligned}\nabla_{ph}^{\uparrow\downarrow}(q,k,k') =& \frac{1}{2}\Big(-\lambda_{\overline{ph}}^{\uparrow\downarrow}(q,k) w_{\overline{ph}}^{\uparrow\downarrow}(q) \bar{\lambda}_{\overline{ph}}^{\uparrow\downarrow}(q,k') \\ &+(\lambda_{\overline{ph}}^{\uparrow\downarrow}(q,k) + 2\lambda_{ph}^{\uparrow\downarrow}(q,k))(w_{\overline{ph}}^{\uparrow\downarrow}(q) + 2w_{ph}^{\uparrow\downarrow}(q))(\bar{\lambda}_{\overline{ph}}^{\uparrow\downarrow}(q,k') + 2\bar{\lambda}_{ph}^{\uparrow\downarrow}(q,k'))\Big) \\ &-\lambda_{ph}^{\uparrow\downarrow}(q,k) w_{ph}^{\uparrow\downarrow}(q) \bar{\lambda}_{ph}^{\uparrow\downarrow}(q,k').\end{aligned}$$

It is now that the numerical advantage of this scheme becomes apparent: a quantity ∇_r that depends on three independent indices can be factorised into quantities that depend on two arguments at most. Diagrams that are two-particle reducible with respect to channel r, and do not fall into this category, are collected into the rest function $M_r(q,k,k')$ containing the multiboson exchange processes.

3.2.1 Parquet equation for the SBE

The parquet decomposition can be rewritten in terms of SBE quantities by substituting $\Phi_r = \nabla_r - U + M_r$ yielding

$$V = \nabla_{pp} + M_{pp} + \nabla_{\overline{ph}} + M_{\overline{ph}} + \nabla_{ph} + M_{ph} - 3U + \mathcal{I}^{\mathrm{2PI}} \tag{3.2}$$

where $\mathcal{I}^{\mathrm{2PI}}$ comprises all completely two-particle irreducible diagrams. Throughout this work the parquet approximation ($\mathcal{I}^{\mathrm{2PI}} = U$) is used, limiting the analysis to the weak coupling regime. The vertex decomposition for the parquet approximation is also shown in Fig. 3.2. The expression of V used for the

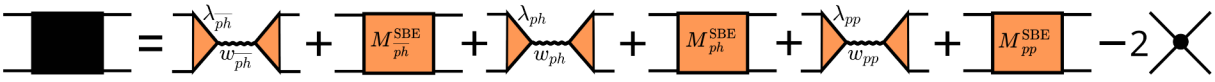

Figure 3.2: Diagrammatic representation of Eq. (3.2), the parquet equation expressed using SBE quantities.

conventional self-energy flow is reported in Appendix B.1.

3.2.2 Fermion-boson coupling λ

The fermion-boson coupling[1], as the name suggests, couples two fermionic particles (or holes) to a bosonic propagator. As such it depends on two linearly independent arguments which are chosen to be one fermionic and one bosonic argument, emphasizing the coupling nature of λ with

$$\lambda_r(q,k) = 1 + \int \mathrm{d}p\, \mathcal{I}_{r,\mathrm{SBE}}(q,k,p)\Pi_r(q,p) \tag{3.3}$$

$$= 1 + \int \mathrm{d}p\, S_r(q,k,p)\Pi_r(q,p)\lambda_r(q,p), \tag{3.4}$$

[1] Often also referred to as Yukawa coupling or Hedin vertex.

where $\mathcal{I}_{r,\mathrm{SBE}} = \sum_{r' \neq r}(\nabla_{r'} - U + M_{r'}) + M_r$ differs from $\mathcal{I}_r$ (diagrams that are two-particle irreducible, see Eq. (2.10)) by $M_r - U$ and $S_r = \mathcal{I}_{r,\mathrm{SBE}} - M_r$. The first expression is taken from [18] and the bottom line is derived in Appendix B.2. The diagrammatic structure is further illustrated by Fig. 3.3. Under time reversal and SU(2) symmetry λ_r and $\bar{\lambda}_r$ contain the same information [18] and using the channel-based notation of Section 2.2.4 yields [24]

$$\lambda_r(q,k) = \bar{\lambda}_r(q,k), \tag{3.5}$$

therefore the bar is dropped going forward. The high-frequency limits calculated from Eq. (3.4) are

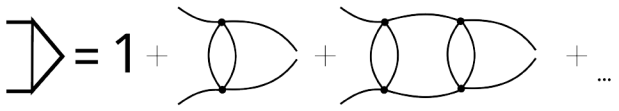

Figure 3.3: Lowest order diagrams included in the fermion-boson coupling λ.

$$\lim_{\Omega\to\infty} \lambda_r(\Omega,\mathbf{q},\nu,\mathbf{k}) = \lim_{\nu\to\infty} \lambda_r(\Omega,\mathbf{q},\nu,\mathbf{k}) = 1. \tag{3.6}$$

The switch from a parquet to SBE decomposition of the vertex does not affect the applicability of the form factor formalism, thus the fermionic momentum arguments are expressed using form factors. For the fermion-boson coupling this yields

$$\begin{aligned}\lambda_r(\Omega,\mathbf{q},\nu,n) &= \int \mathrm{d}\mathbf{k}\, f_n(\mathbf{k})\lambda_r(\Omega,\mathbf{q},\nu,\mathbf{k}) \\ &= \delta_{n,0} + \sum_{m\nu'} \mathcal{I}_{r,\mathrm{SBE}}(\Omega,\mathbf{q},\nu,n,\nu',m)\Pi_r(\Omega,\mathbf{q},\nu',m,0).\end{aligned} \tag{3.7}$$

The fermion-boson coupling is related to the three-point vertex γ_r^3 by

$$\gamma_r^3(\Omega,\mathbf{q},\nu,n,0) = \frac{\lambda_r(\Omega,\mathbf{q},\nu,n)w_r(\Omega,\mathbf{q})}{U}. \tag{3.8}$$

3.2.3 Bosonic propagator w

The bosonic propagator w_r, which forms the central part of each U-reducible diagram, depends only on one bosonic argument and represents the exchange of a single boson seen from a diagrammatic point of view. It is illustrated in Fig. 3.4. In addition, a more physical interpretation may be obtained from the

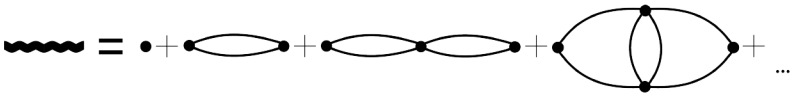

Figure 3.4: Lowest order diagrams of w.

close relation to the s-wave/local susceptibilities

$$w_r = U^2\chi_r + U, \tag{3.9}$$

highlighting the original idea of putting collective excitations centre stage. The bosonic propagator can be expressed as a geometric series [18]

$$\begin{aligned} w_r(q) &= U\sum_n \left(\int \mathrm{d}p\, \lambda_r(q,p)\Pi_r(q,p)U\right)^n \\ \Rightarrow w_r(q) &= \frac{U}{1 - \int \mathrm{d}p\, \lambda_r(q,p)\Pi_r(q,p)U} = \frac{U}{1 - \sum_{\nu,m} \lambda_r(\Omega,\mathbf{q},\nu,m)\Pi_r(\Omega,\mathbf{q},\nu,m,0)U}. \end{aligned} \tag{3.10}$$

When λ_r is set to 1, the expression for the bosonic propagator

$$w_r(q) = \frac{U}{1 - \int \mathrm{d}p\, \Pi_r(q,p)U} \tag{3.11}$$

in the *random phase approximation* (RPA) is recovered. For large frequencies the bosonic propagator reduces to the bare interaction:

$$\lim_{\Omega\to\infty} w_r(\Omega,\mathbf{q}) = U. \tag{3.12}$$

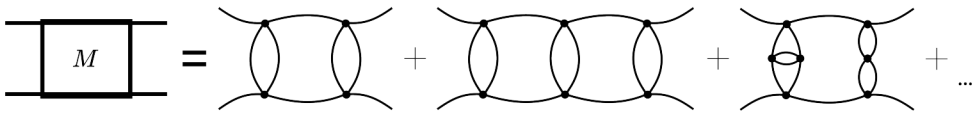

Figure 3.5: Multiboson rest function M.

3.2.4 Multiboson rest function M

All multiboson exchange processes are U-irreducible and are gathered into the rest functions M_r, illustrated in Fig. 3.5. As such, the rest function truly depends on three independent momenta and frequencies with the high-frequency behaviour

$$\lim_{\nu/\nu'\to\infty} M_r(\Omega,\mathbf{q},\nu,\mathbf{k},\nu',\mathbf{k}') = \lim_{\Omega\to\infty} M_r(\Omega,\mathbf{q},\nu,\mathbf{k},\nu',\mathbf{k}') = 0. \tag{3.13}$$

It is this high-frequency property that lies at the heart of the numerical advantage of the SBE decomposition. The frequencies for which the treatment of a three argument object is necessary, are restricted to an inner box, similarly to the Wentzell asymptotics [29] discussed in the next section. Further numerical gains are achieved by completely neglecting the rest function, see Sections 4.2 and 4.3. The rest function vanishes in the non-interacting case. Analogous to the Bethe-Salpeter equation the rest function may be expressed as [22]

$$M_r(q,k,k') = \int \mathrm{d}p\, \mathcal{I}_{r,\mathrm{SBE}}(q,k,p)\Pi_r(q,p)S_r(q,p,k') \tag{3.14}$$

where $S_r = \mathcal{I}_{r,\mathrm{SBE}} - M_r = \sum_{r'\neq r}(\nabla_{r'} - U + M_{r'})$. In form factor notation the rest function reads

$$\begin{aligned} M_r(\Omega,\mathbf{q},\nu,n,\nu',n') &= \int \mathrm{d}\mathbf{k}\mathrm{d}\mathbf{k}'\, f_n(\mathbf{k})f_{n'}(\mathbf{k}')M_r(\Omega,\mathbf{q},\nu,\mathbf{k},\nu',\mathbf{k}') \\ &= \sum_{\nu''}\sum_{m,m'} \mathcal{I}_{r,\mathrm{SBE}}(\Omega,\mathbf{q},\nu,n,\nu'',m)\Pi_r(\Omega,\mathbf{q},\nu'',m,m')S_r(\Omega,\mathbf{q},\nu'',m',\nu',n'). \end{aligned} \tag{3.15}$$

3.2.5 Connection to the high-frequency Wentzell asymptotics

The high-frequency asymptotics introduced in [29] exploit related properties to also further subdivide two-particle reducible diagrams. Here, the focus is on easing the numerics by dividing diagrams based on their asymptotic behaviour, as one or both fermionic frequencies become large. Diagrams where either the incoming or outgoing legs collapse into a single bare vertex do not explicitly depend on the incoming/outgoing arguments. The resulting objects are

$$K_{r,1}(q) = \lim_{\nu\to\infty}\lim_{\nu'\to\infty} \Phi_r(q,k,k') \tag{3.16a}$$

$$K_{r,1}(q) + K_{r,2}(q,k) = \lim_{\nu'\to\infty} \Phi_r(q,k,k') \tag{3.16b}$$

$$K_{r,1}(q) + \overline{K}_{r,2}(q,k') = \lim_{\nu\to\infty} \Phi_r(q,k,k'). \tag{3.16c}$$

The others are gathered into a rest function $\mathcal{R}_r$ that truly depends on all three arguments, but decays at least as $1/\nu$ in the fermionic arguments (slower in Ω). To ensure this behaviour, symmetrized notation must be used for the frequencies [69]. As a consequence, $\mathcal{R}_r$ can be calculated on a small window of fermionic frequencies. Thus, the frequency plane is divided into sections as illustrated in Fig. 3.6. They

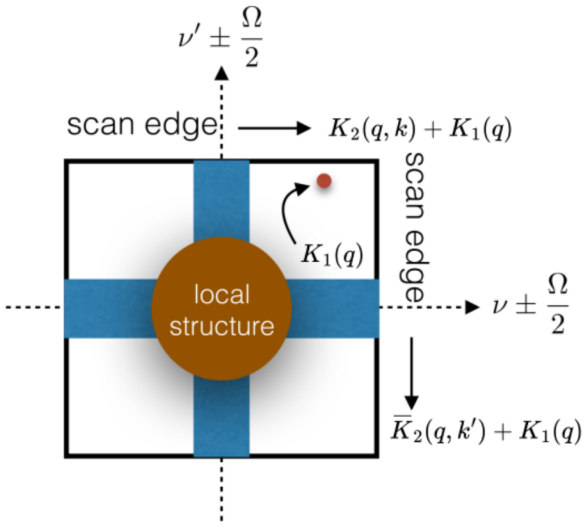

Figure 3.6: Illustration of the high-frequency Wentzell asymptotics, adapted from [29]. It shows the fermionic frequency plane for constant bosonic frequency Ω.

are related to the SBE quantities by [78]

$$w_r = K_{r,1} + U = U^2\chi_r + U \tag{3.17a}$$
$$\lambda_r = 1 + K_{r,2}/w_r$$
$$= 1 + K_{r,2}/(K_{r,1} + U) \tag{3.17b}$$
$$\overline{\lambda}_r = 1 + \overline{K}_{r,2}/w_r$$
$$= 1 + \overline{K}_{r,2}/(K_{r,1} + U) \tag{3.17c}$$
$$M_r = \mathcal{R}_r - (1 - \lambda_r)w_r(1 - \overline{\lambda}_r)$$
$$= \mathcal{R}_r - K_{r,2}\overline{K}_{r,2}/(K_{r,1} + U)$$
$$\nabla_r = \phi_r - M_r + U$$
$$= K_{r,1} + K_{r,2} + \overline{K}_{r,2} + U - K_{r,2}\overline{K}_{r,2}/(K_{r,1} + U) \tag{3.17d}$$

In the SBE decomposition any divergence of ladder diagrams, as they are U-reducible, will be contained in w_r, while the rest function M_r and fermion-boson coupling λ_r remain finite. In contrast, the Wentzell asymptotics are based on how the incoming and outgoing legs are attached to the diagram, but what happens in between is not relevant and may contain a ladder. Therefore all objects are liable to divergence. In fact $\lambda_r - 1$ and M_r are the U-irreducible subset of $K_{r,2}/U$ and $\mathcal{R}_r$, respectively.

The high-frequency limits of the entire vertex in r-notation [29] are included for free in SBE formalism:

$$\lim_{\Omega\to\infty} V^r(\Omega, \mathbf{q}, \nu, \mathbf{k}, \nu', \mathbf{k}') = U \tag{3.18a}$$
$$\lim_{\nu\to\infty} V^r(\Omega, \mathbf{q}, \nu, \mathbf{k}, \nu', \mathbf{k}') = w_r(\Omega, \mathbf{q}) \bullet \lambda_r(\Omega, \mathbf{q}, \nu', \mathbf{k}') \tag{3.18b}$$
$$\lim_{\nu'\to\infty} V^r(\Omega, \mathbf{q}, \nu, \mathbf{k}, \nu', \mathbf{k}') = \lambda_r(\Omega, \mathbf{q}, \nu, \mathbf{k}) \bullet w_r(\Omega, \mathbf{q}) \tag{3.18c}$$
$$\lim_{\nu/\nu'\to\infty} V^r(\Omega, \mathbf{q}, \nu, \mathbf{k}, \nu', \mathbf{k}') = w_r(\Omega, \mathbf{q}). \tag{3.18d}$$

By definition of ∇^η and $\mathcal{I}^\eta$ these limits also hold for the physical channels.

Another useful expression can be derived from Eqs. (3.4) and (3.10):

$$w_r \bullet \lambda_r = U + U \circ \Pi_r \circ V. \tag{3.19}$$

3.3 SBE flow equations

In the previous chapter the fRG was introduced and the flow equations were given for the two-particle reducible vertices. The fRG may also be applied to the SBE decomposition. A formal derivation of the SBE flow equations is presented in [28]. Here, the flow equations are merely reported and adapted to the conventions used in this work. In particular, a switch from diagrammatic channels to physical channels is performed. The former are most suited for the discussion of diagrammatic properties, in particular the notion of the bare interaction reducibility. The latter, on the other hand, are favourable going forward due to the close link of w^η and χ^η as well as the structurally simpler form of the flow equations in the density channel compared to the *ph*-channel. The translation between diagrammatic and physical channels for general two-particle vertex objects introduced in Section 2.2.6, also applies to SBE quantities $\nabla, \mathcal{I}_{\mathrm{SBE}}, S, \mathcal{I}_{\mathrm{bare}}, w$, and M. Though possible to define $\lambda^{\mathrm{M}} = -\lambda_{\overline{ph}}$, the convention $\lambda^{\mathrm{M}} = \lambda_{\overline{ph}}$ is chosen here, while the standard translation is used for $\lambda^{\mathrm{D/SC}}$. This ensures that $\lim_{\nu\to\infty} \lambda^\eta = 1$ in all channels. Neither ∇^{M} nor the flow equation of w^{M} are affected by the sign of λ^{M}, as they depend on λ^{M} quadratically.

3.3.1 1ℓ equations

In physical channels the 1ℓ flow equations of the bosonic propagator for the SBE decomposition [24] read

$$\dot{w}^\eta(\Omega, \mathbf{q}) = w^\eta(\Omega, \mathbf{q}) \sum_{m,m',\nu} \left(\lambda^\eta(\Omega, \mathbf{q}, \nu, m)\dot{\Pi}^\eta(\Omega, \mathbf{q}, \nu, m, m')\lambda^\eta(\Omega, \mathbf{q}, \nu, m')\right) w^\eta(\Omega, \mathbf{q}), \tag{3.20}$$

for the fermion-boson couplings

$$\dot{\lambda}^\eta(\Omega, \mathbf{q}, \nu, n) = \sum_{m,m',\nu'} \lambda^\eta(\Omega, \mathbf{q}, \nu', m)\dot{\Pi}^\eta(\Omega, \mathbf{q}, \nu', m, m')\mathcal{I}^\eta_{\mathrm{SBE}}(\Omega, \mathbf{q}, \nu', m', \nu, n), \tag{3.21}$$

and the rest functions

$$\dot{M}^\eta(\Omega, \mathbf{q}, \nu, n, \nu', n') = \sum_{m,m',\nu''} \mathcal{I}^\eta_{\mathrm{SBE}}(\Omega, \mathbf{q}, \nu, n, \nu'', m)\dot{\Pi}^\eta(\Omega, \mathbf{q}, \nu'', m, m')\mathcal{I}^\eta_{\mathrm{SBE}}(\Omega, \mathbf{q}, \nu'', m', \nu', n'). \tag{3.22}$$

A derivation is given in Appendix B.3. The initial conditions for the flow are reported as

$$w^{\eta,\mathrm{init}}(\Omega, \mathbf{q}) = \mathcal{I}^\eta_{\mathrm{bare}} \tag{3.23a}$$

$$\lambda^{\eta,\mathrm{init}}(\Omega, \mathbf{q}, \nu, n) = \delta_{n,0} \tag{3.23b}$$

$$M^{\eta,\mathrm{init}}(\Omega, \mathbf{q}, \nu, n, \nu', n') = 0, \tag{3.23c}$$

with $\mathcal{I}^{\mathrm{SC}/D}_{\mathrm{bare}} = U = -\mathcal{I}^{\mathrm{M}}_{\mathrm{bare}}$. A great reduction of numerical effort can be achieved by neglecting the rest function, which depends on six independent arguments. Such an approximation is not merely based on its numerical advantage, but on the assumption that the relevant physics can be described as the exchange of a single bosonic object and therefore the multiboson processes of the rest function need not be calculated to obtain qualitatively or even quantitatively correct data. Numerical results confirming these assumptions are a main result of this work and will be provided in Section 4.

3.3.2 Multiloop extension

In the multiloop procedure first put forward in a series of papers [27, 73, 74], contributions of the three-particle vertex to lower order vertices are included in an iterative procedure. At infinite loop order the derivatives are completed and the parquet approximation is recovered [30]. The multiloop procedure was generalised to SBE quantities [28]. Here the multiloop extension translated to physical channels and form factor representation is presented. The 2ℓ equations read

$$\dot{\lambda}^{\eta,(2),L} = \dot{\mathcal{I}}^{\eta,(1)}\Pi^\eta\lambda^\eta \tag{3.24a}$$

$$\dot{\lambda}^{\eta,(2),R} = \lambda^\eta\Pi^\eta\dot{\mathcal{I}}^{\eta,(1)} \tag{3.24b}$$

$$\dot{w}^{\eta,(2)} = 0 \tag{3.24c}$$

$$\dot{M}^{\eta,(2),L} = \dot{\mathcal{I}}^{\eta,(1)}\Pi^\eta\mathcal{I}^\eta_{\mathrm{SBE}} \tag{3.24d}$$

$$\dot{M}^{\eta,(2),R} = \mathcal{I}^\eta_{\mathrm{SBE}}\Pi^\eta\dot{\mathcal{I}}^{\eta,(1)} \tag{3.24e}$$

and higher order corrections to λ^η are given by

$$\dot{\lambda}^{\eta,(\ell),L} = \dot{\mathcal{I}}^{\eta,(\ell-1)}\Pi^\eta\lambda^\eta \tag{3.25a}$$
$$\dot{\lambda}^{\eta,(\ell),R} = \lambda^\eta\Pi^\eta\dot{\mathcal{I}}^{\eta,(\ell-1)} \tag{3.25b}$$
$$\begin{aligned}\dot{\lambda}^{\eta,(\ell),C} &= \lambda^\eta\Pi^\eta\dot{\mathcal{I}}^{\eta,(\ell-2)}\Pi^\eta\mathcal{I}^\eta_{\mathrm{SBE}} \\ &= \dot{\lambda}^{\eta,(\ell-1),R}\Pi^\eta\mathcal{I}^\eta_{\mathrm{SBE}}\end{aligned} \tag{3.25c}$$
$$\dot{\lambda}^{\eta,(\ell)} = \dot{\lambda}^{(1)} + \dot{\lambda}^{\eta,(2),L} + \sum_{\ell'=3}^{\ell'\leqq\ell}\dot{\lambda}^{\eta,(\ell'),L} + \dot{\lambda}^{\eta,(\ell'),C}. \tag{3.25d}$$

The multiloop corrections to the bosonic propagator are

$$\begin{aligned}\dot{w}^{\eta,(\ell),C} &= w^\eta\lambda^\eta\Pi^\eta\dot{\mathcal{I}}^{\eta,(\ell-2)}\Pi^\eta\lambda^\eta w^\eta \\ &= w^\eta\dot{\lambda}^{\eta,(\ell-1),L}\Pi^\eta\lambda^\eta w^\eta\end{aligned} \tag{3.26a}$$
$$\dot{w}^{\eta,(\ell)} = \dot{w}^{(1)} + \sum_{\ell'=3}^{\ell'\leqq\ell}\dot{w}^{\eta,(\ell),C} \tag{3.26b}$$

and for the rest function they read

$$\dot{M}^{\eta,(\ell),L} = \dot{\mathcal{I}}^{\eta,(\ell-1)}\Pi^\eta\mathcal{I}^\eta_{\mathrm{SBE}} \tag{3.27}$$
$$\dot{M}^{\eta,(\ell),R} = \mathcal{I}^\eta_{\mathrm{SBE}}\Pi^\eta\dot{\mathcal{I}}^{\eta,(\ell-1)} \tag{3.28}$$
$$\begin{aligned}\dot{M}^{\eta,(\ell),C} &= \mathcal{I}^\eta_{\mathrm{SBE}}\Pi^\eta\dot{\mathcal{I}}^{\eta,(\ell-2)}\Pi^\eta\mathcal{I}^\eta_{\mathrm{SBE}} \\ &= \dot{M}^{\eta,(\ell-1),R}\Pi^\eta\mathcal{I}^\eta_{\mathrm{SBE}}\end{aligned} \tag{3.29}$$
$$\dot{M}^{\eta,(\ell)} = \dot{M}^{\eta,(1)} + \dot{M}^{\eta,(2),L} + \dot{M}^{\eta,(2),R} + \sum_{\ell'=3}^{\ell'\leqq\ell}\dot{M}^{\eta,(\ell'),L} + \dot{M}^{\eta,(\ell'),R} + \dot{M}^{\eta,(\ell'),C} \tag{3.30}$$

with $\dot{\mathcal{I}}^{\eta,(\ell)} = \dot{V}^\eta - \dot{\Phi}^\eta$ given by

$$\dot{\mathcal{I}}^{\mathrm{SC},(\ell)} = P^{ph\to pp}\left[\frac{1}{2}(\dot{\nabla}^{\mathrm{D},(\ell)} + \dot{M}^{\mathrm{D},(\ell)}) - \frac{1}{2}(\dot{\nabla}^{\mathrm{M},(\ell)} + \dot{M}^{\mathrm{M},(\ell)})\right] - P^{\overline{ph}\to pp}\left[(\dot{\nabla}^{\mathrm{M},(\ell)} + \dot{M}^{\mathrm{M},(\ell)})\right] \tag{3.31a}$$
$$\dot{\mathcal{I}}^{\mathrm{M},(\ell)} = P^{ph\to\overline{ph}}\left[-\frac{1}{2}(\dot{\nabla}^{\mathrm{D},(\ell)} + \dot{M}^{\mathrm{D},(\ell)}) + \frac{1}{2}(\dot{\nabla}^{\mathrm{M},(\ell)} + \dot{M}^{\mathrm{M},(\ell)})\right] - P^{pp\to\overline{ph}}\left[(\dot{\nabla}^{\mathrm{SC},(\ell)} + \dot{M}^{\mathrm{SC},(\ell)})\right] \tag{3.31b}$$
$$\begin{aligned}\dot{\mathcal{I}}^{\mathrm{D},(\ell)} = P^{pp\to ph}\left[2(\dot{\nabla}^{\mathrm{SC},(\ell)} + \dot{M}^{\mathrm{SC},(\ell)})\right] - P^{pp\to\overline{ph}}\left[(\dot{\nabla}^{\mathrm{SC},(\ell)} + \dot{M}^{\mathrm{SC},(\ell)})\right] - P^{\overline{ph}\to ph}\left[2(\dot{\nabla}^{\mathrm{M},(\ell)} + \dot{M}^{\mathrm{M},(\ell)})\right] \\ + P^{ph\to\overline{ph}}\left[-\frac{1}{2}(\dot{\nabla}^{\mathrm{D},(\ell)} + \dot{M}^{\mathrm{D},(\ell)}) + \frac{1}{2}(\dot{\nabla}^{\mathrm{M},(\ell)} + \dot{M}^{\mathrm{M},(\ell)})\right].\end{aligned} \tag{3.31c}$$

The derivative ∇^η including all orders up to ℓ reads

$$\dot{\nabla}^{\eta,(\ell)} = \dot{\lambda}^{\eta,(\ell)}w^\eta\lambda^\eta + \lambda^\eta\dot{w}^{\eta,(\ell)}\lambda^\eta + \lambda^\eta w^\eta\dot{\lambda}^{\eta,(\ell)}. \tag{3.32}$$

Note that $\mathcal{I}^\eta$ is defined by Eq. 2.38c and $\mathcal{I}^\eta_{\mathrm{SBE}} = \mathcal{I}^\eta + M^\eta - \mathcal{I}^\eta_{\mathrm{bare}}$. For completeness, the connection to the left, right, and central multiloop corrections is made explicit

$$\begin{aligned}
\dot{\phi}^{\eta,(\ell),L} &= \int \dot{\mathcal{I}}^{\eta,(\ell-1)}\Pi^\eta V^\eta = \int \dot{\mathcal{I}}^{\eta,(\ell-1)}\Pi^\eta(\nabla^\eta + \mathcal{I}^\eta_{\mathrm{SBE}}) = \int \dot{\mathcal{I}}^{\eta,(\ell-1)}\Pi^\eta\lambda^\eta w^\eta\lambda^\eta + \int \dot{\mathcal{I}}^{\eta,(\ell-1)}\Pi^\eta\mathcal{I}^\eta_{\mathrm{SBE}} \\
&= \dot{\lambda}^{\eta,(\ell),L} w^\eta\lambda^\eta + \dot{M}^{\eta,(\ell),L} = \dot{\nabla}^{\eta,(\ell),L} + \dot{M}^{\eta,(\ell),L} \qquad (3.33a)\\
\dot{\phi}^{\eta,(\ell),R} &= \lambda^\eta w^\eta \dot{\lambda}^{\eta,(\ell),R} + \dot{M}^{\eta,(\ell),R} = \dot{\nabla}^{\eta,(\ell),R} + \dot{M}^{\eta,(\ell),R} \qquad (3.33b)\\
\dot{\phi}^{\eta,(\ell),C} &= \int V^\eta\Pi^\eta\dot{\mathcal{I}}^{\eta,(\ell-2)}\Pi^\eta V^\eta = \int (\nabla^\eta + \mathcal{I}^\eta_{\mathrm{SBE}})\Pi^\eta\dot{\mathcal{I}}^{\eta,(\ell-2)}\Pi^\eta(\nabla^\eta + \mathcal{I}^\eta_{\mathrm{SBE}}) \\
&= \int \nabla^\eta\Pi^\eta\dot{\mathcal{I}}^{\eta,(\ell-2)}\Pi^\eta\nabla^\eta + \int \nabla^\eta\Pi^\eta\dot{\mathcal{I}}^{\eta,(\ell-2)}\Pi^\eta\mathcal{I}^\eta_{\mathrm{SBE}} + \int \mathcal{I}^\eta_{\mathrm{SBE}}\Pi^\eta\dot{\mathcal{I}}^{\eta,(\ell-2)}\Pi^\eta\nabla^\eta \\
&+ \int \mathcal{I}^\eta_{\mathrm{SBE}}\Pi^\eta\dot{\mathcal{I}}^{\eta,(\ell-2)}\Pi^\eta\mathcal{I}^\eta_{\mathrm{SBE}} \\
&= \int \lambda^\eta w^\eta\lambda^\eta\Pi^\eta\dot{\mathcal{I}}^{\eta,(\ell-2)}\Pi^\eta\lambda^\eta w^\eta\lambda^\eta + \int \lambda^\eta w^\eta\lambda^\eta\Pi^\eta\dot{\mathcal{I}}^{\eta,(\ell-2)}\Pi^\eta\mathcal{I}^\eta_{\mathrm{SBE}} \\
&+ \int \mathcal{I}^\eta_{\mathrm{SBE}}\Pi^\eta\dot{\mathcal{I}}^{\eta,(\ell-2)}\Pi^\eta\lambda^\eta w^\eta\lambda^\eta + \dot{M}^{\eta,(\ell),C} \\
&= \lambda^\eta\dot{w}^{\eta,(\ell),C}\lambda^\eta + \lambda^\eta w^\eta\dot{\lambda}^{\eta,(\ell),C} + \dot{\lambda}^{\eta,(\ell),C} w^\eta\lambda^\eta + \dot{M}^{\eta,(\ell),C} = \dot{\nabla}^{\eta,(\ell),C} + \dot{M}^{\eta,(\ell),C}. \qquad (3.33c)
\end{aligned}$$

As a consequence of $\lambda^\eta = \bar{\lambda}^\eta$ the left and right corrections are identical $\dot{\lambda}^{\eta,(\ell),L} = \dot{\lambda}^{\eta,(\ell),R}$. Adding the left, right, and central contributions of all multiloop orders up to order ℓ, yields

$$\begin{aligned}
\dot{\phi}^{\eta,(\ell)} =& \dot{\phi}^{\eta,(1)} + \dot{\phi}^{\eta,(2),L} + \dot{\phi}^{\eta,(2),R} + \sum_{\ell'=3}^{\ell'\leqq\ell} \dot{\phi}^{\eta,(\ell'),L} + \dot{\phi}^{\eta,(\ell'),R} + \dot{\phi}^{\eta,(\ell'),C} \\
=& \dot{\nabla}^{\eta,(1)} + \dot{M}^{\eta,(1)} + \dot{\nabla}^{\eta,(2),L} + \dot{M}^{\eta,(2),L} + \dot{\nabla}^{\eta,(2),R} + \dot{M}^{\eta,(2),R} + \sum_{\ell'=3}^{\ell'\leqq\ell} \dot{\lambda}^{\eta,(\ell'),L} w^\eta\lambda^\eta + \dot{M}^{\eta,(\ell'),L} \\
&+ \lambda^\eta w^\eta\dot{\lambda}^{\eta,(\ell'),R} + \dot{M}^{\eta,(\ell'),R} + \lambda^\eta\dot{w}^{\eta,(\ell'),C}\lambda^\eta + \lambda^\eta w^\eta\dot{\lambda}^{\eta,(\ell'),C} + \dot{\lambda}^{\eta,(\ell'),C} w^\eta\lambda^\eta + \dot{M}^{\eta,(\ell'),C} \\
=& \left(\dot{\lambda}^{\eta,(1)} + \dot{\lambda}^{\eta,(2),L} + \dot{\lambda}^{\eta,(2),R} + \sum_{\ell'=3}^{\ell'\leqq\ell} \dot{\lambda}^{\eta,(\ell'),L} + \dot{\lambda}^{\eta,(\ell'),C}\right) w^\eta\lambda^\eta \\
&+ \lambda^\eta w^\eta\left(\dot{\lambda}^{\eta,(1)} + \dot{\lambda}^{\eta,(2),L} + \dot{\lambda}^{\eta,(2),R} + \sum_{\ell'=3}^{\ell'\leqq\ell} \dot{\lambda}^{\eta,(\ell'),R} + \dot{\lambda}^{\eta,(\ell'),C}\right) + \lambda^\eta\left(w^{\eta,(1)} + \sum_{\ell'=3}^{\ell'\leqq\ell} \dot{w}^{\eta,(\ell'),C}\right)\lambda^\eta \\
&+ \left(\dot{M}^{\eta,(1)} + \dot{M}^{\eta,(2),L} + \dot{M}^{\eta,(2),R} + \sum_{\ell'=3}^{\ell'\leqq\ell} \dot{M}^{\eta,(\ell'),L} + \dot{M}^{\eta,(\ell'),R} + \dot{M}^{\eta,(\ell'),C}\right) \\
=& \dot{\lambda}^{\eta,(\ell)} w^\eta\lambda^\eta + \lambda^\eta w^\eta\dot{\lambda}^{\eta,(\ell)} + \lambda^\eta\dot{w}^{\eta,(\ell)}\lambda^\eta + \dot{M}^{\eta,(\ell)} \qquad (3.34)
\end{aligned}$$

and the expected form of $\dot{\nabla}^\eta$ is recovered.

3.3.3 SBE approximation

Neglecting the rest function and the multiboson processes contained therein is referred to as SBE approximation. In contrast to self-consistent methods such as parquet, the fRG formalism offers two paths of translating the idea of neglecting multiboson processes into the flow equations. In this section these two different flavours of the SBE approximation are presented and compared on a diagrammatic level. A quantitative comparison follows in Chapter 4. Neglecting the rest function **after** deriving the flow equations (SBEa approximation) corresponds to using Eqs. (3.20) and (3.21) while setting $\dot{M}^\eta \equiv 0$. This renders the vertex cutoff dependent, even at infinite order multiloop corrections to λ^η and w^η, as the flow equations are not consistent without the rest function. Alternatively, the rest function can be neglected **before** taking the derivative (SBEb approximation), which is more severe, as it alters the flow equations for w^η and λ^η. However, it also restores self-consistency.

SBEb flow equations

As mentioned, self-consistency can be restored by setting the rest function to zero *prior* to deriving the flow equations (SBEb) [28], leading to the simpler flow equations for the single-boson propagator

$$w^\eta(\Omega,\mathbf{q}) = w^\eta(\Omega,\mathbf{q}) \sum_{m,\nu} (2\lambda^\eta(\Omega,\mathbf{q},\nu,m) - \delta_{m,0}) \dot{\Pi}^\eta(\Omega,\mathbf{q},\nu,m,0) w^\eta(\Omega,\mathbf{q}) \tag{3.35}$$

where $\lambda^\eta = \bar{\lambda}^\eta$ and $\dot{\Pi}^\eta(m,m') = \dot{\Pi}^\eta(m',m)$ was exploited to simplify

$$\sum_{m,m'\nu} \lambda^\eta(\Omega,\mathbf{q},\nu,m)\dot{\Pi}^\eta(\Omega,\mathbf{q},\nu,m,m')\delta_{m',0} + \delta_{m,0}\dot{\Pi}^\eta(\Omega,\mathbf{q},\nu,m,m')\bar{\lambda}^\eta(\Omega,\mathbf{q},\nu,m') - \delta_{m,0}\dot{\Pi}^\eta(\Omega,\mathbf{q},\nu,m,m')\delta_{m',m}$$
$$= 2\sum_{m,\nu} (\lambda^\eta(\Omega,\mathbf{q},\nu,m) - \delta_{m,0})\dot{\Pi}^\eta(\Omega,\mathbf{q},\nu,m,0).$$

The fermion-boson couplings flow equation is given by

$$\dot{\lambda}^\eta(\Omega,\mathbf{q},\nu,n) = \sum_{m,\nu'} \dot{\Pi}^\eta(\Omega,\mathbf{q},\nu',0,m) S^\eta(\Omega,\mathbf{q},\nu',m,\nu,n) \tag{3.36}$$

with merely one sum over form factors compared to the two for the 1ℓ equations of SBEa. In addition, the calculation of the bubble can be restricted to $\delta_{0,n}\Pi^\eta(\Omega,q,\nu,n,n')$. By fixing $\lambda^\eta = 1, M^\eta = 0$, and $\Sigma = 0$, the SBEb reduces to the RPA. The only flowing elements remaining are the bosonic propagators given by the simple flow equations

$$w^\eta(\Omega,\mathbf{q}) = w^\eta(\Omega,\mathbf{q}) \sum_{\nu} \dot{\Pi}^\eta(\Omega,\mathbf{q},\nu,0,0) w^\eta(\Omega,\mathbf{q}). \tag{3.37}$$

Diagrams of the SBEa vs SBEb

In the SBEb approximation the expression for the fermion-boson couplings given in Eq. (3.4) holds. However, in the SBEb the U-irreducible vertex is given by $\mathcal{I}_{r,\mathrm{SBE}} = \sum_{r'\neq r}(\nabla_{r'} - U) = S_r$, which restricts λ_r to the eye-diagram type. Similarly, the single-boson exchange propagator (see Eq. (3.10))

$$w_r = \frac{U}{1 - \lambda_r \Pi_r U} \tag{3.38}$$

does not contain any rest-function-like elements, just insertions of single-boson exchange propagators from other channels via λ_r. Adding multiloop corrections completes the derivative but does not add any new diagrams, therefore restoring self-consistency without capturing any of the influence of the rest function; the self-consistency and simpler flow equations come at the cost of neglecting infinitely many diagrams. By contrast, in the SBEa approximation far less diagrams are excluded, however, their derivative is less complete than for a 1ℓ flow and multiloop corrections add some, but not all of the missing derivatives. As even at infinite loop order the derivative is not completed, the parquet approximation is not recovered, nor self-consistency between the one- and two-particle vertices. However, diagrams included in the SBEb at loop convergence are fully reconstructed by the SBEa at loop convergence, too. Neither approximation is able to reproduce the parquet approximation, it remains to be shown whether either is sufficient to observe the Mermin Wagner theorem at infinite multiloop order. In Table 3.1 RPA, SBEb, SBEa, and a full treatment of the rest function are compared with respect to the diagrams included and properties of the flow results. To further illustrate the difference between the SBEa and SBEb approximation, in particular how the SBEa flow allows for at least a partial inclusion of rest function type elements in w_r and λ_r, the lowest order diagrams in the first steps of the flow are shown in Fig. 3.7. Results obtained with the two different flavours of SBE approximations are presented and compared in Section 4.4.2.

	RPA	SBEb 1ℓ	SBEb ∞-ℓ	SBEa 1ℓ	SBEa ∞-ℓ	1ℓ	∞-ℓ
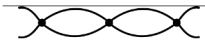	dc	dc	dc	dc	dc	dc	dc
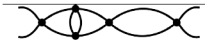	ni	pi	dc	pi	dc	pi	dc
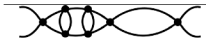	ni	ni	ni	pi	dc	pi	dc
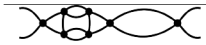	ni	ni	ni	ni	ni	pi	dc
self-consistent	✓	✗	✓	✗	✗	✗	✓
regulator independent	✓	✗	✓	✗	✗	✗	✓
Mermin Wagner	✗	✗	?	✗	?	✗	✓

Table 3.1: Table comparing RPA, SBEa/b and full set of equations including the flow of the rest function. If diagrams of this type are not included the corresponding box is marked with 'ni', if the diagrams are included but the derivative is incomplete they are termed 'pi'=partially included, and 'dc' is used when the derivative is complete. Note that the degree of completeness can vary between two 'partially included' in the same row.

Multiloop flow equations for the SBEb

The multiloop flow equations for the SBEb approximation are structurally simpler than in the SBEa approximation and read

$$\dot{w}^{\eta,(2)}(\Omega,\mathbf{q}) = 0 \tag{3.39a}$$

$$\dot{w}^{\eta,(\ell+2)}(\Omega,\mathbf{q}) = w^{\eta}(\Omega,\mathbf{q}) \sum_{\substack{m,m'\\ \nu,\nu'}} \Pi^{\eta}(\Omega,\mathbf{q},\nu,0,m)\dot{S}^{\eta,(\ell)}(\Omega,\mathbf{q},\nu,m,\nu',m')\Pi^{\eta}(\Omega,\mathbf{q},\nu',m',0)w^{\eta}(\Omega,\mathbf{q}) \tag{3.39b}$$

$$\dot{\lambda}^{\eta,(\ell+1)}(\Omega,\mathbf{q},\nu,n) = \sum_{m,\nu'} \dot{S}^{\eta,(\ell)}(\Omega,\mathbf{q},\nu',n,\nu,m)\Pi^{\eta}(\Omega,\mathbf{q},\nu',m,0). \tag{3.39c}$$

The SBEb multiloop equations are self-consistent and regulator independent at infinite loop order. The same results may be obtained by taking the derivative of the self-consistent equations for λ^{η}, w^{η} and M^{η} as shown in the next section, and then neglecting the rest function.

3.3.4 Self-consistent flow equations

It is possible to derive exact flow equations for λ^{η}, w^{η}, and M^{η} by taking the derivative of the self-consistent equations in Section 3.2. The flow equation of the fermion-boson coupling is obtained by taking the derivative of

$$\lambda^{\eta}(\Omega,\mathbf{q},\nu,n) = \delta_{n,0} + \sum_{m\nu'} \mathcal{I}^{\eta}_{\mathrm{SBE}}(\Omega,\mathbf{q},\nu,n,\nu',m)\Pi^{\eta}(\Omega,\mathbf{q},\nu',m,0) \tag{3.40}$$

yielding

$$\dot{\lambda}^{\eta}(\Omega,\mathbf{q},\nu,n) = \sum_{m\nu'} \dot{\mathcal{I}}^{\eta}_{\mathrm{SBE}}(\Omega,\mathbf{q},\nu,n,\nu',m)\Pi^{\eta}(\Omega,\mathbf{q},\nu',m,0) + \sum_{m\nu'} \mathcal{I}^{\eta}_{\mathrm{SBE}}(\Omega,\mathbf{q},\nu,n,\nu',m)\dot{\Pi}^{\eta}(\Omega,\mathbf{q},\nu',m,0). \tag{3.41}$$

A second option is to use

$$\lambda^{\eta}(\Omega,\mathbf{q},\nu,n) = \delta_{n,0} + \sum_{mm'\nu'} S^{\eta}(\Omega,\mathbf{q},\nu,n,\nu',m)\Pi^{\eta}(\Omega,\mathbf{q},\nu',m,m')\lambda^{\eta}(\Omega,\mathbf{q},\nu',m') \tag{3.42}$$

which also yields a flow equation

$$\begin{aligned}\dot{\lambda}^{\eta}(\Omega,\mathbf{q},\nu,n) = &\sum_{mm'\nu'} \dot{S}^{\eta}(\Omega,\mathbf{q},\nu,n,\nu',m)\Pi^{\eta}(\Omega,\mathbf{q},\nu',m,m')\lambda^{\eta}(\Omega,\mathbf{q},\nu',m')\\ &+ \sum_{mm'\nu'} S^{\eta}(\Omega,\mathbf{q},\nu,n,\nu',m)\dot{\Pi}^{\eta}(\Omega,\mathbf{q},\nu',m,m')\lambda^{\eta}(\Omega,\mathbf{q},\nu',m')\\ &+ \sum_{mm'\nu'} S^{\eta}(\Omega,\mathbf{q},\nu,n,\nu',m)\Pi^{\eta}(\Omega,\mathbf{q},\nu',m,m')\dot{\lambda}^{\eta}(\Omega,\mathbf{q},\nu',m').\end{aligned} \tag{3.43}$$

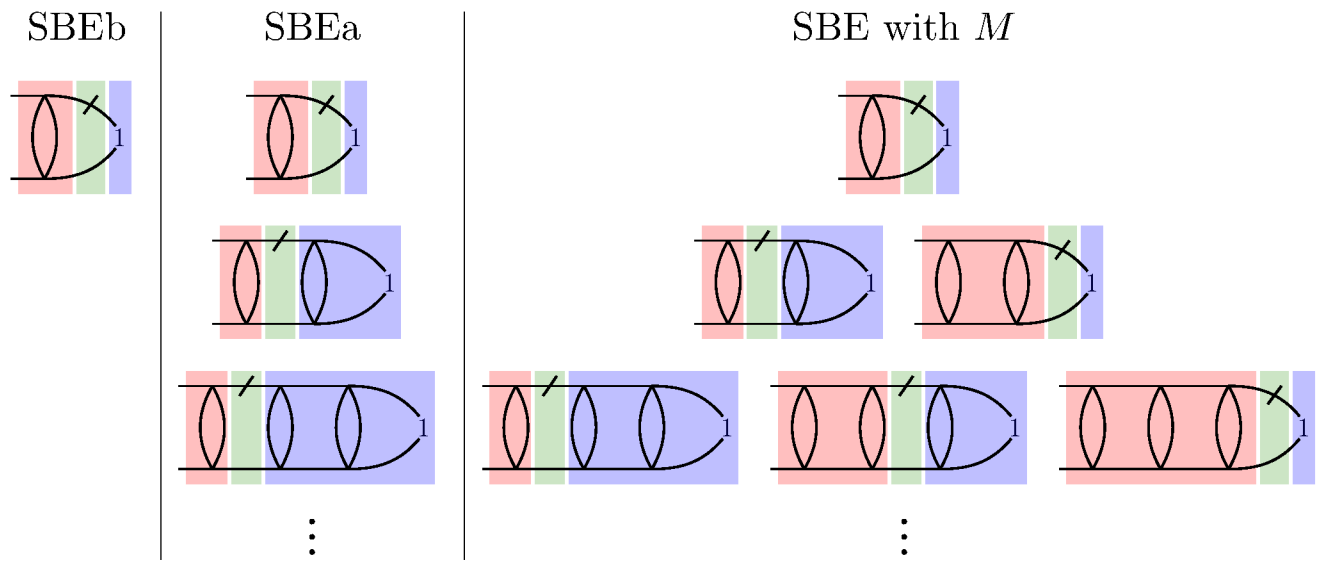

Figure 3.7: Adapted from [78]. Comparison of the derivatives included during the 1ℓ flow of $\dot{\lambda}^\eta(q,k)$ via Eq. 3.36 vs 3.21. The left red box represents $\mathcal{I}^\eta_{\mathrm{SBE}}(q,k,k')$, the central green $\dot{\Pi}^\eta(q,k)$, and the right blue $\lambda^\eta(q,k)$. The diagrams in the first row are generated during the first step of the solver, those of the second and third are added in the second and third step, respectively. While the replacement of $\lambda^\eta(q,k)$ by 1 in the SBEb approximation limits the derivative to the eye diagrams, all types of diagrams (except those of the type shown in Fig. 3.8), are constructed during the flow of the SBEa, albeit with a derivative less complete than for the SBE including M.

The two flow equations are equivalent as long as no approximations are made. The flow equation of the bosonic propagator is obtained by taking the derivative of

$$w^\eta(\Omega,\mathbf{q}) = \frac{U}{1-\sum_{\nu,n}\lambda^\eta(\Omega,\mathbf{q},\nu,n)\Pi^\eta(\Omega,\mathbf{q},\nu,n,0)U} \tag{3.44}$$

yielding

$$\begin{aligned}
\dot{w}^\eta(\Omega,\mathbf{q}) =& \partial_\Lambda\left(\frac{U}{1-\sum_{\nu,n}\lambda^\eta(\Omega,\mathbf{q},\nu,n)\Pi^\eta(\Omega,\mathbf{q},\nu,n,0)U}\right)\\
=&\left(\frac{U}{1-\sum_{\nu,n}\lambda^\eta(\Omega,\mathbf{q},\nu,n)\Pi^\eta(\Omega,\mathbf{q},\nu,n,0)U}\right)^2\cdot\\
&\left(\sum_{\nu,n}\dot{\lambda}^\eta(\Omega,\mathbf{q},\nu,n)\Pi^\eta(\Omega,\mathbf{q},\nu,n,0)+\sum_{\nu,n}\lambda^\eta(\Omega,\mathbf{q},\nu,n)\dot{\Pi}^\eta(\Omega,\mathbf{q},\nu,n,0)\right)\\
=&w^\eta(\Omega,\mathbf{q})\left(\sum_{\nu,n}\dot{\lambda}^\eta(\Omega,\mathbf{q},\nu,n)\Pi^\eta(\Omega,\mathbf{q},\nu,n,0)+\sum_{\nu,n}\lambda^\eta(\Omega,\mathbf{q},\nu,n)\dot{\Pi}^\eta(\Omega,\mathbf{q},\nu,n,0)\right)w^\eta(\Omega,\mathbf{q}).
\end{aligned} \tag{3.45}$$

Alternatively the derivative of the relation

$$w^\eta(\Omega,\mathbf{q}) = (\mathcal{I}^\eta_{\mathrm{bare}})^2\chi^\eta(\Omega,\mathbf{q},0,0)+\mathcal{I}^\eta_{\mathrm{bare}}$$

with

$$\chi^\eta(\Omega,\mathbf{q},n,n') = \sum_\nu \Pi^\eta(\Omega,\mathbf{q},\nu,n,n') + \sum_{\substack{\nu,\nu'\\ m,m'}}\Pi^\eta(\Omega,\mathbf{q},\nu,n,m)V^\eta(\Omega,\mathbf{q},\nu,m,\nu',m')\Pi^\eta(\Omega,\mathbf{q},\nu',m',n')$$

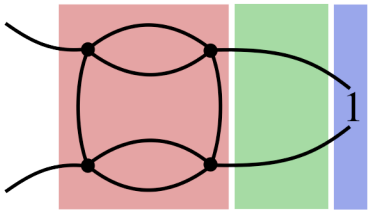

Figure 3.8: Diagrams not included in SBEa type approximations.

can be used yielding

$$\begin{aligned}\dot{w}^\eta(\Omega,\mathbf{q}) =&(\mathcal{I}^\eta_{\text{bare}})^2(\sum_\nu \dot{\Pi}^\eta(\Omega,\mathbf{q},\nu,0,0) + \sum_{\substack{\nu,\nu'\\m,m'}} \dot{\Pi}^\eta(\Omega,\mathbf{q},\nu,n,m)V^\eta(\Omega,\mathbf{q},\nu,m,\nu',m')\Pi^\eta(\Omega,\mathbf{q},\nu',m',n')\\ &+ \sum_{\substack{\nu,\nu'\\m,m'}} \Pi^\eta(\Omega,\mathbf{q},\nu,n,m)\dot{V}^\eta(\Omega,\mathbf{q},\nu,m,\nu',m')\Pi^\eta(\Omega,\mathbf{q},\nu',m',n')\\ &+ \sum_{\substack{\nu,\nu'\\m,m'}} \Pi^\eta(\Omega,\mathbf{q},\nu,n,m)V^\eta(\Omega,\mathbf{q},\nu,m,\nu',m')\dot{\Pi}^\eta(\Omega,\mathbf{q},\nu',m',n')).\end{aligned} \tag{3.46}$$

The flow equation for the multiboson rest function is obtained by taking the derivative of

$$M^\eta(\Omega,\mathbf{q},\nu,n,\nu',n') = \sum_{\nu'',m,m'} \mathcal{I}^\eta_{\text{SBE}}(\Omega,\mathbf{q},\nu,n,\nu'',m)\Pi^\eta(\Omega,\mathbf{q},\nu'',m,m')S^\eta(\Omega,\mathbf{q},\nu'',m',\nu',n') \tag{3.47}$$

yielding

$$\begin{aligned}\dot{M}^\eta(\Omega,\mathbf{q},\nu,n,\nu',n') = &\sum_{\nu'',m,m'} \dot{\mathcal{I}}^\eta_{\text{SBE}}(\Omega,\mathbf{q},\nu,n,\nu'',m)\Pi^\eta(\Omega,\mathbf{q},\nu'',m,m')S^\eta(\Omega,\mathbf{q},\nu'',m',\nu',n')\\ &+ \sum_{\nu'',m,m'} \mathcal{I}^\eta_{\text{SBE}}(\Omega,\mathbf{q},\nu,n,\nu'',m)\dot{\Pi}^\eta(\Omega,\mathbf{q},\nu'',m,m')S^\eta(\Omega,\mathbf{q},\nu'',m',\nu',n')\\ &+ \sum_{\nu'',m,m'} \mathcal{I}^\eta_{\text{SBE}}(\Omega,\mathbf{q},\nu,n,\nu'',m)\Pi^\eta(\Omega,\mathbf{q},\nu'',m,m')\dot{S}^\eta(\Omega,\mathbf{q},\nu'',m',\nu',n')\end{aligned} \tag{3.48}$$

where $S^\eta = \mathcal{I}^\eta_{\text{SBE}} - M^\eta$. As the equations are exact before taking the derivative and no approximations are made to the resulting flow equations, they recover the full parquet solution. The exact flow equations Eq. (3.41) for the fermion-boson vertex, Eq. (3.45) for the bosonic propagator, and Eq. (3.48) were already derived using very similar arguments in [28].
Note that neglecting the flow of the rest function and using Eq. (3.41) here is equivalent to the SBEb approximation at infinite loop order. The alternative Eq. (3.43) in this case yields a different result more closely related to SBEa at infinite multiloop order. The second term in Eq. (3.43) is exactly the 1ℓ flow equation in the SBEa approximation, as $\mathcal{I}^\eta_{\text{SBE}} = S^\eta$ when neglecting the rest function. In fact, the only diagrams that are missing compared with the full solution are of the type shown to the right, where multiboson processes from other channels enter via S^η into λ^η. Contributions of this diagram to V are at least of $\mathcal{O}(U^5)$. The same flow equations may be obtained by taking the derivative of the exact Bethe-Salpeter equation [79] (Eqs. (2.15)-(2.17)) and expressing Φ^η, V^η, and $\mathcal{I}^\eta$ in SBE quantities. Details are provided in Appendix B.4.

3.4 Schwinger-Dyson equation for the self-energy

Using the derivative of the Schwinger-Dyson equation resolves the unfavourable influence the information loss inherent to the TUfRG scheme has on the conventional self-energy, see Section 2.3.1. Here the SDE flow equation will first be expressed in SBE quantities and then rewritten in a form that is natural to the SBE in Section 3.4.2.

3.4.1 Conventional SDE in the SBE formalism

The flow equation for the self-energy can be obtained from the two-particle vertex via the derivative of the Schwinger-Dyson equation by inserting the parquet Eq. (2.9) into the SDE equation

$$\begin{aligned}\dot{\Sigma}(k_1) = &- \sum_{k_2,k_3,k_4} \dot{V}(k_1,k_2,k_3,k_4)G(k_2)G(k_3)G(k_4)\delta_{k_1+k_3-k_2,k_4}U \\ &- \sum_{k_2,k_3,k_4} V(k_1,k_2,k_3,k_4)\partial_\Lambda \left(G(k_2)G(k_3)G(k_4)\right)\delta_{k_1+k_3-k_2,k_4}U.\end{aligned}$$

In the SBE framework the derivative of the parquet equation expressed in SBE quantities

$$\dot{V} = \dot{\nabla}_{pp} + \dot{M}_{pp} + \dot{\nabla}_{\overline{ph}} + \dot{M}_{\overline{ph}} + \dot{\nabla}_{ph} + \dot{M}_{ph}$$

is used with the derivative of ∇_r

$$\dot{\nabla}_r = \dot{\lambda}_r w_r \lambda_r + \lambda_r \dot{w}_r \lambda_r + \lambda_r w_r \dot{\lambda}_r. \tag{3.49}$$

This scheme, referred to as 'conventional SDE flow equation for the SBE' in the following sections, reproduces the exact results of the parquet based implementation [69] using high-frequency asymptotics, in particular the convergence in form factors and loop orders behaves exactly the same. Following [69], the explicit form of the flow equation is given in Appendix B.5.

3.4.2 Natural expression of the SDE in the SBE framework

Alternatively, the SDE equation can be expressed in a way that is more natural to the SBE framework, which is equivalent to the expression of the self-energy in Hedin's theory [21, 80], where it was already used in the context of the SBE. In this work we sketch a derivation starting from the Schwinger-Dyson equation [77], as well as deriving a flow equation from the result. We also discuss the impact of a limited number of form factors and lacking multiloop convergence on the self-energy obtained from this flow equation.

To simplify the derivation, the SDE is rewritten and the flow equation based on the derivative of the SDE is introduced in the final step. Diagrammatic channels are used, as the subtleties are best understood by examining the diagrams involved. Prior to this point the explicit mention of spin indices was avoided for clarity. In this derivation however, it becomes necessary to take spin dependence into account explicitly. We use the symbols $\bullet$ and $\circ$ to represent a summation over spin indices and spin, momenta, and frequency indices, respectively. As a starting point, the SDE equations is expressed in diagrammatic channels [77] as

$$\Sigma = \left(U + \frac{1}{2}\left(U \circ \Pi_{ph} \circ V\right)\right) G \tag{3.50a}$$

$$\Sigma = -\left(U + \frac{1}{2}\left(U \circ \Pi_{\overline{ph}} \circ V\right)\right) G \tag{3.50b}$$

$$\Sigma = -\left(U + \left(U \circ \Pi_{pp} \circ V\right)\right) G. \tag{3.50c}$$

Inserting Eq. 3.19 yields [77]

$$\Sigma^{\uparrow} = \left(w_{ph}^{\hat{\uparrow}\downarrow}\lambda_{ph}^{\hat{\uparrow}\downarrow}\right) G^{\downarrow} \tag{3.51a}$$

$$= -\left(w_{\overline{ph}}^{\uparrow\downarrow}\lambda_{\overline{ph}}^{\uparrow\downarrow}\right) G^{\downarrow} \tag{3.51b}$$

$$= -\left(w_{pp}^{\uparrow\downarrow}\left(2\lambda_{pp}^{\uparrow\downarrow} - 1\right)\right) G^{\downarrow} = \lambda_r \bullet w_r G \tag{3.51c}$$

Note that the Hartree-Fock contribution has been added compared to Eq. (2.28). The SDE thus takes a very simple form and requires only λ_r and w_r of one channel as input. This freedom is known as Fierz ambiguity. Translated to physical channels the equivalent equation reads

$$\Sigma = \lambda^{\mathrm{M}} w^{\mathrm{M}} G \tag{3.52}$$

$$= -\lambda^{\mathrm{SC}} w^{\mathrm{SC}} G \tag{3.53}$$

$$= (\lambda^{\mathrm{D}} w^{\mathrm{D}} - 2U) G. \tag{3.54}$$

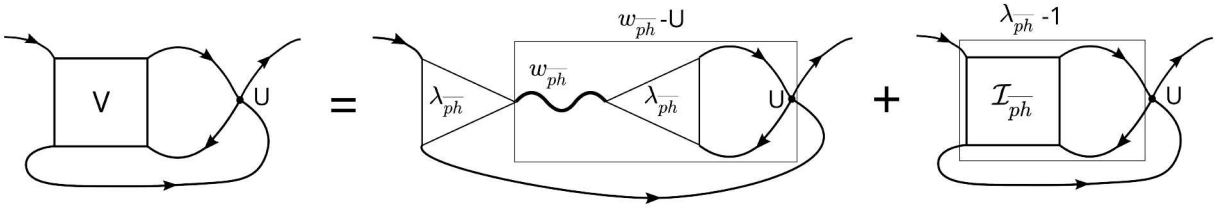

Figure 3.9: Diagrammatic illustration of Eq. (3.55) with $r = \overline{ph}$. The boxes can be simplified to the expression above them.

If no approximations are made, the three ways of expressing the SDE, called SBE-SDE going forth, are equivalent. Input from any one channel alone is sufficient to construct every self-energy diagram, as illustrated using an example in Fig. 3.10. However, the perfect equivalence is broken in the TUfRG and at finite multiloop order, as discussed in the following sections. In [20] an equal mixing of the charge and

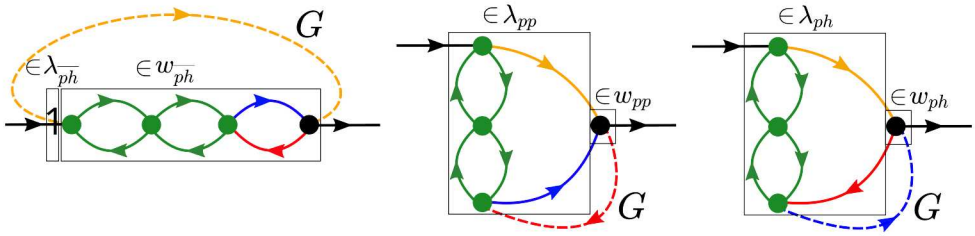

Figure 3.10: The same self-energy diagram drawn as $\lambda_{\overline{ph}} w_{\overline{ph}} G$ on the left, $\lambda_{pp} w_{pp} G$ in the middle, and $\lambda_{ph} w_{ph} G$ on the right. The same elements of the diagram are drawn in the same color and the dashed line indicates which internal line is the closing Green's function. If calculated by $\lambda_{\overline{ph}} w_{\overline{ph}} G$, using only an s-wave form factor is sufficient to make it exact. For $\lambda_{pp/ph} w_{pp/ph} G$ only s-wave is not exact (but maybe still sufficient). This is a similar issue to the one that made using the SDE for TUfRG necessary in the first place.

magnetic channels is observed to yield the most accurate results.

3.4.3 SBE-SDE equations in form factor notation

When expanding the fermionic momentum dependence of λ_r in form factors, the SBE-SDE equation reads

$$\Sigma^{\uparrow}(\mathbf{k}_1) = \sum_{\mathbf{q}} w_{ph}^{\hat{\uparrow}\downarrow}(\mathbf{q}) \left(\sum_m f_m(\mathbf{k}_1) f_0(\mathbf{k}_1) \lambda_{ph}^{\hat{\uparrow}\downarrow}(\mathbf{q}, m) \right) G^{\downarrow}(\mathbf{k}_1 + \mathbf{q}) \tag{3.55a}$$

$$\Sigma^{\uparrow}(\mathbf{k}_1) = -\sum_{\mathbf{q}} w_{\overline{ph}}^{\uparrow\downarrow}(\mathbf{q}) \left(\sum_m f_m(\mathbf{k}_1) f_0(\mathbf{k}_1) \lambda_{\overline{ph}}^{\uparrow\downarrow}(\mathbf{q}, m) \right) G^{\downarrow}(\mathbf{k}_1 + \mathbf{q}) \tag{3.55b}$$

$$\Sigma^{\uparrow}(\mathbf{k}_1) = -\sum_{\mathbf{q}} w_{pp}^{\uparrow\downarrow}(\mathbf{q}) \left(\sum_m f_m(\mathbf{k}_1) f_0(\mathbf{k}_1) \left(2\lambda_{pp}^{\uparrow\downarrow}(\mathbf{q}, m) - 1\delta_{m,0} \right) \right) G^{\downarrow}(\mathbf{q} - \mathbf{k}_1), \tag{3.55c}$$

with $f_0 = \text{const}$ and suppressed frequency arguments to lighten the notation. Unfortunately, choosing one of the three formulations of the SBE-SDE equation means that the form factor truncation is less optimal for some diagrams contributing to Σ than others. Any r-reducible diagram is treated optimally with respect to form factors by $f_m(\mathbf{k}_1) f_0(\mathbf{k}_1) \lambda_r(\mathbf{q}, m)$, however, diagrams belonging to the other channels are not. To make this idea clearer let us revisit Fig. 3.10: If the SBE-SDE equation using $\overline{ph}$ objects is chosen, then using only an s-wave form factor in the calculation is sufficient to describe the diagram exactly. However, the same diagram is not calculated exactly with just one form factor when using pp/ph based SBE-SDE equations because $\lambda_{pp/ph}$ are eye-diagram-like and truly depend on their fermionic argument. With the SBE-SDE, all ladder diagrams from the channel that was chosen for the SBE-SDE equation are treated exactly (see left side of Fig. 3.10 as an example), whereas the corrections from the

other channels to these ladders are adversely affected. To summarize, some diagrams are not treated optimally in the SBE-SDE equation with respect to a truncation in form factors. Which diagrams this affects depends on which channel is chosen to calculate Σ. This issue is not identical to the issue arising in the conventional fRG flow equation where every diagram beyond the bubble is affected [69]. In particular, the $\overline{ph}$-ladder diagrams that are the driver of the pseudogap opening as found in [70] can all be captured correctly if $\overline{ph}$ objects are chosen to evaluate the SBE-SDE equation. While the natural expression of the SBE introduces some information loss compared to the conventional SDE it is sufficient to observe the pseudogap if the correct channel is chosen [77]. The advantage is a much simpler equation. At convergence in form factors all three SBE-SDE equations again yield the same result. Originally the SDE was introduced to circumvent problems of the TUfRG.

3.4.4 SBE-SDE flow equations: comparison to the conventional SDE

The SBE-SDE equation is exact and the same holds for the derivative as long as it is complete. Problems and differences to the derivative of the conventional SDE can, and indeed do, arise when it is incomplete, as is the case at finite multiloop order when the self-consistency of the parquet equations is not yet recovered. At finite loop order the SBE-SDE does not exactly reproduce the result of the conventional SDE at the same loop level. As an example for which derivatives are included to which level, the derivative of pp-channel-based SBE-SDE equation is compared to the derivative of the conventional SDE equation in Fig. 3.11. Diagrams in which the derivative is on the closing line of the SBE-SDE (first diagram of

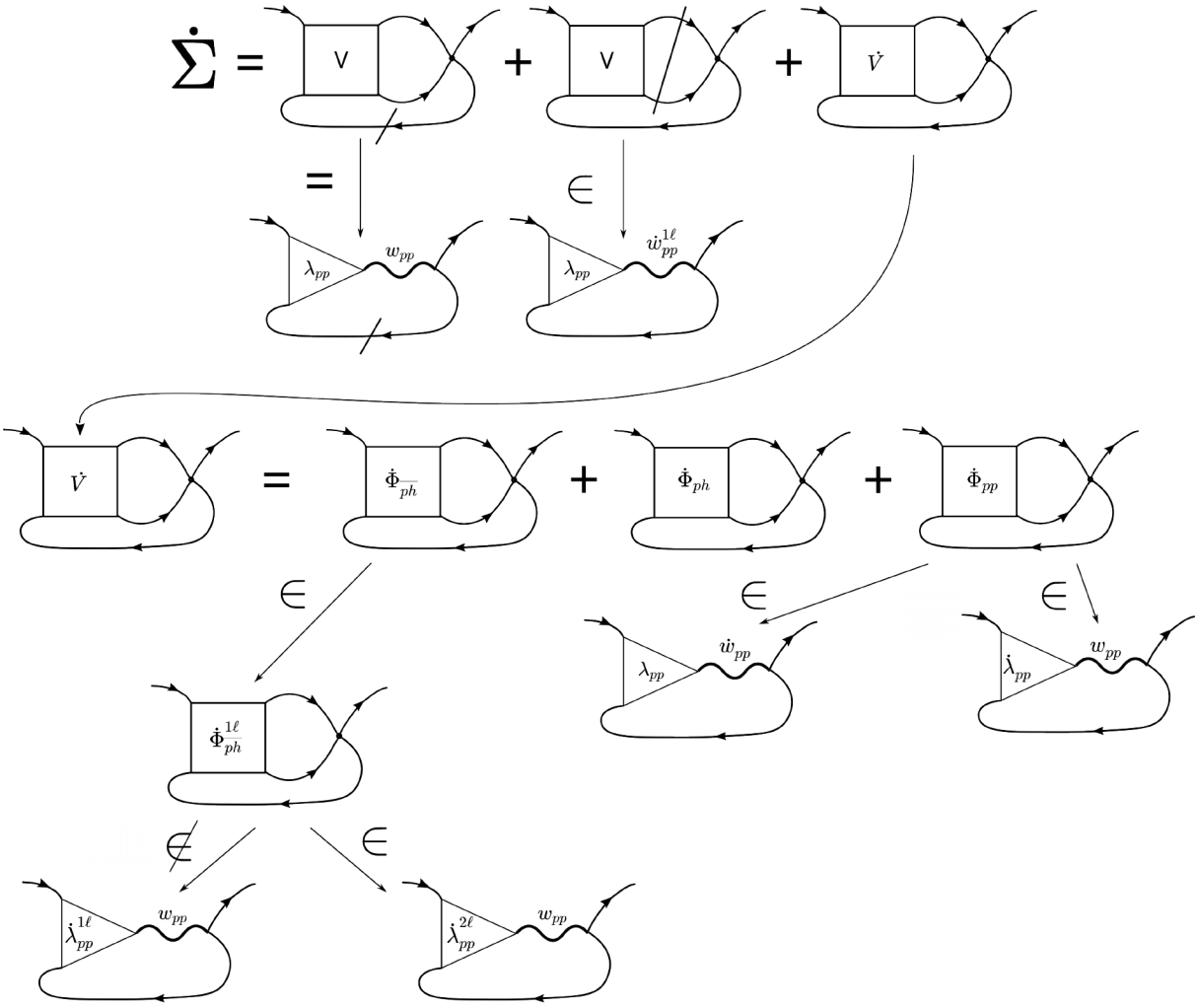

Figure 3.11: Comparison of the derivative for the conventional SDE and the SBE-SDE.

the first row), are treated exactly the same way in both methods. The second diagram (in which the dash through two internal Green's functions represents $SG + GS$ to save drawing two diagrams that are

essentially the same), is complete in the SBE-SDE at 1ℓ, as the single-scale propagator is on a pp-bubble of w_{pp}. Diagrams included in $\dot{\Phi}_{pp}GGGU$ are captured to the same multiloop level in $\lambda_{pp}\dot{w}_{pp}G$ or $\dot{\lambda}_{pp}w_{pp}G$ (see rows 3 and 4), as they are when using the conventional SDE. Diagrams of the type $\sum_{r\neq pp}\dot{\Phi}_r GGGU$, however, are not captured to the same multiloop level ℓ by the SBE-SDE where $\ell+1$ loops are necessary to complete the derivative to the same level. To better understand this, examine Fig. 3.10 once again: for derivatives of the form $\sum_{r'\neq r}\dot{\Phi}_r GGGU$, the single-scale propagator is located on an insertion from another channel into $\dot{\lambda}_r$ thus requiring 2ℓ to complete the derivative. On the other hand, the same diagram could be complete at the 1ℓ level had we chosen the $\overline{ph}$-based Eq. 3.55b instead of the pp-based Eq. 3.55c when taking the derivative. At infinite loop order the result is independent of the choice of channel again. Note that the diagrams that are adversely affected by this are the same ones whose momentum dependence is not captured effectively by the TUfRG when using the natural expression of the SDE.

3.4.5 SDE equation expressed in high-frequency asymptotics and three-point vertices

The close connection of the SBE quantities to the frequency asymptotics means that the SBE-SDE equation (3.51) can be rewritten in terms of K_1 and K_2 using (3.17) as

$$\Sigma = -\left(\lambda_r \bullet w_r\right) G = -(K_{1,r} + K_{2,r} + U)G. \tag{3.56}$$

Alternatively the three-point vertex γ_r^3 and its connection to $\lambda_r w_r$, given in Eq. (3.8), can be exploited to yield

$$\Sigma = -\left(\lambda_r \bullet w_r\right) G = -\gamma_r^3 U G. \tag{3.57}$$

Both options have the same limitations with respect to the form factor expansion and multiloop order discussed in the previous sections.

3.5 SBE for the Extended Hubbard Model

The Coulomb interaction is long-ranged. While it may be well screened in many materials, a purely local interaction is nevertheless not realistic in most scenarios. Introducing an interaction between neighbouring sites, the nearest-neighbour interaction V serves as a first step beyond the local Hubbard model towards a more realistic description of real materials, see Section 2.1.3. The bare interaction

$$\mathcal{I}^{\uparrow\downarrow}_{\text{bare}}(\mathbf{k}_1,\mathbf{k}_2,\mathbf{k}_3,\mathbf{k}_4) = U + 2V(\cos(k_{2,x}-k_{1,x}) + \cos(k_{2,y}-k_{2,y})) \tag{3.58}$$

develops a momentum dependence due to its non-locality, which must be considered carefully in a way that captures the relevant physics, without pushing the numerical effort out of range. Several properties of vertex quantities discussed so far, such as the high-frequency behaviour and effect of bare interaction reducibility, rest on the locality of the bare interaction. Without this condition, assumptions need to be checked explicitly and modified if needed. For example, more spin combinations are possible, and the exact form of the bare vertex $\mathcal{I}^{r,\uparrow\downarrow}_{\text{bare}}$ depends on the channel

$$\mathcal{I}^{pp}_{\text{bare}}(\mathbf{q},k,k') = U + 2V(\cos(k_x-k'_x) + \cos(k_y-k'_y)) \tag{3.59a}$$
$$\mathcal{I}^{ph}_{\text{bare}}(\mathbf{q},k,k') = U + 2V(\cos(q_x) + \cos(q_y)) \tag{3.59b}$$
$$\mathcal{I}^{\overline{ph}}_{\text{bare}}(\mathbf{q},k,k') = U + 2V(\cos(k_x-k'_x) + \cos(k_y-k'_y)), \tag{3.59c}$$

illustrated diagrammatically in Fig. 3.12. Note that while there is only one bare interaction, its momentum dependence takes different forms in the different channel notations. Translated to physical channels the bare interaction reads

$$\mathcal{I}^{\text{SC}}_{\text{bare}}(\mathbf{q},\mathbf{k},\mathbf{k}') = U + 2V(\cos(k_x-k'_x) + \cos(k_y-k'_y)) \tag{3.60a}$$
$$\mathcal{I}^{\text{D}}_{\text{bare}}(\mathbf{q},\mathbf{k},\mathbf{k}') = U + 4V(\cos(q_x) + \cos(q_y)) - 2V(\cos(k_x-k'_x) + \cos(k_y-k'_y)) \tag{3.60b}$$
$$\mathcal{I}^{\text{M}}_{\text{bare}}(\mathbf{q},\mathbf{k},\mathbf{k}') = -U - 2V(\cos(k_x-k'_x) + \cos(k_y-k'_y)). \tag{3.60c}$$

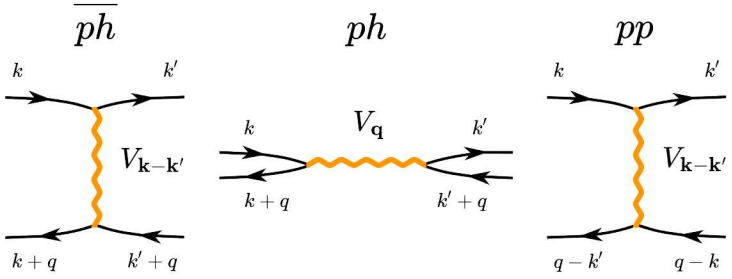

Figure 3.12: Bare interaction of the extended Hubbard model in the different channels.

The bare interaction expanded in form factors is reported in Appendix B.6. The following sections present possible adaptions of the SBE framework to include nearest-neighbour interactions: first a straightforward, but inefficient extension, and a second, more subtle, with a focus on maintaining the advantages of the SBE. The latter allows us direct access to physical quantities and reduced numerical effort, by redefining the notion of bare interaction reducibility. Results for different approximations, based on the latter approach and a comparison of their numerical effort, are presented in Section 4.5.

3.5.1 Straightforward extension

The favourable properties of the SBE implementation, as seen so far, are mainly related to the bare interaction being local. For a non-local interaction such as that of the extended Hubbard model, classifying diagrams according to their reducibility in the, now form factor dependent, bare interaction is still possible. However, if done naïvely, it undermines the original spirit of the SBE and erases its numerical advantages. The SBE's strength for implementation lies in the factorization of the most relevant diagrams into fermion-boson couplings and the exchange of a single bosonic quantity. A bare interaction dependent on fermionic momenta leads to a 'bosonic' propagator that also depends on fermionic momentum arguments and thus defys the purpose of the SBE. The fermion-boson couplings also gain an additional fermionic momentum argument. Figure 3.13 shows how the non-local interaction alters the diagram's structure. Worse still, the flow equations of w^η now require two extra form factor summations, and ∇^η

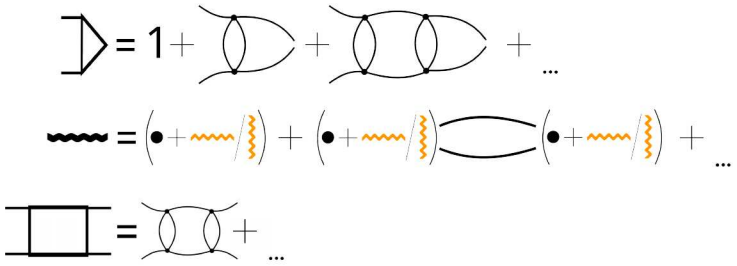

Figure 3.13: Diagrammatic illustration of applying the notion of bare interaction reducibility to the extended Hubbard model naïvely. The horizontal and vertical lines represent the $\mathbf{q}$ and $\mathbf{k}-\mathbf{k}'$ dependent extended bare interaction respectively.

is no longer a simple product but also comprises internal sums over form factors. The equations for w^η read

$$\dot{w}^\eta(\Omega,\mathbf{q},n,n') = \sum_{m,m',l,l'\nu} w^\eta(\Omega,\mathbf{q},n,l)\lambda^\eta(\Omega,\mathbf{q},\nu,l,m)\dot{\Pi}^\eta(\Omega,\mathbf{q},\nu,m,m')\bar{\lambda}^\eta(\Omega,\mathbf{q},\nu,m',l')w^\eta(\Omega,\mathbf{q},l',n'), \tag{3.61}$$

for λ^η

$$\dot{\lambda}^\eta(\Omega,\mathbf{q},\nu,n,n') = \sum_{m,m',\nu'} \lambda^\eta(\Omega,\mathbf{q},\nu',n,m)\dot{\Pi}^\eta(\Omega,\mathbf{q},\nu',m,m')\mathcal{I}^\eta(\Omega,\mathbf{q},\nu',m',\nu,n'), \tag{3.62}$$

and

$$\nabla^\eta(\Omega,\mathbf{q},\nu,n,\nu',n') = \sum_{m,m',\nu} \lambda^\eta(\Omega,\mathbf{q},\nu,n,m)w^\eta(\Omega,\mathbf{q},m,m')\bar{\lambda}^\eta(\Omega,\mathbf{q},\nu,m',n'), \tag{3.63}$$

while the rest function flow equation remains the same. Note that the two form factor dependencies of λ are not the same in nature and $\lambda^\eta(\Omega, \mathbf{q}, \nu, n, \nu', n') \neq \lambda^\eta(\Omega, \mathbf{q}, \nu, n', \nu', n)$: for the left hand fermion-boson coupling the incoming form factor dependence does not change structurally with the addition of a non-local interaction, while the outgoing form factor index couples only to the bare interaction, therefore the first shell of form factors exactly captures the fermionic momentum dependence. Numerical effort can be reduced by exploiting $\lambda^\eta(\Omega, \mathbf{q}, \nu, n, \nu', n') = \bar{\lambda}^\eta(\Omega, \mathbf{q}, \nu, n', \nu', n)$. The nearest-neighbour interaction requires the inclusion of the full first shell of form factors, so the explosion in form factor arguments and summations renders this approach numerically unfeasible. This might lead one to think more generally, that the SBE is not the natural framework to treat these kinds of models, as the conventional fermionic fRG is not plagued by these problems[2]. The initial conditions are now

$$w^{\eta,\text{init}}(\Omega, \mathbf{q}, n, n') = \mathcal{I}^{\text{X}}_{\text{bare}}(\mathbf{q}, n, n') \tag{3.64a}$$

$$\lambda^{\eta,\text{init}}(\Omega, \mathbf{q}, \nu, n, n') = \begin{cases} 1 & n = n' < 5 \\ 0 & \text{else} \end{cases} \tag{3.64b}$$

$$M^{\eta,\text{init}}(\Omega, \mathbf{q}, \nu, n, \nu', n') = 0. \tag{3.64c}$$

The rest function is expected to be negligible in the same parameter regime as determined in Section 4.2.3.

3.5.2 Refined approach: natural bosonization

To save the SBE idea in the context of a non-local bare interaction, it is necessary to take a step back and revisit the original motivation for the formalism: collective excitations. The nearest-neighbour interaction enhances the charge density wave (CDW) fluctuations, which are encoded in the s-wave susceptibility χ^{D}. It should, therefore, be possible to encode this collective excitation in a purely s-wave bosonic propagator w^{D}. The influence of V on other objects is expected to be of secondary importance. In practice, the challenge is how to adapt the SBE formalism such that it ideally i) includes the influence of V on all SBE quantities and w^{D} in particular, ii) does not destroy the numerically favourable factorization of $\nabla^\eta(q, k, k') = \lambda^\eta(q, k) w^\eta(q) \lambda^\eta(q, k')$, iii) retains the close connection between χ^η and w^η, all while iv) not introducing any approximations. We will here demonstrate that by cleverly modifying the notion of bare interaction reducibility, all four conditions can be met simultaneously.

For a bare interaction, like the one in question here, that can be divided into a purely bosonic part and one that depends on fermionic arguments

$$\mathcal{I}^\eta_{\text{bare}}(\mathbf{q}, \mathbf{k}, \mathbf{k}') = \mathcal{I}^\eta_{\text{bos}}(\mathbf{q}) + \mathcal{I}^\eta_{\text{ferm}}(\mathbf{k}, \mathbf{k}'), \tag{3.65}$$

the notion of bare interaction reducibility should be based solely on the purely bosonic part [81, 82]. In physical channels the bosonic bare interactions then reads

$$\mathcal{I}^{\text{SC}}_{\text{bos}}(\mathbf{q}) = U \tag{3.66a}$$

$$\mathcal{I}^{\text{M}}_{\text{bos}}(\mathbf{q}) = -U \tag{3.66b}$$

$$\mathcal{I}^{\text{D}}_{\text{bos}}(\mathbf{q}) = U + 4V(\cos(q_x) + \cos(q_y)), \tag{3.66c}$$

and the fermionic bare interaction is given by

$$\mathcal{I}^{\text{SC}}_{\text{ferm}}(\mathbf{k}, \mathbf{k}') = 2V(\cos(k_x - k') + \cos(k_y - k'_y)) \tag{3.67a}$$

$$\mathcal{I}^{\text{M}}_{\text{ferm}}(\mathbf{k}, \mathbf{k}') = -2V(\cos(k_x - k') + \cos(k_y - k'_y)) \tag{3.67b}$$

$$\mathcal{I}^{\text{D}}_{\text{ferm}}(\mathbf{k}, \mathbf{k}') = -2V(\cos(k_x - k') + \cos(k_y - k'_y)). \tag{3.67c}$$

The former are used as initial values for the bosonic propagators whereas the latter are moved to the rest function as its initial value. Expansion in form factors and projections between the channels are reported in Appendix B.6. This split guarantees the bosonic propagator remains bosonic and the fermionic parts of the interaction are treated exactly in the rest function, an object that already depended on fermionic arguments thus not giving rise to any additional form factor dependencies. Likewise, the multiplicative nature of ∇^η is upheld and no additional form factor sums are introduced. Figure 3.14

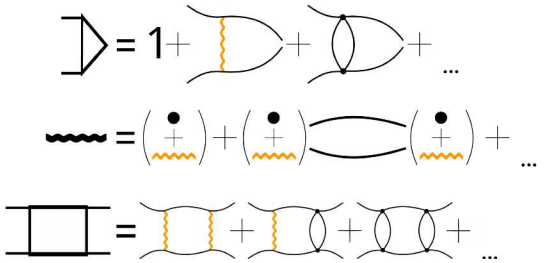

Figure 3.14: Diagrammatic illustration of applying the notion of bare interaction reducibility adapted to the non-local interaction of the extended Hubbard model.

diagrammatically illustrates the improved approach. On the downside, both the rest functions and the fermion-boson couplings develop non-trivial high-frequency asymptotics that possibly require larger numbers of frequencies for convergence. It is also unclear a priori whether the rest function can be neglected in this approximation. Both questions will be addressed in Section 4.5. The flow equations do not require any modifications compared to those for a purely local interaction introduced in Section 3.3, including the multiloop extensions. Instead, the initial conditions of the bosonic propagator and the rest function change

$$w^{\eta,\mathrm{init}}(\Omega,\mathbf{q}) = \mathcal{I}^{\eta}_{\mathrm{bos}}(\mathbf{q}) \tag{3.68}$$

$$\lambda^{\eta,\mathrm{init}}(\Omega,\mathbf{q},\nu,n) = \delta_{n,0} \tag{3.69}$$

$$M^{\eta,\mathrm{init}}(\Omega,\mathbf{q},\nu,n,\nu',n') = \mathcal{I}^{\eta}_{\mathrm{ferm}}(n,n'), \tag{3.70}$$

while the initial value of the fermion-boson couplings remain unchanged. The relation between the s-wave susceptibility χ^{η} and the bosonic propagator Eq. (3.9) has to be adjusted slightly, to

$$\chi^{\eta}(\Omega,\mathbf{q}) = \frac{w^{\eta}(\Omega,\mathbf{q}) - \mathcal{I}^{\eta}_{\mathrm{bos}}(\mathbf{q})}{(\mathcal{I}^{\eta}_{\mathrm{bos}}(\mathbf{q}))^2}. \tag{3.71}$$

The high-frequency asymptotic of the fermion-boson coupling λ are

$$\lim_{\nu\to\infty} \lambda^{\eta}(\Omega,\mathbf{q},\nu,n) = \begin{cases} 1 & n = 0 \\ \lambda^{\eta,\mathrm{asympt}}(\Omega,\mathbf{q},n) & 1 < n < 5 \\ 0 & \text{else} \end{cases} \tag{3.72}$$

and the rest functions asymptotics are given by

$$\lim_{\nu\to\infty} M^{\eta}(\Omega,\mathbf{q},\nu,n,\nu',n') = \begin{cases} M^{\eta}_2(\Omega,\mathbf{q},n,\nu',n') & 1 < n < 5 \\ 0 & \text{else} \end{cases} \tag{3.73a}$$

$$\lim_{\substack{\nu\to\infty \\ \nu'\to\infty}} M^{\eta}(\Omega,\mathbf{q},\nu,n,\nu',n') = \begin{cases} M^{\eta}_1(\Omega,\mathbf{q},n,n') & 1 < n < 5 \\ 0 & \text{else.} \end{cases} \tag{3.73b}$$

They can be treated analogously to the high-frequency asymptotics of the two-particle reducible vertices, see Section 3.2.5. The flow equations given in Section 3.3 apply also to the high-frequency asymptotics as long as the appropriate frequencies are replaced by ∞.

The bare interaction irreducible in a specific channel $\mathcal{I}^{\eta}_{\mathrm{SBE}}$ needs to be considered carefully, as translating the bare interaction from one channel to another can change it from bosonic to fermionic in nature and vice versa, see Appendix B.6. Also the double counting correction D^{η} in V^{η} and $\mathcal{I}^{\eta}_{\mathrm{SBE}}$ must be

[2]The Wentzell asymptotics K_1 and K_2 do acquire additional form factor arguments, but the flow equations remain unchanged.

reconsidered. The initial value of $\mathcal{I}_{\mathrm{SBE}}^{\eta,\mathrm{init}} = M^{\eta,\mathrm{init}} = \mathcal{I}_{\mathrm{ferm}}^{\eta}$ must be ensured. We use

$$\begin{aligned}
\mathcal{I}_{\mathrm{SBE}}^{\mathrm{SC,init}} &= M^{\mathrm{SC,init}} + P^{ph\to pp}\left[\frac{1}{2}(\nabla^{\mathrm{D,init}} + M^{\mathrm{D,init}}) - \frac{1}{2}(\nabla^{\mathrm{M,init}} + M^{\mathrm{M,init}})\right] - P^{\overline{ph}\to pp}\left[\nabla^{\mathrm{M,init}} + M^{\mathrm{M,init}}\right] + D^{\mathrm{SC}} \\
&= 2V_{\mathbf{k}-\mathbf{k}'} + P^{ph\to pp}\left[\frac{1}{2}(U + 4V_{\mathbf{q}} - 2V_{\mathbf{k}-\mathbf{k}'}) - \frac{1}{2}(-U - 2V_{\mathbf{k}-\mathbf{k}'})\right] - P^{\overline{ph}\to pp}\left[-U - 2V_{\mathbf{k}-\mathbf{k}'}\right] + D^{\mathrm{SC}} \\
&= 2V_{\mathbf{k}-\mathbf{k}'} + U + 2V_{\mathbf{k}-\mathbf{k}'} + U + 2V_{\mathbf{k}-\mathbf{k}'} + D^{\mathrm{SC}} \\
&= \mathcal{I}_{\mathrm{ferm}}^{\mathrm{SC}} + 2\mathcal{I}_{\mathrm{bare}}^{\mathrm{SC}} + D^{\mathrm{SC}} \\
&\Rightarrow D^{\mathrm{SC}} = -2\mathcal{I}_{\mathrm{bare}}^{\mathrm{SC}}
\end{aligned} \tag{3.74}$$

to determine D^{SC}. If the rest function is neglected, the double counting prevention has to be changed to $D^{\mathrm{SC}} = -2\mathcal{I}_{\mathrm{bos}}^{\mathrm{SC}}$

$$\begin{aligned}
\mathcal{I}_{\mathrm{SBE}}^{\mathrm{SC,init}} &= P^{ph\to pp}\left[\frac{1}{2}\nabla^{\mathrm{D,init}} - \frac{1}{2}\nabla^{\mathrm{M,init}}\right] - P^{\overline{ph}\to pp}\left[\nabla^{\mathrm{M,init}}\right] - 2D^{\mathrm{SC}} \\
&= P^{ph\to pp}\left[\frac{1}{2}(U + 4V_{\mathbf{q}}) - \frac{1}{2}(-U)\right] - P^{\overline{ph}\to pp}\left[-U\right] - 2D^{\mathrm{SC}} \\
&= U + P^{ph\to pp}\left[2V_{\mathbf{q}}\right] + U - 2D^{\mathrm{SC}} \\
&= \mathcal{I}_{\mathrm{ferm}}^{\mathrm{SC}} + 2\mathcal{I}_{\mathrm{bos}}^{\mathrm{SC}} + 2D^{\mathrm{SC}} \\
&\Rightarrow D^{\mathrm{SC}} = -2\mathcal{I}_{\mathrm{bos}}^{\mathrm{SC}},
\end{aligned} \tag{3.75}$$

or the value of M^{η} has to be fixed to the initial value, thus only neglecting the flow of the rest function, not the entire object. For the magnetic and density channel we make the ansatz $D^{\mathrm{M/D}} = -2\mathcal{I}_{\mathrm{bare}}^{\mathrm{M/D}}$ when including the rest function, and $D^{\mathrm{M}} = -2\mathcal{I}_{\mathrm{bos}}^{\mathrm{M}}$ and $D^{\mathrm{D}} = -2U$ when neglecting the rest function. This yields

$$\begin{aligned}
\mathcal{I}_{\mathrm{SBE}}^{\mathrm{M,init}} &= M^{\mathrm{M,init}} - P^{ph\to\overline{ph}}\left[\frac{1}{2}\left(\nabla^{\mathrm{D,init}} + M^{\mathrm{D,init}}\right) - \frac{1}{2}\left(\nabla^{\mathrm{M,init}} + M^{\mathrm{M,init}}\right)\right] - P^{pp\to\overline{ph}}\left[\nabla^{\mathrm{SC,init}} + M^{\mathrm{SC,init}}\right] - 2\mathcal{I}_{\mathrm{bare}}^{\mathrm{M}} \\
&= \mathcal{I}_{\mathrm{ferm}}^{\mathrm{M}}
\end{aligned} \tag{3.76}$$

and

$$\begin{aligned}
\mathcal{I}_{\mathrm{SBE}}^{\mathrm{M,init}} &= -P^{ph\to\overline{ph}}\left[\frac{1}{2}\left(\nabla^{\mathrm{D,init}}\right) - \frac{1}{2}\left(\nabla^{\mathrm{M,init}}\right)\right] - P^{pp\to\overline{ph}}\left[\nabla^{\mathrm{SC,init}}\right] - 2\mathcal{I}_{\mathrm{bos}}^{\mathrm{M}} \\
&= \mathcal{I}_{\mathrm{ferm}}^{\mathrm{M}}.
\end{aligned} \tag{3.77}$$

and for the density channel

$$\begin{aligned}
\mathcal{I}_{\mathrm{SBE}}^{\mathrm{D,init}} =& M^{\mathrm{D,init}} + 2P^{pp\to ph}\left[\nabla^{\mathrm{SC,init}} + M^{\mathrm{SC,init}}\right] - P^{pp\to\overline{ph}}\left[\nabla^{\mathrm{SC,init}} + M^{\mathrm{SC,init}}\right] && (3.78) \\
&- 2P^{\overline{ph}\to ph}\left[\nabla^{\mathrm{M,init}} + M^{\mathrm{M,init}}\right] - P^{ph\to\overline{ph}}\left[\frac{1}{2}(\nabla^{\mathrm{D,init}} + M^{\mathrm{D,init}}) - \frac{1}{2}(\nabla^{\mathrm{M,init}} + M^{\mathrm{M,init}})\right] - 2\mathcal{I}_{\mathrm{bare}}^{\mathrm{D}} \\
&= \mathcal{I}_{\mathrm{ferm}}^{\mathrm{D}}. && (3.79)
\end{aligned}$$

When neglecting the rest function extra care is due in the density channel

$$\begin{aligned}
\mathcal{I}_{\mathrm{SBE}}^{\mathrm{D,init}} &= 2P^{pp\to ph}\left[\nabla^{\mathrm{SC,init}}\right] - P^{pp\to\overline{ph}}\left[\nabla^{\mathrm{SC,init}}\right] - 2P^{\overline{ph}\to ph}\left[\nabla^{\mathrm{M,init}}\right] - P^{ph\to\overline{ph}}\left[\frac{1}{2}\nabla^{\mathrm{D,init}} - \frac{1}{2}\nabla^{\mathrm{M,init}}\right] - 2U \\
&= \mathcal{I}_{\mathrm{ferm}}^{\mathrm{D}}.
\end{aligned} \tag{3.80}$$

In Appendix B.7 a different, yet equivalent way of handling double counting and initial values is presented. It is less intuitive from a diagrammatic stand point, but better suited to numerical implementations.

The setup so far does not include any approximations. The extended part of the bare interaction has been moved to the rest function in the magnetic and superconducting channels. In addition to the algorithmic advantages, this choice is made in the expectation that the main effect of V is on the charge density wave tendencies captured in w^{D}, while the influence of $\mathcal{I}_{\mathrm{ferm}}^{\eta}$ and thus the non-trivial high-frequency asymptotics are expected to be negligible. If the rest function and non-trivial high-frequency asymptotics are indeed negligible, the scheme is already set up to take advantage optimally from a numerical stand point. Where, on the other hand, the rest function and high-frequency asymptotics are non-negligible, there is no approximation favouring CDW fluctuations over other possible ordering tendencies when they are included. The quantitative accuracy of the assumptions about the relative influence of V on the various SBE quantities will be investigated in Section 4.5.

3.5.3 Schwinger-Dyson equation

Applying the SDE equation to the extended Hubbard model requires careful re-evaluation, as the approaches so far made implicit use of the locality of the bare interaction. In [71] the SDE for the extended Hubbard model is derived to be

$$\begin{aligned}\Sigma_k \equiv \Sigma_{k\uparrow} = &-\sum_{k'q} G_{k+q}G_{k'}G_{k'+q}\left[(U+V_{\mathbf{q}})F_{\uparrow\downarrow}(k,k+q,k'+q,k') + V_{\mathbf{q}}F_{\uparrow\uparrow}(k,k+q,k'+q,k')\right] \\ &-\sum_{k'} G_{k'}(U+2V_{\mathbf{q}=0}) - \sum_{q} G_{k+q}V_{\mathbf{q}}\end{aligned} \tag{3.81}$$

where F is used to denote the vertex instead of the usual V, to avoid confusion with the non-local part of the bare interaction, $V_{\mathbf{q}} = 2V(\cos(q_x) + \cos(q_y))$. A diagrammatic illustration of the individual terms from left to right is given in Fig. 3.15. Note that the extended bare interaction gives rise to new spin

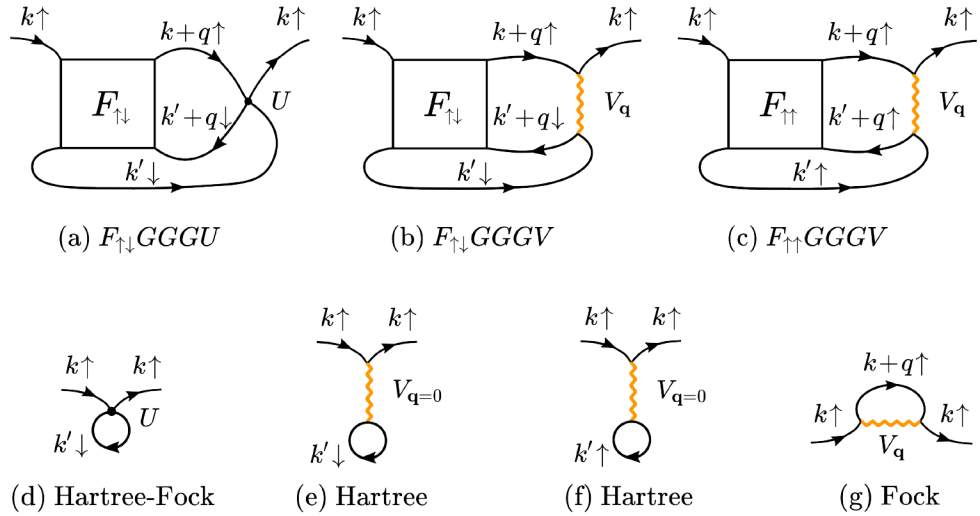

Figure 3.15: Diagrammatic illustration of the SDE for the extended Hubbard model. The momentum labels are chosen in accordance with *ph*-notation.

combinations and the Hartree and Fock terms no longer necessarily coincide. The identity from Eq. 3.19 holds in a generalized form for the extended Hubbard model,

$$w_r \bullet \lambda_r = \mathcal{I}^r_{\text{bos}} + \mathcal{I}^r_{\text{bos}} \circ \Pi_r \circ F_r. \tag{3.82}$$

Thus, the SDE will not reduce to the expression found for the local Hubbard model unless $\mathcal{I}^r_{\text{ferm}} \circ \Pi_r \circ F_r = 0$, which is the case in the s-wave truncation [77].

4 Results for the SBE scheme

In this centrepiece of the thesis the applicability and advantages of the SBE to the fRG for the (extended) Hubbard model are demonstrated. After an overview of the implementation in Section 4.1 used to obtain the data in this chapter, the SBE approximation is analysed in detail in Section 4.2 (at half filling), and Section 4.3 (finite doping). In particular, the dependence of the fermion-boson couplings, susceptibilities, and rest function on frequencies, momenta, filling, interaction strength, and next-nearest-neighbour hopping are investigated, with a focus on establishing the applicability of the SBE approximation. Next, the SBEb approximation, neglecting the flow of the fermion-boson coupling, and neglecting the rest function of the high-frequency Wentzell asymptotics, are compared in Section 4.4, which along with the Section 4.2 details results published in [78]. Note that notation and sign conventions may differ with respect to the publication to ensure consistency within this work. The remainder of the results section expands on the published results, beginning with an analysis of the extended Hubbard model, implemented using the natural bosonization of bare interaction reducibility, as outlined in Section 2.1.3.

4.1 Implementation

A general overview of the implementation is given in Section 2.3.4. For completeness, the technical parameters used in the calculations are reported in Table 4.1. A one-loop (1ℓ) truncation and Ω cutoff was used, unless specified otherwise.

4.2 The SBE approximation at half filling

The SBE approximation consists of setting the flow of the rest function to zero after the derivation of the flow equations, reducing the numerical effort by roughly a factor of four. This approximation was introduced under the name SBEa approximation in Section 3.3.3, to distinguish it from the SBEb approximation (neglecting the rest function before taking the derivative). Unless specified otherwise, the term SBE approximation equates to SBEa throughout this chapter. The influence of this approximation on the accuracy of λ, χ, and Σ at half filling is explored in detail: the momentum and frequency dependencies are analysed as well as the change in behaviour with U and β. The accuracy is established by comparing results of the SBE to 1ℓ data, including the rest function. As the AF tendencies dominate the picture at half filling even at weak coupling, the treatment of the fermionic momenta is restricted to a single, constant s-wave form factor [17].

4.2.1 Fermion-boson couplings

Results for the fermion-boson couplings λ^η are shown in Figs. 4.1 for $U = 2$, $\mu = 0$, $t' = 0$ and different values of the temperature.

	bosonic frequencies	ferm. frequencies	bosonic momenta	form factors
w	$128{\cdot}n$		$k_x^2 + p_x^2$ -1	
λ	$4{\cdot}n$	$4{\cdot}n$	$k_x^2 + p_x^2$ -1	1-2
M	$4{\cdot}n$	$4{\cdot}n$	$k_x^2 + p_x^2$ -1	1-2
Π	$128{\cdot}n$	$64{\cdot}n$	$k_x^2 + p_x^2$ -1	1-2
S		$8{\cdot}n$	$(k_x p_x)^2$	
Σ		$8{\cdot}n$	$(k_x p_x)^2$	

Table 4.1: Number of frequencies, momenta and form factors. At half filling the constant s-wave form factor is used, at finite doping the d-wave form factor $f_1(\mathbf{k}) = 1/(4\pi)(\cos(k_x) - \cos(k_y))$ is added. For the largest $T = 0.4 - 0.2$ we use $n = 6, k_x = 18$ and $p_x = 5$. At $T = 0.15$ we increase n to 8 and at $T = 0.1$ k_x is adjusted to 18 to resolve the sharpening AF peak.

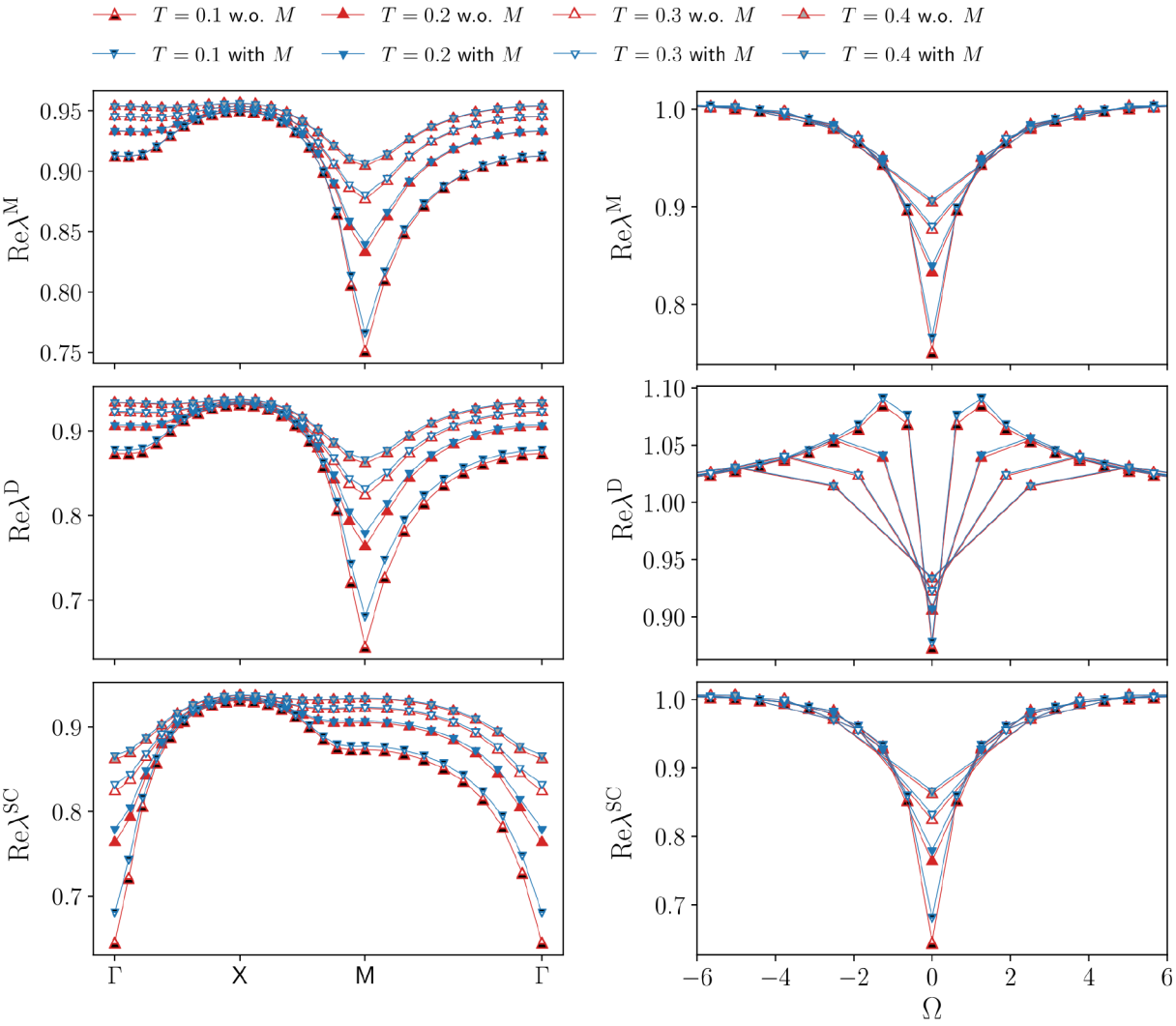

Figure 4.1: Momentum and frequency dependence of the fermion-boson couplings. The left panels show the momentum dependence of the static ($\Omega = 0$) fermion-boson couplings for the magnetic $\lambda^{\mathrm{M}}(\Omega, \mathbf{q}, \nu = \pi T, n = 0)$, density $\lambda^{\mathrm{D}}(\Omega, \mathbf{q}, \nu = \pi T, n = 0)$, and s-wave superconducting channel $\lambda^{\mathrm{SC}}(\Omega, \mathbf{q}, \nu = \pi T, n = 0)$. The right panels show the frequency dependence for fixed momentum ($\mathbf{q} = (0,0)/(\pi,\pi)$ for SC/D and M respectively). The data sets are obtained with rest function (blue symbols) and with the SBE approximation (red symbols), for $U = 2$ and different values of the temperature ($t' = 0$, $\mu = 0$).

More specifically, the (bosonic) momentum and frequency dependence of the real parts in the magnetic, density, and superconducting channels respectively, are displayed. Note that at half filling and $t' = 0$ $\lambda^{\mathrm{SC}}(\Omega, \mathbf{q}, \nu, n = 0) = \lambda^{\mathrm{D}}(\Omega, \mathbf{q} + (\pi,\pi), \nu, n = 0)$ for the s-wave components. The overall reduction with

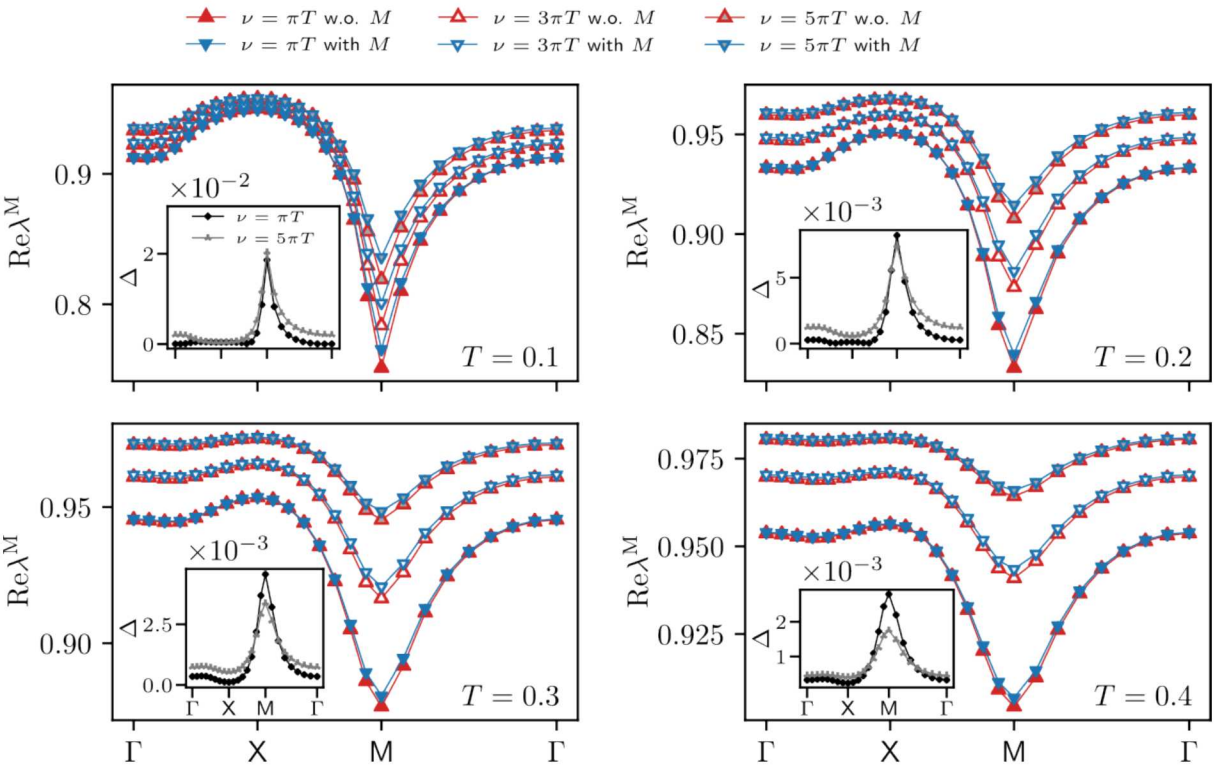

Figure 4.2: Magnetic channel of the static fermion-boson coupling $\lambda^{\mathrm{M}}(\Omega = 0, \mathbf{q}, \nu, n = 0)$, for the same parameters as in Fig. 4.1, and different fermionic frequencies. The relative difference Δ between the results with and without rest function is shown in the insets.

respect to the bare initial value of the fermion-boson couplings $\lambda^{\mathrm{init}} \equiv 1$ due to Kanamori screening [23], shows that their flow cannot be neglected (see Section 4.4.3 for the effects of the approximation $\lambda^{\eta} = 1$). The observed structures become increasingly sharp at low temperature, where the difference between the results obtained with and without rest function also becomes larger. On a quantitative level, the relative error amounts to 5.2 % at $T = 0.1$, but does not exceed 2.1 % for $T \geq 0.2$ in the reported momentum and frequency ranges. The overall agreement in both panels of Fig. 4.1 is very good, demonstrating that the contribution of the rest functions to the fermion-boson couplings is minimal in all channels for the smallest fermionic frequency $\nu = \pi T$.

Next, the question is addressed whether this observation also holds for larger fermionic frequencies, see Figure 4.2, where the focus is on the dominant magnetic channel. Equivalent plots for the superconducting and density channel are provided in Appendix C.1. The results for the static (i.e. evaluated at $\Omega = 0$) fermion-boson couplings at the different temperatures exhibit a moderate dependence on the fermionic frequency ν, featuring an overall slight suppression of the asymptotic value $\lambda^{\eta} \sim 1$. Such a reduction is due to the metallic screening effects [75, 83] in the proximity of the Fermi level. This behavior is observed also in the other channels, see Appendix C.1.

It may, therefore, be concluded that neglecting the rest functions leads to quantitatively marginal differences in the fermion-boson couplings, for the considered parameter regime at half filling.

4.2.2 Susceptibilities

Next, the impact of the rest functions M^{η} on numerical results for the susceptibilities χ^{η} is studied, starting with their evolution with the temperature, displayed in the left column of Fig. 4.3 for $U = 2$.

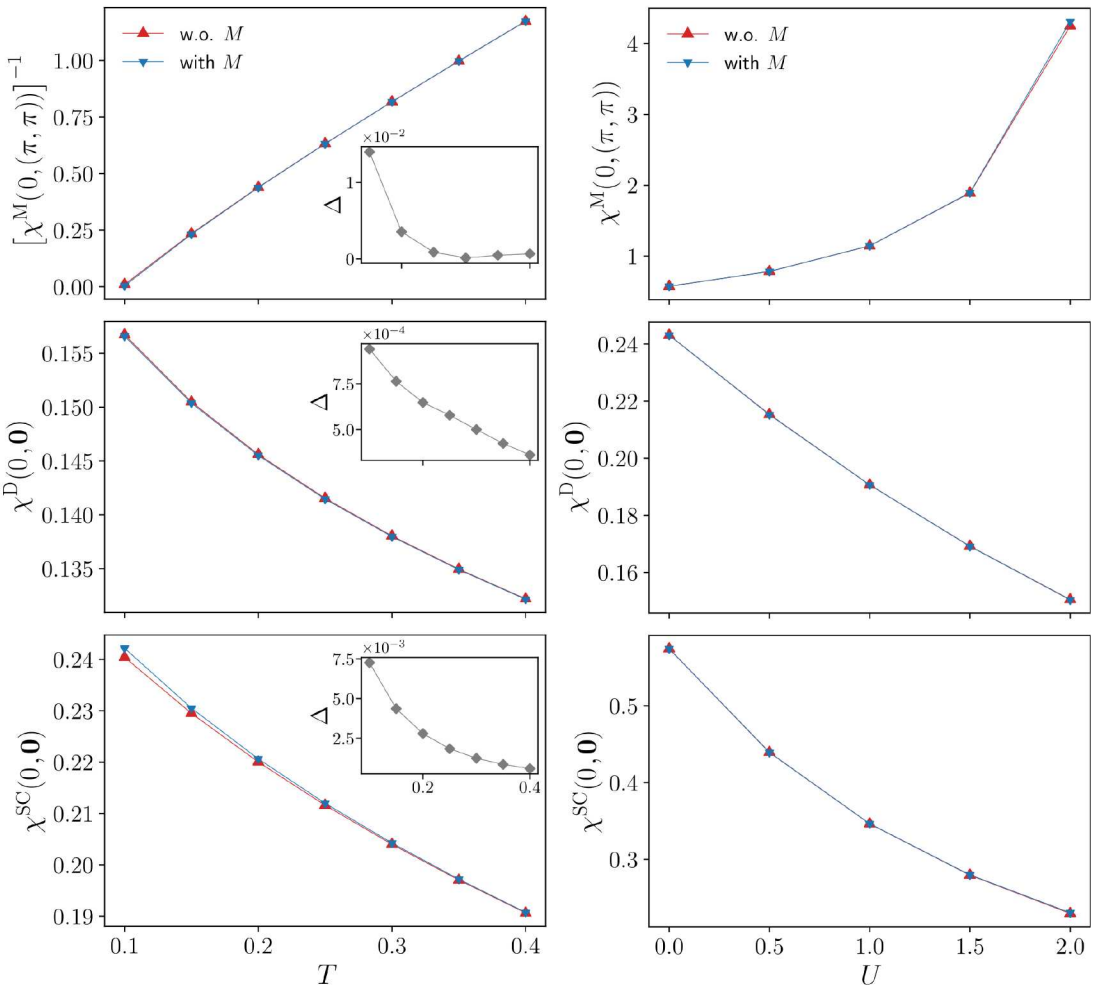

Figure 4.3: Magnetic $\chi^{\mathrm{M}}(\Omega = 0, \mathbf{q} = (\pi,\pi))$, density $\chi^{\mathrm{D}}(\Omega = 0, \mathbf{q} = (0,0))$, and s-wave superconducting static susceptibility $\chi^{\mathrm{SC}}(\Omega = 0, \mathbf{q} = (0,0))$, as obtained from the SBE formulation of the fRG with and without rest function at $t' = 0$ and $\mu = 0$. The data is presented as a function of T (left column, $U = 2$) and a function of U (right panel, $T = 0.15$). The relative difference Δ between results for different temperatures with and without rest function displayed in the insets is below 1 %, except for $T < 0.2$ in the magnetic channel. For the different U the relative difference between the results with and without rest function is below 0.1 % in the density and 0.5 % in the superconducting channel, while it reaches 1.4 % in the magnetic one (for $U = 2$).

As for the previous figures, the static susceptibilities, evaluated at the relevant momentum values $\mathbf{q}$ in the magnetic, density, and s-wave superconducting channels, are compared to the ones obtained without the SBE rest functions M^{η}. From the relative difference shown in the insets it can be seen that the contribution of the rest function increases with the inverse temperature. At the same time, the absolute values are very small, leading to a marginal effect of the rest functions, except for the magnetic susceptibility at $T = 0.1$. Note that in the density and superconducting channels the importance of the rest function is significantly smaller than in the dominant magnetic channel. A similar behavior is also observed for the interaction dependence of the susceptibilities, see right column of Fig. 4.3 and Section 5.4.5. As expected, the contribution of the rest function increases with U, but remains marginal in all channels for $T > 0.1$. Note also that the susceptibility of the dominant magnetic channel χ^{M}, which is mostly driven by vertex corrections, significantly increases with the interaction. In contrast, the bubble dominated subleading susceptibilities decrease with U, since the growing AF fluctuations lead to stronger damping via the electronic self-energy. The increase at lower temperatures is due to the growing AF fluctuations for the magnetic channel and a Fermi-liquid-like behavior for the subleading channels.

Next, attention is turned to the large contribution of the rest function obtained for the magnetic channel at low temperatures, with a deviation of $\Delta > 50$ % between the results with and without rest

function. In the inverse susceptibility displayed in the upper left most panel of Fig. 4.3 this is not so clearly visible because of the small absolute values. At the same time, the almost vanishing inverse susceptibility at $T = 0.1$ indicates the proximity to a divergence in the magnetic channel[1]. The diverging 1ℓ flow in correspondence of a finite temperature (or interaction) marks the pseudo-critical transition towards a magnetic instability. Including higher loop orders within the multiloop fRG extension [17, 30, 84] would reduce the strong AF peak due to the stronger channel interference, see Fig. 5.6. In particular, the resummation to infinite loop order in the parquet approximation would recover the Mermin-Wagner theorem. Here, as at half filling, the observation holds that sizable differences for the computation with and without the rest functions M^η arise only in the dominant magnetic susceptibility close to the pseudo-critical AF transition. Away from it, the tiny differences justify the approximation to neglect the rest function.

The appearance of the pseudo-critical transition characteristic of the 1ℓ fRG approximation is further illustrated in Fig. 4.4, more specifically in the inset of the panel reporting the magnetic susceptibility. This figure shows the momentum dependence of the static magnetic, density, and s-wave superconducting susceptibilities as obtained from the inversion of Eq. (3.9) for the screened interactions, for $U = 2$ and different temperatures. The corresponding results for the frequency dependence are provided in Fig. 4.5. The magnetic susceptibility exhibits a pronounced peak around momentum $\mathbf{q} = (\pi, \pi)$, indicating strong AF fluctuations. Except for $\chi^{\mathrm{M}}(\Omega = 0, \mathbf{q})$ at $T = 0.1$, the results of the computation with and without the rest function for the dominating magnetic channel, as well as for the subleading channels related by $\chi^{\mathrm{SC}}(\Omega = 0, \mathbf{q}, \Omega) = \chi^{\mathrm{D}}(\Omega = 0, \mathbf{q} + (\pi, \pi))$ at particle-hole symmetry, present an excellent quantitative agreement, with the largest deviation in correspondence of the AF wave vector. The relative difference for $\chi^{\mathrm{M}}(\mathbf{q}, 0)$ is below 1 % (except for $T = 0.1$) and, as a consequence, the inclusion of the rest function only sightly affects the pseudo-critical temperature [24]. For $\chi^{\mathrm{D}}(\Omega = 0, \mathbf{q})$ and $\chi^{\mathrm{SC}}(\Omega = 0, \mathbf{q})$, the relative difference is even smaller, below 0.1 % for all values of the temperature.

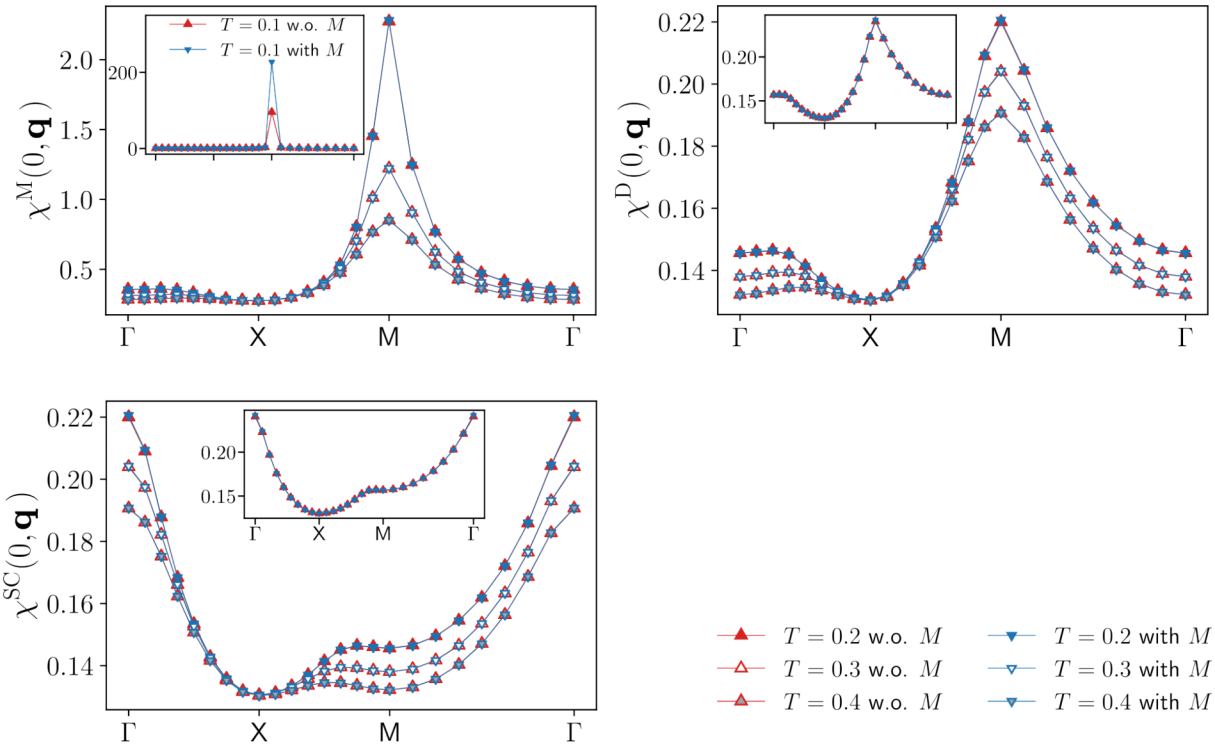

Figure 4.4: Magnetic $\chi^{\mathrm{M}}(\Omega = 0, \mathbf{q})$, density $\chi^{\mathrm{D}}(\Omega = 0, \mathbf{q})$, and s-wave superconducting $\chi^{\mathrm{SC}}(\Omega = 0, \mathbf{q})$ static susceptibilities for $U = 2$, and different values of the temperature ($t' = 0$, $\mu = 0$). The results for $T = 0.1$ are shown in the insets. The relative differences between the results with and without rest function is below 1 % (see also the insets of the left column of Fig. 4.3), with the exception of the magnetic channel for $T = 0.1$.

[1] To access temperatures below the pseudo-critical temperature, one needs to allow for the formation of an order parameter in the system and therefore to include anomalous components of the vertices [36].

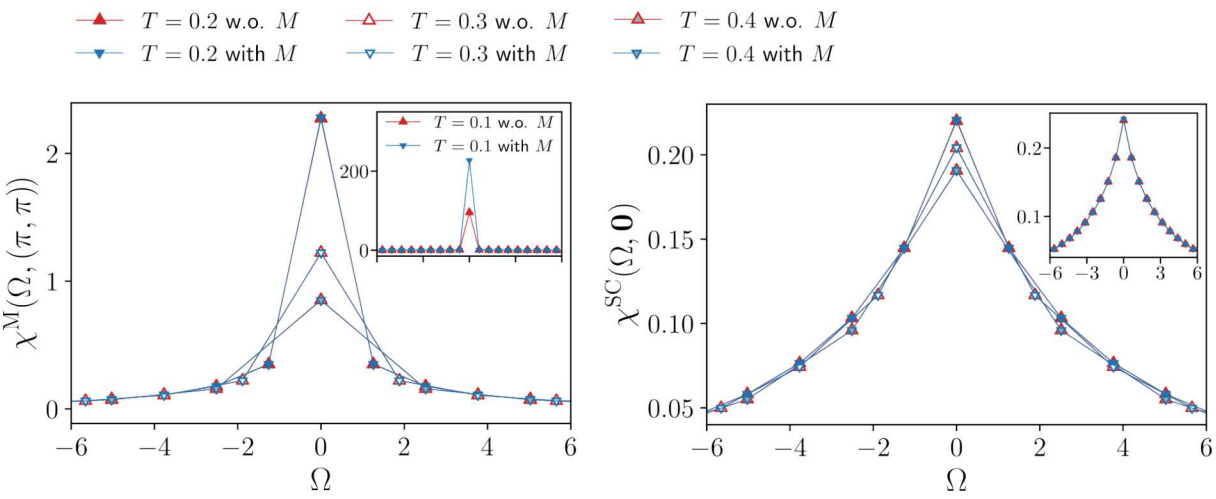

Figure 4.5: Bosonic frequency dependence of the magnetic χ^{M} and superconducting χ^{SC} susceptibilities for the same parameters as in Fig. 4.1. The relative difference Δ between the results with and without rest function does not exceed 0.8 %, except for the magnetic channel at $T = 0.1$, where Δ reaches 58 %.

$T = 0.1$ is very close to the pseudo-critical transition temperature. Note that the associated divergence in the susceptibility is reflected in the corresponding screened interaction, but *not* in the fermion-boson coupling, see Figs. 4.1 and 4.2. The multiboson exchange processes associated to spin fluctuations at low temperatures, appear to induce only a marginal increase of the fermion-boson couplings. While the rest function M^{M}, too does not diverge (discussed in the following section), its influence on χ^{M} may become non-negligible, as close to the divergence w^{M} is very sensitive to small changes in λ^{η}, see Eq. B.5.

4.2.3 Rest function

The upper panels of Fig. 4.18 show the fermionic frequency dependence of the rest functions M^{η} evaluated at the relevant $\mathbf{q}$ and $\Omega = 0$ for $T = 0.15$, as well as $T = 0.1$ in proximity of the AF pseudo-critical transition.

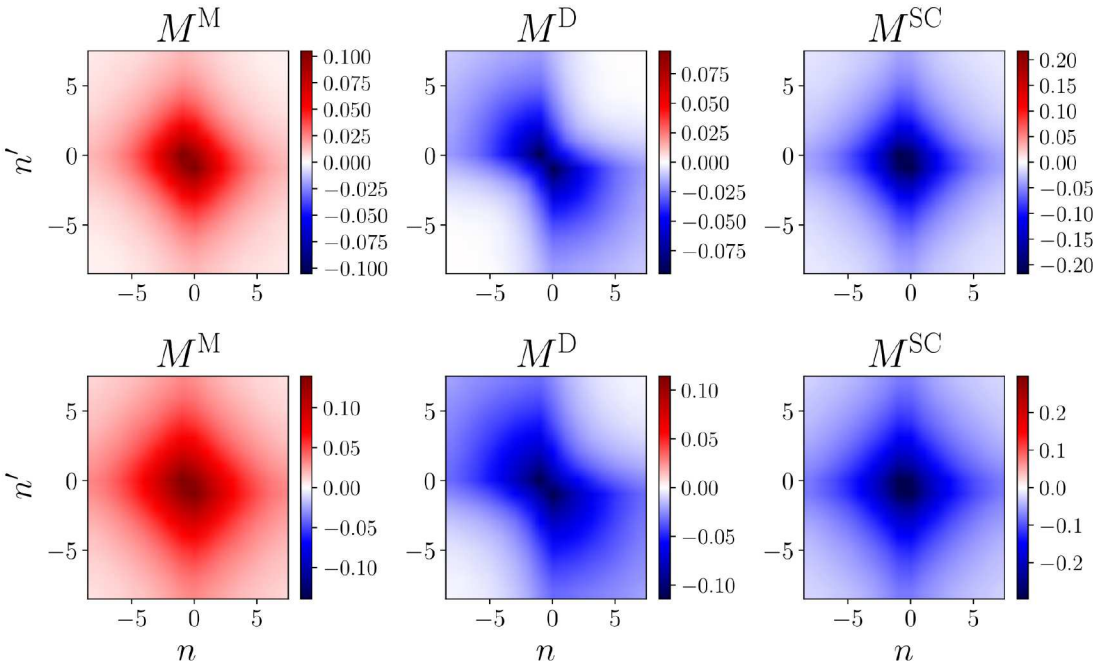

Figure 4.6: Rest functions for the magnetic $M^{\mathrm{M}}(\Omega = 0, \mathbf{q} = (\pi, \pi), \nu, m = 0, \nu', m' = 0)$, density $M^{\mathrm{D}}(\Omega = 0, \mathbf{q} = (0, 0), \nu, m = 0, \nu', m' = 0)$, and s-wave superconducting $M^{\mathrm{SC}}(\Omega = 0, \mathbf{q} = (0, 0), \nu, m = 0, \nu', m' = 0)$ channels at $T = 0.15$ (upper panels) and $T = 0.1$ (lower panels), with n and n' labeling the fermionic Matsubara frequencies according to $\nu^{(\prime)} = (2n^{(\prime)} + 1)\pi T$, for $U = 2$, $t' = 0$ and $\mu = 0$.

It highlights a key feature of the rest function: its characteristic decay to zero at large frequencies (which is particularly pronounced for larger values of the interaction [24]). This implies that the high-frequency asymptotics of the two-particle vertex functions is fully captured by the screened interactions w^η and the fermion-boson couplings λ^η.

Also this regime can thus be reliably described by the SBE scheme without rest function, which significantly reduces the numerical effort of the fRG flow. For the considered parameter regime, the gain in the run times for the computation without SBE rest function is ($\sim 3-4$ for $T = 0.1-0.15$), but most importantly the lower number of required momentum and frequency variables entails a better scaling.

Summarizing, it has been shown that in the SBE formulation of the fRG the contribution of the rest function is marginal, as long as the 1ℓ flow does not diverge. In proximity of the divergence it becomes relevant on a quantitative level, but does not qualitatively affect the physics. Thus, the U-reducible part of the two-particle vertex captures the physically relevant information near the pseudo-critical transition. The physical susceptibilities (as well as the self-energy, see following Section 4.2.4), can hence be reliably determined by the flow of the screened interactions and fermion-boson couplings, without including the rest function. This puts forward the SBE-based fRG as a computationally more efficient alternative to the conventional fermionic description. In Section 4.3 the validity of this finding at finite doping is examined, where superconducting correlations are expected to play a more prominent role.

Figure 4.18 illustrates a basic symmetry property of the rest functions, namely, the rest functions can be decomposed as

$$M^\eta(q,k,k') = M^{+,\eta}(q,k,k') + M^{-,\eta}(q,k,k'), \tag{4.1}$$

with $M^{+/-,\eta}$ being symmetric/antisymmetric with respect to the inversion of a single fermionic frequency, i.e.,

$$M^{\pm,\eta}(\Omega=0,\mathbf{q},\nu,\mathbf{k},\nu') = \frac{1}{2}\big[M^\eta(\Omega=0,\mathbf{q},\nu,\mathbf{k},\nu') \pm M^\eta(\Omega=0,\mathbf{q},-\nu,\mathbf{k},\nu')\big]. \tag{4.2}$$

In most situations, $M^{+,\eta}$ is the dominant contribution, which is clearly the case for M^{M} in Fig. 4.6.

4.2.4 Self-energy

The results for the self-energy, as obtained from the SBE formulation, are displayed in Fig. 4.7 for the representative parameters of $U = 2$ and $T = 0.15$ at half filling. The frequency dependence of the imaginary part presents a typical Fermi-liquid behavior at small frequencies, both at the node $\mathbf{k} = (\pi/2,\pi/2)$ in the left and at the anti-node $\mathbf{k} = (\pi,0)$ in the right panel. For these parameters the resulting self-energy does not develop a momentum-selective gap. The computation without rest functions M^η almost perfectly reproduces the full one including the rest function. The deviations of the order of a few per cent are maximal for the lowest Matsubara frequency $\Omega = \pi T$ and decrease for larger frequencies. On a quantitative level, in the full Green's function $G(\nu,\mathbf{k})$ the differences between the computation with and without rest function are almost negligible, due to the large ν contribution of the bare Green's function.

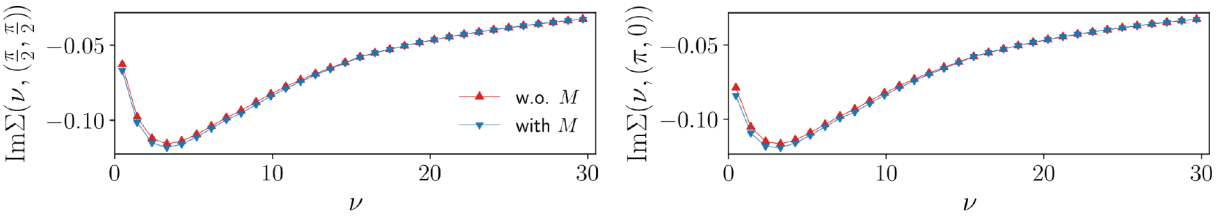

Figure 4.7: Imaginary part of the self-energy $\Sigma(\nu,\mathbf{k})$ at the node $\mathbf{k} = (\pi/2,\pi/2)$ and anti-node $\mathbf{k} = (\pi,0)$ for $U = 2$ and $T = 0.15$ ($t' = 0$, $\mu = 0$).

4.3 The SBE approximation at finite doping

In order to illustrate the validity of the SBE approximation in a physically more relevant parameter regime than the perfectly particle-hole symmetric case, results at finite doping are presented. Specifically, a next-nearest-neighbour hopping close to van Hove filling at $\mu = 4t'$ (due to the flow of the self-energy, the initial value of the chemical potential is renormalized during the flow), is considered for which the magnetic fluctuations are expected to be suppressed in favor of superconducting correlations. These are taken into

account by the flow of the d-wave components (and their interplay with the s-wave components) in the different channels. As in Section 4.2, the effects of the rest functions on the fermion-boson couplings and physical susceptibilities will be analysed, including also a comparison to the conventional fermionic formulation.

4.3.1 Fermion-boson couplings

The results for the fermion-boson couplings in all relevant channels are shown in Figs. 4.8 and 4.9, illustrating the (bosonic) momentum and frequency dependence of the real parts evaluated at the lowest fermionic Matsubara frequency $\nu = \pi T$, for $U = 2$, $t' = -0.2$, and different temperatures. The general shapes in the magnetic, density and s-wave superconducting channels resemble those of Figs. 4.1 and 4.2 at half filling. For the momentum dependence, λ^{M} and λ^{D} are suppressed in correspondence with the magnetic ordering wavevector $\mathbf{q} = (\pi, \pi)$, whereas $\lambda^{\mathrm{SC},s}$ falls off near the Γ-point. For the frequency dependence the reduction in the low-frequency regime results from the electronic screening. Lowering the temperature, these features become sharper.

An important difference to the previous study at half filling consists in the finite d-wave component $\lambda^{\mathrm{SC},d}$, which exhibits a slight dip between the Γ- and X-points (see Fig. 4.8). Further note that $\lambda^{\mathrm{SC}}(\Omega, \mathbf{q} = \mathbf{0}, \nu, n = d\text{-wave}) = 0$ for all bosonic frequencies due to the vanishing of all mixed form-factor bubbles at the Γ-point in a framework involving only s- and d-wave form factors [85]. This can be understood diagrammatically: the U-reducible part of the two-particle vertex in the d-wave superconducting channel involves the product

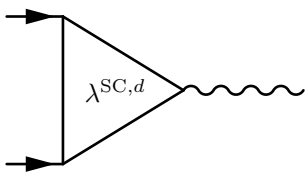

(4.3)

between the fermion-boson coupling $\lambda^{\mathrm{SC},d}$ and the screened interaction w^{SC}. Since the latter has only s-wave components, all contributions to (4.3) contain mixed bubbles with at least one propagator connecting different form factors, such as

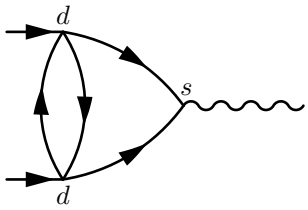

(4.4)

where the form factor indices are indicated explicitly and the fermionic propagators $G(\nu, \mathbf{k})$ are represented by solid lines. The reason why these mixed bubbles vanish exactly at the Γ-point ($\mathbf{q} = \mathbf{0}$) can be illustrated through the bare superconducting susceptibility

$$\left[\chi_0^{\mathrm{SC}}\right]_{mn}(\Omega, \mathbf{q}) = \sum_{\nu} \int \mathrm{d}\mathbf{k} f_n^*(\mathbf{k}) f_m(\mathbf{k}) G(\nu, \mathbf{k}) \times G(\Omega - \nu, \mathbf{q} - \mathbf{k}), \tag{4.5}$$

with m and n form factor indices. This simplest mixed bubble of interest for $m = 0$ and $n = 1 \neq m$ reads (for $\Omega = 0$)

$$\left[\chi_0^{\mathrm{SC}}\right]_{01}(\Omega = 0, \mathbf{q}) = \sum_{i\nu} \int \mathrm{d}\mathbf{k} (\cos(k_x) - \cos(k_y)) G(\nu, \mathbf{k}) \times G(-\nu, \mathbf{q} - \mathbf{k}), \tag{4.6}$$

where the s-wave $f_0(\mathbf{k}) = 1$ and d-wave $f_1(\mathbf{k}) = \cos(k_x) - \cos(k_y)$ form factors have been inserted. At $\mathbf{q} = \mathbf{0}$ the momentum integral in Eq. (4.6) vanishes exactly. This reasoning can be straightforwardly generalised to all mixed bubbles involving s- and d-wave form factors, such as that of Fig. (4.4).

Concerning the contribution of the rest function to the results for the fermion-boson couplings at finite doping, the relative difference between the results with and without rest function in the magnetic, density, and s-wave superconducting channels is below 2.2 % in both Figs. 4.8 and 4.9. Because of the zeros of $\mathbf{Re}\{\lambda^{\mathrm{SC}}\}(\Omega = 0, \mathbf{q}, \nu = \pi T, n = d\text{-wave})$, for the d-wave superconducting channel the absolute difference is considered, which does not exceed 10^{-4} for all temperatures. Hence, the overall contribution of the rest function to the fermion-boson couplings is still negligible in all channels.

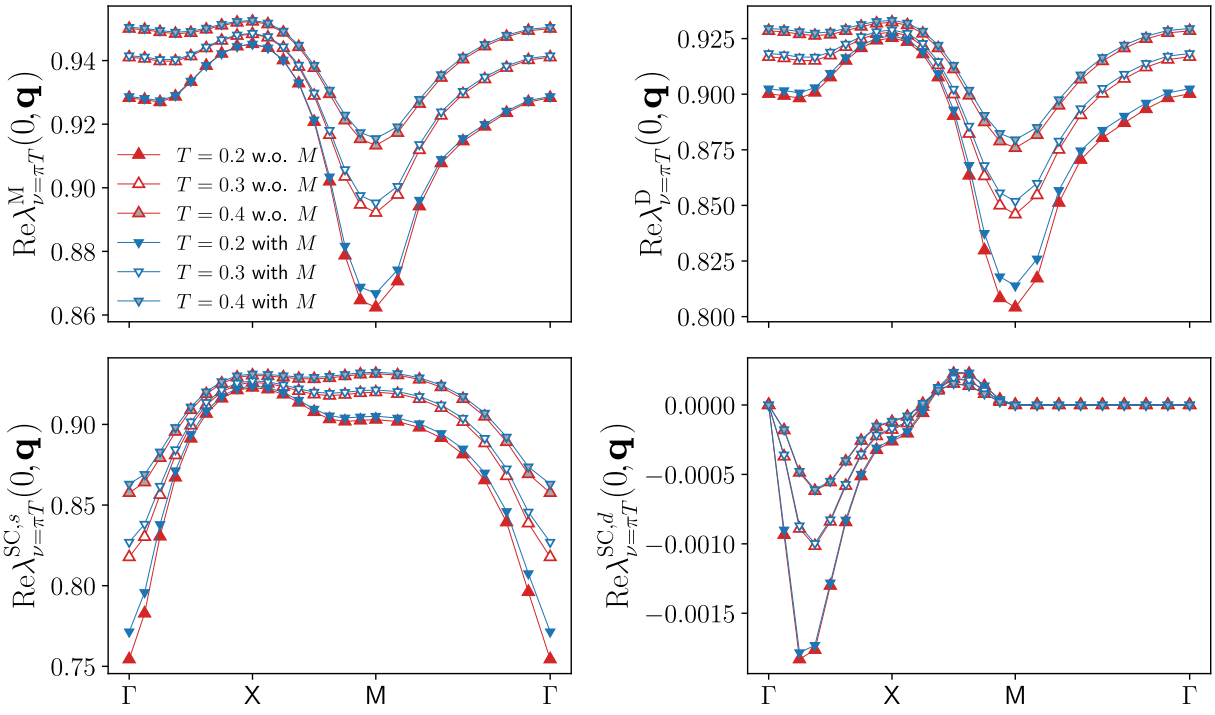

Figure 4.8: Momentum dependence of the static fermion-boson couplings for the magnetic $\lambda^{\mathrm{M}}(\Omega = 0, \mathbf{q}, \nu = \pi T, n = 0)$, density $\lambda^{\mathrm{D}}(\Omega = 0, \mathbf{q}, \nu = \pi T, n = s-\text{wave})$, and both $\lambda^{\mathrm{SC},s}(\Omega = 0, \mathbf{q}, \nu = \pi T, n = s-\text{wave})$ and $\lambda^{\mathrm{SC},d}(\Omega = 0, \mathbf{q}, \nu = \pi T, n = d-\text{wave})$ superconducting channel, as obtained from the SBE formulation of the fRG with (blue symbols) and without rest function (red symbols), for $U = 2$, $t' = -0.2$, $\mu = 4t'$, and different values of the temperature. At the end of the flow the filling equals 0.44 for all temperatures (with 0.5 corresponding to half filling), with or without rest function.

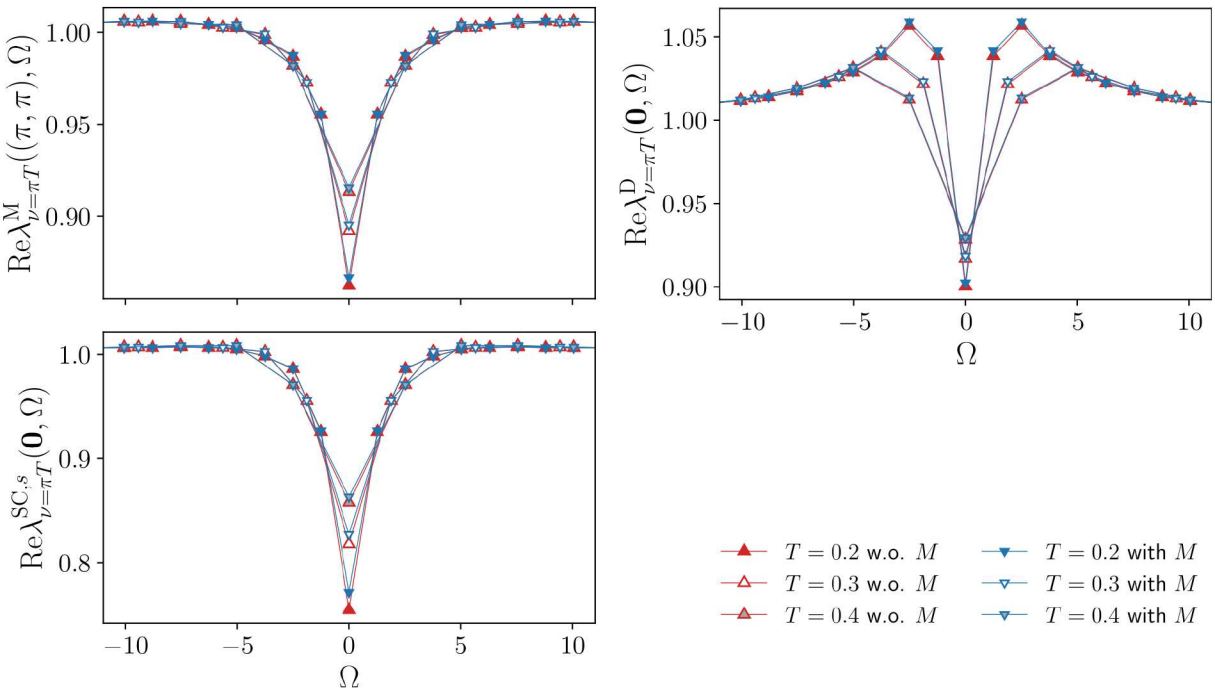

Figure 4.9: Frequency dependence of the fermion-boson couplings for the magnetic $\lambda^{\mathrm{M}}(\Omega, \mathbf{q} = (\pi,\pi), \nu = \pi T, n = 0)$, density $\lambda^{\mathrm{D}}(\Omega, \mathbf{q} = (0,0), \nu = \pi T, n = 0)$, and s-wave superconducting channel $\lambda^{\mathrm{SC}}_{\nu=\pi T}(\Omega, \mathbf{q} = (0,0), \nu = \pi T, n = 0)$ for the same parameters as in Fig. 4.8. Note that $\lambda^{\mathrm{SC}}(\Omega, \mathbf{q} = (0,0), \nu = \pi T, n = d\text{-wave}) = 0$.

4.3.2 Susceptibilities

Next, the physical susceptibilities are analysed. The results for the magnetic χ^{M}, density χ^{D}, and s-wave superconducting $\chi^{\mathrm{SC},s}$ static susceptibilities along the Γ-X-M-Γ path in the Brillouin zone are shown in Fig. 4.10, for the same parameters used for the fermion-boson couplings. The corresponding results for the frequency dependent susceptibilities are provided in Fig 4.11. The AF peak in the magnetic susceptibility appears reduced with respect to half filling, while the subleading density and s-wave superconducting susceptibilities exhibit a rather weak momentum dependence. The agreement of the results with and without rest function is also very good at finite doping (the deviations are below 1 % for all temperatures considered here), justifying the application of the SBE approximation.

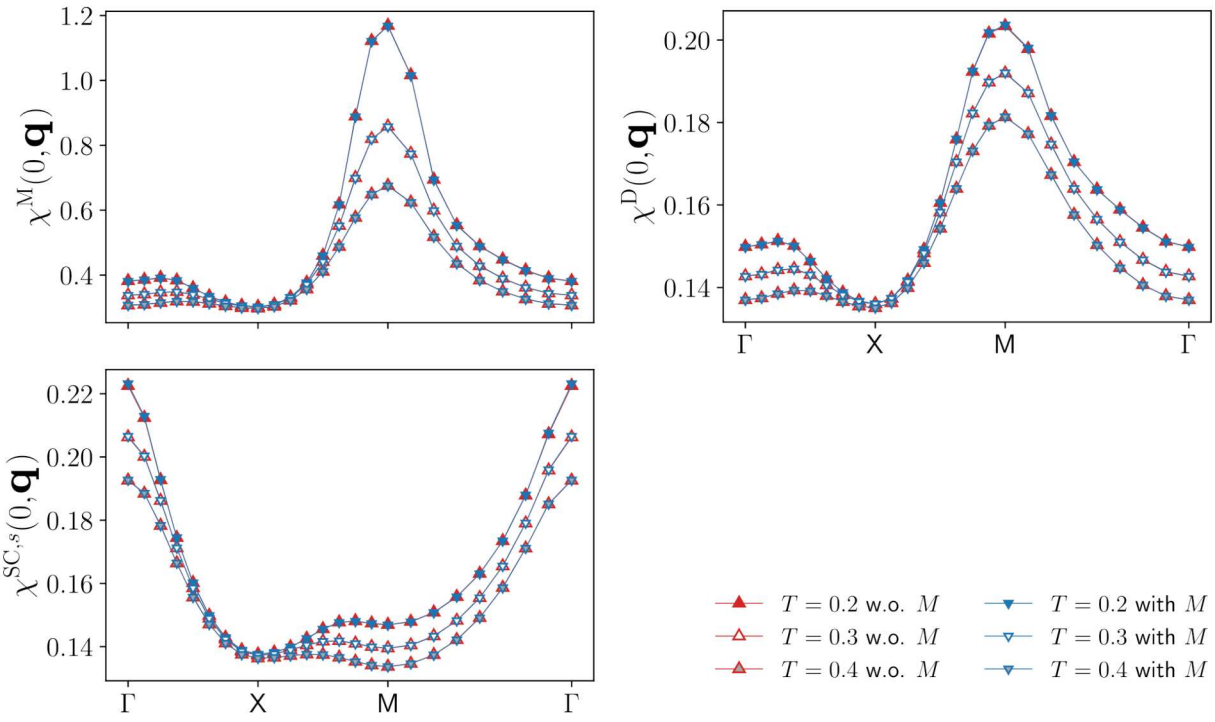

Figure 4.10: Magnetic $\chi^{\mathrm{M}}(\Omega = 0, \mathbf{q})$, density $\chi^{\mathrm{D}}(\Omega = 0, \mathbf{q})$, and s-wave superconducting static susceptibility $\chi^{\mathrm{SC},s}(\Omega = 0, \mathbf{q})$. The relative difference between the results with and without rest function is below 1 % for all temperatures in the magnetic, density, and s-wave superconducting channels. Data obtained from the SBE formulation of the fRG with and without rest function, for the same parameters as in Fig. 4.8.

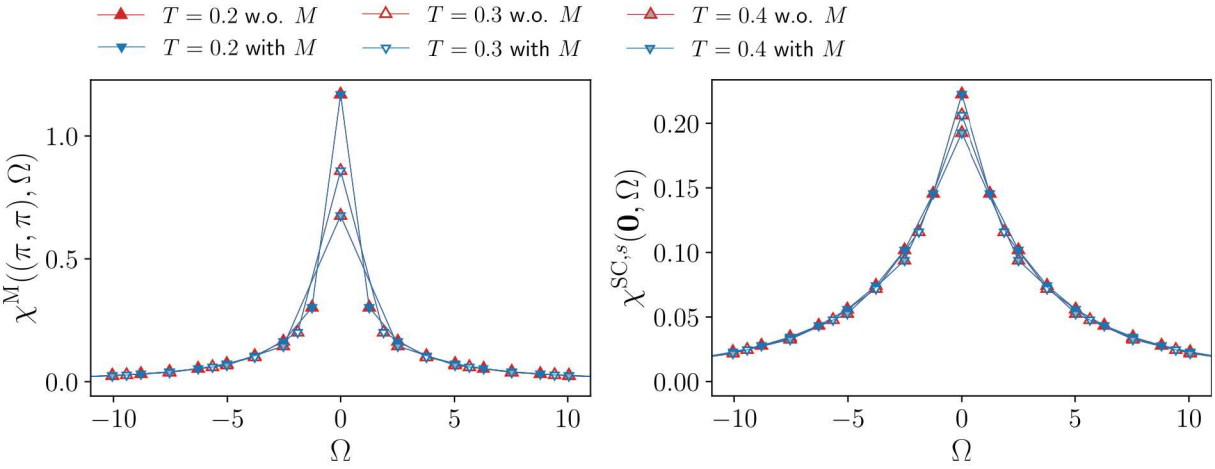

Figure 4.11: Bosonic frequency dependence of the magnetic χ^{M} and superconducting χ^{SC} susceptibilities for the same parameters as in Fig. 4.8. The relative difference between the results with and without rest function is always below 4% in both the magnetic and s-wave superconducting channels.

The corresponding d-wave superconducting $\chi^{\mathrm{SC},d}$ susceptibility displayed in Figure 4.12 cannot be determined from the (s-wave) screened interaction as above and is obtained by postprocessing using Eq. (5.1). Note that for the s-wave susceptibilities the differences to the postprocessing results that arise at the 1ℓ level are the same as the ones observed in the conventional fermionic fRG [30] (for details on the (dis-)agreement of flowing and postprocessing results see Section 5.2). For the considered parameters at $U = 2$ the d-wave superconducting susceptibility appears to be well described by the bare bubble contribution χ_0, shown for the lowest temperature $T = 0.2$. Compared to the results from the full computation, the vertex corrections turn out to be very small (and consequently also the ones due to

inclusion of the rest function), with an appreciable contribution only around the Γ-point. Moreover, the absolute values of $\chi^{\mathrm{SC},d}$ are not very large with respect to the dominating magnetic channel of Fig. 4.10, but the peak at $\mathbf{q} = (0,0)$ is expected to increase and become more pronounced for larger values of U, as well as at lower temperatures. A detailed analysis of the vertex' contribution to $\chi^{\mathrm{SC},d}$, including its temperature dependence, is performed in Chapter 5.

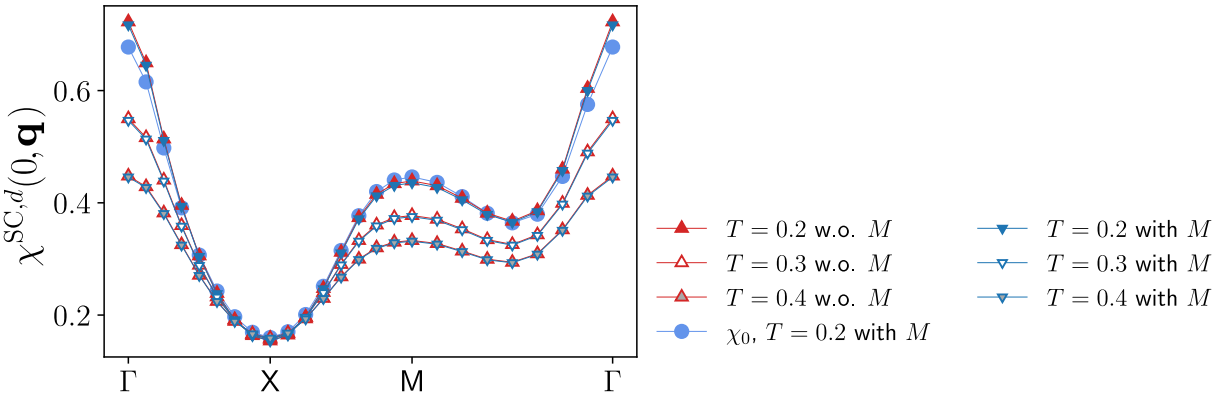

Figure 4.12: Momentum dependence of the d-wave superconducting susceptibility $\chi^{\mathrm{SC},d}$, determined from postprocessing with and without rest function, for the same parameters as in Fig. 4.8. The relative difference between the results with and without rest function is below 1 % for all temperatures. Additionally, results for the bare bubble contribution χ_0 are provided for $T = 0.2$. There, the relative difference between the full d-wave superconducting susceptibility and its bare bubble contribution reaches 5 % at the Γ-point (with or without rest function), which decreases for larger temperatures.

The small differences between the results with and without rest function in the d-wave superconducting susceptibilities demonstrate that the SBE effective interactions correctly account for the vertex corrections in this parameter regime. These can be inferred from the difference to the respective bubble contribution χ_0, reaching a relative difference of 15 % (13 %) at the Γ-point for $t' = -0.2$ ($t' = -0.25$). In this parameter regime the vertex corrections originate in the s-wave contributions. In fact, the computation with only an s-wave form factor yields no visible difference in the results (Fig. 4.13).

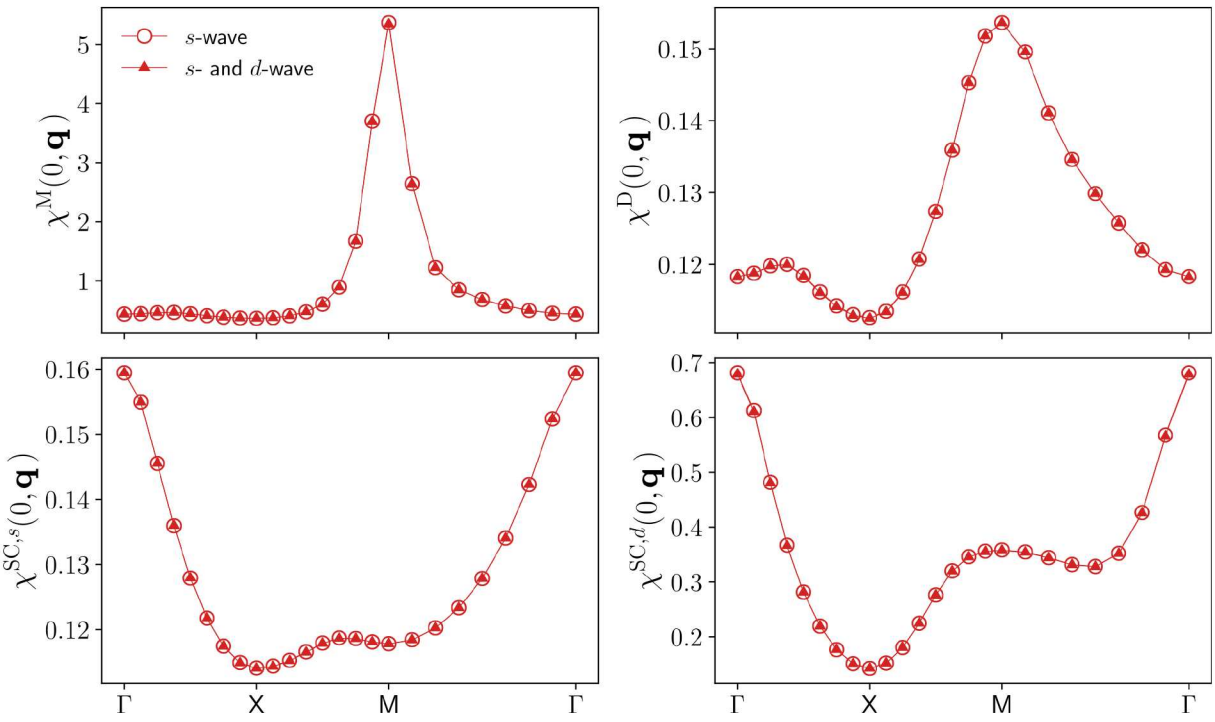

Figure 4.13: χ^{η} calculated with only s-wave (open circles) and $s+d$-wave form factors (triangles), $T = 0.2, t' = -0.2, U = 3, \mu = 0.8$. $\chi^{\mathrm{SC},d}$ is calculated via postprocessing.

A more detailed analysis may be obtained from a fluctuation diagnostics [86, 87, 88], as performed in Chapter 5. Finally, let it be remarked that, in contrast to the d-wave superconducting susceptibility, for the magnetic susceptibility the vertex corrections dominate the physical behavior and exceed the bubble contribution (see Section 5.3), by far.

Figure 4.20 shows the results for the most relevant magnetic and d-wave superconducting susceptibilities as a function of momentum for $U = 3$ and, in addition to a next-nearest-neighbour hopping of $t' = -0.2$, also for $t' = -0.25$ (at van Hove filling). Compared to the results for $U = 2$ (for $t' = -0.2$), an enhanced tendency towards magnetic ordering is detected. At the same time, changing the value of the next-nearest-neighbour hopping to $t' = -0.25$ induces a reduction of the AF peak. Also, a trend towards an incommensurate peak is observed, as expected for larger dopings [36, 89, 90, 91]. In contrast, the d-wave pairing susceptibility is almost invariant under these changes. The considered parameter regime is still far away from any instability and the d-wave pairing susceptibility is expected to increase only at lower temperatures (see Section 5.4 for a detailed analysis). Due to the increasing computational cost, the superconducting transition temperature is currently not accessible. Including the flow of the fermionic rest functions M^{η} (for which the SBE approach is equivalent to the conventional fRG formalism based on the 1PI vertex function), leads to slightly larger corrections as for $U = 2$, but still below 4 %.

It can thus be concluded that in the entire weak- to intermediate-coupling regime the susceptibilities obtained without M^{η} correctly describe the physical behavior, confirming the reliability of a description in terms of the SBE effective interactions. On a practical level, this means that the momentum and frequency dependence of the two-particle vertex can be efficiently parametrised by ∇^{η}, i.e., through the screened interactions and fermion-boson couplings (with the exception of the pseudo-critical transition, where the weak-coupling approximation breaks down and quantitatively accurate results are not feasible, even by taking into account the rest function). Finally, the importance of the d-wave form factor is shown in Fig. 4.14.

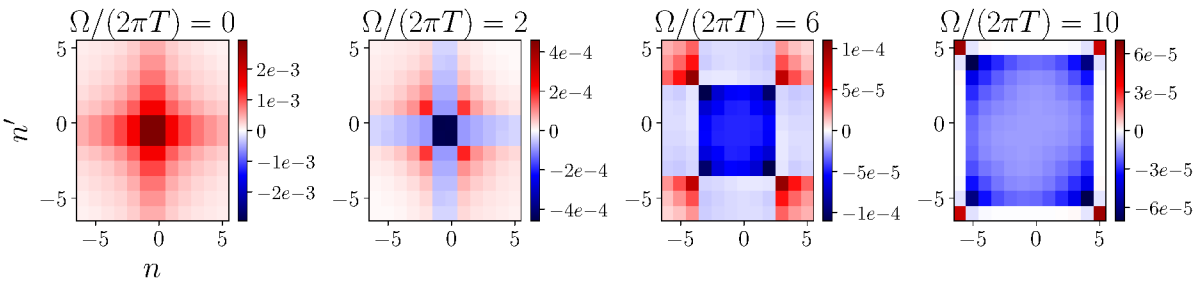

Figure 4.15: Rest function $M^{\mathrm{SC}}(\Omega, \mathbf{q} = (0,0), \nu, m = d\text{-wave}, \nu', m' = d\text{-wave}) = \phi^{\mathrm{SC},d}(\Omega, \mathbf{q} = (0,0), \nu, m = d\text{-wave}, \nu', m' = d\text{-wave})$ in the d-wave pairing channel, with n and n' labeling the fermionic Matsubara frequencies according to $\nu^{(\prime)} = (2n^{(\prime)} + 1)\pi T$, for $U = 2$, $t' = -0.2$, $\mu = 4t'$, and different choices of the bosonic frequency Ω.

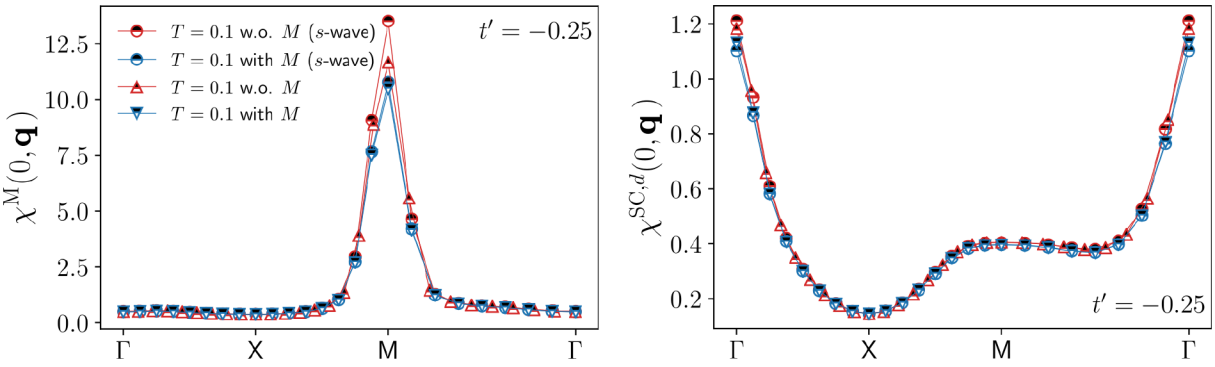

Figure 4.14: Data obtained with only an s-wave form factor (circles) compared to $s + d$-wave (triangles) at $T = 0.1, t' = -0.25, U = 2, \mu = 0.8$. The former overestimates the results compared to the latter. While the relative difference δ in the magnetic channel between results with and without rest function is < 2 % for the $s + d$-wave data, it increases to 14 % when using only an s-wave form factor.

4.3.3 Rest function

As discussed in the previous section (and in more detail in Section 5.4), a divergence of χ^{SC} must be driven by the value of Φ^{SC} at $\mathbf{q} = (0,0)$. As $\lambda^{\mathrm{SC},d} = 0$ at this momentum vector, $\Phi^{\mathrm{SC},d} = M^{\mathrm{SC},d}$ whose momentum dependence is displayed in Figs. 4.15 and 4.16 for $U = 2$ and $U = 3$ respectively. Unsurprisingly, as the rest functions were already established to be negligible in this parameter regime in the previous sections, the absolute values of $M^{\mathrm{SC},d}$ are vanishingly small, marking the regime as being far from a superconducting phase. Note however, that the maximum does increase by an order of magnitude for $U = 3$ compared to $U = 2$ hinting at the rest function possibly becoming relevant for larger couplings. Thus the validity of the SBE approximation may be cast in physical language: as long as AF dominates over superconducting tendencies (or indeed other ordering tendencies not well captured by single-boson exchange processes) neglecting the rest function yields reliable results. However, to capture the competition between the two in more challenging regimes, the multiboson processes are expected to become necessary even for qualitatively correct data.

4.4 Comparison of approximations

4.4.1 SBE approximation versus neglecting the high-frequency asymptotics rest function

The convenience of the SBE formulation also emerges from the direct comparison with data obtained from the conventional fermionic fRG. Figure 4.17 provides the results for the leading magnetic susceptibility as a function of both the (bosonic) momentum and frequency, for $U = 2$ and $T = 0.15$. At the maximum at

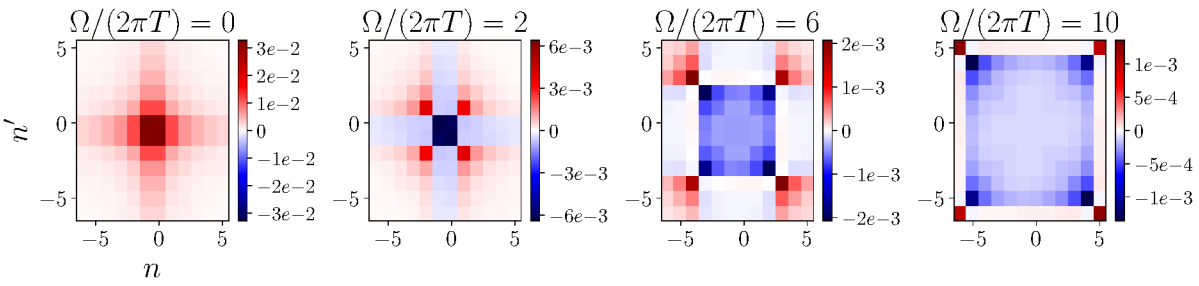

Figure 4.16: Same as Fig. 4.15 with $U = 3$ instead. Note the increase of one order of magnitude in the absolute values as compared to Fig. 4.15.

$\mathbf{q} = (\pi, \pi)$ and $\Omega = 0$, the relative difference between the results with and without rest function reported in the insets is about 10 times smaller in the SBE decomposition with respect to the one in the conventional fermionic formulation, while away from it, the contribution of both (SBE and conventional fermionic fRG) rest functions rapidly decay. Both 1ℓ results agree exactly, confirming that the SBE algorithm was implemented correctly and convergence in numerical parameters was reached in both cases. Away from the AF-peak in momentum space and at finite bosonic frequencies all four agree very well, the differences are concentrated on the AF-peak. In particular, the effect of the SBE rest function is marginal in the whole momentum and frequency range, in contrast to the conventional fRG implementation. In the following, an explanation for this discrepancy will be provided by comparing the respective rest functions in detail.

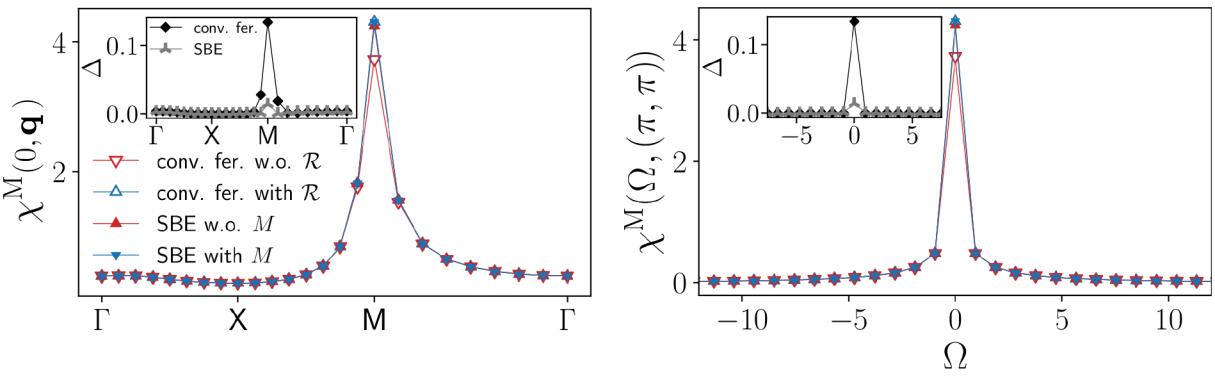

Figure 4.17: Bosonic momentum and frequency dependence of the magnetic susceptibility χ^{M}, as obtained from the SBE and conventional fermionic fRG formulation with and without rest function, for $U = 2$ and $T = 0.15$ ($t' = 0$, $\mu = 0$). The insets show the relative difference Δ between results with and without rest function.

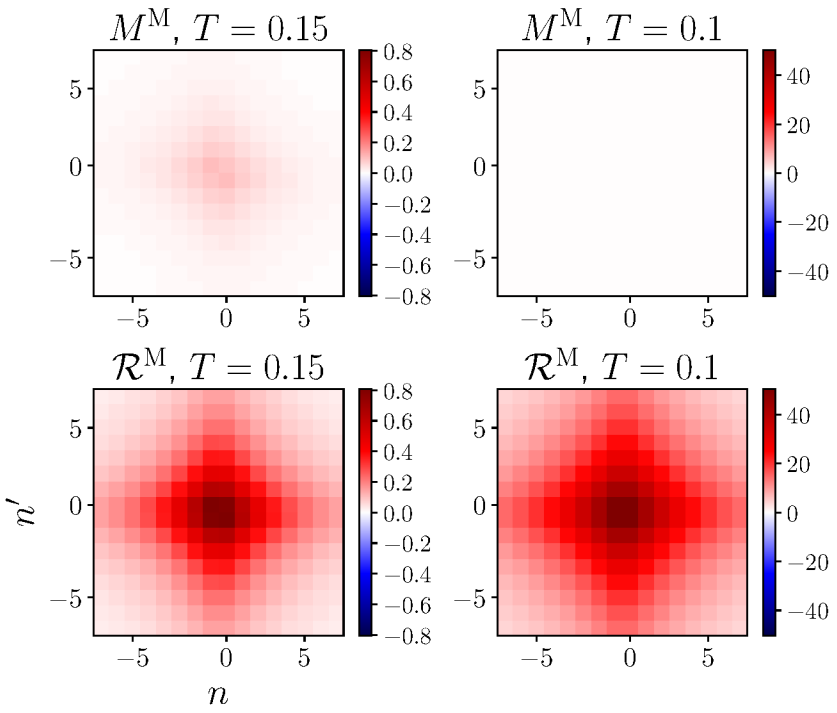

Figure 4.18: Rest function $M^{\mathrm{M}}(\Omega = 0, \mathbf{q} = (\pi, \pi), \nu, m = 0, \nu', m' = 0)$ in the magnetic channel, as obtained from the SBE (upper panels) and the Wentzell asymptotics fRG formulation (lower panels), with n and n' labeling the fermionic Matsubara frequencies according to $\nu^{(\prime)} = (2n^{(\prime)} + 1)\pi T$, for $U = 2$ and $T = 0.1$ and $T = 0.15$ ($t' = 0$, $\mu = 0$). Note that the SBE rest function almost vanishes in comparison.

Comparing the results for the SBE and the conventional fermionic decompositions in Fig. 4.18 a marked difference in the absolute values of the rest functions becomes apparent. For $T = 0.15$ the SBE rest function is almost an order of magnitude smaller, with $M(\Omega = 0, \mathbf{q} = (\pi, \pi), \nu, n = 0, \nu', m = 0) \ll \mathcal{R}(\Omega = 0, \mathbf{q} = (\pi, \pi), \nu, n = 0, \nu', m = 0)$ for the maximal values. As seen in Fig. 4.17, it is in fact essential to include the contribution of the rest function in the conventional fermionic fRG, while in the SBE formulation it leads only to minor corrections. This discrepancy is further enhanced as the temperature is lowered down to $T = 0.1$, due to the dramatic increase of $\mathcal{R}^{\mathrm{M}}$ in proximity of the pseudo-critical transition. In contrast, M^{M} is of the same order as for $T = 0.15$ (see Fig. 4.6). The difference between M^{M} and $\mathcal{R}^{\mathrm{M}}$ can be traced back to the (magnetic) screened interaction: according to $\mathcal{R}^{\mathrm{M}} = (\lambda^{\mathrm{M}} - 1)w^{\mathrm{M}}(\lambda^{\mathrm{M}} - 1) + M^{\mathrm{M}}$ (see Eq. (3.17)), the increase of $\mathcal{R}^{\mathrm{M}}(\Omega = 0, \mathbf{q} = (\pi, \pi), \nu, n = 0, \nu', m = 0)$ is absorbed by its U-reducible part, specifically by the growing screened interaction, while the SBE rest function stays small even in the vicinity of the pseudo-critical transition. Figure 4.19 shows an example of such a U-reducible diagram of the type $(\lambda^{\mathrm{M}} - 1)w^{\mathrm{M}}(\lambda^{\mathrm{M}} - 1)$ included in $\mathcal{R}^{\mathrm{M}}$ but not M^{M}.

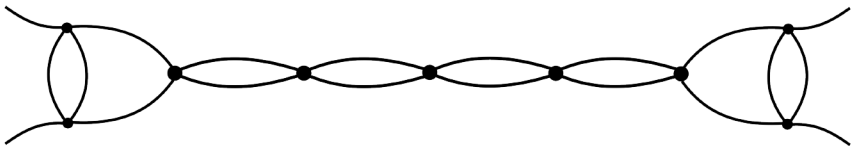

Figure 4.19: Example of a diagram included in $\mathcal{R}$ but not part of M.

Note that despite M^{M} showing no sign of a divergence at $T = 0.1$ the results of the SBE approximation are still quantitatively incorrect.

Calculating the susceptibilities via the postprocessing equation

$$\chi^{\mathrm{M}} = \chi_0^{\mathrm{M}} + \chi_0^{\mathrm{M}} V^{\mathrm{M}} \chi_0^{\mathrm{M}} \tag{4.7}$$

shows that the direct contribution of the rest function is negligible, as the rest function contribution to V^{M} is vanishingly small. Close to the AF-divergence, feedback between different objects such as

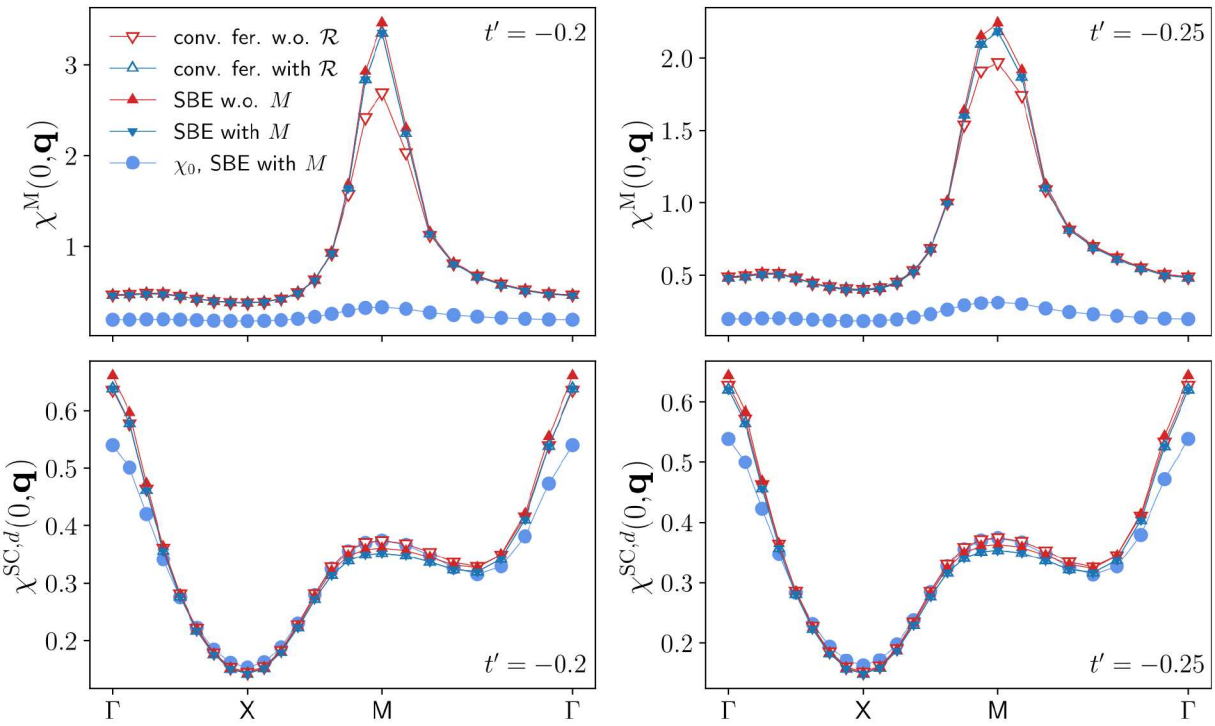

Figure 4.20: Magnetic $\chi^{\mathrm{M}}(\Omega = 0, \mathbf{q})$ and d-wave superconducting static susceptibility $\chi^{\mathrm{SC},d}(\Omega = 0, \mathbf{q})$, including both the results obtained from the SBE and the conventional fermionic fRG formulation of the fRG with and without rest function, for $U = 3$ and $t' = -0.2$ (left panels) and $t' = -0.25$ (right panels), with $\mu = 4t'$, and $T = 0.2$. At the end of the flow the filling equals 0.45 and 0.44 at $t' = -0.2$ and $t' = -0.25$ respectively, for both the SBE and conventional fermionic decompositions, with or without rest function. Note that $\chi^{\mathrm{M}}(\Omega = 0, \mathbf{q})$ is determined from the screened interaction, whereas $\chi^{\mathrm{SC},d}(\Omega = 0, \mathbf{q})$ from postprocessing. The relative difference between the data with and without rest function is always below 4 % for the SBE decomposition. For the conventional fermionic fRG, however, this relative difference reaches 20 % (10 %) in the magnetic and 6 % (6 %) in the superconducting channel for $t' = -0.2$ ($t' = -0.25$). Results for the bare bubble contribution χ_0 to the susceptibilities are shown as well.

the self-energy and bosonic propagators becomes very strong and any slight changes to the algorithm and approximations to the flow equations can cause different outcomes, indicating that the method is approaching the edge of its applicable parameter regime. Even though the SBE approximation is not applicable, if quantitatively correct results are needed in this regime, the SBE decomposition still has the advantage as numerical convergence in frequencies of the rest function is faster than for the Wentzell asymptotics rest function.

These observations are not limited to half filling: at finite doping, for $U = 3$ and different t's, the same picture emerges. While the SBE approximation gives quantitatively correct results away from the AF divergence, neglecting the Wentzell rest function leads to qualitatively correct, but quantitatively unreliable results.

4.4.2 SBEa versus SBEb approximation

As detailed in Section 3.3.3, neglecting the flow of the rest function after deriving the flow equations (SBEa approximation) and setting the rest function to zero prior to deriving the flow equations (SBEb approximation), though similar in spirit, are not equivalent. In Fig. 4.21 susceptibilities are compared using the SBEa/b approximation and parquet decomposition based algorithm without the high-frequency rest function. The SBEb approximation yields results that capture the correct qualitative behaviour, but fails at a quantitative level. In fact the AF-peak is underestimated even more than when neglecting $\mathcal{R}^{\eta}$. While the SBEb could be seen as a first step beyond RPA towards SBEa, the data shows that it underestimates rather than overestimates the AF-peak as both RPA and SBEa (though only slightly) do. Without self-energy feedback, which makes the setup more comparable to RPA, SBEb yields lower peak

values than both RPA and SBEa. Disentangling the exact effect of different types of diagrams is highly challenging, due to the complex feedback between different quantities. This raises the question how the SBEb multiloop AF-peak value compares to the SBEa multiloop and multiloop result including the rest function. In particular, does the SBEb also yield lower results at higher loop order (which would indicate observance of the Mermin-Wagner theorem)?

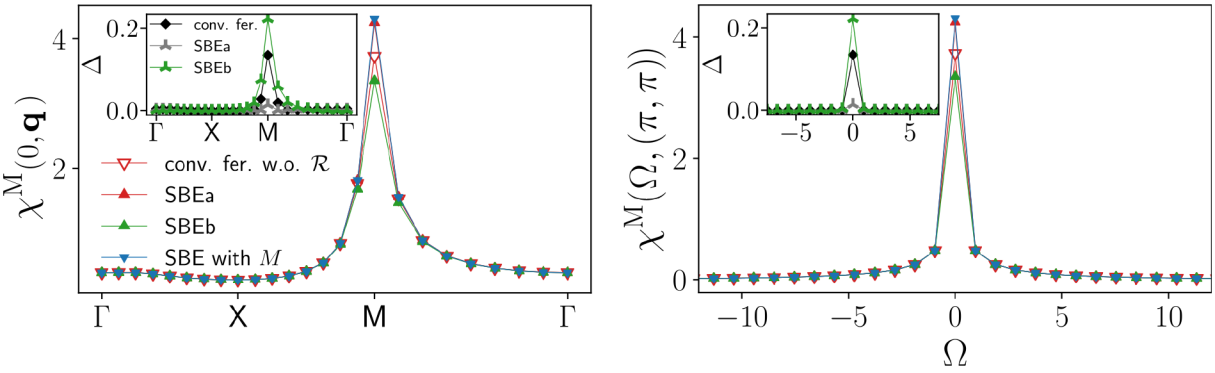

Figure 4.21: Bosonic momentum and frequency dependence of the magnetic susceptibility χ^{M}, as obtained from the SBE with rest function, SBEa/b, and conventional fermionic fRG formulations with and without rest function, for $U = 2$ and $T = 0.15$ ($t' = 0$, $\mu = 0$). The insets show the relative difference Δ between results with and without rest function.

4.4.3 Neglecting the flow of the fermion-boson couplings

Setting the flow of the fermion-boson coupling to zero on top of neglecting the rest function results in calculating only ladder diagrams for the single-boson propagator with the simplified flow equation Eq. (3.37). Without the self-energy flow this would correspond to doing an RPA calculation.

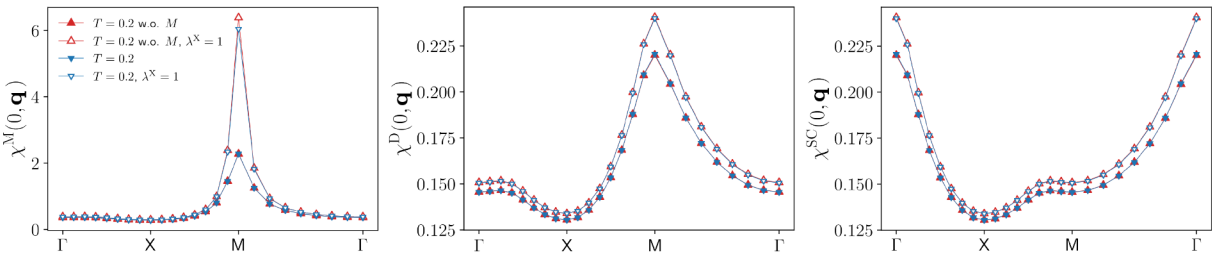

Figure 4.22: Magnetic $\chi^{\mathrm{M}}(\Omega = 0, \mathbf{q})$, density $\chi^{\mathrm{D}}(\Omega = 0, \mathbf{q})$, and s-wave superconducting $\chi^{\mathrm{SC}}(\Omega = 0, \mathbf{q})$ static susceptibilities, for $U = 2$ and $T = 0.2$ ($t' = 0$, $\mu = 0$), see also Fig. 4.4 for comparison. Data as obtained from the SBE formulation of the fRG (with rest functions), where the flow of the fermion-boson couplings has been discarded, i.e., by fixing $\lambda^{\eta} = 1$ throughout the flow. The relative difference between the results obtained with and without imposing this condition reaches 9 % in both the density and superconducting channels, and 165 % in the magnetic one. Including the rest function does not alter these findings.

A fermion-boson coupling fixed to 1 leads to an increased $\chi^{\eta}(\Omega = 0)$, as in general $\lambda^{\eta}(\Omega = 0) < 1$, which renormalizes $w^{\eta}(\Omega = 0)$. Results for χ^{η} with and without the flow of λ^{η} are compared in Fig. 4.22. Neglecting the flow of the fermion-boson coupling has a much stronger effect than neglecting the rest function.

4.5 Extended Hubbard model

In Section 3.5 we discussed how to apply the concept of the SBE to the extended Hubbard model and its non-local interaction. Due to the favourable numerical scaling and physical insights into the relevant collective excitations, the natural bosonization introduced in Section 3.5.2 was chosen for the implementation.

First, the importance of the now non-trivial high-frequency asymptotics and rest function, as well as the necessity of including the full first shell of form factors, are analysed in Section 4.5.1. Armed with an understanding of which approximations are permissible first, data investigating the influence of the non-local interaction V on the physics at half filling are presented in the following Section 4.5.2.

4.5.1 Implementation and approximations

The increase in form factors that are necessary to include even the bare interaction correctly along with the additional non-trivial high-frequency asymptotics, result in a drastic increase of run times. Approximations are necessary to venture into the regions of parameter space of physical interest. In this chapter several possible approximations resulting in reduced numerical effort are inspected and evaluated based on the reduction of run times balanced against loss of accuracy. We perform this analysis at $U = 2, V = U/4, T = 0.2$ and $\mu = 0$[2] and use numerical parameters $n = 6, k_x = 12$ and p_x, according to Table 4.1. As run times including high-frequency asymptotics and rest functions with the full first shell of form factors are well beyond feasible (on the order of months), we test their relevance separately. Neglecting the non-trivial high-frequency asymptotics in practice means using $\lambda^\eta = \lambda^{\eta,\text{init}}$ outside the frequency box and setting $M^\eta_{1/2} = \mathcal{I}^\eta_{\text{ferm}}$ for all values.

Mixed bubbles

Bubbles $\Pi_{l,l'}$ with $l \neq l'$ are referred to as 'mixed bubbles' and are generally significantly smaller than their counterparts with $l = l'$. This observation prompts a simplification of the flow of the bosonic propagator

$$\dot{w}^\eta(\Omega, \mathbf{q}) = w^\eta(\Omega, \mathbf{q}) \sum_{\nu l l'} \lambda^\eta(\Omega, \mathbf{q}, \nu, l) \dot{\Pi}^\eta(\Omega, \mathbf{q}, \nu, l, l') \lambda^\eta(\Omega, \mathbf{q}, \nu, l') w(\Omega, \mathbf{q}) \tag{4.8}$$

$$\approx w^\eta(\Omega, \mathbf{q}) \sum_{\nu l} \lambda^\eta(\Omega, \mathbf{q}, \nu, l) \dot{\Pi}^\eta(\Omega, \mathbf{q}, \nu, l, l) \lambda^\eta(\Omega, \mathbf{q}, \nu, l) w^\eta(\Omega, \mathbf{q}), \tag{4.9}$$

which transforms the scaling of $\dot{w}^\eta$ from quadratic to linear in the number of form factors. Figure 4.23 shows the minimal effect (< 0.1 % at $T = 0.2, U = 2, V = U/4$, half filling) this approximation has on the results. The flow of the rest function, including the flow of its high-frequency asymptotics, as well as the non-trivial high-frequency behaviour of λ^η, have been neglected here. The fermion-boson couplings are even less affected due to the approximation entering only indirectly (not shown). However, since the approximation rests on a general observation on the properties of mixed bubbles, it is fair to assume that the presence or absence of high-frequency asymptotics and rest functions cannot alter the validity of said approximation notably. As a default going forward we use the data set labelled as $l = l'$ in Fig. 4.23.

[2] At the end of the flow the doping is $\delta \approx 4$ % hole doping, due to the flow of $\Re\Sigma$.

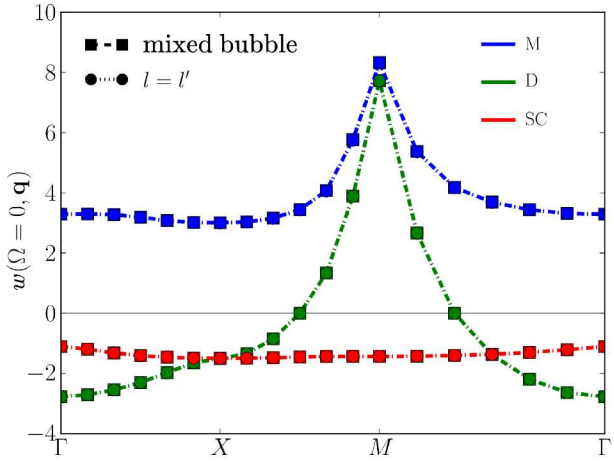

Figure 4.23: Bosonic propagator w^η calculated with and without mixed bubbles. At $T = 0.2, U = 2, V = U/4$, half filling with a local and full first shell of form factors. The non-trivial high-frequency asymptotics and the flow of the rest function are neglected.

Fermion-boson coupling high-frequency asymptotics λ^{asympt}

In the natural bosonization formulation non-trivial high-frequency behaviour of the fermion-boson couplings arises as a consequence of moving parts of the bare interaction that depend on fermionic momenta from the bosonic propagator to λ^η and M^η. The high-frequency asymptotics $\lambda^{\eta,\text{asympt}}$, M_1^η, and M_2^η are calculated in analogy to the fermionic high-frequency asymptotics of the two-particle reducible vertex functions, as explained in Section 3.2.5. Fortunately, as Fig. 4.24 shows, the influence of $\lambda^{\eta,\text{asympt}}$ on the bosonic propagator is negligible (< 1 %) and even smaller (< 0.1 %) on $\lambda^\eta_{s-\text{wave}}$ itself (Fig. 4.25, left panel). For the non-local form factors of the first shell the relative difference in the fermion-boson coupling is much larger (up to 15 %), however, in absolute terms $\lambda^\eta(l > 0) \ll \lambda^\eta(s\text{-wave})$ the difference is orders of magnitude smaller. If w^η and $\lambda^\eta(s\text{-wave})$ are the objects of interest, the non-trivial high-frequency asymptotics need not be included. For completeness the frequency dependence of λ^η, with and without the inclusion of high-frequency asymptotics beyond $\lambda^{\eta,\text{asympt}} = 1$, is reported in Appendix C.2. To avoid repetition a thorough discussion of λ^{asympt} and Fig. 4.25 is deferred to Section 4.5.1.

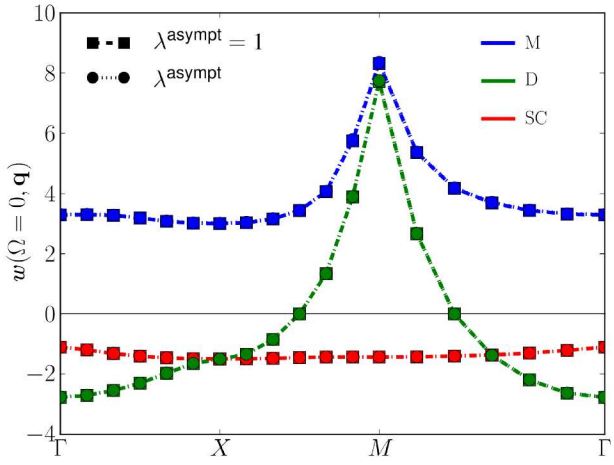

Figure 4.24: Bosonic propagator w^η calculated with and without high-frequency asymptotics λ^{asympt}.

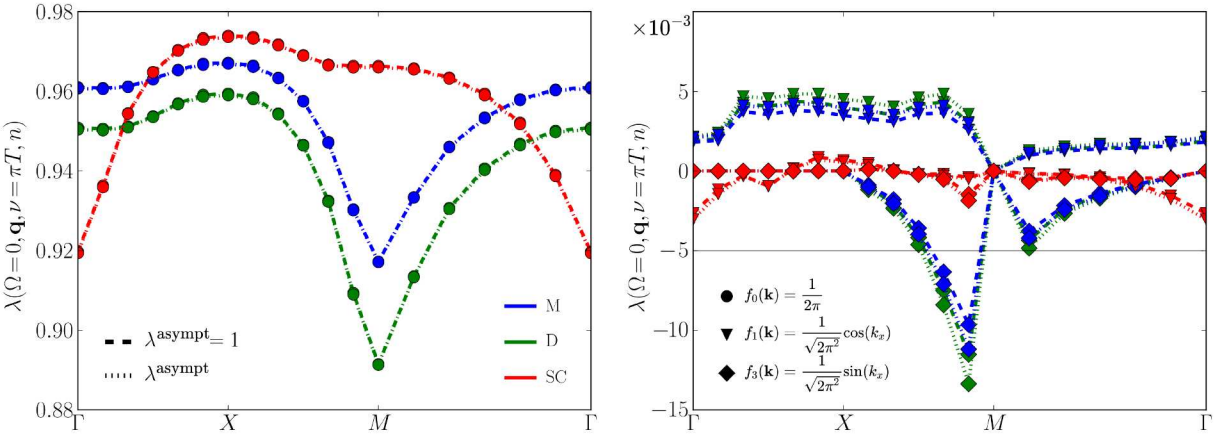

Figure 4.25: Fermion-boson coupling λ^η calculated with and without high-frequency asymptotics $\lambda^{\eta,\text{asympt}}$.

Rest function asymptotics M_1 and M_2

To keep the run times to a reasonable length, the non-trivial high-frequency asymptotics of λ^η are neglected, and M_1^η and M_2^η are treated individually. The influence of the high-frequency asymptotics of the rest functions M_1^η and M_2^η is shown in Fig. 4.26. The inclusion of the flow of M_1^η and M_2^η leads to corrections of less than 1 %. Note that the initial value of $M_{1/2}^\eta = \mathcal{I}_{\text{ferm}}^\eta$ and thus the rest function asymptotics are not small. However, their influence on w^η and the s-wave component of $\lambda^\eta(s\text{-wave})$, is, similar to $\lambda^{\eta,\text{asympt}}$.

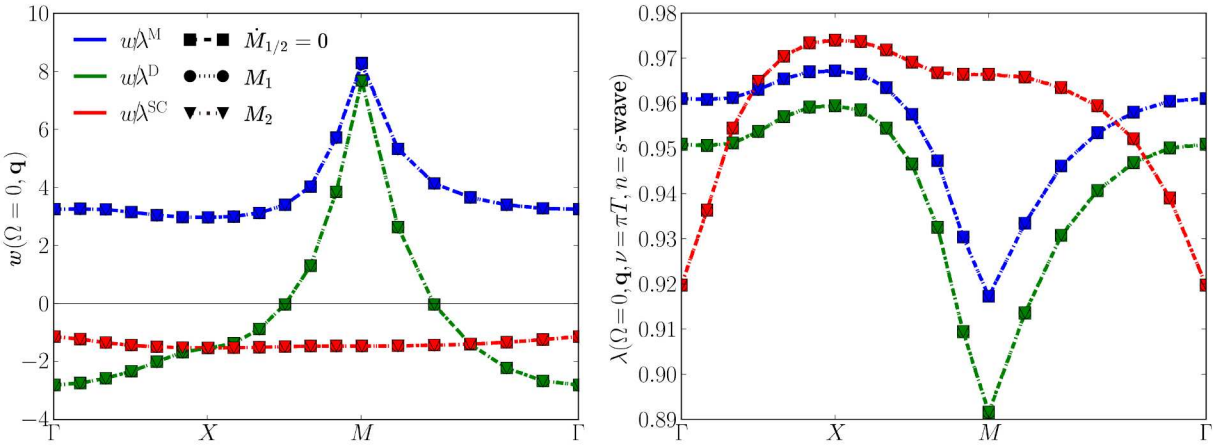

Figure 4.26: Rest function asymptotics M_1^η and M_2^η. $\dot{M}_{1/2}^\eta = 0$ is equivalent to $l = l'$ of Fig. 4.23. Note that the rest function is also approximated by $M_{1/2}$ here at low frequencies.

Form factors

The greatest source of increased numerical effort of the extended compared to the local Hubbard model is the jump from one form factor at half filling (two at higher dopings) to five in the extended model even at half filling.

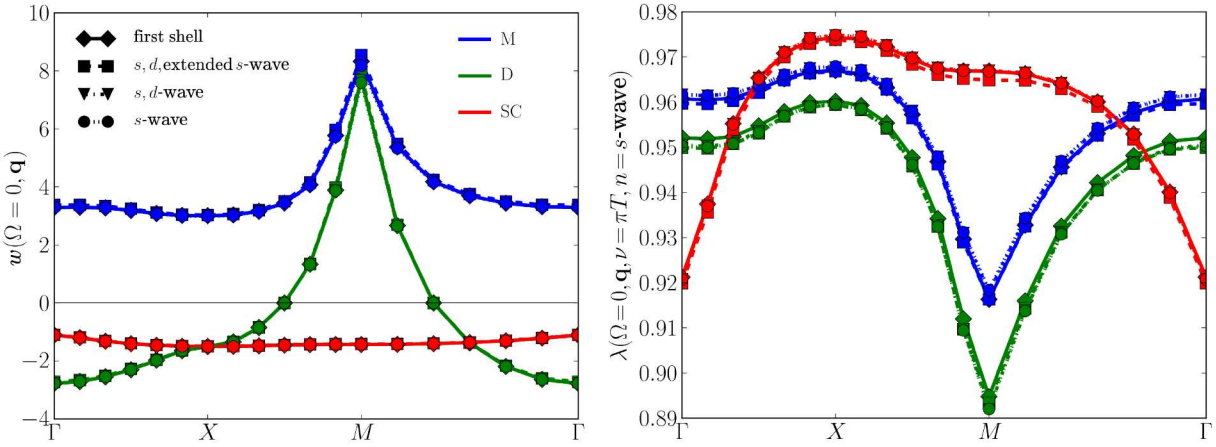

Figure 4.27: Influence of form factors on w^η and λ^η. Results calculated with the full first shell (same data as $l = l'$ of Fig. 4.23) are compared to different subsets of form factors.

Figure 4.27 compares the bosonic propagator and fermion-boson coupling calculated with only an s-wave, $s+d$-wave, $s+d+$extended s-wave, and the full first shell of form factors. While five form factors are necessary to expand $\mathcal{I}^\eta_{\text{ferm}}$ without loss of information, Fig. 4.27 shows that a local form factor is sufficient for qualitatively and also quantitatively accurate results at half filling.

This can be understood by examining the way $\mathcal{I}^\eta_{\text{ferm}}$ enters into the flow equations of $\dot{\lambda}^\eta$ and $\dot{w}^\eta$. The flow of the bosonic propagator

$$\dot{w}^\eta(\Omega,\mathbf{q}) = w^\eta(\Omega,\mathbf{q}) \sum_{\nu ll'} \lambda^\eta(\Omega,\mathbf{q},\nu,l)\dot{\Pi}^\eta(\Omega,\mathbf{q},\nu,l,l')\lambda^\eta(\Omega,\mathbf{q},\nu,l')w^\eta(\Omega,\mathbf{q}),$$

being a purely bosonic quantity, favours s-wave quantities in two ways. Firstly, mixed bubbles ($\Pi^\eta_{ll'}$ with $l \neq l'$) are small, suppressing most non s-wave contributions to $\dot{w}^\eta$. Figure 4.23 illustrates the negligible effect of the approximation of $\dot{\Pi}^\eta(l,l') = 0$ in the flow of $\dot{w}^\eta$ (Eq. (4.9)). Secondly, $\lambda^\eta_{s-\text{wave}}$ is of the order of unity, whereas $\lambda^\eta_{l>0}$ is initialised to zero and remains orders of magnitude smaller throughout the flow. Consequently, the non-local contributions $w^\eta(\Omega,\mathbf{q})\lambda^\eta(\Omega,\mathbf{q},\nu,l)\Pi^\eta(\Omega,\mathbf{q},\nu,l,l)\lambda^\eta(\Omega,\mathbf{q},\nu,l)w^\eta(\Omega,\mathbf{q})$, that are not suppressed by mixed bubbles, are instead rendered insignificant by $\lambda^\eta_{l>0} \approx 0$.

The same arguments can be applied to the flow of the fermion-boson coupling

$$\dot{\lambda}^\eta(\Omega,\mathbf{q},\nu,n) = \sum_{\nu' ll'} \lambda^\eta(\Omega,\mathbf{q},\nu,l)\dot{\Pi}^\eta(\Omega,\mathbf{q},\nu',l,l')\mathcal{I}^\eta_{\text{SBE}}(\Omega,\mathbf{q},\nu,l',\nu',n). \tag{4.10}$$

Any contribution that is not $\lambda^\eta(\Omega,\mathbf{q},\nu,s\text{-wave})\dot{\Pi}^\eta(\Omega,\mathbf{q},\nu',s\text{-wave},s\text{-wave})\mathcal{I}^\eta_{\text{SBE}}(\Omega,\mathbf{q},\nu,s\text{-wave},\nu',s\text{-wave})$ is suppressed either by a mixed bubble or $\lambda^\eta(l>0) \ll \lambda^\eta(s\text{-wave})$. Note that an s-wave only calculation automatically excludes the calculation of the non-trivial asymptotics, as these occur only for non-local form factors and $\mathcal{I}^{\eta,\text{init}} = 0$ in this case as $\mathcal{I}_{\text{ferm}}$ does not have an s-wave component.

In the light of the thought experiments of Chapter 2.1.3 about the influence of nearest-neighbour interactions, these findings can be given a physical underpinning: The charge configuration is the one directly affected by the introduction of non-locality into the bare interaction. Consequently, it is the s-wave density susceptibility that exhibits the strongest dependence on V, mirroring the direct connection. Susceptibilities of other channels and higher form factor quantities are mostly indirectly affected. This is reflected by a bosonic bare interaction (initial value of w^η) that differs from the local model only in the density channel. Taking a step back to the considerations of collective excitations, the findings can also be interpreted as having successfully identified and appropriately handled the main ordering tendencies in the bosonic propagators w^η. It highlights how both the employment of form factors for the fermionic momenta, as well as the single-boson exchange decomposition, serve not only to reduce numerical effort but can also encourage physical insights by exposing which processes/diagrams matter and which do not. Note that while the influence of the rest function on s-wave quantities remains small for the same reasons as detailed above, the absolute value of M^η may not in itself be small and could have a non-negligible effect on $\chi^\eta_{l>0}$, calculated from the vertex and bubble in a postprocessing procedure.

SBE approximation

Finally, the validity of the SBE approximation, established in detail in Section 4.2, is confirmed in the presence of a finite V in Fig. 4.28. The relative difference between the fermion-boson coupling λ^{η}, calculated with and without the flow of the rest function, is below 2 % in all channels including the lowest temperature $T = 0.1$. The same holds for χ^{SC} at all temperatures and $\chi^{\mathrm{D/M}}$ above $T = 0.1$. At $T = 0.1$ both the magnetic and charge channel are approaching a divergence and the relative difference increases to 6 % and 8 % respectively, comparable to the behaviour in the local Hubbard model as shown in Fig. 4.4. At finite frequencies the approximation holds likewise (not shown).

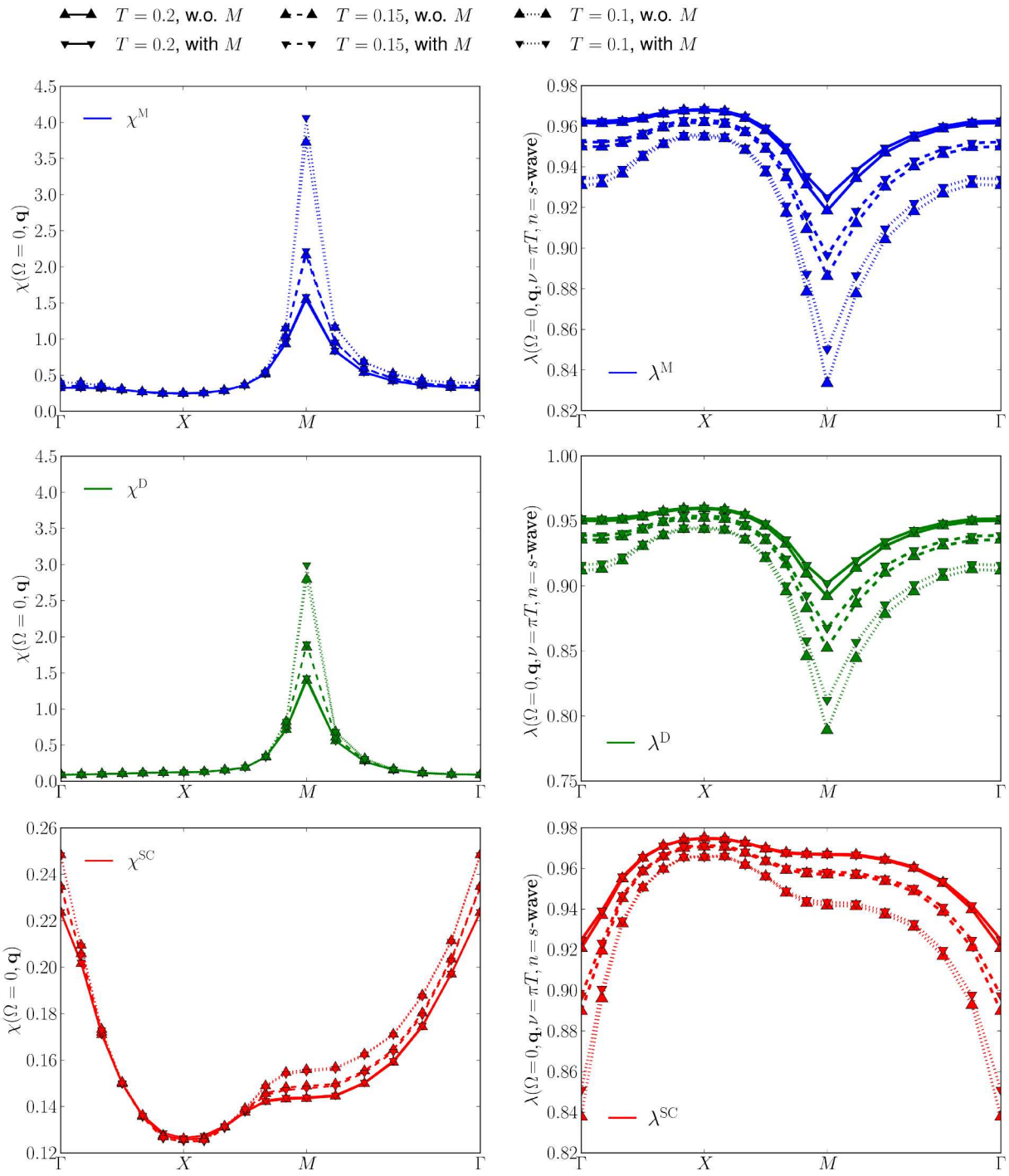

Figure 4.28: χ^{η} (left panels) and λ^{η} (right panels) calculated with and without the flow of the rest function for various temperatures and same parameters as Fig. 4.23, except that only a local form factor was employed.

4.5.2 Results at half filling

After establishing an s-wave only calculation neglecting the non-trivial high-frequency asymptotics and the flow of the rest functions as sufficient, the reduced run times allow for an investigation of the effect the non-local interaction has on the physics at half filling.

Effect of V on SBE quantities

Figure 4.29 reports the evolution of λ^η and w^η with increasing V. The fermion-boson couplings are not strongly affected by the non-local interaction strength V and show no sign of divergence also for the largest $V = U/4$ close to the divergence of the charge density wave. This observation is another confirmation of the natural bosonization formulation: the fermion-boson couplings remain finite and undergo only quantitative changes, whereas any divergence and qualitative change with V is observed only in w^η and χ^η. While λ^{D} and λ^{M} are slightly decreased with V, the opposite is true for the superconducting channel. Though λ^{SC} exhibits the strongest dependence on V, χ^{SC} shows little alteration. In χ^{M} and χ^{D} the competition between AF and the charge density wave (CDW) can be observed. The increase in charge ordering interferes with AF ordering and thus χ^{M} is reduced with increasing V, whereas χ^{D} increases. The growth is slow at first and ever more steep as the pseudo-critical transition is approached, see Fig. 4.31.

The bosonic bare interaction $\mathcal{I}^{\mathrm{D}}_{\mathrm{bos}}(\mathbf{q}) = U + 4V(\cos(q_x) + \cos(q_y))$ leads to a momentum dependent initial value of w^{D}. It is extremal at the M- and X- points of the BZ, with $\mathcal{I}^{\mathrm{D}}_{\mathrm{bos}}(\mathbf{q} = (0,0)) = U + 8V$ and $\mathcal{I}^{\mathrm{D}}_{\mathrm{bos}}(\mathbf{q} = (\pi,\pi)) = U - 8V$ respectively. Along the magnetic zone boundary (defined by $|k_x| + |k_y| = \pi$), which includes the X-points of the BZ, $\mathcal{I}^{\mathrm{D}}_{\mathrm{bos}}(\mathbf{q} = (0,\pi)) = U$ reduces to the local bare interaction. At this boundary the non-local part of $\mathcal{I}^{\mathrm{D}}_{\mathrm{bos}}(\mathbf{q})$ changes sign. In accordance, the V-dependence of χ^{D} is strongest around the M-point, where it leads to an enhancement of the maximum and vanishes almost exactly along the magnetic zone boundary. Outside, an increasing V results in a decrease of χ^{D}, which is most pronounced at the Γ-point.

Phase diagram

As discussed in Section 2.1.3 and shown in Section 4.5.2, in Fig. 4.29 an increasing nearest-neighbour interaction enhances χ^{D}, while simultaneously dampening χ^{M}. The interaction flow is most suited for a sweep of the $U - V$ plane of parameter space, as the results of the intermediate solver steps at cutoff parameter Λ are related to the physical system at $\tilde{U} = l^2 U$ and $\tilde{V} = l^2 V$. For details on the interaction flow and relations linking the intermediate results to the corresponding physical systems, see Section 2.3.3. Note, however, that the pseudo-critical transition is pushed to low coupling strengths compared to the Ω-flow. Figure 4.30 shows a phase diagram of the $U-V$ Hubbard model at half filling for $T = 0.1$. At half filling, the energy cost per site of a perfectly even charge distribution in the atomic limit is lV, where l is the number of bonds per site, $l = 4$ in the case of a square lattice, and U is the average cost per site for a charge density wave with $\mathbf{q} = (\pi,\pi)$. In keeping with this simple picture, a crossover from the dominant feature being $\chi^{\mathrm{M}}(\mathbf{q} = (\pi,\pi))$ to $\chi^{\mathrm{D}}(\mathbf{q} = (\pi,\pi))$ is observed for $4V \gtrsim U$ [56]. Upon further increase of V the density susceptibility diverges, indicating the onset of a strong tendency to CDW order, as the fRG in the 1ℓ approximation violates the Mermin Wagner theorem. Note that the competition between CDW and AF ordering tendencies effectively slightly extends the weak coupling regime to higher U and V.

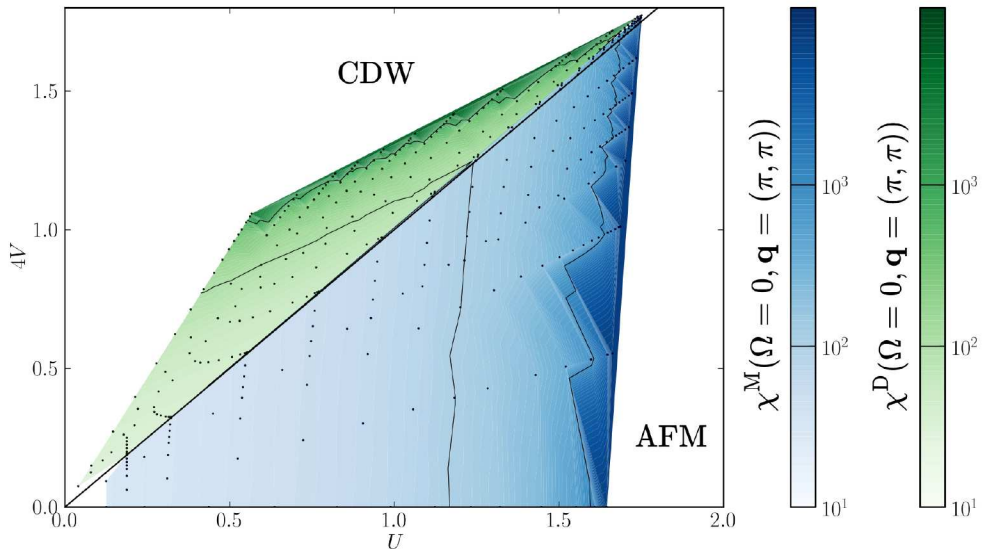

Figure 4.30: Phase diagram of the extended Hubbard model at half filling and $\beta = 10$, data obtained with the interaction flow. Green indicates a dominance of $\chi^{\mathrm{D}}(\Omega = 0, \mathbf{q} = (\pi, \pi))$, and blue of $\chi^{\mathrm{M}}(\Omega = 0, \mathbf{q} = (\pi, \pi))$, while the intensity of the colour reflects the height of the maximum. The white areas to the right and at the top are areas of parameter space where the 1ℓ approximation yields a divergence. Note that the contour lines' rugged features are a result of lack of data points. The divergence occurs at lower U/V compared to data obtained with the Ω-flow.

Figure 4.31 shows how the maxima of χ^{M}, and the $s + d$-wave components of χ^{SC} and χ^{D} evolve relative to one another with V. At $V = 0$, χ^{M} is close to a divergence, all other susceptibilities are orders of magnitude smaller. As V is increased χ^{M} decreases and χ^{D} increases, finally reversing roles around $4V/U = 1$ before diverging at $4V/U = 1.1$. While χ^{SC}, s-wave increases with V, the opposite is true for χ^{SC}, d-wave, however both remain an order of magnitude smaller than the maximum of χ^{M} for all V. The symmetry between $\chi^{\mathrm{D}}(\mathbf{q} = (\pi, \pi))$ and $\chi^{\mathrm{SC}}(\mathbf{q} = (0, 0))$ is broken at finite V.

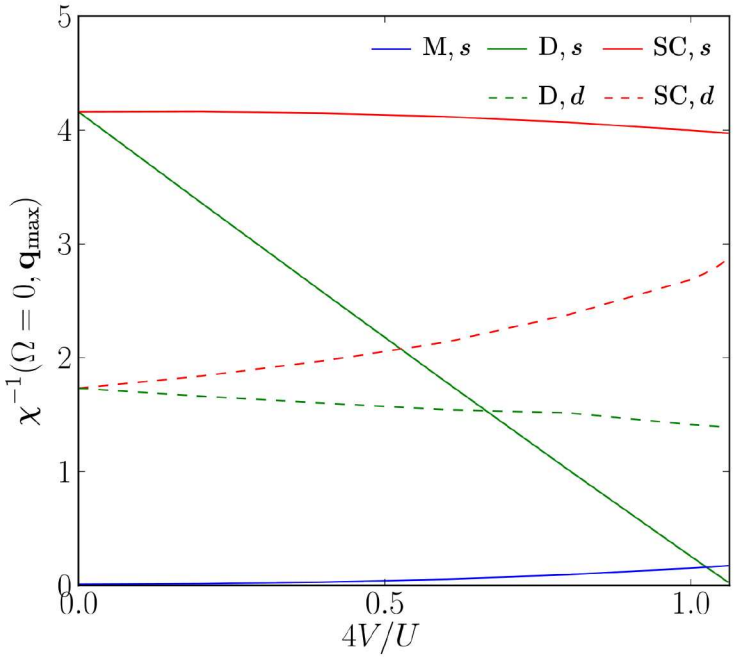

Figure 4.31: Maximum of $\chi^{\mathrm{M}} s$-wave, $\chi^{\mathrm{D}} s + d$-wave, and $\chi^{\mathrm{SC}} s + d$-wave over $4V/U$ at $T = 0.1, U = 2, \mu = 0, t' = 0$, for data obtained with the Ω-flow.

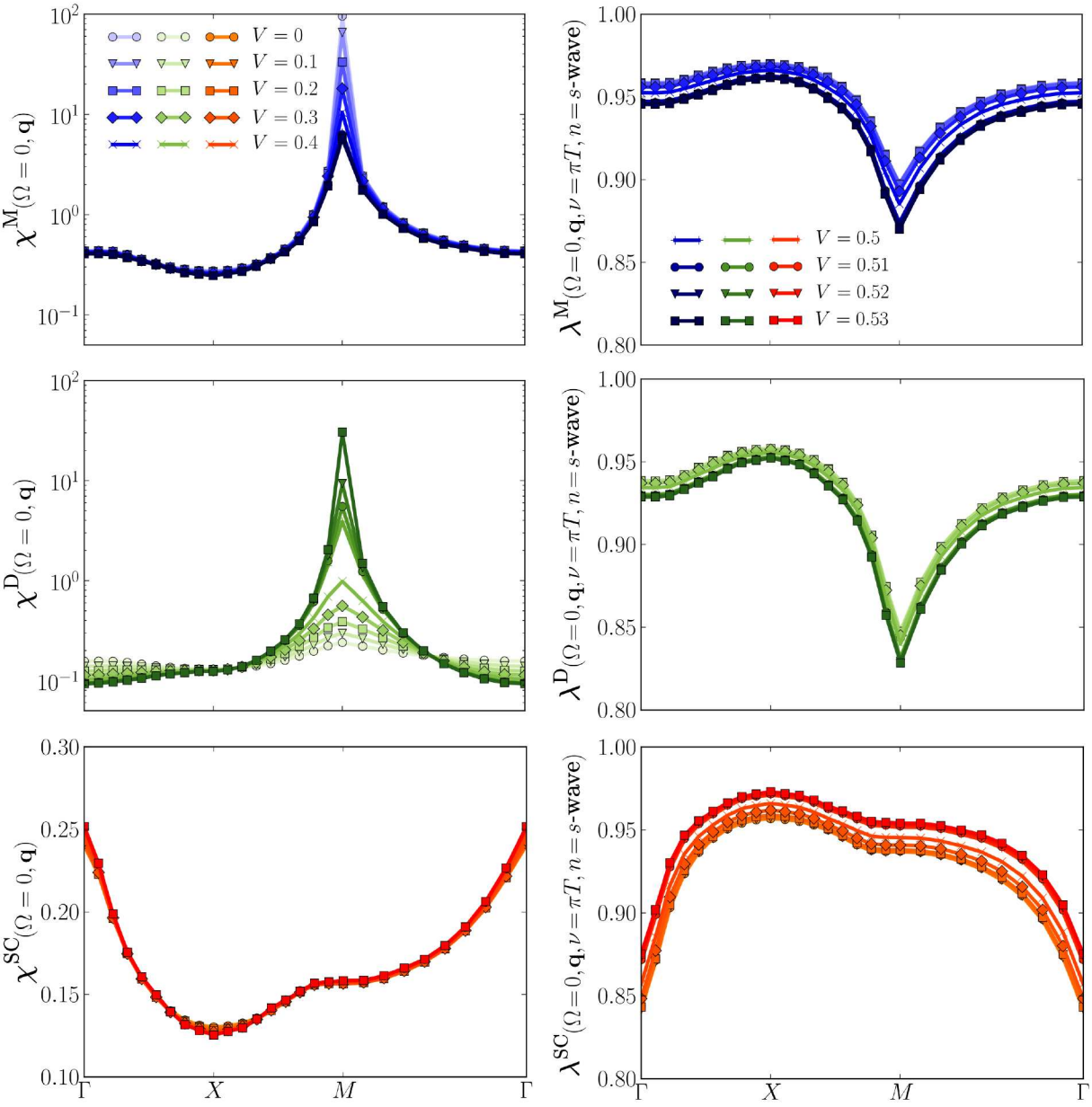

Figure 4.29: Momentum dependence of λ^{η} and χ^{η} and their evolution with V. The data is obtained using the minimal, s-wave only approximation for $U = 2, T = 0.1, \mu = 0, t' = 0$.

5 Fluctuation diagnostics of the susceptibilities

This chapter is dedicated to presenting the results to be published in [85]. After an introduction of the so-called 'postprocessing' procedure in Section 5.1, an overview of the phase diagram at $U = 3, t' = -0.15$ and $\beta = 15$ is given in Section 5.2, followed by a detailed fluctuation diagnostic of the physical susceptibilities $\chi^{\mathrm{M}}, \chi^{\mathrm{SC}}$, and χ^{D} in Sections 5.3, 5.4, and 5.5 respectively. The data was calculated using the Ω-flow and numerical parameters listed in Appendix D.1.

5.1 Postprocessing

The results of the flow used in this analysis are the self-energy Σ, the two-particle reducible vertices ϕ^η and susceptibilities χ^η. A multitude of physical observables can be calculated from the information contained therein, such as the filling, double occupancy, correlation functions and lengths, and spectral functions. A 'postprocessed' susceptibility can be obtained by inserting the vertex V into the exact equation [1]

$$\begin{aligned}\chi^\eta(\Omega,\mathbf{q},\mathbf{k},\mathbf{k}') =& \sum_\nu \Pi^\eta(\Omega,\mathbf{q},\nu,\mathbf{k},\mathbf{k}') + \sum_{\substack{\nu,\nu'\\ \mathbf{p},\mathbf{p}'}} \Pi^\eta(\Omega,\mathbf{q},\nu,\mathbf{k},\mathbf{p}) V^\eta(\Omega,\mathbf{q},\nu,\mathbf{p},\nu',\mathbf{p}') \Pi^\eta(\Omega,\mathbf{q},\nu',\mathbf{p}',\mathbf{k}') \\ :=& \chi^{\eta,0}(\Omega,\mathbf{q},\mathbf{k},\mathbf{k}') + [\chi^{\eta,0} V^\eta \chi^{\eta,0}](\Omega,\mathbf{q},\mathbf{k},\mathbf{k}'),\end{aligned} \tag{5.1}$$

with $\chi^{\eta,0}(\Omega,\mathbf{q},\mathbf{k},\mathbf{k}') = \sum_\nu \Pi^\eta(\Omega,\mathbf{q},\nu,\mathbf{k},\mathbf{k}')$. A comparison between the result of the flow for χ_r compared to the result of the postprocessed χ_r gives insight into multiloop convergence, as for $\ell \to \infty$ the two methods yield the same results. At lower ℓ the derivative of χ_r and V^r are incomplete, leading to inconsistencies between the flow and postprocessed results. In addition, the postprocessing relation can be employed to perform a fluctuation diagnostic and thereby trace the relative influence of the different channels on features of χ^η. The individual physical channels' contribution to χ^η can be extracted by inserting the parquet decomposition Eq. (2.19) into the postprocessing relation Eq. (5.1) and rewriting it as

$$\chi^\eta = \chi^{\eta,0} + \chi^{\eta,0}\phi^{\mathrm{SC}}\chi^{\eta,0} + \frac{1}{2}\chi^{\eta,0}\phi^{\mathrm{D}}\chi^{\eta,0} - \frac{3}{2}\chi^{\eta,0}\phi^{\mathrm{M}}\chi^{\eta,0} + \chi^{\eta,0}U\chi^{\eta,0}. \tag{5.2}$$

This relation will be used extensively to shed light on the interplay between the channels.

5.2 Overview

An overview of the 2ℓ results for the static magnetic, density, and superconducting susceptibilities for the representative parameters of $U = 3$, $t' = -0.15$, and $\beta = 15$ is shown in Fig. 5.1, reporting the evolution of their maximal values with the doping $\delta = (1 - n)$, where n is the occupation number. The asymmetry around half filling is a consequence of the finite next-nearest-neighbour hopping amplitude t' breaking particle-hole symmetry. The dominant susceptibility is the s-wave magnetic χ^{M} one, for almost all dopings except for very large values, where two-particle interaction effects play a vanishing role and the physics is dominated by Fermi-liquid behavior. The maximum around half filling occurs in correspondence with the AF wave vector $\mathbf{q} = (\pi, \pi)$. Its height decreases with doping, leading to a damping at large dopings.

[1] The result for χ is only exact if the exact V is inserted.

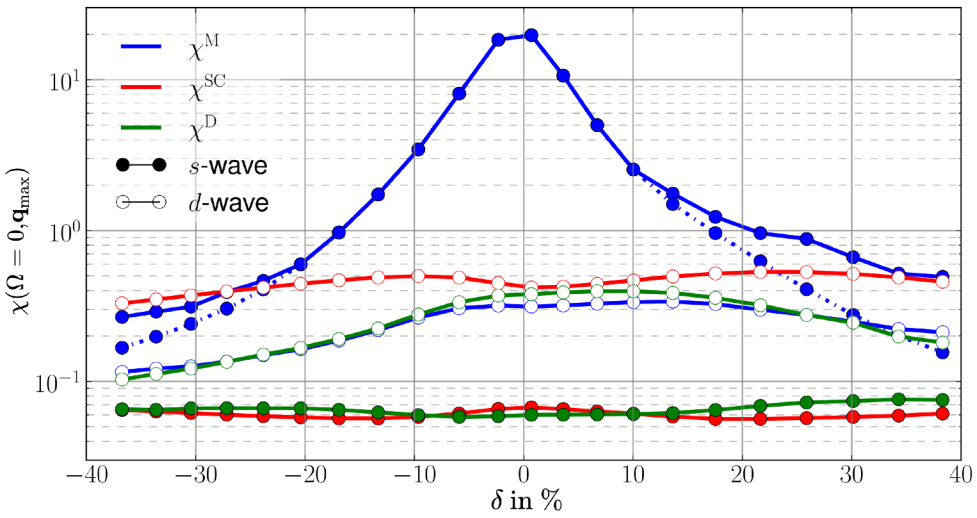

Figure 5.1: Maximal values of s- and d-wave magnetic $\chi^{\mathrm{M}}(\Omega = 0, \mathbf{q}_{\mathrm{max}})$, density $\chi^{\mathrm{D}}(\Omega = 0, \mathbf{q}_{\mathrm{max}})$, and superconducting $\chi^{\mathrm{SC}}(\Omega = 0, \mathbf{q}_{\mathrm{max}})$ susceptibilities as obtained from the fRG in the 2ℓ truncation (by postprocessing), for $U = 3$, $t' = -0.15$, and $\beta = 15$. We refer to the text for the definition of $\mathbf{q}_{\mathrm{max}}$. In the magnetic channel, the value at $\mathbf{q} = (\pi, \pi)$ is added (dashed line). Note the logarithmic scale, highlighting the different orders of magnitude.

At the same time, χ^{M} eventually becomes incommensurate at around 10% hole and 20% electron doping, as indicated by the departure of the solid from the dashed line (see also Fig. 5.2 discussed below). The largest subleading susceptibility is d-wave χ^{SC}, followed by the other d-wave components χ^{D} and χ^{M}, while the s-wave χ^{D} and χ^{SC} appear to be much smaller. The considered parameter regime is still far away from any superconducting instability and we expect the d-wave pairing susceptibility to increase only at lower temperatures, see also discussion below.

The characteristic behavior along a path in the Brillouin zone is illustrated in Fig. 5.2 both around half filling and at finite doping. Close to half filling, shown in the left panel, the dominant feature is the AF peak of χ^{M} at $\mathbf{q} = (\pi, \pi)$. The situation is more complex at finite doping, reported in the right

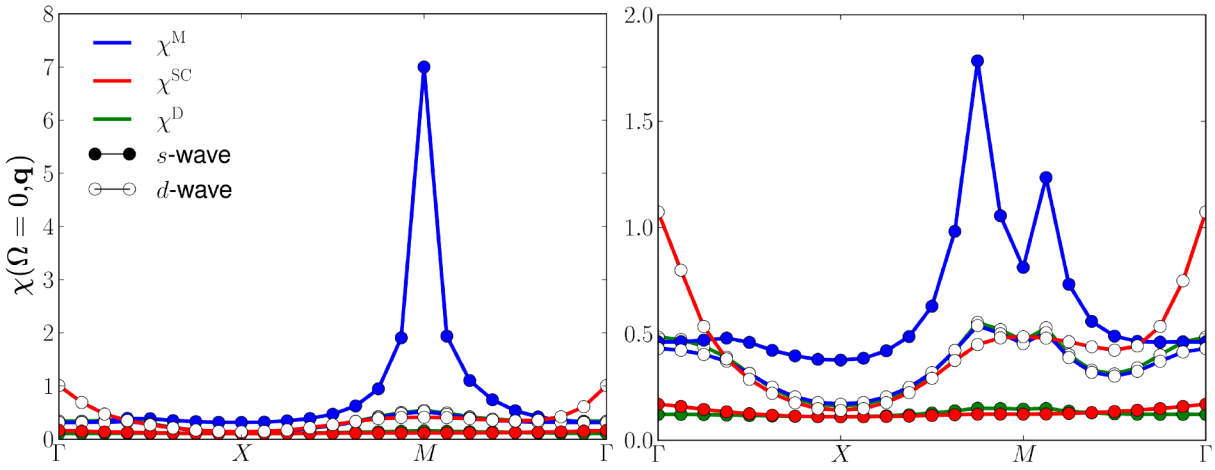

Figure 5.2: Susceptibilities of Fig. 5.1 along a path in the Brillouin zone, for $\delta = 10\%$ electron and 26% hole doping on the left and right panel respectively.

panel: the AF peak splits and the maximum shifts to incommensurate wave vectors. At the same time, d-wave χ^{SC} is of the same order of magnitude at its maximum value in correspondence with $\mathbf{q} = (0, 0)$. In the following analysis $\mathbf{q}_{\mathrm{max}}$ refers to the wave vector where the susceptibility reaches its maximum and, as such, depends on the channel and doping. In Fig. 5.3 we show the leading magnetic, density, and superconducting susceptibilities of Fig. 5.2 along a path in the Brillouin zone for $\delta = 1\%$. From the bubble and vertex contributions for the different channels one can infer their importance in driving

the respective susceptibilities. In particular, we observe that the maximal values are dominated by the vertex in the magnetic channel, while the density and superconducting ones are determined mainly by the bubble. Nevertheless, a relevant vertex contribution is detected, especially around half filling. A more detailed analysis is presented in the sections on the fluctuation diagnostics. For completeness, the

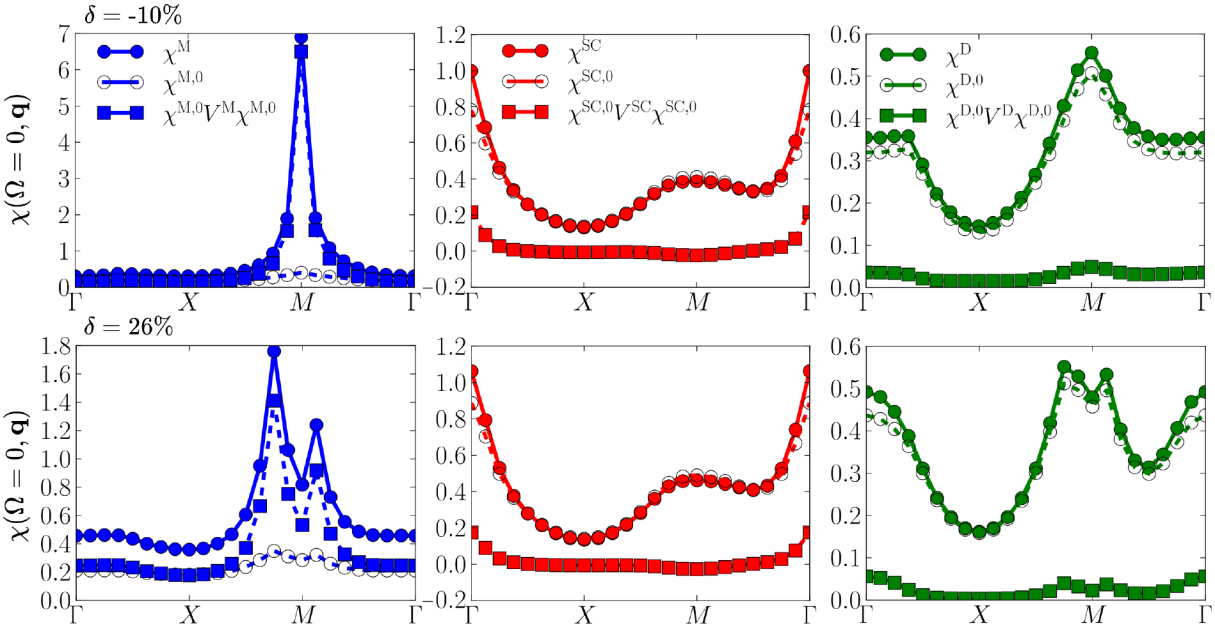

Figure 5.3: Susceptibilities of Fig. 5.1 along a path in the Brillouin zone, for $\delta = 1\%$ hole doping.

evolution of the Fermi surface, as extracted from the self-energy at the lowest Matsubara frequency, is provided in Appendix D.2.

While the 2ℓ computations are not converged in loop order, they include the first explicit correction terms to the two-particle vertex flow [75, 92], extending the Katanin substitution. These correspond to the first two diagrams of Fig. 2.6. On a qualitative level, the 2ℓ fRG is correct up to $O(U^3)$, in contrast to $O(U^2)$ of the conventional 1ℓ scheme. On a quantitative level, the 2ℓ contributions are typically the most important ones [72]. This is confirmed by the small deviations with respect to the results obtained from the flow of the response function, reported in Fig. 5.4. Except for the region around half filling,

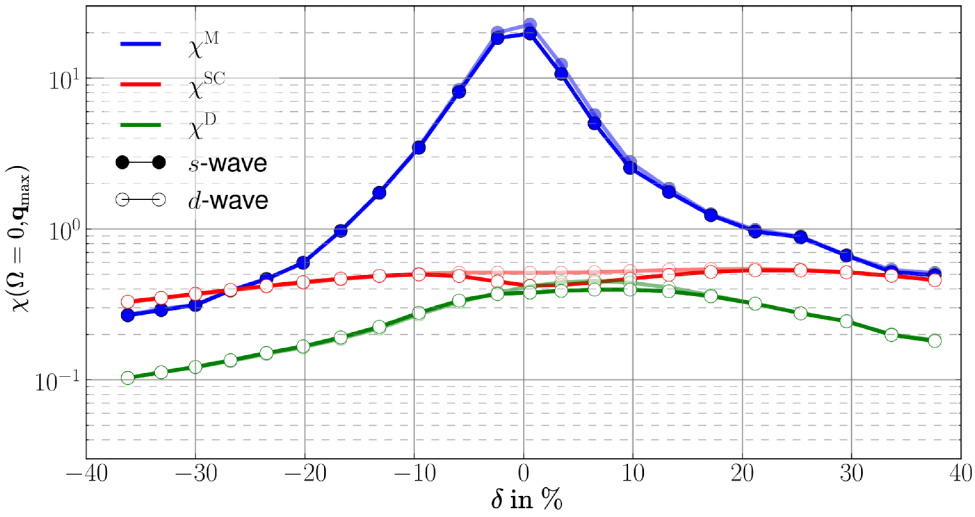

Figure 5.4: Leading magnetic $\chi^{\mathrm{M}}_{00}(\Omega = 0, \mathbf{q}_{\max})$, density $\chi^{\mathrm{D}}_{11}(\Omega = 0, \mathbf{q}_{\max})$, and superconducting $\chi^{\mathrm{SC}}_{11}(\Omega = 0, \mathbf{q}_{\max})$ susceptibilities of Fig. 5.1, with comparison of the results obtained from the flow (lighter colors) to the ones from postprocessing (darker colors).

we observe almost no differences with respect to the postprocessing data of Fig. 5.1. A more detailed

analysis of the effects of higher loop orders is presented in Section 5.4.2.

In the following we will perform a fluctuation diagnostics and analyse the contribution of the different channels to identify the dominant two-particle scattering processes controlling the physical response of the system. We will also discuss the effects of higher loop orders and explore different parameter regimes.

5.3 Magnetic susceptibility

The s-wave component of χ^{M} is the dominant susceptibility at half filling, exceeding the largest subleading susceptibilities by two orders of magnitudes (see Fig. 5.1). The pronounced peak around the Néel wave vector $\mathbf{q} = (\pi, \pi)$ indicates strong AF fluctuations. At finite doping the absolute value decreases considerably with δ. We also observe that the wave vector $\mathbf{q}_{\max}$ corresponding to the maximum becomes incommensurate, as expected for larger dopings [36, 89, 90, 91]. At hole doping the associated maximal value of χ^{M} exhibits a pronounced "shoulder".

In order to perform a fluctuation diagnostics for the s-wave magnetic susceptibility χ^{M}, and thereby trace the driving contributions to the AF peak, we insert the self-energy and the two-particle vertex obtained from the flow into the postprocessing Eq. (5.2) for $\eta = \mathrm{M}$. Using the parquet decomposition for the magnetic vertex in form factor expansion, yields

$$\mathbf{V}^{\mathrm{M}} = -U + \mathbf{\Phi}^{\mathrm{M}} + \frac{1}{2} P^{ph\to\overline{ph}} \left(\mathbf{\Phi}^{\mathrm{M}} - \mathbf{\Phi}^{\mathrm{D}}\right) - P^{pp\to\overline{ph}} \mathbf{\Phi}^{\mathrm{SC}}. \tag{5.3}$$

As a consequence, there are two contributions of $\mathbf{\Phi}_{\mathrm{M}}$: one originating from $\mathbf{\Phi}^{\overline{ph}} = -\mathbf{\Phi}^{\mathrm{M}}$ and the other one from $\mathbf{\Phi}^{ph} = -\left(\mathbf{\Phi}^{\mathrm{M}} - \mathbf{\Phi}^{\mathrm{D}}\right)/2$, in which the projection from the particle-hole to the crossed particle-hole notation used for V^{M} leads to a different momentum and frequency dependence. Thus, the s-wave magnetic susceptibility is composed of

$$\begin{aligned}
\chi^{\mathrm{M}}_{00}(\Omega, \mathbf{q}) =& \chi^{\mathrm{M},0}_{00}(\Omega, \mathbf{q}) - \left[\chi^{\mathrm{M},0} U \chi^{\mathrm{M},0}\right]_{00}(\Omega, \mathbf{q}) \\
&+ \left[\chi^{\mathrm{M},0} \mathbf{\Phi}^{\mathrm{M}} \chi^{\mathrm{M},0}\right]_{00}(\Omega, \mathbf{q}) \\
&+ \frac{1}{2}\left[\chi^{\mathrm{M},0} P^{ph\to\overline{ph}} \left(\mathbf{\Phi}^{\mathrm{M}} - \mathbf{\Phi}^{\mathrm{D}}\right) \chi^{\mathrm{M},0}\right]_{00}(\Omega, \mathbf{q}) \\
&- \left[\chi^{\mathrm{M},0} P^{pp\to\overline{ph}} \mathbf{\Phi}^{\mathrm{SC}} \chi^{\mathrm{M},0}\right]_{00}(\Omega, \mathbf{q}) \,,
\end{aligned} \tag{5.4}$$

where $\chi^{\mathrm{M},0}_{00}(\Omega, \mathbf{q}) = \sum_\nu \Pi^{\mathrm{M}}_{00}(\Omega, \mathbf{q}, \nu)$ is the s-wave magnetic bare bubble. For this chapter the notation of form factor dependencies is changed from $A(n, n')$ to $A_{nn'}$ and the expressions of the form $[\chi^{\eta,0} A^\eta \chi^0]_{nn'}(\Omega, \mathbf{q})$ are to be read as $\sum_{\substack{\nu\nu' \\ ll'}} \Pi^\eta_{nl}(\Omega, \mathbf{q}, \nu) A^\eta_{ll'}(\Omega, \mathbf{q}, \nu, \nu') \Pi^\eta_{l'n'}(\Omega, \mathbf{q}, \nu')$. Bold symbols $\mathbf{\Phi}^\eta$ represents a 'form factor matrix' with elements $[\mathbf{\Phi}^\eta]_{ij} = \Phi^\eta_{ij}$. The form factor sums run over s-wave $f_{n=0} = 1$ and d-wave form factor $f_{n=1} = \cos(k_x) - \cos(k_y)$. Equation (5.4) allows to determine the importance of the different channels. As shown in Fig. 5.5, the static (s-wave) magnetic susceptibility χ^{M} is driven by the vertex correction, in particular by the contribution of the crossed particle-hole channel $\mathbf{\Phi}^{\mathrm{M}} = -\mathbf{\Phi}^{\overline{ph}}$ and not by $P^{ph\to\overline{ph}} \mathbf{\Phi}^{\mathrm{M}}$ (in the figure we refer to them as $\mathbf{\Phi}^{\mathrm{M},\overline{ph}}$ and $\mathbf{\Phi}^{\mathrm{M},ph}$, respectively). In fact, in the projection from the particle-hole to the crossed particle-hole channel, only the momentum average adds to the latter. All other contributions are negligible for the considered parameters of $U = 3$, $t' = -0.15$, and $\beta = 15$.

The large AF fluctuations, which increase both with the interaction U and at lower temperatures, originate in the ladder diagrams. This can be deduced from the comparison with RPA data[2] reported in Fig. 5.6. The susceptibility obtained from the crossed particle-hole ladder of the RPA is drastically lowered by the inclusion of the inter-channel feedback in the 1ℓ fRG without self-energy. This trend is enhanced with the inclusion of the self-energy and increasing loop order. It can be understood from a diagrammatic point of view: the RPA includes only ladder diagrams yielding a magnetic susceptibility of the form $\chi^{\mathrm{M},0}/\left(1 - U\chi^{\mathrm{M},0}\right)$ which is prone to divergences. The 1ℓ fRG, while still biased towards ladder diagrams, also partially accounts for all other parquet diagrams. With increasing loop order this bias is gradually lifted [3] as diagrams of increasing order in U are fully included. For 2ℓ they are accounted for

[2] RPA data is obtained by performing a 1ℓ calculation without the flow of the self-energy and no inter-channel feedback.

[3] We note that the convergence towards the parquet approximation exhibits a characteristic oscillatory behavior in the loop order [30, 84].

correctly up to $O(U^3)$. Also the imaginary part of the self-energy plays a crucial role in renormalizing the bubble contribution $\chi^{\mathrm{M},0}$, in particular around half filling. In its evaluation with the Schwinger-Dyson equation the self-energy itself appears to be controlled by AF fluctuations [70, 93].

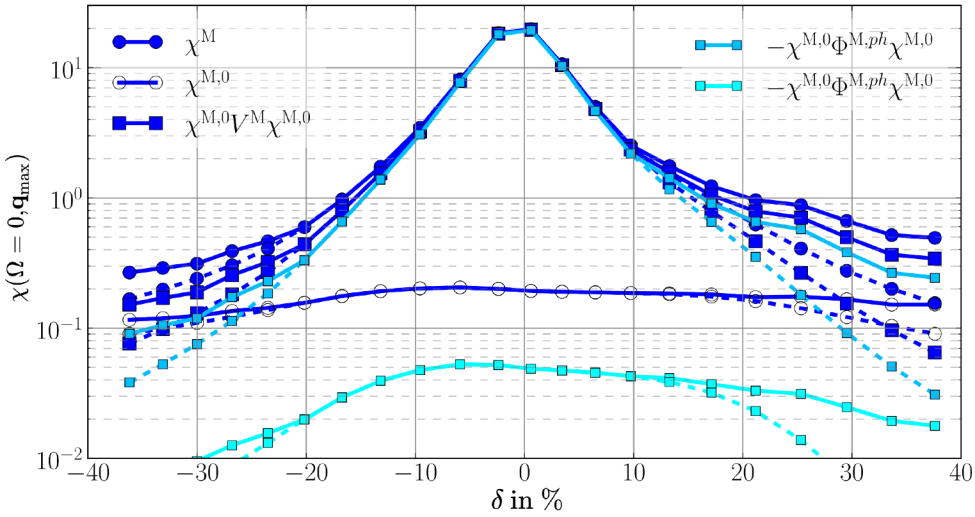

Figure 5.5: Fluctuation diagnostics for the s-wave magnetic susceptibility $\chi^{\mathrm{M}}_{00}(\Omega=0,\mathbf{q})$ of Fig. 5.1, evaluated both in correspondence with $\mathbf{q}_{\max}$ (solid lines) and $\mathbf{q}=(\pi,\pi)$ (dashed lines). The vertex corrections dominate over the bare bubble and are determined essentially by the contribution from the crossed particle-hole channel $\chi^{\mathrm{M},0}\mathbf{\Phi}^{\mathrm{M},\overline{ph}}\chi^{\mathrm{M},0}$, whereas the one from the particle-hole channel $\chi^{\mathrm{M},0}\mathbf{\Phi}^{\mathrm{M},ph}\chi^{\mathrm{M},0}$ is negligible. (The contributions from $\chi^{\mathrm{M},0}\mathbf{\Phi}^{\mathrm{SC}}\chi^{\mathrm{M},0}$ and $\chi^{\mathrm{M},0}\mathbf{\Phi}^{\mathrm{D}}\chi^{\mathrm{M},0}$ are smaller than 0.01 and not reported).

5.4 Superconducting susceptibility

In analogy to the analysis performed for the magnetic channel, the bubble and vertex contributions to the s- and d-wave superconducting susceptibility χ^{SC} are determined. Inserting the parquet decomposition of V^{SC} into the postprocessing Eq. (5.2), we obtain

$$\begin{aligned}\chi^{\mathrm{SC}}_{11}(\Omega,\mathbf{q}) =& \chi^{\mathrm{SC},0}_{11}(\Omega,\mathbf{q}) + \left[\chi^{\mathrm{SC},0}\mathbf{\Lambda}^{2\mathrm{PI}}\chi^{\mathrm{SC},0}\right]_{11}(\Omega,\mathbf{q}) \\ &- \left[\chi^{\mathrm{SC},0}P^{\overline{ph}\to pp}\mathbf{\Phi}^{\mathrm{M}}\chi^{\mathrm{SC},0}\right]_{11}(\Omega,\mathbf{q}) \\ &- \frac{1}{2}\left[\chi^{\mathrm{SC},0}P^{ph\to pp}\left(\mathbf{\Phi}^{\mathrm{M}}-\mathbf{\Phi}^{\mathrm{D}}\right)\chi^{\mathrm{SC},0}\right]_{11}(\Omega,\mathbf{q}) \\ &+ \left[\chi^{\mathrm{SC},0}\mathbf{\Phi}^{\mathrm{SC}}\chi^{\mathrm{SC},0}\right]_{11}(\Omega,\mathbf{q})\,. \end{aligned} \tag{5.5}$$

The different contributions both for s- and d-wave superconducting susceptibilities, evaluated at the maximum of χ^{SC} at $\mathbf{q}_{\max}=(0,0)$ and $\Omega=0$, are displayed in Fig. 5.7 as a function of the doping, for the reference parameters of Fig. 5.1. Comparing the overall values, the d-wave χ^{SC} clearly dominates over the s-wave one. This is due to the cancellation between the s-wave bubble and the vertex contribution, which is absent in the d-wave components. The latter will be discussed in detail in the following, through an analysis of the terms in Eq. (5.5).

5.4.1 The d-wave bubble contribution to χ^{SC}

For the considered parameters ($U=3$, $t'=-0.15$, and $\beta=15$), the bare bubble is the dominating contribution in the whole doping range. However, when the temperature is lowered, the growth of the bubble is much slower than that of the vertex part (see left panel of Fig. 5.9). For large absolute values of the doping $|\delta|$, the large chemical potential $|\mu|$ leads to a decrease of the Green's functions, reflecting the transition to an effectively "uncorrelated" area of the phase diagram. The origin of the suppression around half filling can be traced back to the renormalization of the self-energy. Specifically, the imaginary

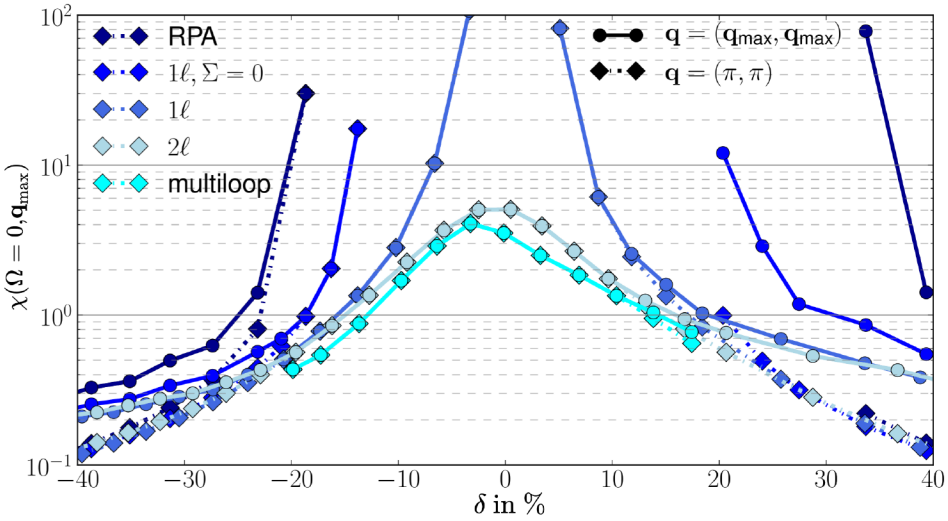

Figure 5.6: Magnetic $\chi^{\mathrm{M}}_{00}(\Omega = 0, \mathbf{q}_{\max})$ as obtained from RPA and the fRG in the 1ℓ truncation (neglecting the self-energy flow), for the same parameters as in Fig. 5.1, but for $\beta = 10$, since for lower temperatures both RPA and 1ℓ fRG without self-energy flow do not converge. For comparison, data with self-energy are also shown for 1ℓ and 2ℓ. Finally 'multiloop' labels 8ℓ data sets with five self-energy iterations as a converged benchmark.

part of the self-energy becomes large close to half filling. Without self-energy feedback the bubble has a single broad maximum around $\delta = 10\%$ as shown in Fig. 5.8. Performing a fluctuation diagnostics in analogy to the susceptibilities, the imaginary part can be split into the individual contributions according to the parquet equation. The insets in Fig. 5.8 show the imaginary part of the magnetic contribution $\Im\{\Sigma^{\mathrm{M}}\}(\mathbf{k} = (\pi/2, \pi/2), \nu) = \Im\{\int -\frac{3}{2}\Phi^{\mathrm{M}} GGGU\}(\mathbf{k} = (\pi/2, \pi/2), \nu)$ and the sum of the other components. Σ^{M} depends strongly on doping, in contrast to the other contributions, which remain almost constant.

5.4.2 The vertex corrections $\chi^{\mathrm{SC},0}\mathbf{V}^{\mathrm{SC}}\chi^{\mathrm{SC},0}$

At lower temperatures the vertex term increases in importance whereas the bubble growth stagnates, see left panel of Fig. 5.9. Since any divergence must ultimately be vertex, not bubble, driven we now examine the vertex part in more detail. The doping dependence of the bubble translates to the vertex part, as this consists of a matrix-like product in form factors with a convolution in frequency space of two bare bubbles and the vertex itself, see Eq. (5.5), so the presence of the same double dome structure in the vertex part is not surprising. The largest contribution to the d-wave vertex correction $[\chi^{\mathrm{SC},0}\mathbf{V}^{\mathrm{SC}}\chi^{\mathrm{SC},0}]_{11}$ comes from $\mathbf{\Phi}^{\mathrm{M}}$ followed by $\mathbf{\Phi}^{\mathrm{SC}}$ and $\mathbf{\Phi}^{\mathrm{D}}$, see bottom right panel of Fig. 5.7. Interestingly, $[\chi^{\mathrm{SC},0}P^{ph\to pp}\mathbf{\Phi}^{\mathrm{D}}\chi^{\mathrm{SC},0}]_{11} \approx [\chi^{\mathrm{SC},0}P^{ph\to pp}\Phi^{\mathrm{D}}_{00}\chi^{\mathrm{SC},0}]_{11}$ even though $\Phi^{\mathrm{D}}_{00} \ll \Phi^{\mathrm{D}}_{11}$ due to the projection from the ph to the pp channel. While the bare interaction U is not small itself the mixed s- and d-wave bubbles in

$$\left[\chi^{\mathrm{SC},0}U\chi^{\mathrm{SC},0}\right]_{11}(\Omega, \mathbf{q}) = \sum_{\nu,\nu'} \Pi^{\mathrm{SC}}_{10}(\Omega, \mathbf{q}, \nu) U \Pi^{\mathrm{SC}}_{01}(\Omega, \mathbf{q}, \nu') \tag{5.6}$$

vanish for $\mathbf{q} = (0, 0)$, see Section 4.3.1. Both $[\chi^{\mathrm{SC},0}\mathbf{\Phi}^{\mathrm{M}}\chi^{\mathrm{SC},0}]_{11}$ and $[\chi^{\mathrm{SC},0}\mathbf{\Phi}^{\mathrm{SC}}\chi^{\mathrm{SC},0}]_{11}$ increase when lowering the temperature but the growth is strongest for the latter and by $\beta = 40$ they are of the same order of magnitude.

To investigate the influence the magnetic channel in general, and the AF peak in particular, have on the maximum of the d-wave superconducting susceptibility $\chi^{\mathrm{SC}}_{11}(\Omega, \mathbf{q})$, we analyse $\frac{3}{2}\left[\chi^{\mathrm{SC},0}\mathbf{\Phi}^{\mathrm{M}}\chi^{\mathrm{SC},0}\right]_{11}(\Omega, \mathbf{q})$ analytically. The full derivation can be found in Appendix D.3.1 and yields

$$\begin{aligned}\frac{3}{2}\left[\chi^{\mathrm{SC},0}\mathbf{\Phi}^{\mathrm{M}}\chi^{\mathrm{SC},0}\right]_{11}(\Omega = 0, \mathbf{q}) \approx \sum_{\nu,\nu'} \Pi^{\mathrm{SC}}_{11}(\Omega = 0, \mathbf{q}, \nu)\Pi^{\mathrm{SC}}_{11}(\Omega = 0, \mathbf{q}, \nu') \\ \int_{\mathrm{BZ}} \mathrm{d}\mathbf{p}\left(-\frac{1}{2}(\cos p_x + \cos p_y) - (\cos(p_x - q_x) + \cos(p_y - q_y))\right)\Phi^{\mathrm{M}}_{00}(-(\nu + \nu'), \mathbf{p}, (\nu - \nu')/2, (\nu' - \nu)/2).\end{aligned} \tag{5.7}$$

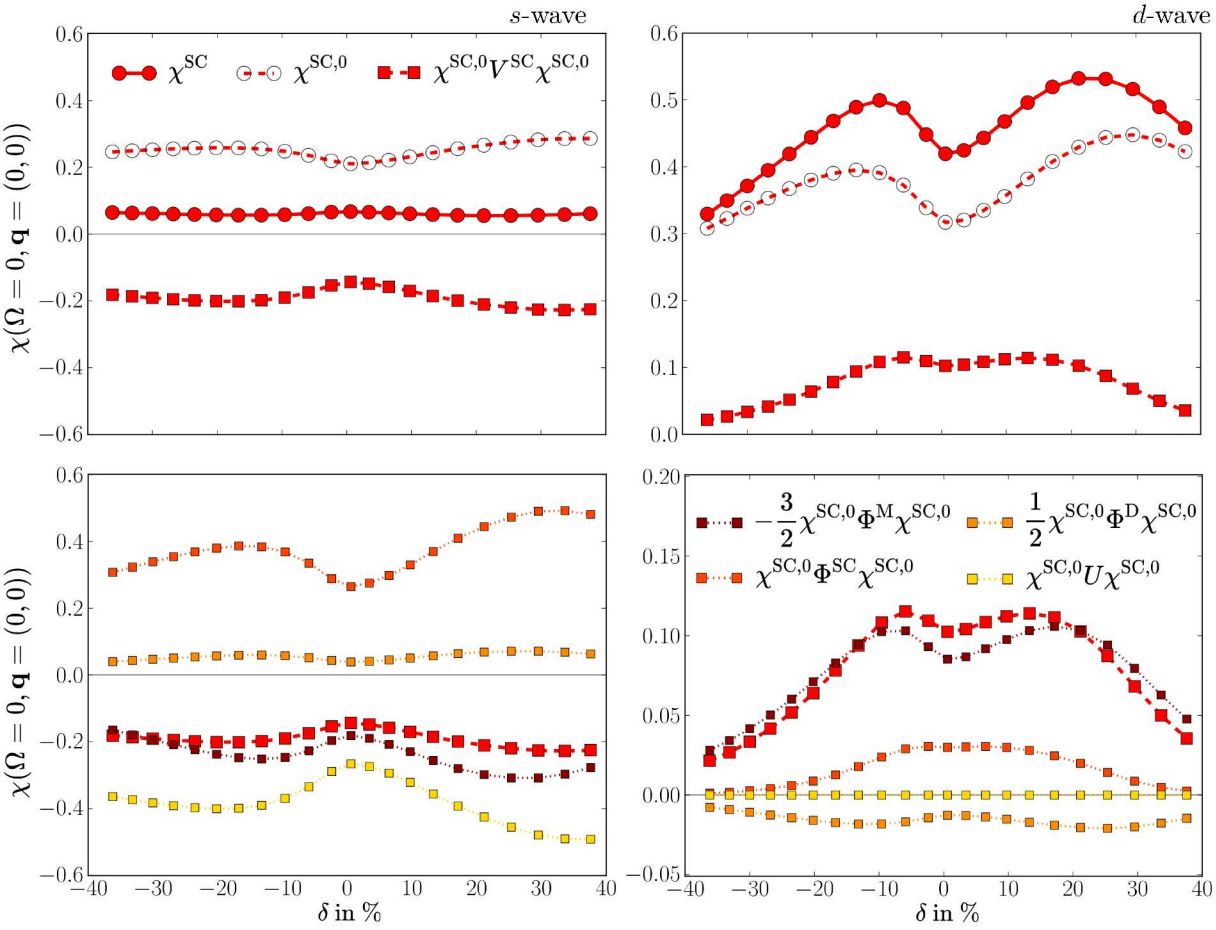

Figure 5.7: Fluctuation diagnostics of the superconducting susceptibility $\chi^{SC}_{11}(\Omega = 0, \mathbf{q}_{max} = (0,0))$ of Fig. 5.1, both for the s- and d-wave components (left and right panels respectively). Note that although the absolute values of the different d-wave contributions are smaller than the respective s-wave ones, they add up. In contrast, the negative sign of several s-wave contributions leads to a partial cancellation.

The bubble Π^{SC}_{11} reaches its maximum at $\mathbf{q} = (0,0)$, independent of doping. In the region where commensurate AF dominates $\Phi^{M}_{00}(\mathbf{p})$ has its maximum at $\mathbf{p} = (\pi,\pi)$, but moves to $(\pi - \delta, \pi)$ for larger dopings. It is weighted by the factor $-\frac{1}{2}(\cos p_x + \cos p_y)\,-(\cos(p_x - q_x) + \cos(p_y - q_y))$, which stems from form factor projections $P^{ph\to pp}$ and $P^{\overline{ph}\to pp}$ between the channels. In the AF region the maximum of the bubble at $\mathbf{q} = (0,0)$ and the maximum of Φ^{M}_{00} at $\mathbf{p} = (\pi,\pi)$ coincide with the maximum of the weight originating in the projections. When moving to larger dopings, into the incommensurate region, this is no longer the case. The maximum of the bubble remains at $\mathbf{q} = (0,0)$, but the maximum of Φ^{M}_{00} moves to $\mathbf{p} = (\pi, \pi - \delta)$, so now the weight coming from the projection matrix's $P^{ph\to pp}$ maximum no longer favours the maximum of Φ^{M}_{00} and the projection matrix's $P^{\overline{ph}\to pp}$ maximum can only favour either the maximum of the bubble or the incommensurate wave vector. In the case of $\max(\Phi^{M}_{00}) \gg \max(\Pi^{SC}_{11})$ the maximum of $\frac{3}{2}\left[\chi^{SC,0}\mathbf{\Phi}^{M}\chi^{SC,0}\right]_{11}(\Omega,\mathbf{q})$ could shift away from $\mathbf{q} = (0,0)$, something we have, however, not observed for any of the parameter combinations surveyed in this work. Thus, even where the maximum of Φ^{M}_{00} is incommensurate, the commensurate fluctuations are still favoured by the channel projection. Note that for $\mathbf{q} = (0,0)$ both $\left[P^{ph\to pp}\mathbf{\Phi}^{M}\right]_{11}$ and $\left[P^{\overline{ph}\to pp}\mathbf{\Phi}^{M}\right]_{11}$ contribute the same weight, so here it makes sense to combine the two in the fluctuation diagnostic of χ^{SC}, as we have done. Thus for large dopings not only is the bubble as well as the maximum of Φ^{M}_{00} reduced, but they also do not combine together as optimally as in the region of the phase diagram, where the AF wave vector is commensurate.

Around half filling the AF fluctuations are commensurate and strongest in size. However, in this same region the bubble is suppressed. Put together, the influences of the bubble and AF fluctuations lead to a double dome structure qualitatively similar to the bubble. The decline is, however, faster and steeper at larger dopings owing to the decreasing, and less favoured, incommensurate fluctuations and a

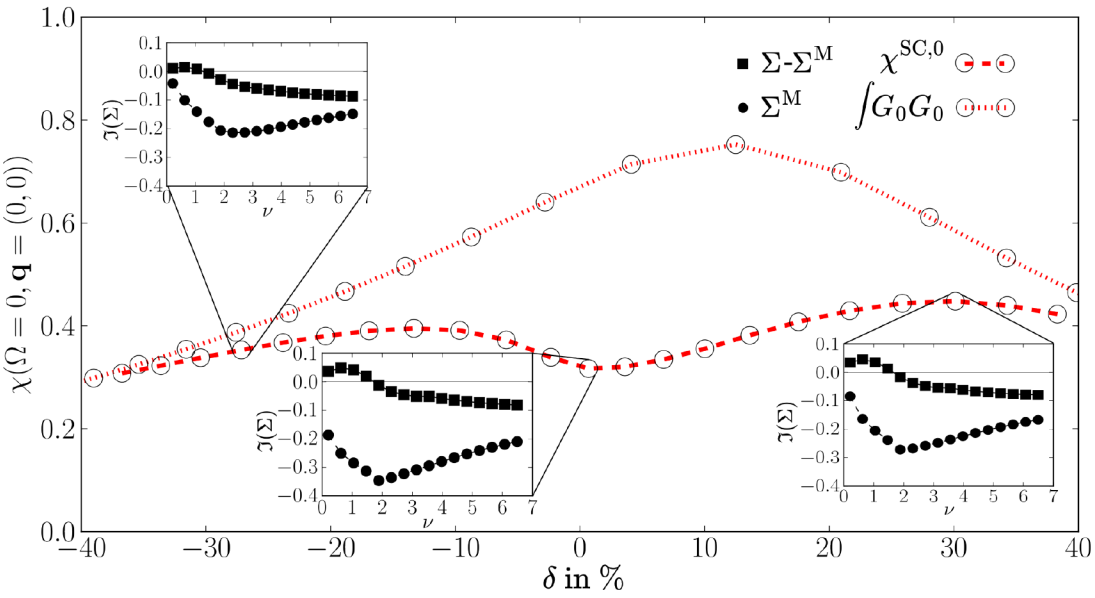

Figure 5.8: Bubble contribution $\chi_{11}^{\mathrm{SC},0}(\Omega = 0, \mathbf{q} = (0,0))$ to the d-wave superconducting susceptibility shown in Fig. 5.7, where the results obtained by using the bare Green's function (dotted line) are compared to the ones of the full Green's function (dashed line) including the self-energy. The insets show the imaginary part of Σ^{M} and the sum of the other contributions to the self-energy for three representative dopings $\Sigma - \Sigma^{\mathrm{M}}$.

less pronounced dip at half filling where the decrease originating in the bubble is reduced in severity by the strong maximum of Φ_{00}^{M}. While presenting as competing influences to $\frac{3}{2}\left[\chi^{\mathrm{SC},0}\mathbf{\Phi}^{\mathrm{M}}\chi^{\mathrm{SC},0}\right]_{11}(\Omega = 0, \mathbf{q})$, here they are at the same time entangled via a feedback loop between Φ_{00}^{M} and $\mathrm{Im}\{\Sigma\}$, as discussed in the previous section.

The next largest contribution to the vertex part is $\left[\chi^{\mathrm{SC},0}\mathbf{\Phi}^{\mathrm{SC}}\chi^{\mathrm{SC},0}\right]_{11}(\Omega = 0, \mathbf{q})$, the contribution of $\mathbf{\Phi}^{\mathrm{SC}}$ itself to χ^{SC}. While Φ_{00}^{SC}, which includes the pp-ladder diagrams, is much larger throughout all dopings than Φ_{11}^{SC}, the vanishing mixed s- and d-wave bubble means that the former does not enter into $\left[\chi^{\mathrm{SC},0}\mathbf{\Phi}^{\mathrm{SC}}\chi^{\mathrm{SC},0}\right]_{11}$ at all for $\mathbf{q}_{\max} = (0,0)$. The only diagrams that have a d-wave component are those where neither the two incoming nor the two outgoing legs respectively combine into a purely local bare vertex, which coincides exactly with those included in M^{SC} [78]. The lowest order diagram fulfilling these criteria (shown in Fig. 5.10) is of 4^{th} order in U and not completely included in the 1ℓ approximation where only the Green's functions belonging to the pp-bubble are replaced by their derivative. As part of the 2ℓ corrections the other Green's functions that are part of $\overline{ph}$-bubbles also undergo derivation.

5.4.3 Multiloop effects

We proceed by investigating the effect of higher loop orders on the different contributions to the d-wave χ^{SC}. The results are reported in the right panel of Fig. 5.9. In the analysis of the magnetic susceptibility we saw that multiloop corrections (as well as the self-energy feedback) quench the effect of the ladder diagrams in the $\overline{ph}$-channel, suppressing the tendency towards a magnetic instability. For the d-wave superconducting χ^{SC} we find the opposite behavior: removing the bias towards ladder diagrams in the multiloop scheme leads to an *increase* of χ^{SC}. All contributions present a distinct enhancement from the 1ℓ (also with Katanin substitution) to the 2ℓ results, followed by a saturation for higher loop orders. This behavior confirms the 2ℓ approximation to be an optimal compromise between quantitative accuracy at loop convergence and reduced numerical effort, besides being correct up to $\mathcal{O}(U^3)$.

By far the largest relative increase occurs in the $\mathbf{\Phi}^{\mathrm{SC}}$ component which more than doubles between the Katanin approximation and the 2ℓ result (see also discussion above). Though its share in the sum is modest for the considered parameters, in particular when compared to its counterpart in the magnetic channel, it increases rapidly with β as shown in the left panel of Fig. 5.9. Their analytic expressions for the lowest order diagrams $\mathbf{q} = (0,0)$ are derived in Appendix D.3.2.

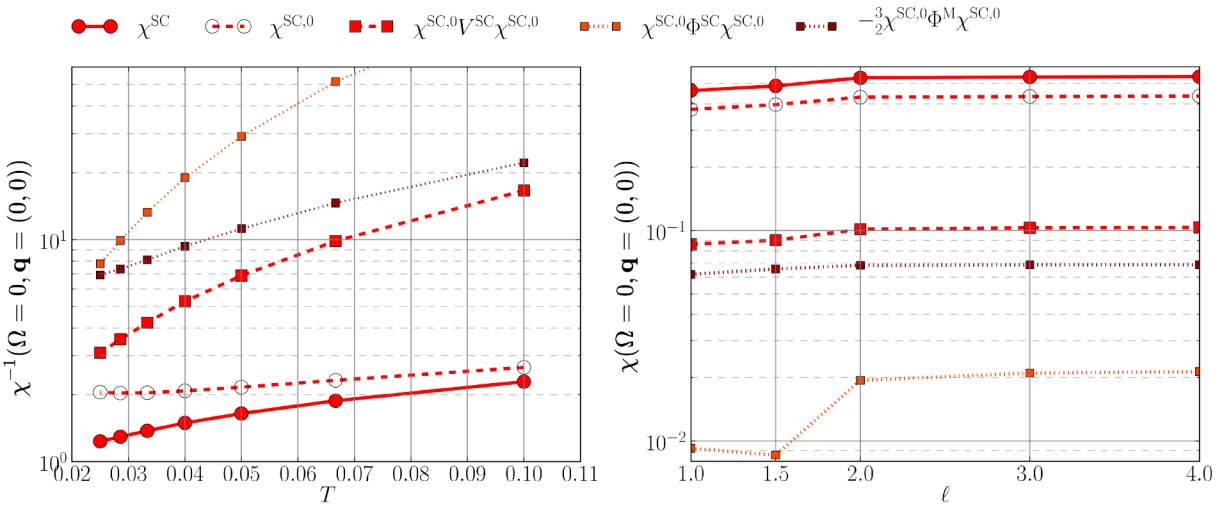

Figure 5.9: Contributions to the d-wave superconducting susceptibility $\chi^{\mathrm{SC}}(\Omega=0,\mathbf{q}=(0,0))$ of Fig. 5.7, for $\delta = 21.5$ over temperature in the left panel and multiloop order in the right panel. Note that the Katanin substitution is added as 1.5ℓ.

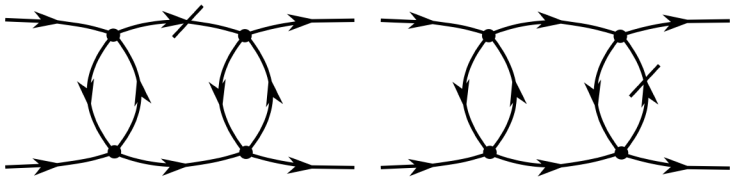

Figure 5.10: The diagram on the left is included in derivative with the 1ℓ truncation, whereas the right hand diagram is introduced only at the 2ℓ level.

5.4.4 Fluctuation diagnostic in terms of bosonic fluctuations

Rather than performing a fluctuation diagnostic based on the parquet decomposition, it can be based on the exchange of bosonic fluctuations of the SBE formalism [78]. Here, instead of inserting the individual channel components of the full vertex separately into our postprocessing relation for the susceptibility, see Eq. 5.2, vertex corrections of the $d-$wave superconducting susceptibility may be calculated from a series of boson exchanges [24]. The single-boson exchange processes are

$$-\left[\chi^{\mathrm{SC},0}\left(P^{\overline{ph}\to pp}\nabla^{\mathrm{M}}+\frac{1}{2}P^{\overline{ph}\to pp}\nabla^{\mathrm{M}}\right)\chi^{\mathrm{SC},0}\right]_{11}\approx-\frac{3}{2}\left[\chi^{\mathrm{SC},0}\mathbf{\Phi}^{\mathrm{M}}\chi^{\mathrm{SC},0}\right]_{11} \tag{5.8a}$$

$$\frac{1}{2}\left[\chi^{\mathrm{SC},0}P^{ph\to pp}\nabla^{\mathrm{D}}\chi^{\mathrm{SC},0}\right]_{11}\approx\frac{1}{2}\left[\chi^{\mathrm{SC},0}\mathbf{\Phi}^{\mathrm{D}}\chi^{\mathrm{SC},0}\right]_{11}, \tag{5.8b}$$

and the difference lies in the SBE rest function.

In the SBE framework the multiboson exchange processes are gathered into $\mathbf{M}^{\mathrm{SC}}$. As discussed in Section 4.3.3, $\mathbf{\Phi}^{\mathrm{SC}}_{11}(\Omega,\mathbf{q}=(0,0),\nu,\nu')=\mathbf{M}^{\mathrm{SC}}_{11}(\Omega,\mathbf{q}=(0,0),\nu,\nu')$ and thus for $\mathbf{q}=(0,0)$

$$\begin{aligned}
&+(-\frac{3}{2})^2\left[\chi^{\mathrm{SC},0}P^{\overline{ph}\to pp}\nabla^{\mathrm{M}}\chi^{\mathrm{SC},0}P^{\overline{ph}\to pp}\nabla^{\mathrm{M}}\chi^{\mathrm{SC},0}\right]_{11}\\
&+(\frac{1}{2})^2\left[\chi^{\mathrm{SC},0}P^{ph\to pp}\nabla^{\mathrm{D}}\chi^{\mathrm{SC},0}P^{ph\to pp}\nabla^{\mathrm{D}}\chi^{\mathrm{SC},0}\right]_{11}\\
&-2\frac{3}{2}\frac{1}{2}\left[\chi^{\mathrm{SC},0}P^{ph\to pp}\nabla^{\mathrm{D}}\chi^{\mathrm{SC},0}P^{\overline{ph}\to pp}\nabla^{\mathrm{M}}\chi^{\mathrm{SC},0}\right]_{11}\\
&+(-\frac{3}{2})^3\left[\chi^{\mathrm{SC},0}P^{\overline{ph}\to pp}\nabla^{\mathrm{M}}\chi^{\mathrm{SC},0}P^{\overline{ph}\to pp}\nabla^{\mathrm{M}}\chi^{\mathrm{SC},0}P^{\overline{ph}\to pp}\nabla^{\mathrm{M}}\chi^{\mathrm{SC},0}\right]_{11}+\ldots\\
&\approx\left[\chi^{\mathrm{SC},0}\mathbf{M}^{\mathrm{SC}}\chi^{\mathrm{SC},0}\right]_{11}=\left[\chi^{\mathrm{SC},0}\mathbf{\Phi}^{\mathrm{SC}}\chi^{\mathrm{SC},0}\right]_{11}.
\end{aligned} \tag{5.9}$$

This alternative decomposition is illustrated diagrammatically in Fig. 5.11, the results for the corresponding fluctuation diagnostics together with a comparison to the previous data are displayed in Fig. 5.12.

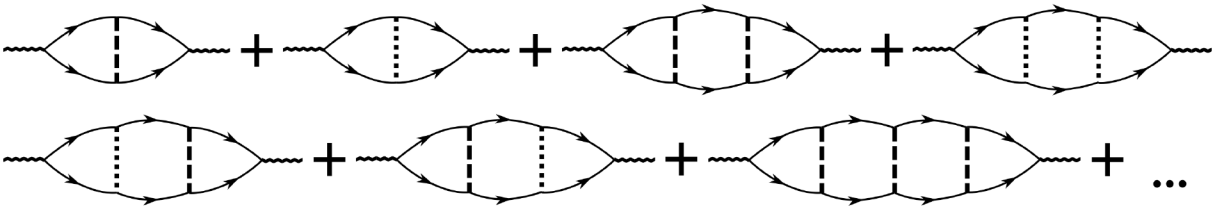

Figure 5.11: Bosonic fluctuation contributions to the d-wave superconducting susceptibility, where the dashed and dotted lines represent s-wave magnetic and density fluctuations ∇^{M} and ∇^{D} respectively. The first and second term corresponds to Eq. (5.8a) and Eq. (5.8b) respectively, while the sum of the remaining diagrams represent the multiboson exchange processes of $\left[\chi^{\mathrm{SC},0} M^{\mathrm{SC}} \chi^{\mathrm{SC},0}\right]_{11}$, given in Eq. (5.9).

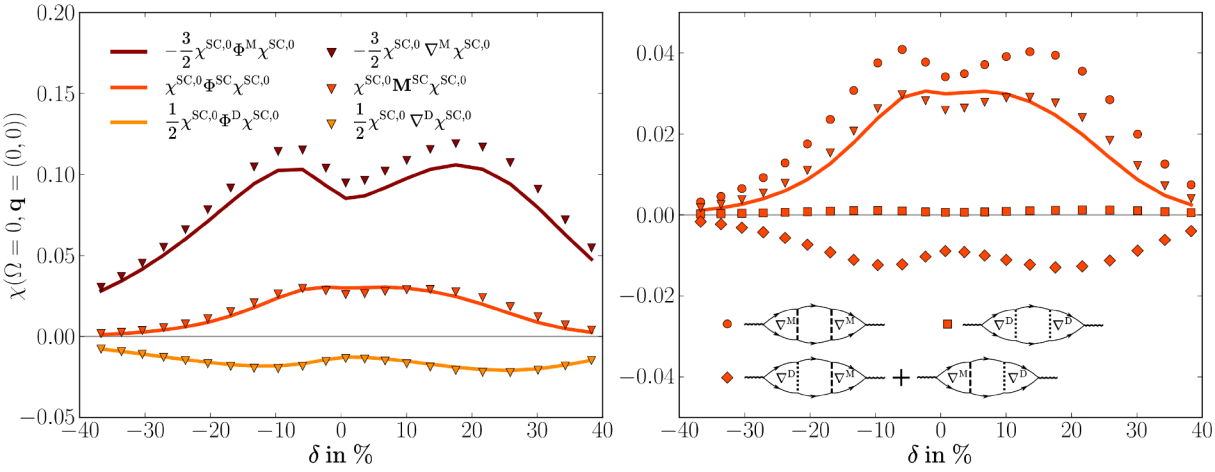

Figure 5.12: Fluctuation diagnostics based on single and multiboson processes. The SBE based fluctuation diagnostics is compared to the parquet based in the left panel. In the right panel $\left[\chi^{\mathrm{SC},0}\mathbf{M}^{\mathrm{SC}}\chi^{\mathrm{SC},0}\right]_{11}$ is broken down into the different two-boson contributions.

As we do not have direct access to $\nabla^{\mathrm{M/D}}$ within the parquet decomposition, we construct them from the high-frequency asymptotics (see Eq. 3.17). The contribution of the magnetic channel encoded in ∇^{M} is in qualitative agreement with the contribution of $\mathbf{\Phi}^{\mathrm{M}}$. The quantitative differences are due to the effect of the SBE rest function, which is most pronounced in the leading channel as discussed in Section 4.3. In fact, it does not affect the contribution of ∇^{D} that agrees very well with the one of $\mathbf{\Phi}^{\mathrm{D}}$ for all dopings. For the contributions to $\mathbf{\Phi}^{\mathrm{SC}}$ we focus on the two-boson processes for simplicity, since higher order multiboson diagrams are not fully included at the 2ℓ level. In Fig. 5.12 the results for the sum of the two-boson exchange processes reproduce the contribution of $\mathbf{\Phi}^{\mathrm{SC}}$ fairly well. This allows for the inclusion of multiboson exchanges in the postprocessing of χ^{SC} even when the flow of the rest function is neglected. We finally note that the magnetic and density fluctuations have opposite signs: while the magnetic fluctuations enhance the d-wave superconducting susceptibility, the density ones reduce it (see also the negative contribution of $\mathbf{\Phi}^{\mathrm{D}}$ in Fig. 5.7). Similarly, the multiboson contributions including an odd number of density bosons are negative as shown in the right panel of Fig. 5.12. This alternative decomposition hence offers a physically intuitive interpretation of the underlying fluctuations.

5.4.5 Role of U and t'

We now explore the role of the parameters U and t', which have been fixed for the previous analysis. In Fig. 5.13 we present a fluctuation diagnostics for $\delta = 21.5\%$, where χ^{SC} reaches its maximum for $\beta = 15$. For smaller values of the interaction, a qualitatively different picture with respect to the default $U = 3$ emerges: χ^{SC} is larger but entirely bubble driven, while the vertex corrections are almost negligible due to lack of AF fluctuations. For the same reason, the bubble itself is larger due to the reduced self-energy corrections. As a consequence, the dome structure is absent at weak coupling. It is, as of yet, unclear whether a minimal U is required to observe the behaviour detailed above, or if simply lower temperatures are necessary to see it in this case. As the interaction strength is increased, Φ^{M}_{00} grows and with it the

vertex as well as the self-energy, which in turn dampens the bubble, thus inducing a more correlated regime by $U = 3$.

The left panel of Fig. 5.14 shows the result for different values of t' for the same doping and $U = 3$ ($\beta = 15$). With increasing nearest-neighbour hopping amplitudes, the growing asymmetry leads to an enhancement of the dome at hole doping and to a suppression of the one in the electron-doped regime. However, the overall doping dependence of the different components turns out to be rather weak. Concerning the behavior as a function displayed in the right panel of Fig. 5.14, the maxima of both bubble and vertex contribution to the superconducting susceptibility shift to larger values with increasing $|t'|$. This effect is more pronounced for the bubble, whose maximum increases with $|t'|$, whereas the one of the vertex exhibits the largest value for $t' = 0$.

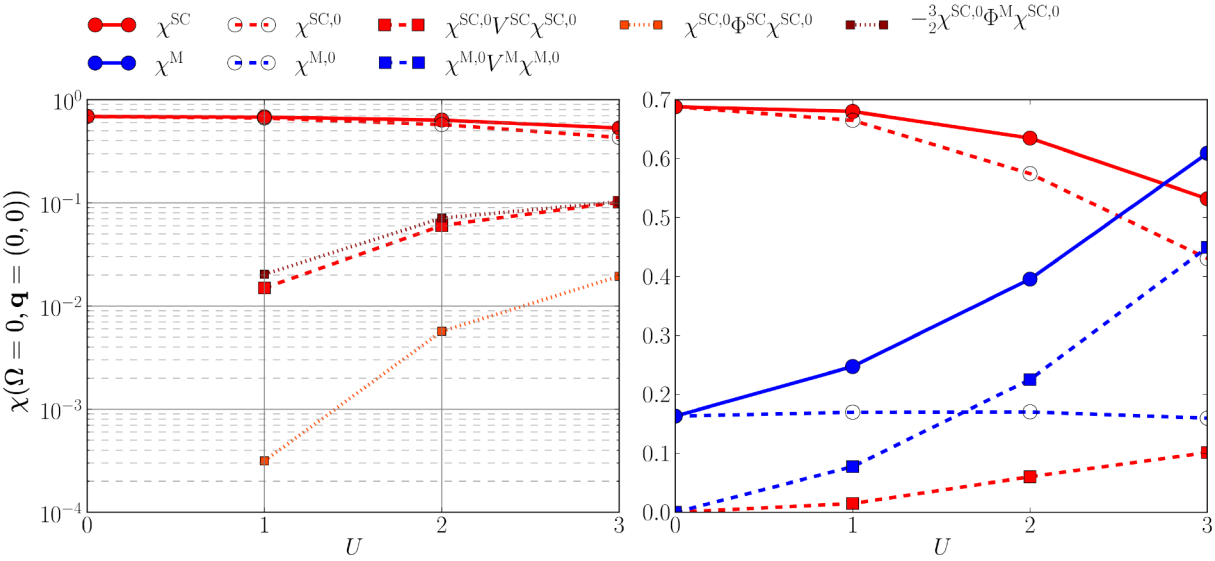

Figure 5.13: Dependence on the interaction strength U of the different contributions to the d-wave superconducting susceptibility $\chi^{SC}(\mathbf{q} = (0,0), i\omega = 0)$ of Fig. 5.7, for $\delta = 21.5$. The vertex contributions are shown in the left, the bubble and vertex corrections in the right panel, where the data for the magnetic susceptibility are reported for comparison.

We note that a large t' hopping amplitude of $\mathcal{O}(1)$ effectively alters the lattice geometry, leading to frustration that dampens the AF peak as well as all other susceptibilities. The optimal doping is hence determined by the maxima of both contributions being as close as possible in doping, and their sum (of the decreasing vertex and increasing bubble) being maximal. We note that these effects are very small on a quantitative level, as observed in Fig. 5.14. This also means that the reported results for the considered parameters are generic.

5.4.6 Summary: What drives superconductivity?

While the divergence of the magnetic channel can easily be traced to ladder diagrams and nesting of the Fermi surface, the picture is much more complex for the (d-wave) superconducting channel, characterized by a subtle interplay between various competing effects. In the following we will summarize the physical picture resulting from our detailed analysis.

A first prerequisite for substantial vertex corrections in the superconducting susceptibility are strong AF fluctuations. These are generated for sufficiently strong interactions. In addition, both the doping and the nearest-neighbour hopping amplitude has to be sufficiently small, since they suppress the AF fluctuations. We now discuss the interaction effects in more detail, considering the various components contributing to the susceptibility as introduced in the fluctuation diagnostics and the self-energy.

We saw that feedback of its imaginary part to $\mathbf{\Phi}^{M}$ leads to a double dome structure with a local minimum close to half filling. Hence, the large AF fluctuations around half filling drive both the importance of the magnetic channel in the vertex corrections and the screening induced by the self-energy. Another relevant mechanism is provided by the interplay between the magnetic, density, and superconducting channels and their mutual feedback: a large Φ^{M}_{00} enhances the other channels, whose feedback, on the

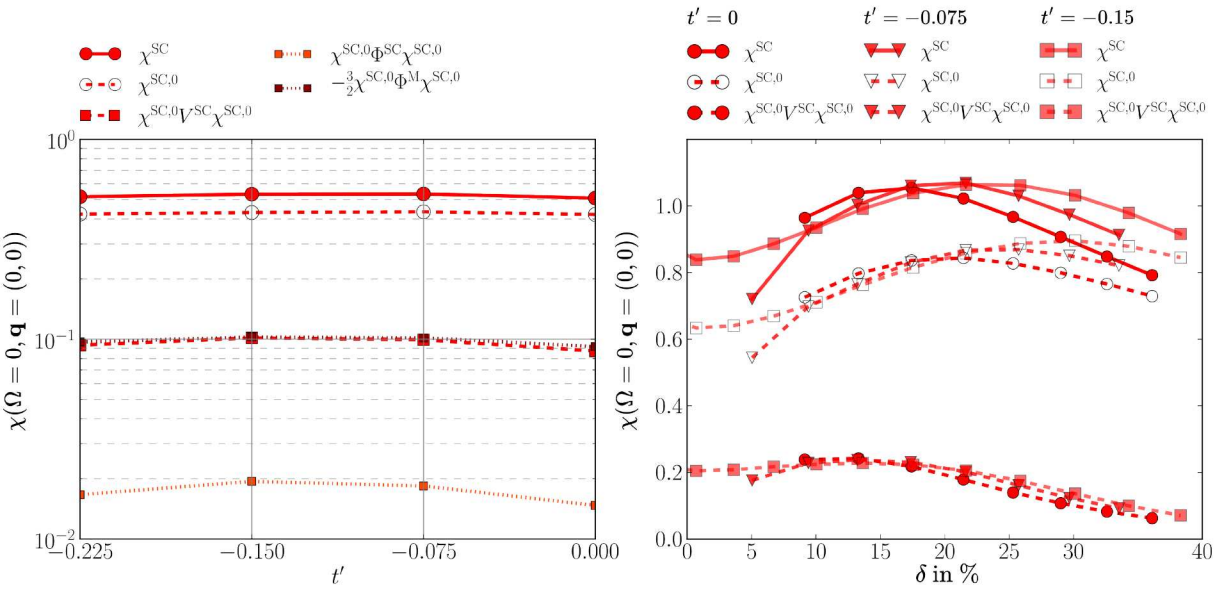

Figure 5.14: Contributions to the d-wave superconducting susceptibility $\chi^{\mathrm{SC}}(\Omega = 0, \mathbf{q} = (0,0))$ of Fig. 5.7, for $\delta = 21.5$ over the next-nearest-neighbour hopping parameter t'.

other hand, controls the divergent tendencies of $\overline{ph}$-ladders.

With increasing multiloop order Φ^{M}_{00} is renormalized, while the other d-wave channels and in particular the superconducting one, gain in importance as they rely on the input from other channels. The individual components of the susceptibility are influenced to varying degrees by the different mechanisms and physical parameters, such as temperature, doping, interaction strength, and next-nearest-neighbour hopping amplitudes.

5.5 Density susceptibility

For completeness, we briefly also discuss the results for the fluctuation diagnostics of the d-wave density susceptibility, shown in Fig. 5.15 for the same parameters as in Fig. 5.1. For χ^{D} significant vertex contributions are observed only around half filling for the d-wave component. In contrast, the s-wave components (see first and second rows of Fig. 5.15) of the bubble and vertex corrections are of a similar size but opposing sign. Their mutual cancellation leads to a very small overall s-wave density susceptibility χ^{D}_{00} with little dependence on δ, a behavior similar to the superconducting one discussed in the previous section. We also note that the wave vector corresponding to the maximal value shifts from $\mathbf{q} = (\pi, \pi)$ around half filling to incommensurate values at finite doping (shown in Fig. 5.3). Finally, we also consider the charge ordering, i.e., the charge density wave susceptibility at $\mathbf{q} = (0,0)$. This can be directly related to the (s-wave) charge compressibility $\kappa = 4\chi^{\mathrm{D}}$. The results are displayed in the bottom panels of Fig. 5.15.

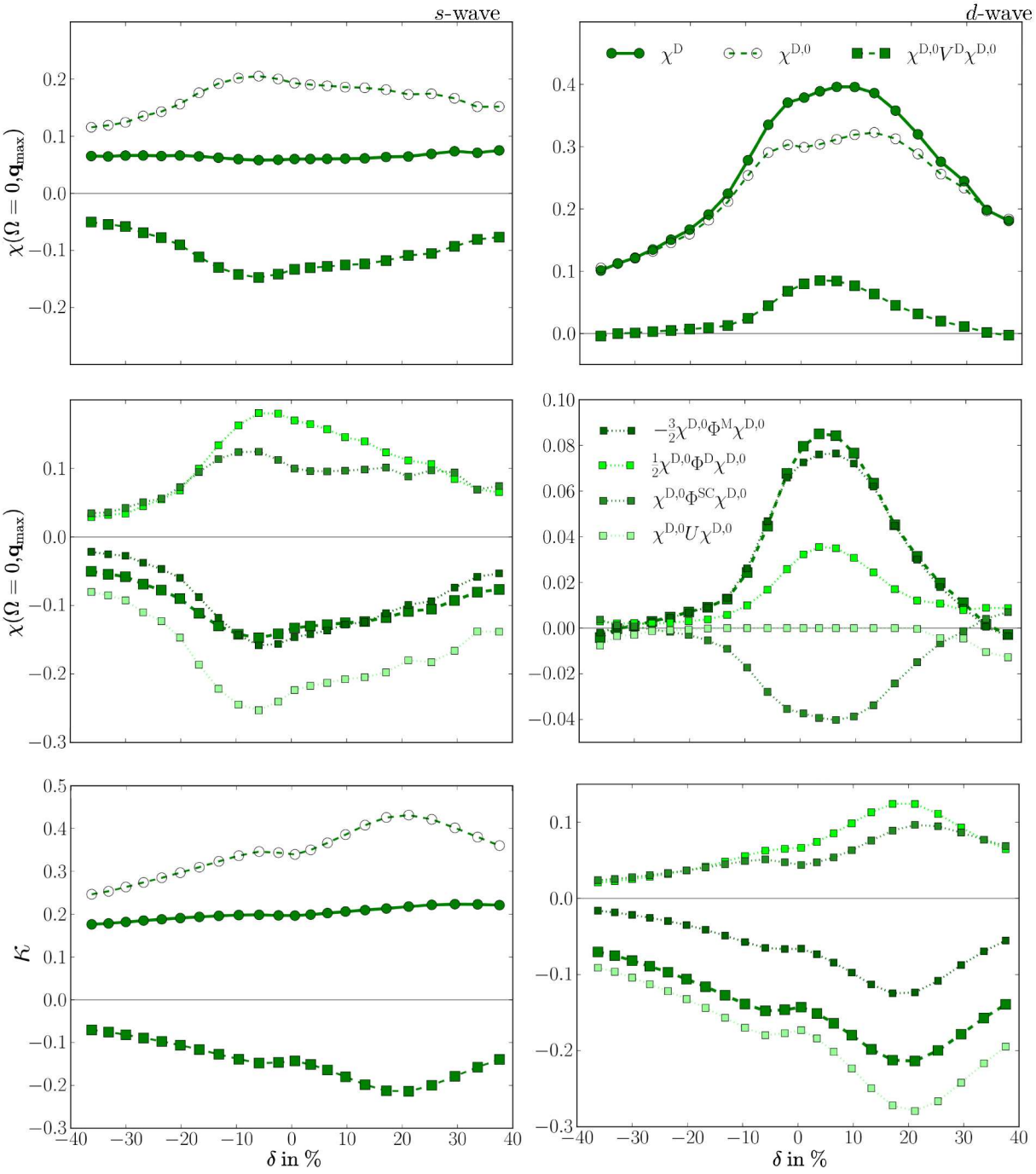

Figure 5.15: Fluctuation diagnostics of the density susceptibility $\chi^{\mathrm{D}}(\Omega = 0, \mathbf{q}_{\max})$ of Fig. 5.1, both for the s- and d-wave components (left and right panels respectively). Note that although the absolute values of the different d-wave contributions are smaller than the respective s-wave ones, they add up instead. In contrast, the negative sign of several s-wave contributions leads to a partial cancellation. The two bottom panels show the compressibility $\kappa = 4\chi^{\mathrm{D}}(\Omega = 0, \mathbf{q} = (0, 0))$.

6 Conclusions and Outlook

We have introduced the SBE formalism which splits the two-particle reducible vertices into single- and multiboson exchange processes and performed a detailed analysis of the advantages arising from bosonizing the two-particle reducible vertices in this way. In particular, we applied to the fRG for strongly correlated electron systems.

The fRG has proven to be particularly versatile in the way the SBE may be applied, leading to powerful new approximation schemes. Neglecting the flow of the rest function after deriving the flow equations was demonstrated to have a negligible effect on physical observables at the 1ℓ level, while resulting in a substantial reduction of the numerical effort in the weak coupling regime both at half filling and finite doping. We note that this approximation is not accessible in inherently self-consistent methods such as the parquet approximation. At larger couplings and lower temperatures, where the d-wave pairing correlations are expected to become relevant, the rest function should, however, be included. Additionally, the divergent behavior arising in proximity of the pseudo-critical temperature affects only the bosonic propagator, while the fermion-boson couplings and the rest functions, which depend on more frequency and momentum variables, remain finite. In contrast, in the conventional fermionic formulation of the fRG with high-frequency asymptotics all objects of a given channel grow very large in the RG flow by approaching the pseudo-critical instability.

On top of the algorithmic advantages, the classification of diagrams into a bosonic propagator, a fermion-boson coupling, and multiboson rest functions facilitates a deeper physical understanding of the two-particle vertex. The high-frequency behaviour is easily accessible and the relative importance of single- versus multiboson processes is highlighted. Moreover, the characteristic picture of bosons mediating effective interactions offers not only interpretative advantages for identifying the relevant degrees of freedom, but remains valid even at strong coupling [19, 94] and the close connection between w and χ allows direct access to physical observables.

Likewise, prior knowledge about the dominant collective excitations can be used to devise optimal approximations, as developed for the extended Hubbard model and its algorithmic implementation. By modifying the notion of bare interaction reducibility a handy computation scheme has been derived for the extension to nearest neighbour interactions, which does not increase the numerical effort compared to the conventional Hubbard model. Data obtained with and without accounting for the fermionic momentum dependence of the bare vertex and non-trivial high-frequency behaviour of the rest function and fermion-boson couplings were demonstrated to be in quantitative agreement. The SBE approximation was also confirmed to be applicable, which allowed us to perform numerically feasible scans of parameter space of the extended Hubbard model. Additionally, this scheme requires very little modification with respect to an existing implementation of the local Hubbard model. The reported flow equations for the multiloop extension of the fRG are applicable to the local and non-local Hubbard model alike. The same options of treating (or neglecting) the rest function, discussed in detail in the 1ℓ analysis, are also available at the multiloop level.

In addition to the multiloop corrections for the two-particle vertex, the flow equations for the self-energy has to be modified in the TUfRG in order to correctly account for the form factor projections and hence to recover the parquet approximation at loop convergence. To develop the TUfRG into a quantitative method the derivative of the SDE is used to replace the conventional self-energy flow equation [17]. Inserting the vertex expressed in SBE quantities (instead of two-particle reducible vertices) into the SDE flow equation is possible, however, a simpler expression for the SDE equation more natural to the SBE formalism is derived and its advantages discussed. In particular, the natural expression may also be directly employed for the extended Hubbard model, whereas the conventional formulation of the SDE was shown to be ill-suited to this case. Its effect in the different parameter regimes has to be further analysed in subsequent studies.

In summary, the SBE offers an intuitive connection to physical observables, reduced numerical effort, and a simplified implementation for the self-energy flow with the SDE, which allows for the extension to non-local interactions. These improvements could make quantitative fRG results available within reasonable run times. A promising alternative to the multiloop extensions is obtained by taking the derivatives of self-consistent equations for the bosonic propagator, the fermion-boson coupling, and the rest function directly, without their expansion in loop orders (see also [28, 79]). Whether the inclusion of the rest function is necessary to recover the Mermin Wagner theorem, remains an open question.

The SBE formulation paves a promising route for the combination with the dynamical mean-field theory (DMFT) [12, 95] in the so-called DMF^{2}RG [96, 97]. This would allow to access the non-perturbative regime on a quantitative level. Further, the SBE formulation offers the possibility to study mixed boson-fermion systems in presence of additional bosonic fields. Another promising future direction is the combination with recent advancements in the description of symmetry-broken phases [91, 98, 99, 100].

In the second part of the thesis, the magnetic, density, and superconducting pairing susceptibilities of the two-dimensional Hubbard model at weak coupling were calculated by using a fully frequency and momentum dependent fRG at the two-loop truncation level, which takes into account all channels in an unbiased way. Analysing the different fluctuation channels and their impact on the observed physical behavior, their evolution with temperature, interaction strength, and loop order was investigated, both in the electron as well as in the hole doped regime. A fluctuation diagnostic was performed by splitting the susceptibilities into the contribution from the various two-particle reducible vertices as well as a bare bubble contribution. This allows for a detailed study of the interplay between the channels. In particular, the impact of vertex corrections on both s- and d-wave components was determined and relevant normalization effects were identified. The performed fluctuation diagnostics allowed us to trace the influence of anti-ferromagnetic fluctuations on the d-wave superconductivity and provide an analytical understanding for the observed behavior. Finally, a connection is made to the SBE formalism, in particular the role of single- versus multiboson exchange processes.

Despite the consensus on the general phase diagram of the Hubbard model, many open challenges remain such as the determination of the precise location of phase boundaries and, in particular, the parameter region with d-wave superconductivity. The physics of models with more orbitals and/or longer ranged interactions remains largely unexplored with accurate methods, and reliable algorithms are yet to be developed. Using the implementation of the extended Hubbard model introduced here serves as a first step towards tackling nearest-neighbour interactions and longer ranged interactions may easily be added and/or applied to lattice geometries other than the square lattice. Such methods will be essential to connect calculations on the single-band model to multi-band Hubbard models and electronic structure Hamiltonians without resorting to crude downfolding techniques. Recent years have seen a rapid progress in this direction [10]. Nevertheless, the development of new, generally applicable numerical techniques which overcome the shortcomings of existing methods remains the most urgent need for addressing the open issues.

A Supplementary material: Model and Method

A.1 TUfRG: Form factors and channel projections

Throughout this appendix $\Phi_{nn'}(\Omega, \mathbf{q}, \nu, \nu')$ and $\Phi(\Omega, \mathbf{q}, \nu, n, \nu', n')$ are used interchangeably. The former serves to highlight the form factor arguments, where they are the main focus.

A.1.1 Projection matrices

Translating two-particle vertex-like quantities such as Φ, M or ∇ from one diagrammatic channel r to another r' is achieved with the help of the so-called 'projection matrices' $A^{r,r'}_{n,n',m,m'}(\mathbf{l}, \mathbf{q})$:

$$\Phi_x^{r'}(\Omega, \mathbf{q}, \nu, n, \nu', n') = P^{r\to r'}[\Phi_x^r](\Omega, \mathbf{q}, \nu, n, \nu', n') = \frac{1}{4\pi^2} \sum_{m,m',\mathbf{l}} A^{r,r'}_{n,n',m,m'}(\mathbf{l}, \mathbf{q}) \Phi_x^r(\tilde{\Omega}, \mathbf{l}, \tilde{\nu}, m, \tilde{\nu'}, m')$$

projects $\Phi_x^{r'}$ in r' notation to Φ_x^r in r notation. The frequency arguments $\tilde{\Omega}, \tilde{\nu}$ and $\tilde{\nu'}$ are chosen shifted (see Section 2.3.4), such that entering them in $\Phi_x^{r'}$ will yield the same result as entering Ω, ν and ν' in Φ_x^r.

ph → pp

$$\begin{aligned}\Phi_x^{pp} =& P^{ph\to pp}[\Phi_x^{ph}](\Omega, \mathbf{l}, \nu, n, \nu', n) \\ =& \frac{1}{4\pi^2} \sum_{m,m',\mathbf{l}} A^{ph,pp}_{n,n',m,m'}(\mathbf{l}, \mathbf{q}) \Phi_x^{ph}\left(\nu' - \nu, \mathbf{l}, \nu + \left\lceil \frac{\Omega}{2} \right\rceil + \left\lfloor \frac{\nu' - \nu}{2} \right\rfloor, m, \left\lfloor \frac{\Omega}{2} \right\rfloor - \nu' + \left\lfloor \frac{\nu' - \nu}{2} \right\rfloor - 1, m'\right)\end{aligned}$$

$$A^{ph,pp}_{n,n',m,m'}(\mathbf{l}, \mathbf{q}) = \sum_{\mathbf{R},\mathbf{R_1},\mathbf{R_2}} e^{i\mathbf{l}\mathbf{R} + i\mathbf{q}\mathbf{R_2}} \tilde{f}^*_n(\mathbf{R_1} - \mathbf{R}) \tilde{f}_{n'}(-\mathbf{R_2} - \mathbf{R}) \tilde{f}_m(\mathbf{R_1}) \tilde{f}^*_{m'}(\mathbf{R_2})$$

$\overline{\text{ph}}$ → pp

$$\begin{aligned}\Phi_x^{pp} =& P^{\overline{ph}\to pp}[\Phi_{\overline{ph}}](\Omega, \mathbf{q}, \nu, n, \nu', n') \\ =& \frac{1}{4\pi^2} \sum_{m,m',\mathbf{l}} A^{\overline{ph},pp}_{n,n',m,m'}(\mathbf{l}, \mathbf{q}) \cdot \\ & \Phi_x^{\overline{ph}}\left(-\nu - \nu' - \Omega\%2 - 1, \mathbf{l}, \nu + \left\lceil \frac{\Omega}{2} \right\rceil + \left\lfloor \frac{-\Omega\%2 - \nu - \nu' - 1}{2} \right\rfloor, m, \nu' + \left\lceil \frac{\Omega}{2} \right\rceil + \left\lfloor \frac{-\Omega\%2 - \nu - \nu' - 1}{2} \right\rfloor, m'\right)\end{aligned}$$

$$A^{\overline{ph},pp}_{n,n',m,m'}(\mathbf{l}, \mathbf{q}) = \sum_{\mathbf{R},\mathbf{R_1},\mathbf{R_2}} e^{i\mathbf{l}\mathbf{R} - i\mathbf{q}\mathbf{R}} \tilde{f}^*_n(\mathbf{R_1} - \mathbf{R}) \tilde{f}_{n'}(\mathbf{R_2} + \mathbf{R}) \tilde{f}_m(\mathbf{R_1}) \tilde{f}^*_{m'}(\mathbf{R_2})$$

pp → ph

$$\begin{aligned}\Phi_x^{ph} =& P^{pp\to ph}[\Phi_x^{pp}](\Omega, \mathbf{q}, \nu, n, \nu', n') \\ =& \frac{1}{4\pi^2} \sum_{m,m',\mathbf{l}} A^{pp,ph}_{n,n',m,m'}(\mathbf{l}, \mathbf{q}) \cdot \\ & \Phi_x^{pp}\left(\nu + \nu' + \Omega\%2 + 1, \mathbf{l}, \nu - \left\lfloor \frac{\Omega}{2} \right\rfloor - \left\lceil \frac{\nu + \nu' + \Omega\%2 + 1}{2} \right\rceil, m, \nu + \left\lceil \frac{\Omega}{2} \right\rceil - \left\lceil \frac{\nu + \nu' + \Omega\%2 + 1}{2} \right\rceil, m'\right)\end{aligned}$$

$$A^{pp,ph}_{n,n',m,m'}(\mathbf{l},\mathbf{q}) = \sum_{\mathbf{R},\mathbf{R_1},\mathbf{R_2}} e^{i\mathbf{l}(\mathbf{R_2}-\mathbf{R})+i\mathbf{q}\mathbf{R}} \tilde{f}^*_n(\mathbf{R_1}-\mathbf{R})\tilde{f}_{n'}(\mathbf{R}-\mathbf{R_2})\tilde{f}_m(\mathbf{R_1})\tilde{f}^*_{m'}(\mathbf{R_2})$$

$\overline{\text{ph}} \to \text{ph}$

$$\begin{aligned}\Phi^{ph}_x =& P^{\overline{ph}\to ph}[\Phi^{\overline{ph}}_x](\Omega,\mathbf{q},\nu,n,\nu',n') \\ =& \frac{1}{4\pi^2}\sum_{m,m',\mathbf{l}} A^{\overline{ph},ph}_{n,n',m,m'}(\mathbf{l},\mathbf{q})\Phi^{\overline{ph}}_x\left(\nu'-\nu,\mathbf{l},\nu-\left\lfloor\frac{\Omega}{2}\right\rfloor+\left\lfloor\frac{\nu'-\nu}{2}\right\rfloor,m,\nu'+\left\lceil\frac{\Omega}{2}\right\rceil+\left\lceil\frac{\nu'-\nu}{2}\right\rceil,m'\right)\end{aligned}$$

$$A^{\overline{ph},ph}_{n,n',m,m'}(\mathbf{l},\mathbf{q}) = \sum_{\mathbf{R},\mathbf{R_1},\mathbf{R_2}} e^{i\mathbf{l}\mathbf{R}+i\mathbf{q}\mathbf{R_2}} \tilde{f}^*_n(\mathbf{R_1}-\mathbf{R_2}-\mathbf{R})\tilde{f}_{n'}(-\mathbf{R})\tilde{f}_m(\mathbf{R_1})\tilde{f}^*_{m'}(\mathbf{R_2})$$

$\text{pp} \to \overline{\text{ph}}$

$$\begin{aligned}\Phi^{\overline{ph}}_x =& P^{pp\to\overline{ph}}[\Phi^{pp}_x](\Omega,\mathbf{q},\nu,n,\nu',n') \\ =& \frac{1}{4\pi^2}\sum_{m,m',\mathbf{l}} A^{pp,\overline{ph}}_{n,n',m,m'}(\mathbf{l},\mathbf{q})\cdot \\ & \Phi^{pp}_x\left(\nu+\nu'+\Omega\%2+1,\mathbf{l},\nu-\left\lfloor\frac{\Omega}{2}\right\rfloor-\left\lceil\frac{\nu+\nu'+\Omega\%2+1}{2}\right\rceil,m,\nu'-\left\lfloor\frac{\Omega}{2}\right\rfloor-\left\lceil\frac{\nu+\nu'+\Omega\%2+1}{2}\right\rceil,m'\right)\end{aligned}$$

$$A^{pp,\overline{ph}}_{n,n',m,m'}(\mathbf{l},\mathbf{q}) = \sum_{\mathbf{R},\mathbf{R_1},\mathbf{R_2}} e^{i\mathbf{l}\mathbf{R}-i\mathbf{q}\mathbf{R}} \tilde{f}^*_n(\mathbf{R}+\mathbf{R_1})\tilde{f}_{n'}(-\mathbf{R}+\mathbf{R_2})\tilde{f}_m(\mathbf{R_1})\tilde{f}^*_{m'}(\mathbf{R_2})$$

$\text{ph} \to \overline{\text{ph}}$

$$\begin{aligned}\Phi^{\overline{ph}}_x =& P^{ph\to\overline{ph}}[\Phi^{ph}_x](\Omega,\mathbf{q},\nu,n,\nu',n') \\ =& \frac{1}{4\pi^2}\sum_{m,m',\mathbf{l}} A^{ph,\overline{ph}}_{n,n',m,m'}(\mathbf{l},\mathbf{q})\Phi^{ph}_x\left(\nu'-\nu,\mathbf{l},\nu-\left\lfloor\frac{\Omega}{2}\right\rfloor+\left\lfloor\frac{\nu'-\nu}{2}\right\rfloor,m,\nu'+\left\lceil\frac{\Omega}{2}\right\rceil-\left\lceil\frac{\nu'-\nu}{2}\right\rceil,m'\right)\end{aligned}$$

$$A^{ph,\overline{ph}}_{n,n',m,m'}(\mathbf{l},\mathbf{q}) = \sum_{\mathbf{R},\mathbf{R_1},\mathbf{R_2}} e^{i\mathbf{l}\mathbf{R}+i\mathbf{q}\mathbf{R_2}} \tilde{f}^*_n(\mathbf{R_1}-\mathbf{R}-\mathbf{R_2})\tilde{f}_{n'}(-\mathbf{R})\tilde{f}_m(\mathbf{R_1})\tilde{f}^*_{m'}(\mathbf{R_2})$$

The 'physical channels' are linear combinations of diagrammatic channels. They do not come with their own notation, instead they are expressed in purely fermionic or diagrammatic notation. Due to the close connection between diagrammatic and physical channels, the natural notation of the SC/D/M-channel is *pp*/*ph*/$\overline{ph}$-notation respectively. Projection matrices are used in the same way to translate from one notation to another.

A.1.2 Derivation of the TUfRG

In the main body the flow equations were given in terms of fermionic momenta. In this section the flow equations for the form factor expanded Φ are derived by insertion of unity [68]. These insertions are expressed via the completeness relation of the form factor basis, which is subsequently approximated by limiting the basis to a select few form factors; the eponymous truncated unity.

By exploiting $\mathbb{1} = \int d\mathbf{p}'\ \delta(\mathbf{p}-\mathbf{p}') = \int d\mathbf{p}' \sum_n f_n(\mathbf{p}')f_n(\mathbf{p})$ with $\sum_n f_n(\mathbf{p}')f_n(\mathbf{p}) = \delta(\mathbf{p}-\mathbf{p}')$ the 1ℓ flow

equations can be rewritten as

$$
\begin{aligned}
\dot{\Phi}^{\eta}(q,k,k') &= \int \mathrm{d}p\ \mathbb{1} V^{\eta}(q,k,p)\mathbb{1}\dot{\Pi}^{\eta}(q,p)\mathbb{1}V^{\eta}(q,p,k')\mathbb{1} \\
&= \int \mathrm{d}p \int \mathrm{d}\tilde{k}\delta(\mathbf{k}-\tilde{\mathbf{k}}) \int \mathrm{d}\tilde{p}\delta(\mathbf{p}-\tilde{\mathbf{p}})V^{\eta}(q,\tilde{k},\tilde{p})\dot{\Pi}^{\eta}(q,p) \int \mathrm{d}\tilde{\tilde{p}}\delta(\mathbf{p}-\tilde{\tilde{\mathbf{p}}}) \int \mathrm{d}\tilde{k}'\delta(\mathbf{k}'-\tilde{\mathbf{k}}')V^{\eta}(q,\tilde{\tilde{p}},\tilde{k}') \\
&= \int \mathrm{d}p \int \mathrm{d}\tilde{k} \sum_{m} f_m(\tilde{\mathbf{k}})f_m(\mathbf{k}) \int \mathrm{d}\tilde{p} \sum_{m'} f_{m'}(\tilde{\mathbf{p}})f_{m'}(\mathbf{p})V^{\eta}(q,\tilde{k},\tilde{p})\dot{\Pi}^{\eta}(q,p) \\
&\quad \int \mathrm{d}\tilde{\tilde{p}} \sum_{n'} f_{n'}(\tilde{\tilde{\mathbf{p}}})f_{n'}(\mathbf{p}) \int \mathrm{d}\tilde{k}' \sum_{n} f_n(\tilde{\mathbf{k}}')f_n(\mathbf{k}')V^{\eta}(q,\tilde{\tilde{p}},\tilde{k}') \\
&= \sum_{\substack{m,n \\ m',n'}} f_m(\mathbf{k})f_n(\mathbf{k}') \underbrace{\left(\int \mathrm{d}\tilde{k}\ f_m(\tilde{\mathbf{k}}) \int \mathrm{d}\tilde{p}\ f_{m'}(\tilde{\mathbf{p}})V^{\eta}(q,\tilde{k},\tilde{p}) \right)}_{V^{\eta}_{m,m'}(\Omega,\mathbf{q},\nu,\nu')} \underbrace{\left(\int \mathrm{d}p\ f_{m'}(\mathbf{p})f_{n'}(\mathbf{p})\dot{\Pi}(q,p) \right)}_{\dot{\Pi}^{\eta}_{m',n'}(\Omega,\mathbf{q},\nu')} \\
&\quad \underbrace{\left(\int \mathrm{d}\tilde{k}'\ f_n(\tilde{\mathbf{k}}') \int \mathrm{d}\tilde{\tilde{p}}\ f_{n'}(\tilde{\tilde{\mathbf{p}}})V^{\eta}(q,\tilde{\tilde{p}},\tilde{k}') \right)}_{V^{\eta}_{n',n}(\Omega,\mathbf{q},\nu',\nu'')} \\
&= \sum_{m,n} f_m(\mathbf{k})f_n(\mathbf{k}') \boxed{\sum_{m',n',\nu',\nu''} V^{\eta}_{m,m'}(\Omega,\mathbf{q},\nu,\nu')\dot{\Pi}^{\eta}_{m',n'}(\Omega,\mathbf{q},\nu')V_{n',n}(\Omega,\mathbf{q},\nu')} \\
&= \sum_{m,n} f_m(\mathbf{k})f_n(\mathbf{k}')\dot{\Phi}^{\eta}_{mn}(\Omega,\mathbf{q},\nu,\nu'').
\end{aligned}
$$

The content of the box represents the flow equation expanded in form factors. Limiting the number of form factors considered corresponds to truncating the sum $\int \mathrm{d}\mathbf{p}' \sum_n f_n(\mathbf{p}')f_n(\mathbf{p}) = \mathbb{1}$. Note that the bubble depends on two form factors, despite having only one fermionic momentum dependence before the expansion.

A.2 Relations between diagrammatic and physical channels

The parquet decomposition in diagrammatic channels and expanded in form factors yields

$$
\begin{aligned}
V^{pp}_{nn'}(\Omega,\mathbf{q},\nu,\nu') &= \Phi_{pp,nn'}(\Omega,\mathbf{q},\nu,\nu') + P^{ph\to pp}[\Phi_{ph}]_{nn'}(\Omega,\mathbf{q},\nu,\nu') + P^{\overline{ph}\to pp}[\Phi_{\overline{ph}}]_{nn'}(\Omega,\mathbf{q},\nu,\nu') + U \\
V^{ph}_{nn'}(\Omega,\mathbf{q},\nu,\nu') &= P^{pp\to ph}[\Phi_{pp}]_{nn'}(\Omega,\mathbf{q},\nu,\nu') + \Phi_{ph,nn'}(\Omega,\mathbf{q},\nu,\nu') + P^{\overline{ph}\to ph}[\Phi_{\overline{ph}}]_{nn'}(\Omega,\mathbf{q},\nu,\nu') + U \\
V^{\overline{ph}}_{nn'}(\Omega,\mathbf{q},\nu,\nu') &= P^{pp\to \overline{ph}}[\Phi_{pp}]_{nn'}(\Omega,\mathbf{q},\nu,\nu') + P^{ph\to \overline{ph}}[\Phi_{ph}]_{nn'}(\Omega,\mathbf{q},\nu,\nu') + \Phi_{\overline{ph},nn'}(\Omega,\mathbf{q},\nu,\nu') + U
\end{aligned}
$$

and $\mathcal{I}_{r,nn'} = V^{r}_{nn'} - \Phi_{r,nn'}$. The equivalent equations in physical channels are

$$
\begin{aligned}
V^{\mathrm{SC}}_{nn'}(\Omega,\mathbf{q},\nu,\nu') &= \Phi^{\mathrm{SC}}_{nn'}(\Omega,\mathbf{q},\nu,\nu') + \frac{1}{2}P^{ph\to pp}[\Phi^{\mathrm{D}} - \Phi^{\mathrm{M}}]_{nn'}(\Omega,\mathbf{q},\nu,\nu') - P^{\overline{ph}\to pp}[\Phi^{\mathrm{M}}]_{nn'}(\Omega,\mathbf{q},\nu,\nu') + U \\
V^{\mathrm{D}}_{nn'}(\Omega,\mathbf{q},\nu,\nu') &= 2P^{pp\to ph}[\Phi^{\mathrm{SC}}]_{nn'}(\Omega,\mathbf{q},\nu,\nu') - P^{pp\to \overline{ph}}[\Phi^{\mathrm{SC}}]_{nn'}(\Omega,\mathbf{q},\nu,\nu') + \Phi^{\mathrm{D}}_{nn'}(\Omega,\mathbf{q},\nu,\nu') \\
&\quad -2P^{\overline{ph}\to ph}[\Phi^{\mathrm{M}}]_{nn'}(\Omega,\mathbf{q},\nu,\nu') - \frac{1}{2}P^{ph\to \overline{ph}}[\Phi^{\mathrm{D}} - \Phi^{\mathrm{M}}]_{nn'}(\Omega,\mathbf{q},\nu,\nu') + U \\
V^{\mathrm{M}}_{nn'}(\Omega,\mathbf{q},\nu,\nu') &= -P^{pp\to \overline{ph}}[\Phi^{\mathrm{SC}}]_{nn'}(\Omega,\mathbf{q},\nu,\nu') - \frac{1}{2}P^{ph\to \overline{ph}}[\Phi^{\mathrm{D}} - \Phi^{\mathrm{M}}]_{nn'}(\Omega,\mathbf{q},\nu,\nu') + \Phi^{\mathrm{M}}_{nn'}(\Omega,\mathbf{q},\nu,\nu') - U
\end{aligned}
$$

and again $\mathcal{I}^{\eta}_{nn'} = V^{\eta}_{nn'} - \Phi^{\eta}_{nn'}$.

A.3 Flow equations in diagrammatic channels

The flow equations of the two-particle vertex expressed in diagrammatic channels are [30]

$$\begin{aligned}
\dot{\phi}_{pp}(k_1+k_3,k_1,k_2) :=& \partial_\Lambda \phi^\Lambda_{pp}(k_1+k_3,k_1,k_2) \\
=& \int \mathrm{d}p\; V(k_1,p,k_3,k_1+k_3-p)\dot{\Pi}_{pp}(k_1+k_3,p)V(p,k_2,k_1+k_3-p,k_4) \qquad \text{(A.1)} \\
\dot{\phi}_{\overline{ph}}(k_3-k_2,k_1,k_2) :=& \partial_\Lambda \phi^\Lambda_{\overline{ph}}(k_3-k_2,k_1,k_2) \\
=& \int \mathrm{d}p\; V(k_1,p,k_3-k_2+p,k_4)\dot{\Pi}_{ph}(k_3-k_2,p)V(p,k_2,k_3,k_3-k_2+p) \qquad \text{(A.2)} \\
\dot{\phi}_{ph}(k_2-k_1,k_1,k_4) :=& \partial_\Lambda \phi^\Lambda_{ph}(k_2-k_1,k_1,k_4) \\
=& \int \mathrm{d}p\; -2V(k_1,k_2,k_2-k_1,p)\dot{\Pi}_{ph}(k_2-k_1+p,p)V(p,k_2-k_1+p,k_3,k_4) \\
&+ V(k_1,p,k_2-k_1+p,k_2)\dot{\Pi}_{ph}(k_2-k_1+p,p)V(p,k_2-k_1+p,k_3,k_4) \\
&+ V(k_1,k_2,k_2-k_1,p)\dot{\Pi}_{ph}(k_2-k_1+p,p)V(p,k_4,k_3,k_2-k_1+p). \qquad \text{(A.3)}
\end{aligned}$$

The slightly more involved form of $\dot{\phi}_{ph}$ is one of the motivating factors for the use of physical channels. Multiloop flow equations in physical and diagrammatic channels are also found in [30].

A.4 Flow equations expanded in form factors

The 1ℓ flow equations expanded in form factors are

$$\dot{\Phi}^{\eta,(1)}_{nn'}(\Omega,\mathbf{q},\nu,\nu') = \sum_{mm'\nu''} V^\eta_{nm}(\Omega,\mathbf{q},\nu,\nu'')\dot{\Pi}^\eta_{mm'}(\Omega,\mathbf{q},\nu'')V^\eta_{m'n'}(\Omega,\mathbf{q},\nu'',\nu'). \qquad \text{(A.4)}$$

The multiloop corrections are

$$\dot{\Phi}^{\eta,(\ell+1),L}_{nn'}(\Omega,\mathbf{q},\nu,\nu') = \sum_{mm'\nu''} \dot{\mathcal{I}}^{\eta,(\ell)}_{nm}(\Omega,\mathbf{q},\nu,\nu'')\Pi^\eta_{mm'}(\Omega,\mathbf{q},\nu'')V^\eta_{m'n'}(\Omega,\mathbf{q},\nu'',\nu') \qquad \text{(A.5a)}$$

$$\dot{\Phi}^{\eta,(\ell+1),R}_{nn'}(\Omega,\mathbf{q},\nu,\nu') = \sum_{mm'\nu''} V^\eta_{nm}(\Omega,\mathbf{q},\nu,\nu'')\Pi^\eta_{pp,mm'}(\Omega,\mathbf{q},\nu'')\dot{\mathcal{I}}^{\eta,(\ell)}_{m'n'}(\Omega,\mathbf{q},\nu'',\nu') \qquad \text{(A.5b)}$$

$$\dot{\Phi}^{\eta,(\ell+2),C}_{nn'}(\Omega,\mathbf{q},\nu,\nu') = \sum_{mm'\nu''} \dot{\Phi}^{\eta,(\ell),R}_{nm}(\Omega,\mathbf{q},\nu,\nu'')\Pi^\eta_{mm'}(\Omega,\mathbf{q},\nu'')V^\eta_{m'n'}(\Omega,\mathbf{q},\nu'',\nu'). \qquad \text{(A.5c)}$$

B Supplementary material: SBE for fRG

B.1 Input V for the conventional self-energy flow equation

In physical channels and form factor notation the vertex, as it is inserted into the conventional flow equation of Σ (Eq. (2.24)), reads

$$\begin{aligned}
&V((\nu_1,\mathbf{k}_1),(\nu_2,\mathbf{k}_2),(\nu_3,\mathbf{k}_3),(\nu_4,\mathbf{k}_4))\\
&\quad=\sum_{n,n'}\big[f_n(\mathbf{k}_1)\lambda_{pp}(\nu_1+\nu_3,\mathbf{k}_1+\mathbf{k}_3,\nu_1,n)(w_{pp}(\nu_1+\nu_3,\mathbf{k}_1+\mathbf{k}_3)-U)\bar{\lambda}_{pp}(\nu_1+\nu_3,\mathbf{k}_1+\mathbf{k}_3,\nu_2,n')f_{n'}(\mathbf{k}_2)\\
&\qquad+f_n(\mathbf{k}_1)M_{pp}(\nu_1+\nu_3,\mathbf{k}_1+\mathbf{k}_3,\nu_1,n,\nu_2,n')f_{n'}(\mathbf{k}_2)\\
&\qquad+f_n(\mathbf{k}_1)\lambda_{\overline{ph}}(\nu_3-\nu_2,\mathbf{k}_3-\mathbf{k}_2,\nu_1,n)(w_{\overline{ph}}(\nu_3-\nu_2,\mathbf{k}_3-\mathbf{k}_2)-U)\bar{\lambda}_{\overline{ph}}(\nu_3-\nu_2,\mathbf{k}_3-\mathbf{k}_2,\nu_2,n')f_{n'}(\mathbf{k}_2)\\
&\qquad+f_n(\mathbf{k}_1)M_{\overline{ph}}(\nu_3-\nu_2,\mathbf{k}_3-\mathbf{k}_2,\nu_1,n,\nu_2,n')f_{n'}(\mathbf{k}_2)\\
&\qquad+f_n(\mathbf{k}_1)\lambda_{ph}(\nu_2-\nu_1,\mathbf{k}_2-\mathbf{k}_1,\nu_1,n)(w_{ph}(\nu_2-\nu_1,\mathbf{k}_2-\mathbf{k}_1)-U)\bar{\lambda}_{ph}(\nu_2-\nu_1,\mathbf{k}_2-\mathbf{k}_1,\nu_4,n')f_{n'}(\mathbf{k}_4)\\
&\qquad+f_n(\mathbf{k}_1)M_{ph}(\nu_2-\nu_1,\mathbf{k}_2-\mathbf{k}_1,\nu_1,n,\nu_4,n')f_{n'}(\mathbf{k}_4)+U\big],
\end{aligned}\tag{B.1}$$

and in physical channels

$$\begin{aligned}
&V((\nu_1,\mathbf{k}_1),(\nu_2,\mathbf{k}_2),(\nu_3,\mathbf{k}_3),(\nu_4,\mathbf{k}_4))\\
&\quad=\sum_{n,n'}\big[f_n(\mathbf{k}_1)\lambda^{\mathrm{SC}}(\nu_1+\nu_3,\mathbf{k}_1+\mathbf{k}_3,\nu_1,n)(w^{\mathrm{SC}}(\nu_1+\nu_3,\mathbf{k}_1+\mathbf{k}_3)-U)\lambda^{\mathrm{SC}}(\nu_1+\nu_3,\mathbf{k}_1+\mathbf{k}_3,\nu_2,n')f_{n'}(\mathbf{k}_2)\\
&\qquad+f_n(\mathbf{k}_1)M^{\mathrm{SC}}(\nu_1+\nu_3,\mathbf{k}_1+\mathbf{k}_3,\nu_1,n,\nu_2,n')f_{n'}(\mathbf{k}_2)\\
&\qquad-f_n(\mathbf{k}_1)\lambda^{\mathrm{M}}(\nu_3-\nu_2,\mathbf{k}_3-\mathbf{k}_2,\nu_1,n)(w^{\mathrm{M}}(\nu_3-\nu_2,\mathbf{k}_3-\mathbf{k}_2)-U)\lambda^{\mathrm{M}}(\nu_3-\nu_2,\mathbf{k}_3-\mathbf{k}_2,\nu_2,n')f_{n'}(\mathbf{k}_2)\\
&\qquad-f_n(\mathbf{k}_1)M^{\mathrm{M}}(\nu_3-\nu_2,\mathbf{k}_3-\mathbf{k}_2,\nu_1,n,\nu_2,n')f_{n'}(\mathbf{k}_2)\\
&\qquad-\frac{1}{2}f_n(\mathbf{k}_1)\lambda^{\mathrm{M}}(\nu_2-\nu_1,\mathbf{k}_2-\mathbf{k}_1,\nu_1,n)(w^{\mathrm{M}}(\nu_2-\nu_1,\mathbf{k}_2-\mathbf{k}_1)-U)\lambda^{\mathrm{M}}(\nu_2-\nu_1,\mathbf{k}_2-\mathbf{k}_1,\nu_4,n')f_{n'}(\mathbf{k}_4)\\
&\qquad-\frac{1}{2}f_n(\mathbf{k}_1)M^{\mathrm{M}}(\nu_2-\nu_1,\mathbf{k}_2-\mathbf{k}_1,\nu_1,n,\nu_4,n')f_{n'}(\mathbf{k}_4)\\
&\qquad+\frac{1}{2}f_n(\mathbf{k}_1)\lambda^{\mathrm{D}}(\nu_2-\nu_1,\mathbf{k}_2-\mathbf{k}_1,\nu_1,n)(w^{\mathrm{D}}(\nu_2-\nu_1,\mathbf{k}_2-\mathbf{k}_1)-U)\lambda^{\mathrm{D}}(\nu_2-\nu_1,\mathbf{k}_2-\mathbf{k}_1,\nu_4,n')f_{n'}(\mathbf{k}_4)\\
&\qquad+\frac{1}{2}f_n(\mathbf{k}_1)M^{\mathrm{D}}(\nu_2-\nu_1,\mathbf{k}_2-\mathbf{k}_1,\nu_1,n,\nu_4,n')f_{n'}(\mathbf{k}_4)\\
&\qquad+U\big].
\end{aligned}\tag{B.2}$$

B.2 SBE quantities in physical channels

This appendix translates the equations given in Section 3.2 to physical channels. The physical channels are labelled by η compared to r used for diagrammatic channels. Unless specified otherwise, the magnetic/density/superconducting channels are given in $\overline{ph}$/ph/pp-notation respectively. The bare interaction in physical channels is

$$\begin{aligned}
\mathcal{I}^{\mathrm{M}}_{\mathrm{bare}}(\mathbf{q},k,k') &= -U\\
\mathcal{I}^{\mathrm{D}}_{\mathrm{bare}}(\mathbf{q},k,k') &= U\\
\mathcal{I}^{\mathrm{SC}}_{\mathrm{bare}}(\mathbf{q},k,k') &= U.
\end{aligned}$$

The sum of all U-reducible diagrams of a given physical channel is

$$\nabla^\eta = \lambda^\eta w^\eta \lambda^\eta.$$

and the sum of all two-particle reducible diagrams of a given physical channel are

$$\Phi^\eta = \nabla^\eta - \mathcal{I}^\eta_{\text{bare}} + M^\eta.$$

The bare interaction irreducible vertex in a physical channel is defined by $\mathcal{I}^\eta_{\text{SBE}} = V^\eta - \nabla^\eta$ with

$$\mathcal{I}^{\text{SC}}_{\text{SBE}} = M^{\text{SC}} + \frac{1}{2}P^{ph\to pp}[\nabla^{\text{D}} + M^{\text{D}} - (\nabla^{\text{M}} + M^{\text{M}})] - P^{\overline{ph}\to pp}[\nabla^{\text{M}} + M^{\text{M}}] - 2\mathcal{I}^{\text{SC}}_{\text{bare}} \tag{B.3a}$$

$$\mathcal{I}^{\text{D}}_{\text{SBE}} = 2P^{pp\to ph}\left[\nabla^{\text{SC}} + M^{\text{SC}}\right] - P^{pp\to\overline{ph}}\left[\nabla^{\text{SC}} + M^{\text{SC}}\right] + M^{\text{D}} - 2P^{\overline{ph}\to ph}\left[\nabla^{\text{M}} + M^{\text{M}}\right] - \frac{1}{2}P^{ph\to\overline{ph}}\left[\nabla^{\text{D}} + M^{\text{D}} - \left(\nabla^{\text{M}} + M^{\text{M}}\right)\right] - 2\mathcal{I}^{\text{D}}_{\text{bare}} \tag{B.3b}$$

$$\mathcal{I}^{\text{M}}_{\text{SBE}} = -P^{pp\to\overline{ph}}\left[\nabla^{\text{SC}} + M^{\text{SC}}\right] - \frac{1}{2}P^{ph\to\overline{ph}}\left[\nabla^{\text{D}} + M^{\text{D}} - \left(\nabla^{\text{M}} + M^{\text{M}}\right)\right] + M^{\text{M}} - 2\mathcal{I}^{\text{M}}_{\text{bare}}. \tag{B.3c}$$

The structure of the fermion-boson vertices remains unchanged

$$\lambda^\eta(q,k) = 1 + \int \mathrm{d}p\, \mathcal{I}^\eta_{\text{SBE}}(q,k,p)\Pi^\eta(q,p) \tag{B.4a}$$

$$\begin{aligned}
\lambda^\eta(\Omega,\mathbf{q},\nu,n) =& \delta_{n,0} + \sum_{\nu' m} \mathcal{I}^\eta_{\text{SBE}}(\Omega,\mathbf{q},\nu,n,\nu',m)\Pi^\eta(\Omega,\mathbf{q},\nu',m,0) \qquad \text{(B.4b)}\\
=& \delta_{n,0} + \sum_{\nu' m} (S^\eta(\Omega,\mathbf{q},\nu,n,\nu',m) + M^\eta(\Omega,\mathbf{q},\nu,n,\nu',m))\Pi^\eta(\Omega,\mathbf{q},\nu',m,0)\\
=& \delta_{n,0} + \sum_{\nu' m} S^\eta(\Omega,\mathbf{q},\nu,n,\nu',m)\Pi^\eta(\Omega,\mathbf{q},\nu',m,0)\\
&+ \sum_{\nu' m}\sum_{ll'}\sum_{\tilde\nu} S^\eta(\Omega,\mathbf{q},\nu,n,\tilde\nu,l)\Pi^\eta(\Omega,\mathbf{q},\tilde\nu,l,l')\mathcal{I}^\eta_{\text{SBE}}(\Omega,\mathbf{q},\tilde\nu,l',\nu',m)\Pi^\eta(\Omega,\mathbf{q},\nu',m,0)\\
=& \delta_{n,0} + \sum_{ll'}\sum_{\tilde\nu} S^\eta(\Omega,\mathbf{q},\nu,n,\tilde\nu,l)\Pi^\eta(\Omega,\mathbf{q},\tilde\nu,l,l')\delta_{l',0}\\
&+ \sum_{ll'}\sum_{\tilde\nu} S^\eta(\Omega,\mathbf{q},\nu,n,\tilde\nu,l)\Pi^\eta(\Omega,\mathbf{q},\tilde\nu,l,l')\sum_{\nu' m}\mathcal{I}^\eta_{\text{SBE}}(\Omega,\mathbf{q},\tilde\nu,l',\nu',m)\Pi^\eta(\Omega,\mathbf{q},\nu',m,0)\\
=& \delta_{n,0} + \sum_{ll'}\sum_{\tilde\nu} S^\eta(\Omega,\mathbf{q},\nu,n,\tilde\nu,l)\Pi^\eta(\Omega,\mathbf{q},\tilde\nu,l,l')\left(\delta_{l',0} + \sum_{\nu' m}\mathcal{I}^\eta_{\text{SBE}}(\Omega,\mathbf{q},\tilde\nu,l',\nu',m)\Pi^\eta(\Omega,\mathbf{q},\nu',m,0)\right)\\
=& \delta_{n,0} + \sum_{ll'}\sum_{\tilde\nu} S^\eta(\Omega,\mathbf{q},\nu,n,\tilde\nu,l)\Pi^\eta(\Omega,\mathbf{q},\tilde\nu,l,l')\lambda^\eta(\Omega,\mathbf{q},\tilde\nu,l'). \qquad \text{(B.4c)}
\end{aligned}$$

The high-frequency limit is also unaffected by the change in channel basis

$$\lim_{\Omega\to\infty}\lambda^\eta(\Omega,\mathbf{q},\nu,\mathbf{k}) = \lim_{\nu\to\infty}\lambda^\eta(\Omega,\mathbf{q},\nu,\mathbf{k}) = 1.$$

Note that $\lambda^{\text{M}} = \lambda_{\overline{ph}}$ without the relative minus sign. The connection to the three-point vertex $\gamma^{3,\eta}$ is also not affected by the channel change

$$\gamma^{3,\eta}(\Omega,\mathbf{q},\nu,n,0) = \frac{\lambda^\eta(\Omega,\mathbf{q},\nu,n)w^\eta(\Omega,\mathbf{q})}{\mathcal{I}^\eta_{\text{bare}}}.$$

The connection of the bosonic propagators and susceptibilities is

$$w^\eta = (\mathcal{I}^\eta_{\text{bare}})^2\chi^\eta + \mathcal{I}^\eta_{\text{bare}}$$

and

$$w^\eta(q) = \frac{\mathcal{I}^\eta_{\text{bare}}}{1 - \int \mathrm{d}p\, \lambda^\eta(q,p)\Pi^\eta(q,p)\mathcal{I}^\eta_{\text{bare}}}. \tag{B.5}$$

For large frequencies

$$\lim_{\Omega\to\infty} w^\eta(\Omega,\mathbf{q}) = \mathcal{I}^\eta_{\text{bare}}$$

the bosonic propagator reduces to the (now channel dependent) bare interaction. The high-frequency behaviour of the multiboson rest function is not affected by the channel switch

$$\lim_{\nu/\nu'\to\infty} M^\eta(\Omega,\mathbf{q},\nu,\mathbf{k},\nu',\mathbf{k}') = \lim_{\Omega\to\infty} M^\eta(\Omega,\mathbf{q},\nu,\mathbf{k},\nu',\mathbf{k}') = 0.$$

Analogous to the Bethe-Salpeter equation the rest function may be expressed as

$$\begin{aligned} M^\eta(q,k,k') &= \int \mathrm{d}p\, \mathcal{I}^\eta_{\mathrm{SBE}}(q,k,p)\Pi^\eta(q,p)S^\eta(q,p,k') \\ M^\eta(\Omega,\mathbf{q},\nu,n,\nu',n') &= \sum_{mm'}\sum_{\tilde\nu} \mathcal{I}^\eta_{\mathrm{SBE}}(\Omega,\mathbf{q},\nu,n,\tilde\nu,m)\Pi^\eta(\Omega,\mathbf{q},\tilde\nu,m,m')S^\eta(\Omega,\mathbf{q},\tilde\nu,m',\nu',n') \end{aligned}$$

where $S_r = \mathcal{I}_{r,\mathrm{SBE}} - M^\eta$. The Wentzell asymptotics in physical channels are obtained by merely switching r for η and read

$$\begin{aligned} K_1^\eta(q) &= \lim_{\nu\to\infty}\lim_{\nu'\to\infty} \Phi^\eta(q,k,k') \\ K_2^\eta(q,k) &= \lim_{\nu'\to\infty} \Phi^\eta(q,k,k') \\ \bar K_2^\eta(q,k') &= \lim_{\nu\to\infty} \Phi^\eta(q,k,k'). \end{aligned}$$

They are related to SBE quantities by the familiar relations

$$\begin{aligned} w^\eta &= K_1^\eta + \mathcal{I}^\eta_{\mathrm{bare}} \\ \lambda^\eta &= 1 + K_2^\eta/w^\eta \\ M^\eta &= \mathcal{R}^\eta - (1-\lambda^\eta)w^\eta(1-\lambda^\eta). \end{aligned}$$

The high frequency asymptotics of the vertex are

$$\begin{aligned} \lim_{\Omega\to\infty} V^\eta(\Omega,\mathbf{q},\nu,\mathbf{k},\nu',\mathbf{k}') &= U \\ \lim_{\nu\to\infty} V^\eta(\Omega,\mathbf{q},\nu,\mathbf{k},\nu',\mathbf{k}') &= w^\eta(\Omega,\mathbf{q})\lambda^\eta(\Omega,\mathbf{q},\nu',\mathbf{k}') \\ \lim_{\nu'\to\infty} V^\eta(\Omega,\mathbf{q},\nu,\mathbf{k},\nu',\mathbf{k}') &= \lambda^\eta(\Omega,\mathbf{q},\nu,\mathbf{k})w^\eta(\Omega,\mathbf{q}) \\ \lim_{\nu/\nu'\to\infty} V^\eta(\Omega,\mathbf{q},\nu,\mathbf{k},\nu',\mathbf{k}') &= w^\eta(\Omega,\mathbf{q}). \end{aligned}$$

B.3 Derivation of the SBE 1ℓ flow equations

The flow equations of the SBE quantities can be derived from those of the two-particle irreducible vertices using $\Phi^\eta = \nabla^\eta - U + M^\eta$. The flow equations of Φ^η are reported in Eq. (2.30) and expressed in SBE quantities they are given by

$$\begin{aligned} \dot\phi^{\eta,(1)}(q,k,k') &= \int \mathrm{d}p\; V^\eta(q,k,p)\dot\Pi^\eta(q,p)V^\eta(q,p,k') \\ &= \int \mathrm{d}p\; (\nabla^\eta(q,p,k') + \mathcal{I}^\eta_{\mathrm{SBE}}(q,p,k'))\dot\Pi^\eta(q,p)(\nabla^\eta(q,p,k') + \mathcal{I}^\eta_{\mathrm{SBE}}(q,p,k')) \\ &= \int \mathrm{d}p\; \nabla^\eta(q,p,k')\dot\Pi^\eta(q,p)\nabla^\eta(q,p,k') + \nabla^\eta(q,p,k')\dot\Pi^\eta(q,p)\mathcal{I}^\eta_{\mathrm{SBE}}(q,p,k') \\ &\quad + \mathcal{I}^\eta_{\mathrm{SBE}}(q,p,k')\dot\Pi^\eta(q,p)\nabla^\eta(q,p,k') + \mathcal{I}^\eta_{\mathrm{SBE}}(q,p,k'))\dot\Pi^\eta(q,p)\mathcal{I}^\eta_{\mathrm{SBE}}(q,p,k') \\ &= \int \mathrm{d}p\; \lambda^\eta(q,k)w^\eta(q)\lambda^\eta(q,p)\dot\Pi^\eta(q,p)\lambda^\eta(q,p)w^\eta(q)\lambda^\eta(q,k') \\ &\quad + \lambda^\eta(q,k)w^\eta(q)\lambda^\eta(q,p)\dot\Pi^\eta(q,p)\mathcal{I}^\eta_{\mathrm{SBE}}(q,p,k') + \mathcal{I}^\eta_{\mathrm{SBE}}(q,p,k')\dot\Pi^\eta(q,p)\lambda^\eta(q,p)w^\eta(q)\lambda^\eta(q,k') \\ &\quad + \mathcal{I}^\eta_{\mathrm{SBE}}(q,p,k'))\dot\Pi^\eta(q,p)\mathcal{I}^\eta_{\mathrm{SBE}}(q,p,k') \end{aligned}$$

By expressing the derivative as

$$\dot\Phi^{\eta,(1)} = \dot\nabla^{\eta,(1)} + \dot M^{\eta,(1)} = \dot\lambda^{\eta,(1)}w^\eta\lambda^\eta + \lambda^\eta\dot w^{\eta,(1)}\lambda^\eta + \lambda^\eta w^\eta\dot\lambda^{\eta,(1)} + \dot M^{\eta,(1)}$$

it is possible to compare and match the two expressions [28], yielding

$$\begin{aligned}\dot{\phi}^{\eta,(1)}(q,k,k') = \int \mathrm{d}p\ & \underbrace{\lambda^\eta(q,k)w^\eta(q)\lambda^\eta(q,p)\dot{\Pi}^\eta(q,p)\lambda^\eta(q,p)w^\eta(q)\lambda^\eta(q,k')}_{\lambda^\eta \dot{w}^{\eta,(1)}\lambda^\eta} \\ & + \underbrace{\lambda^\eta(q,k)w^\eta(q)\lambda^\eta(q,p)\dot{\Pi}^\eta(q,p)\mathcal{I}^\eta_{\mathrm{SBE}}(q,p,k')}_{\lambda^\eta w^\eta \dot{\lambda}^{\eta,(1)}} + \underbrace{\mathcal{I}^\eta_{\mathrm{SBE}}(q,p,k')\dot{\Pi}^\eta(q,p)\lambda^\eta(q,p)w^\eta(q)\lambda^\eta(q,k')}_{\dot{\lambda}^{\eta,(1)}w^\eta\lambda^\eta} \\ & + \underbrace{\mathcal{I}^\eta_{\mathrm{SBE}}(q,p,k'))\dot{\Pi}^\eta(q,p)\mathcal{I}^\eta_{\mathrm{SBE}}(q,p,k')}_{\dot{M}^{\eta,(1)}}.\end{aligned}$$

The resulting 1ℓ-flow equations for w^η, λ^η and M^η are

$$\begin{aligned}\dot{w}^{\eta,(1)}(q) &= w^\eta(q)\lambda^\eta(q,p)\dot{\Pi}^\eta(q,p)\lambda^\eta(q,p)w^\eta(q) \\ \dot{\lambda}^{\eta,(1)}(q,k) &= \lambda^\eta(q,p)\dot{\Pi}^\eta(q,p)\mathcal{I}^\eta_{\mathrm{SBE}}(q,p,k) \\ \dot{M}^{\eta,(1)}(q,k,k') &= \mathcal{I}^\eta_{\mathrm{SBE}}(q,p,k')\dot{\Pi}^\eta(q,p)\mathcal{I}^\eta_{\mathrm{SBE}}(q,p,k').\end{aligned}$$

Note that as long as $\bar{\lambda}^\eta = \lambda^\eta$

$$\begin{aligned}\dot{\lambda}^{\eta,(1)}(q,k) &= \lambda^\eta(q,p)\dot{\Pi}^\eta(q,p)\mathcal{I}^\eta_{\mathrm{SBE}}(q,p,k) \\ &= \mathcal{I}^\eta_{\mathrm{SBE}}(q,p,k)\dot{\Pi}^\eta(q,p)\lambda^\eta(q,p) \\ &= \dot{\bar{\lambda}}^{\eta,(1)}(q,k).\end{aligned}$$

Alternatively, the connection between the high-frequency limits of Φ and the SBE quantities may be exploited. Using Eq. 3.17 for the bosonic propagator the derivative is

$$\begin{aligned}\dot{w}^{\eta,(1)}(q) &= \lim_{\nu\to\infty}\lim_{\nu'\to\infty}(\partial_\Lambda(\dot{\Phi}^{\eta,(1)}(q,k,k') + \mathcal{I}^\eta_{\mathrm{bare}}(q,k,k'))) = \lim_{\nu\to\infty}\lim_{\nu'\to\infty}\left(\int \mathrm{d}p\ V^\eta(q,k,p)\dot{\Pi}^\eta(q,p)V^\eta(q,p,k'))\right) \\ &= \lim_{\nu\to\infty}\lim_{\nu'\to\infty}\left(\int \mathrm{d}p\ (\lambda^\eta(q,k)w^\eta(q)\lambda^\eta(q,p) + \mathcal{I}^\eta_{\mathrm{SBE}}(q,k,p))\dot{\Pi}^\eta(q,p)(\lambda^\eta(q,p)w^\eta(q)\lambda^\eta(q,k') + \mathcal{I}^\eta_{\mathrm{SBE}}(q,p,k')))\right) \\ &= \int \mathrm{d}p\ w^\eta(q)\lambda^\eta(q,p)\dot{\Pi}^\eta(q,p)\lambda^\eta(q,p)w^\eta(q).\end{aligned}$$

Similarly the λ^η can be obtained from Eq. (3.17) by taking the derivative of the equation that links λ^η to the asymptotic frequency behaviour of Φ^η:

$$\dot{\lambda}^{\eta,(1)}(q,k) = \left(\left(\lim_{\nu'\to\infty}\dot{\Phi}^{\eta,(1)}(q,k,k')\right) - \lambda^\eta(q,k)\dot{w}^{\eta,(1)}(q)\right)/w^\eta(q).$$

Inserting the flow equations for $\dot{\Phi}^{\eta,(1)}$ and $\dot{w}^{\eta,(1)}$ yields

$$\begin{aligned}\dot{\lambda}^{\eta,(1)}(q,k) =& \left(\left(\lim_{\nu'\to\infty}\int \mathrm{d}p\ V^\eta(q,k,p)\dot{\Pi}^\eta(q,p)V^\eta(q,p,k')\right) - \lambda^\eta(q,k)\int \mathrm{d}p\ w^\eta(q)\lambda^\eta(q,p)\dot{\Pi}^\eta(q,p)\lambda^\eta(q,p)w^\eta(q)\right)/w^\eta(q) \\ =& \left(\left(\lim_{\nu'\to\infty}\int \mathrm{d}p\ (\lambda^\eta(q,k)w^\eta(q)\lambda^\eta(q,p) + \mathcal{I}^\eta_{\mathrm{SBE}}(q,k,p))\dot{\Pi}^\eta(q,p)(\lambda^\eta(q,p)w^\eta(q)\lambda^\eta(q,k') + \mathcal{I}^\eta_{\mathrm{SBE}}(q,p,k'))\right)\right. \\ & \left. - \lambda^\eta(q,k)\int \mathrm{d}p\ w^\eta(q)\lambda^\eta(q,p)\dot{\Pi}^\eta(q,p)\lambda^\eta(q,p)w^\eta(q)\right)/w^\eta(q) \\ =& \int \mathrm{d}p\ \lambda^\eta(q,k)w^\eta(q)\lambda^\eta(q,p)\dot{\Pi}^\eta(q,p)\lambda^\eta(q,p) + \mathcal{I}^\eta_{\mathrm{SBE}}(q,k,p)\dot{\Pi}^\eta(q,p)\lambda^\eta(q,p) \\ & - \lambda^\eta(q,k)w^\eta(q)\lambda^\eta(q,p)\dot{\Pi}^\eta(q,p)\lambda^\eta(q,p) \\ =& \int \mathrm{d}p\ \mathcal{I}^\eta_{\mathrm{SBE}}(q,k,p)\dot{\Pi}^\eta(q,p)\lambda^\eta(q,p).\end{aligned}$$

B.4 Self-consistent SBE flow equations derived from the Bethe-Salpeter equations

Self-consistent flow equations for the SBE quantities can be calculated from the derivative of the Bethe-Salpeter equations. First we summarize the identities used in the derivation

$$\begin{aligned}
\phi^\eta &= \mathcal{I}^\eta \Pi^\eta V^\eta \\
\mathcal{I}^\eta &= \mathcal{I}^\eta_{\mathrm{SBE}} - M^\eta + U \\
&= S^\eta + U \\
S^\eta &= \mathcal{I}^\eta_{\mathrm{SBE}} - M^\eta \\
M^\eta &= S^\eta \Pi^\eta \mathcal{I}^\eta_{\mathrm{SBE}} \\
V^\eta &= \nabla^\eta + \mathcal{I}^\eta_{\mathrm{SBE}} \\
&= \lambda^\eta w^\eta \bar{\lambda}^\eta + \mathcal{I}^\eta_{\mathrm{SBE}} \\
\lambda^\eta &= 1 + S^\eta \Pi^\eta \lambda^\eta = 1 + \mathcal{I}^\eta_{\mathrm{SBE}} \Pi^\eta \\
w^\eta &= U + U \lambda^\eta \Pi^\eta w^\eta \\
\dot{\nabla}^\eta &= \dot{\lambda}^\eta w^\eta \bar{\lambda}^\eta + \lambda^\eta \dot{w}^\eta \bar{\lambda}^\eta + \lambda^\eta w^\eta \dot{\bar{\lambda}}^\eta.
\end{aligned}$$

The starting point is the derivative of the two-particle vertex based on the Bethe-Salpeter equation:

$$\begin{aligned}
\dot{\phi}^\eta =& \dot{\mathcal{I}}^\eta \Pi^\eta V^\eta + \mathcal{I}^\eta \dot{\Pi}^\eta V^\eta + \mathcal{I}^\eta \Pi^\eta \dot{V}^\eta \qquad \text{(B.6)} \\
=& \dot{S}^\eta \Pi^\eta (\lambda^\eta w^\eta \bar{\lambda}^\eta + \mathcal{I}^\eta_{\mathrm{SBE}}) + (S^\eta + U) \dot{\Pi}^\eta (\lambda^\eta w^\eta \bar{\lambda}^\eta + \mathcal{I}^\eta_{\mathrm{SBE}}) + (S^\eta + U) \Pi^\eta (\dot{\lambda}^\eta w^\eta \bar{\lambda}^\eta + \lambda^\eta \dot{w}^\eta \bar{\lambda}^\eta + \lambda^\eta w^\eta \dot{\bar{\lambda}}^\eta + \dot{\mathcal{I}}^\eta_{\mathrm{SBE}}) \\
=& \dot{S}^\eta \Pi^\eta \lambda^\eta w^\eta \bar{\lambda}^\eta + \dot{S}^\eta \Pi^\eta \mathcal{I}^\eta_{\mathrm{SBE}} + S^\eta \dot{\Pi}^\eta \lambda^\eta w^\eta \bar{\lambda}^\eta + U \dot{\Pi}^\eta \lambda^\eta w^\eta \bar{\lambda}^\eta + S^\eta \dot{\Pi}^\eta \mathcal{I}^\eta_{\mathrm{SBE}} + U \dot{\Pi}^\eta \mathcal{I}^\eta_{\mathrm{SBE}} \\
&+ S^\eta \Pi^\eta \dot{\lambda}^\eta w^\eta \bar{\lambda}^\eta + U \Pi^\eta \dot{\lambda}^\eta w^\eta \bar{\lambda}^\eta + S^\eta \Pi^\eta \lambda^\eta \dot{w}^\eta \bar{\lambda}^\eta + U \Pi^\eta \lambda^\eta \dot{w}^\eta \bar{\lambda}^\eta \\
&+ S^\eta \Pi^\eta \lambda^\eta w^\eta \dot{\bar{\lambda}}^\eta + U \Pi^\eta \lambda^\eta w^\eta \dot{\bar{\lambda}}^\eta + S^\eta \Pi^\eta \dot{\mathcal{I}}^\eta_{\mathrm{SBE}} + U \Pi^\eta \dot{\mathcal{I}}^\eta_{\mathrm{SBE}} \\
=& U (\dot{\Pi}^\eta \mathcal{I}^\eta_{\mathrm{SBE}} + \Pi^\eta \dot{\mathcal{I}}^\eta_{\mathrm{SBE}}) + S^\eta \Pi^\eta \lambda^\eta w^\eta \dot{\bar{\lambda}}^\eta + U \Pi^\eta \lambda^\eta w^\eta \dot{\bar{\lambda}}^\eta + (\dot{S}^\eta \Pi^\eta \bar{\lambda}^\eta + S^\eta \dot{\Pi}^\eta \bar{\lambda}^\eta + S^\eta \Pi^\eta \dot{\lambda})^\eta w^\eta \bar{\lambda}^\eta \\
&+ (\lambda^\eta - 1) \dot{w}^\eta \bar{\lambda}^\eta + U (\dot{\Pi}^\eta \lambda^\eta w^\eta + \Pi^\eta \dot{\lambda}^\eta w^\eta + \Pi^\eta \lambda^\eta \dot{w}^\eta) \bar{\lambda}^\eta + \dot{S}^\eta \Pi^\eta \mathcal{I}^\eta_{\mathrm{SBE}} + S^\eta \dot{\Pi}^\eta \mathcal{I}^\eta_{\mathrm{SBE}} + S^\eta \Pi^\eta \dot{\mathcal{I}}^\eta_{\mathrm{SBE}} \\
=& U \partial_\Lambda (\Pi^\eta \mathcal{I}^\eta_{\mathrm{SBE}}) + (\lambda^\eta - 1) w^\eta \dot{\bar{\lambda}}^\eta + (w^\eta - U) \dot{\bar{\lambda}}^\eta + \partial_\Lambda (S^\eta \Pi^\eta \lambda^\eta) w^\eta \bar{\lambda}^\eta + (\lambda^\eta - 1) \dot{w}^\eta \bar{\lambda}^\eta + U \partial_\Lambda (\Pi^\eta \lambda^\eta w^\eta) \bar{\lambda}^\eta \\
&+ \partial_\Lambda (S^\eta \Pi^\eta \mathcal{I}^\eta_{\mathrm{SBE}}) \\
=& U \partial_\Lambda (\Pi^\eta \mathcal{I}^\eta_{\mathrm{SBE}}) + \lambda^\eta w^\eta \dot{\bar{\lambda}}^\eta - U \dot{\bar{\lambda}}^\eta + \partial_\Lambda (S^\eta \Pi^\eta \lambda^\eta) w^\eta \bar{\lambda}^\eta + (\lambda^\eta - 1) \dot{w}^\eta \bar{\lambda}^\eta + U \partial_\Lambda (\Pi^\eta \lambda^\eta w^\eta) \bar{\lambda}^\eta + \partial_\Lambda (S^\eta \Pi^\eta \mathcal{I}^\eta_{\mathrm{SBE}}) \\
=& \partial_\Lambda (S^\eta \Pi^\eta \lambda^\eta) w^\eta \bar{\lambda}^\eta + \lambda^\eta \dot{w}^\eta \bar{\lambda}^\eta + \lambda^\eta w^\eta \dot{\bar{\lambda}}^\eta + \partial_\Lambda (S^\eta \Pi^\eta \mathcal{I}^\eta_{\mathrm{SBE}}) + (U \partial_\Lambda (\Pi^\eta \lambda^\eta w^\eta) - \dot{w}^\eta) \bar{\lambda}^\eta + U (\partial_\Lambda (\Pi^\eta \mathcal{I}^\eta_{\mathrm{SBE}}) - \dot{\bar{\lambda}}^\eta), \qquad \text{(B.7)}
\end{aligned}$$

where frequency, momentum and form factor arguments are suppressed to make the derivation more easily readable. The terms can now be matched according to $\dot{\phi}^\eta = \dot{\lambda}^\eta w^\eta \bar{\lambda}^\eta + \lambda^\eta \dot{w}^\eta \bar{\lambda}^\eta + \lambda^\eta w^\eta \dot{\bar{\lambda}}^\eta + \dot{M}^\eta$:

$$\dot{\lambda}^\eta = \partial_\Lambda (S^\eta \Pi^\eta \lambda^\eta) \qquad \text{(B.8)}$$

$$\dot{M}^\eta = \partial_\Lambda (S^\eta \Pi^\eta \mathcal{I}^\eta_{\mathrm{SBE}}) \qquad \text{(B.9)}$$

as well as

$$(U \partial_\Lambda (\Pi^\eta \lambda^\eta w^\eta) - \dot{w}^\eta) = 0 \qquad \text{(B.10)}$$

$$\partial_\Lambda (\Pi^\eta \mathcal{I}^\eta_{\mathrm{SBE}}) - \dot{\bar{\lambda}}^\eta = 0. \qquad \text{(B.11)}$$

For the fermion-boson coupling we obtain two flow equations

$$\dot{\bar{\lambda}}^\eta = \partial_\Lambda (\Pi^\eta \mathcal{I}^\eta_{\mathrm{SBE}}) = \dot{\Pi}^\eta \mathcal{I}^\eta_{\mathrm{SBE}} + \Pi^\eta \dot{\mathcal{I}}^\eta_{\mathrm{SBE}} \qquad \text{(B.12)}$$

and

$$\dot{\lambda}^\eta = \partial_\Lambda (S^\eta \Pi^\eta \lambda^\eta) = \dot{S}^\eta \Pi^\eta \lambda^\eta + S^\eta \dot{\Pi}^\eta \lambda^\eta + S^\eta \Pi^\eta \dot{\lambda}^\eta. \qquad \text{(B.13)}$$

Note that if we had chosen $\phi^\eta = V^\eta \Pi^\eta \mathcal{I}^\eta$ instead of $\phi^\eta = \mathcal{I}^\eta \Pi^\eta V^\eta$, the roles of λ^η and $\bar{\lambda}^\eta$ would be reversed. The flow equation for the rest function is

$$\dot{M}^\eta = \partial_\Lambda (S^\eta \Pi^\eta \mathcal{I}^\eta_{\mathrm{SBE}}) = \dot{S}^\eta \Pi^\eta \mathcal{I}^\eta_{\mathrm{SBE}} + S^\eta \dot{\Pi}^\eta \mathcal{I}^\eta_{\mathrm{SBE}} + S^\eta \Pi^\eta \dot{\mathcal{I}}^\eta_{\mathrm{SBE}}. \tag{B.14}$$

For the bosonic propagator we find

$$\dot{w}^\eta = U \partial_\Lambda (\Pi^\eta \lambda^\eta w^\eta) = U(\dot{\Pi}^\eta \lambda^\eta w^\eta + \Pi^\eta \dot{\lambda}^\eta w^\eta + \Pi^\eta \lambda^\eta \dot{w}^\eta) \tag{B.15}$$

$$\Rightarrow \dot{w}^\eta = \frac{U}{1 - U \Pi^\eta \lambda^\eta} (\dot{\Pi}^\eta \lambda^\eta w^\eta + \Pi^\eta \dot{\lambda}^\eta w^\eta) = (w^\eta)^2 (\dot{\Pi}^\eta \lambda^\eta + \Pi^\eta \dot{\lambda}^\eta). \tag{B.16}$$

This derivation confirms the results for the flow equations as obtained in Section 3.3.4.

B.5 Conventional SDE in the SBE framework

The derivative of the SDE is given by

$$\dot{\Sigma}(\nu, \mathbf{k}) = \dot{\Sigma}_G(\nu, \mathbf{k}) + \dot{\Sigma}_{GGG}(\nu, \mathbf{k}) + \dot{\Sigma}_{ph}(\nu, \mathbf{k}) + \dot{\Sigma}_{\overline{ph}}(\nu, \mathbf{k}) + \dot{\Sigma}_{pp}(\nu, \mathbf{k}),$$

where in the SBE framework

$$\begin{aligned}
\dot{\Sigma}_G(\nu, \mathbf{k}) =& U \sum_{\nu' \mathbf{k}'} \partial_\Lambda G^\Lambda(\nu', \mathbf{k}') \\
\dot{\Sigma}_{GGG}(\nu, \mathbf{k}) =& -U^2 \sum_{\mathbf{q}, \mathbf{k}'} \sum_{\nu', \Omega} \partial_\Lambda \left(G^\Lambda(\nu', \mathbf{k}') G^\Lambda(\Omega + \nu, \mathbf{q} + \mathbf{k}) G^\Lambda(\Omega + \nu', \mathbf{q} + \mathbf{k}') \right) \\
\dot{\Sigma}_{ph}(\nu, \mathbf{k}) =& -\sum_n f_n(\mathbf{k}) f_0(\mathbf{k}) \sum_{\nu', \mathbf{k}'} \partial_\Lambda (G^\Lambda(\nu', \mathbf{k}') \\
& (\nabla_{ph}(\nu' - \nu, \mathbf{k}' - \mathbf{k}, \nu, n, \nu'', n'') - U + M_{ph}(\nu' - \nu, \mathbf{k}' - \mathbf{k}, \nu, n, \nu'', n'')) \\
& \Pi_{ph}(\nu' - \nu, \mathbf{k}' - \mathbf{k}, \nu'', n'', n') \delta_{n'0} U) \\
\dot{\Sigma}_{\overline{ph}}(\nu, \mathbf{k}) =& -\sum_n f_n(\mathbf{k}) f_0(\mathbf{k}) \sum_{\nu', \mathbf{k}'} \partial_\Lambda (G^\Lambda(\nu', \mathbf{k}') \\
& (\nabla_{\overline{ph}}(\nu' - \nu, \mathbf{k}' - \mathbf{k}, \nu, n, \nu'', n'') - U + M_{\overline{ph}}(\nu' - \nu, \mathbf{k}' - \mathbf{k}, \nu, n, \nu'', n'')) \\
& \Pi_{ph}(\nu' - \nu, \mathbf{k}' - \mathbf{k}, \nu'', n'', n') \delta_{n'0} U) \\
\dot{\Sigma}_{pp}(\nu, \mathbf{k}) =& -\sum_n f_n(\mathbf{k}) f_0(\mathbf{k}) \sum_{\nu', \mathbf{k}'} \partial_\Lambda (G^\Lambda(\nu', \mathbf{k}') \\
& (\nabla_{pp}(\nu' + \nu, \mathbf{k}' + \mathbf{k}, \nu, n, \nu'', n'') - U + M_{pp}(\nu' + \nu, \mathbf{k}' + \mathbf{k}, \nu, n, \nu'', n'')) \\
& \Pi_{pp}(\nu' + \nu, \mathbf{k}' + \mathbf{k}, \nu'', n'', n') \delta_{n'0} U).
\end{aligned}$$

Note that $\dot{\nabla}_r = \dot{\lambda}_r w_r \lambda_r + \lambda_r \dot{w}_r \lambda_r + \lambda_r w_r \dot{\lambda}_r$ is not generated during the flow and thus needs to be constructed at each step, whereas $\dot{\Phi}_r$ is automatically available.

B.6 Bare interaction of the extended Hubbard model: form factor dependence

In physical channels the bare interactions expanded in form factors read

$$\mathcal{I}^\eta_{\mathrm{bare}}(\mathbf{q}, n, n') = \mathcal{I}^\eta_{\mathrm{bos}}(\mathbf{q}) + \mathcal{I}^\eta_{\mathrm{ferm}}(n, n') \tag{B.17}$$

with

$$\begin{aligned}
\mathcal{I}^{\mathrm{SC}}_{\mathrm{ferm}}(n, n') &= 2V(\delta_{n,1}\delta_{n',1} + \delta_{n,2}\delta_{n',2} + \delta_{n,3}\delta_{n',3} + \delta_{n,4}\delta_{n',4}) \\
\mathcal{I}^{\mathrm{M}}_{\mathrm{ferm}}(n, n') &= -2V(\delta_{n,1}\delta_{n',1} + \delta_{n,2}\delta_{n',2} + \delta_{n,3}\delta_{n',3} + \delta_{n,4}\delta_{n',4}) \\
\mathcal{I}^{\mathrm{D}}_{\mathrm{ferm}}(n, n') &= -2V(\delta_{n,1}\delta_{n',1} + \delta_{n,2}\delta_{n',2} + \delta_{n,3}\delta_{n',3} + \delta_{n,4}\delta_{n',4}).
\end{aligned}$$

The bosonic bare interaction depends only on the transfer momentum and is therefore not expanded. Though the interaction may appear in a different form in the channels, there is only **one** bare interaction.

This is highlighted by the relation $\mathcal{I}^r_{\text{bare}}(\mathbf{q}, n, n') = P^{r'\to r}[\mathcal{I}^{r'}_{\text{bare}}](\mathbf{q}, n, n')$ for the diagrammatic channels. Splitting it into bosonic and fermionic parts complicates the picture as $\mathcal{I}^r_{\text{bos/ferm}} \neq P^{r'\to r}[\mathcal{I}^{r'}_{\text{bos/ferm}}]$ in general. The relations are listed below for the diagrammatic channels. Analogous physical channel based relations may easily be deduced from the well-known connections between the two, outlined in Section 2.2.6. Summed up, translating between the pp- and $\overline{ph}$-channel has no effect on the bare interaction. However, translating to and from the ph-channel switches the extended bare interaction from bosonic to fermionic and vice versa:

$$\begin{aligned}
\mathcal{I}^{pp}_{\text{bos/ferm}}(\mathbf{q}, n, n') &= P^{\overline{ph}\to pp}[\mathcal{I}^{\overline{ph}}_{\text{bos/ferm}}](\mathbf{q}, n, n') \\
\mathcal{I}^{\overline{ph}}_{\text{bos/ferm}}(\mathbf{q}, n, n') &= P^{pp\to\overline{ph}}[\mathcal{I}^{pp}_{\text{bos/ferm}}](\mathbf{q}, n, n') \\
\mathcal{I}^{ph}_{\text{bos}}(\mathbf{q}, n, n') - U &= P^{\overline{ph}/pp\to ph}[\mathcal{I}^{\overline{ph}/pp}_{\text{ferm}}](\mathbf{q}, n, n') \\
\mathcal{I}^{\overline{ph}/pp}_{\text{bos}}(\mathbf{q}, n, n') - U &= P^{ph\to\overline{ph}/pp}[\mathcal{I}^{ph}_{\text{ferm}}](\mathbf{q}, n, n') \\
\mathcal{I}^{ph}_{\text{ferm}}(\mathbf{q}, n, n') &= P^{\overline{ph}/pp\to ph}[\mathcal{I}^{\overline{ph}/pp}_{\text{bos}}](\mathbf{q}, n, n') - U \\
\mathcal{I}^{\overline{ph}/pp}_{\text{ferm}}(\mathbf{q}, n, n') &= P^{ph\to\overline{ph}/pp}[\mathcal{I}^{ph}_{\text{bos}}](\mathbf{q}, n, n') - U.
\end{aligned}$$

The switch from $\mathcal{I}^r_{\text{bos}}$ to $\mathcal{I}^r_{\text{ferm}}$ and back means that extra care is due to avoid double counting of the bare interaction.

B.7 Implementation-friendly tweaking of the refined approach to the extended Hubbard model

Section 3.5 explains how $\mathcal{I}^\eta_{\text{bare}}$ can be split into bosonic and fermionic parts. Moving the latter to the rest function yields an insightful and computation friendly expression of the extended Hubbard model in the SBE framework. Here we present a slight variation of said scheme that does not make any approximations and is thus exactly equivalent to the one presented in the main body. While less intuitive at first glance, it offers benefits for practical algorithmic implementations. The main idea is that it is also possible to move the fermionic part of the bare interaction to $\mathcal{I}^\eta_{\text{SBE}}$ directly and thereby restore $M^{\eta,\text{init}}(\Omega, \mathbf{q}, \nu, n, \nu', n') \to \tilde{M}^{\eta,\text{init}}(\Omega, \mathbf{q}, \nu, n, \nu', n') = 0$. As M^η enters the flow equations $\dot{w}^\eta$ and $\dot{\lambda}^\eta$ only via $\mathcal{I}^\eta_{\text{SBE}}$, they are not affected. The rest function $\tilde{M}^\eta$ of this alternative is given by

$$\tilde{M}^\eta = M^\eta - \mathcal{I}^\eta_{\text{ferm}}, \tag{B.18}$$

where M^η is the rest function according to the definition used in the main body, which holds for the initial value as well as the rest function's high-frequency asymptotics. This way, the absolute value of the rest function is expected to be comparable in size to its equivalent for the local Hubbard model. The initial values of w^η and λ^η are not modified compared to the values given in the main body. As the initial value of $\tilde{M}^\eta_{\text{init}} = 0$, the double counting prevention in $\tilde{\mathcal{I}}^\eta_{\text{SBE}}$ has to be modified and is now unaffected by the SBE approximation:

$$\begin{aligned}
\tilde{\mathcal{I}}^{\text{SC,init}}_{\text{SBE}} &= \tilde{M}^{\text{SC,init}} + P^{ph\to pp}\left[\frac{1}{2}(\nabla^{\text{D,init}} + \tilde{M}^{\text{D,init}}) - \frac{1}{2}(\nabla^{\text{M,init}} + \tilde{M}^{\text{M,init}})\right] - P^{\overline{ph}\to pp}\left[\nabla^{\text{M,init}} + \tilde{M}^{\text{M,init}}\right] - 2U \\
&= 0 + P^{ph\to pp}\left[\frac{1}{2}(U + 4V_{\mathbf{q}} + 0) - \frac{1}{2}(-U + 0)\right] - P^{\overline{ph}\to pp}\left[-U + 0\right] - 2U \\
&= 0 + U + 2V_{\mathbf{k}-\mathbf{k}'} + U + 0 - 2U = 2V_{\mathbf{k}-\mathbf{k}'} \\
&= \mathcal{I}^{\text{SC}}_{\text{ferm}}.
\end{aligned} \tag{B.19}$$

Analogous for the magnetic channel

$$\begin{aligned}
\tilde{\mathcal{I}}^{\text{M,init}}_{\text{SBE}} &= \tilde{M}^{\text{M,init}} - P^{ph\to\overline{ph}}\left[\frac{1}{2}\left(\nabla^{\text{D,init}} + \tilde{M}^{\text{D,init}}\right) - \frac{1}{2}\left(\nabla^{\text{M,init}} + \tilde{M}^{\text{M,init}}\right)\right] - P^{pp\to\overline{ph}}\left[\nabla^{\text{SC,init}} + M^{\text{SC,init}}\right] - 2U \\
&= \mathcal{I}^{\text{M}}_{\text{ferm}}
\end{aligned} \tag{B.20}$$

and the density channel

$$\begin{aligned}\tilde{\mathcal{I}}^{\mathrm{D,init}}_{\mathrm{SBE}} =& \tilde{M}^{\mathrm{D,init}} + 2P^{pp\to ph}\left[\nabla^{\mathrm{SC,init}} + \tilde{M}^{\mathrm{SC,init}}\right] - P^{pp\to\overline{ph}}\left[\nabla^{\mathrm{SC,init}} + \tilde{M}^{\mathrm{SC,init}}\right] && \text{(B.21)}\\ & - 2P^{\overline{ph}\to ph}\left[\nabla^{\mathrm{M,init}} + \tilde{M}^{\mathrm{M,init}}\right] - P^{ph\to\overline{ph}}\left[\frac{1}{2}(\nabla^{\mathrm{D,init}} + \tilde{M}^{\mathrm{D,init}}) - \frac{1}{2}(\nabla^{\mathrm{M,init}} + \tilde{M}^{\mathrm{M,init}})\right] - 2U\\ & = \mathcal{I}^{\mathrm{D}}_{\mathrm{ferm}}. && \text{(B.22)}\end{aligned}$$

While it is conceptually more intuitive to define the fermionic part of the bare interaction to be the initial value of the rest function, the approach presented in this appendix was used for the implementation in practice. The main advantage being that the double counting prevention is not dependent on the inclusion of the rest function and no extra bare fermionic interaction functions need to be implemented. In summary, shifting $\tilde{\mathcal{I}}^{\eta}_{\mathrm{ferm}}$ from the rest functions to $\mathcal{I}^{\eta}_{\mathrm{SBE}}$ does not affect any approximations or results, it merely serves to simplify the double counting prevention. The equations affected by this change are

$$\tilde{M}^{\eta}_{\mathrm{init}} = 0 \tag{B.23}$$

and the double counting in $\tilde{V}^{\eta}/\tilde{\mathcal{I}}^{\eta}_{\mathrm{SBE}}$ is taken care of by using the familiar equations of the implementation of the local Hubbard model

$$\begin{aligned}\tilde{V}^{\mathrm{SC}} &= \nabla^{\mathrm{SC}} + \tilde{\mathcal{I}}^{\mathrm{SC}}_{\mathrm{SBE}}\\ &= \nabla^{\mathrm{SC}} + \tilde{M}^{\mathrm{SC}} + P^{ph\to pp}\left[\frac{1}{2}(\nabla^{\mathrm{D}} + \tilde{M}^{\mathrm{D}}) - \frac{1}{2}(\nabla^{\mathrm{M}} + \tilde{M}^{\mathrm{M}})\right] - P^{\overline{ph}\to pp}\left[\nabla^{\mathrm{M}} + \tilde{M}^{\mathrm{M}}\right] - 2U && \text{(B.24a)}\\ \tilde{V}^{\mathrm{M}} &= \nabla^{\mathrm{M}} + \tilde{\mathcal{I}}^{\mathrm{M}}_{\mathrm{SBE}}\\ &= \nabla^{\mathrm{M}} + \tilde{M}^{\mathrm{M}} - P^{ph\to\overline{ph}}\left[\frac{1}{2}\left(\nabla^{\mathrm{D}} + \tilde{M}^{\mathrm{D}}\right) - \frac{1}{2}\left(\nabla^{\mathrm{M,init}} + \tilde{M}^{\mathrm{M}}\right)\right] - P^{pp\to\overline{ph}}\left[\nabla^{\mathrm{SC}} + M^{\mathrm{SC}}\right] - 2U && \text{(B.24b)}\\ \tilde{V}^{\mathrm{D}} &= \nabla^{\mathrm{D}} + \tilde{\mathcal{I}}^{\mathrm{D}}_{\mathrm{SBE}}\\ &= \nabla^{\mathrm{D}} + \tilde{M}^{\mathrm{D}} + 2P^{pp\to ph}\left[\nabla^{\mathrm{SC}} + \tilde{M}^{\mathrm{SC}}\right] - P^{pp\to\overline{ph}}\left[\nabla^{\mathrm{SC}} + \tilde{M}^{\mathrm{SC}}\right] && \text{(B.24c)}\\ &\quad - 2P^{\overline{ph}\to ph}\left[\nabla^{\mathrm{M}} + \tilde{M}^{\mathrm{M}}\right] - P^{ph\to\overline{ph}}\left[\frac{1}{2}(\nabla^{\mathrm{D}} + \tilde{M}^{\mathrm{D}}) - \frac{1}{2}(\nabla^{\mathrm{M}} + \tilde{M}^{\mathrm{M}})\right] - 2U. && \text{(B.24d)}\end{aligned}$$

Of course $V^{\eta}/\mathcal{I}^{\eta}_{\mathrm{SBE}} = \tilde{V}^{\eta}/\tilde{\mathcal{I}}^{\eta}_{\mathrm{SBE}}$: the difference lies in the way they are constructed, not their values. Note that the only necessary changes to fully incorporate the nearest-neighbour interaction given an existing SBE implementation of the local Hubbard model are *i*) changing the initial value of $w^{\mathrm{D}} = U \to U + 4V(\cos(q_x) + \cos(q_y))$ and *ii*) accounting for the non-trivial high-frequency behaviour of λ^{η} and M^{η}. In regions of the phase diagram where the latter may be neglected the only line of code that needs to be modified is the initial value of w^{D}. This reformulation also helps shed light on why the non-trivial frequency asymptotics and non-local form factors may be neglected with such little loss of accuracy: they are generated during the flow and enter only as corrections to the dominant physics in the bosonic propagators.

C Supplementary SBE results

C.1 Additional SBE approximation data

Figure C.1 is equivalent to Fig. 4.2 but displays data for $\lambda^{\mathrm{SC/D}}$ instead of λ^{M}. Even at the lowest temperature the relative difference with and without rest function is $\mathcal{O}(10^{-2})$.

C.2 Additional extended Hubbard model data

Figure C.2 shows the frequency dependence of λ^{η} with and without the inclusion of the high-frequency asymptotics. The bosonic frequency dependence of $\lambda^{\eta}(s\text{-wave})$ is qualitatively the same as for $V = 0$ (see Fig. 4.1) approaching 1 at large frequencies and the much smaller $\lambda^{\eta}(n > 0)$ vanish for large Ω. Though $\lambda^{\eta}(s\text{-wave})$ has not yet reached its high-frequency limit of 1 for the largest fermionic frequency included (bottom left), and $\lim_{\nu\to\infty} \lambda^{\eta}(\Omega = 0, \mathbf{q}, \nu, n > 0) \neq 1$ (bottom right), the negligible influence of $\lambda^{\eta,\mathrm{asympt}}$ proves the inner frequency box to be large enough to obtain qualitatively and quantitatively correct results. Data for $f_2(\mathbf{k}) = \cos(k_y)$ is related to $f_1(\mathbf{k}) = \cos(k_x)$ by rotation symmetry and data for the higher form factors $f_{3/4}(\mathbf{k}) = \sin(k_{x/y})$ are even smaller. They are therefore not included. The non-trivial high-frequency asymptotics $\lambda^{\eta,\mathrm{asympt}}$ are more than a factor 20 smaller, compared to the trivial s-wave high-frequency asymptotics of 1. Since $\lambda^{\eta}(n > 0)$ is only weakly dependent on ν, it may be possible to calculate only $\lambda^{\eta,\mathrm{asympt}}$ if extra accuracy is wanted or the asymptotics do become important in more challenging parameter regimes.

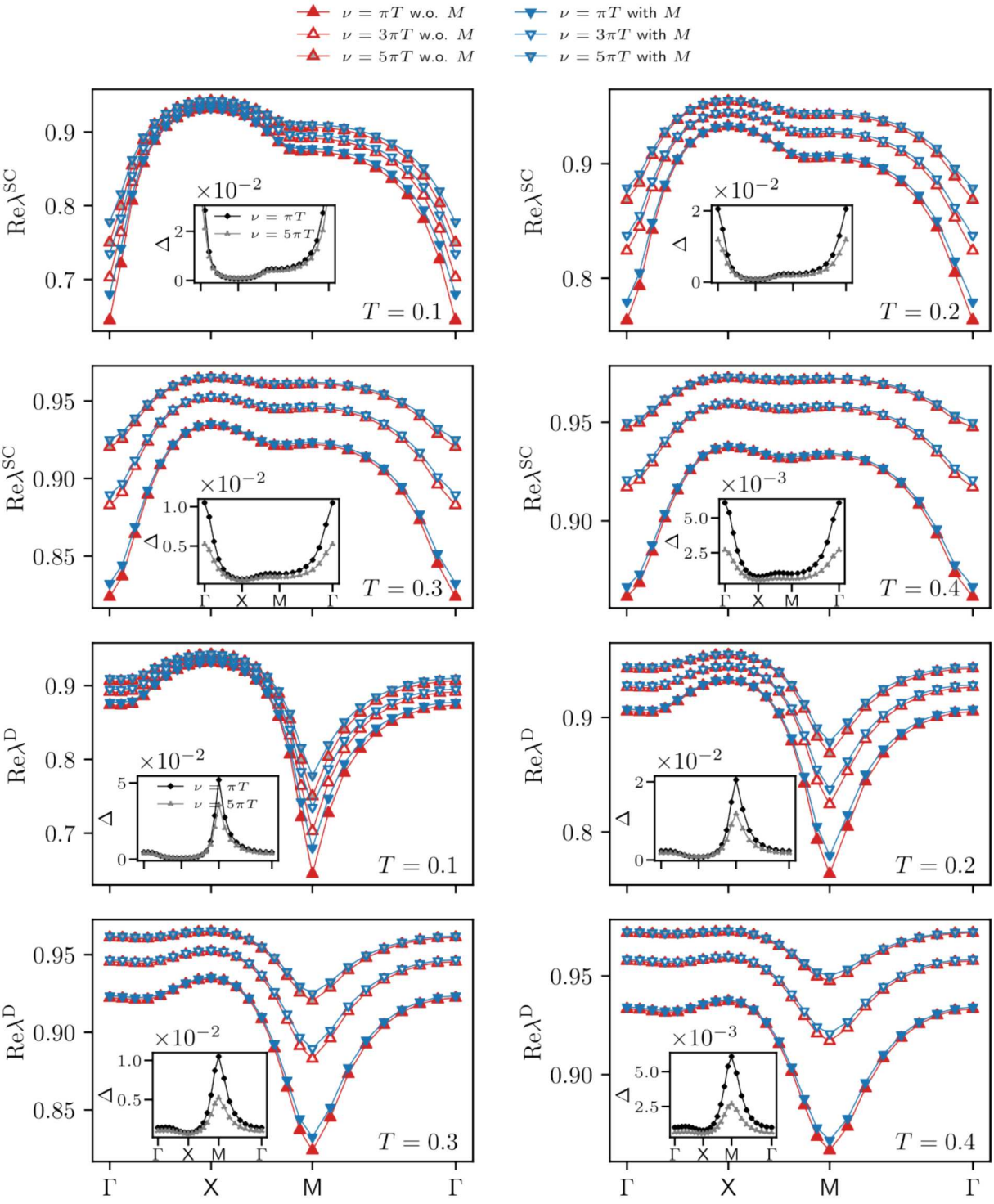

Figure C.1: Density and superconducting channel of the static fermion-boson coupling $\lambda^{\mathrm{SC/D}}(\Omega = 0, \mathbf{q}, \nu, n = s\text{-wave})$ for the same parameters as in Fig. 4.2 and different fermionic frequencies. The relative difference Δ between the results with and without rest function is shown in the insets.

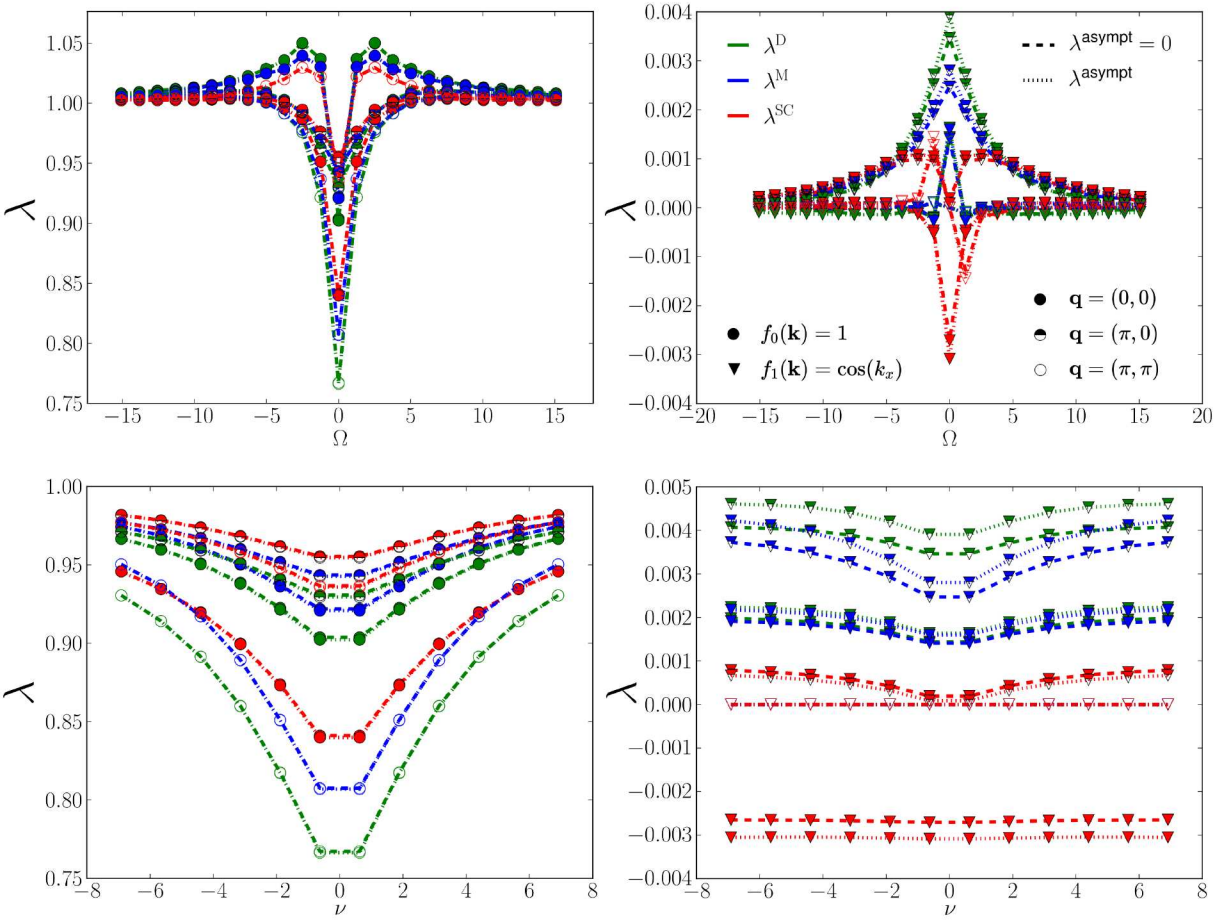

Figure C.2: Fermion boson coupling λ^{η} calculated with and without the inclusion of high-frequency asymptotics at $U = 2, \beta = 5, \mu = 0, t' = 0$ over bosonic frequency Ω for $\nu = \pi T$ (top panels) and over fermionic frequency for $\Omega = 0$ (bottom panels), where the marker shape determines the form factor and the marker filling the bosonic momentum respectively.

D Supplementary material: fluctuation diagnostics

D.1 Technical parameters

We here provide the technical parameters for the fRG calculations performed with a smooth frequency cutoff. We use $n = 4$ positive fermionic frequencies that determine the parametrization of the two-particle vertex (see Ref. [30] for the definitions). The rest function contains $(4n+1)\times(2n)\times(2n)$, the K_2-function and the fermion-boson vertex $(4n + 1) \times (2n)$, the K_1-function $(128n + 1)$, and the self-energy $(8n)$ frequencies. The fermionic momentum dependence of the vertices and response functions is accounted for by a form factor expansion, where we considered the local s-wave and non-local d-wave contributions. The remaining momentum dependence of the vertices, the response functions and the self-energy are calculated on (16×16) equally spaced momentum patches, with a refinement of (5×5) additional patches around $\mathbf{q} = (\pi, \pi)$ to resolve the AF peak. The Green's functions and their summation in the particle-hole and particle-particle bubble are calculated on a (80×80) grid.

D.2 Fermi surface

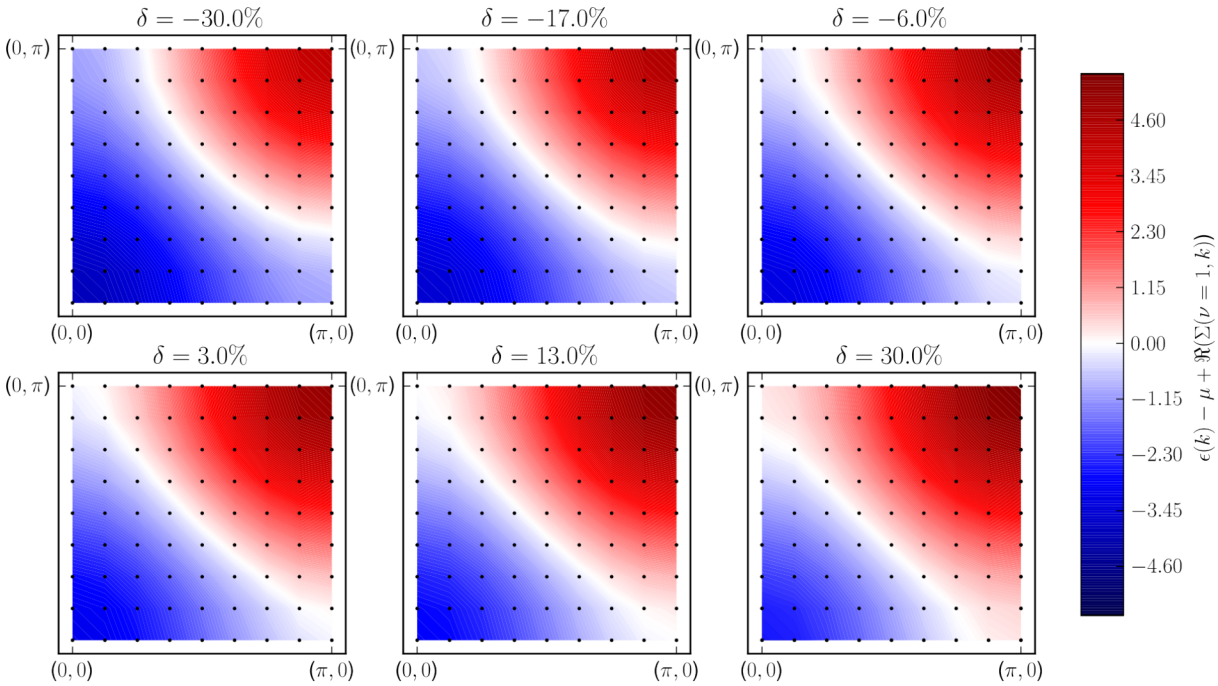

Figure D.1: Fermi surfaces corresponding to the suscpetibilities of Fig. 5.1, for selected values of the doping.

In Fig. D.1 we show the Fermi surface plots associated to Fig. 5.1. For the different values of the doping, the evolution from an electron- to a hole-like shape is clearly visible.

D.3 Analytical calculations

D.3.1 Magnetic contribution to the d-wave superconducting susceptibility

The contribution of the dominant magnetic channel $\mathbf{\Phi}^{\mathrm{M}}$ to the d-wave superconducting susceptibility χ_{11}^{SC} is given by

$$\begin{aligned}\frac{3}{2}\left[\chi^{\mathrm{SC},0}\mathbf{\Phi}^{\mathrm{M}}\chi^{\mathrm{SC},0}\right]_{11}(\Omega=0,\mathbf{q}) &:= -\sum_{\substack{\nu,\nu'\\ m',n'}}\Pi^{\mathrm{SC}}_{1m'}(\Omega=0,\mathbf{q},\nu)\\ &\cdot\left(\frac{1}{2}\left[P^{ph\to pp}\mathbf{\Phi}^{\mathrm{M}}\right]_{m'n'}+\left[P^{\overline{ph}\to pp}\mathbf{\Phi}^{\mathrm{M}}\right]_{m'n'}\right)(\Omega=0,\mathbf{q},\nu,\nu')\Pi^{\mathrm{SC}}_{n'1}(\Omega=0,\mathbf{q},\nu')\,. \end{aligned}\tag{D.1}$$

Since bubbles with mixed form factors are very small and $\Pi^{\mathrm{SC}}_{m'n'}(\Omega,\mathbf{q}=(0,0),\nu)=0$ exactly, we neglect all terms with $m'=n'=0$. Hence, the sum over the different components contains only the elements $n'=m'=1$. In the following we drop the frequency dependence to lighten the notation (with the sums over internal fermionic frequencies implicitly taken into account). Projections from one notation to another are necessary because a simple shift of arguments is not possible for the form factor arguments:

$$\begin{aligned}\left[P^{\overline{ph}\to pp}\mathbf{\Phi}^{\mathrm{M}}\right]_{11}(\mathbf{q}) &= \sum_{m'n'}\int_{\mathrm{BZ}}\mathrm{d}\mathbf{k}\mathrm{d}\mathbf{k}' f_1^*(\mathbf{k})f_1(\mathbf{k}')f_{m'}(\mathbf{k})f^*_{n'}(\mathbf{k}')\Phi^{\mathrm{M},\overline{ph}}_{m'n'}(\mathbf{q}-\mathbf{k}-\mathbf{k}')\\ &\overset{\mathbf{q}-\mathbf{k}-\mathbf{k}'\to\mathbf{p}}{=}\sum_{m'n'}\int_{\mathrm{BZ}}\mathrm{d}\mathbf{k}\mathrm{d}\mathbf{p} f_1^*(\mathbf{k})f_1(\mathbf{q}-\mathbf{k}-\mathbf{p})f_{m'}(\mathbf{k})f^*_{n'}(\mathbf{q}-\mathbf{k}-\mathbf{p})\Phi^{\mathrm{M},\overline{ph}}_{m'n'}(\mathbf{p})\\ &\approx\int_{\mathrm{BZ}}\mathrm{d}\mathbf{k}\mathrm{d}\mathbf{p} f_1^*(\mathbf{k})f_1(\mathbf{q}-\mathbf{k}-\mathbf{p})f_0(\mathbf{k})f^*_0(\mathbf{q}-\mathbf{k}-\mathbf{p})\Phi^{\mathrm{M},\overline{ph}}_{00}(\mathbf{p})\,, \end{aligned}\tag{D.2}$$

where we used that the contributions from Φ^{M}_{11}, and mixed components, are negligible compared to Φ^{M}_{00}. Analogously,

$$\begin{aligned}\left[P^{ph\to pp}\mathbf{\Phi}^{\mathrm{M}}\right]_{11}(\mathbf{q}) &= \sum_{mn}\int_{\mathrm{BZ}}\mathrm{d}\mathbf{k}\mathrm{d}\mathbf{k}' f_1^*(\mathbf{k})f_1(\mathbf{k}')f_m(\mathbf{k})f^*_n(\mathbf{q}-\mathbf{k}')\Phi^{\mathrm{M},ph}_{mn}(\mathbf{k}-\mathbf{k}')\\ &\approx\int_{\mathrm{BZ}}\mathrm{d}\mathbf{k}\mathrm{d}\mathbf{k}' f_1^*(\mathbf{k})f_1(\mathbf{k}-\mathbf{p})f_0(\mathbf{k})f^*_0(\mathbf{k}-\mathbf{p})\Phi^{\mathrm{M},ph}_{00}(\mathbf{p})\,. \end{aligned}\tag{D.3}$$

Inserting the above expressions in Eq. (D.1), together with the explicit form of the s- and d-wave form factors $f_0(\mathbf{k})=1$ and $f_1(\mathbf{k})=\cos(k_x)-\cos(k_y)$, yields

$$\begin{aligned}&\frac{3}{2}\left[\chi^{\mathrm{SC},0}\mathbf{\Phi}^{\mathrm{M}}\chi^{\mathrm{SC},0}\right]_{11}(\mathbf{q})\\ &=-\Pi^{\mathrm{SC}}_{11}(\mathbf{q})\left(\frac{1}{2}\left[P^{\overline{ph}\to pp}\mathbf{\Phi}^{\mathrm{M}}\right]_{11}(\mathbf{q})+\left[P^{ph\to pp}\mathbf{\Phi}^{\mathrm{M}}\right]_{11}(\mathbf{q})\right)\Pi^{\mathrm{SC}}_{11}(\mathbf{q})\\ &=-\Pi^{\mathrm{SC}}_{11}(\mathbf{q})\left(\frac{1}{2}\int_{\mathrm{BZ}}\mathrm{d}\mathbf{k}\mathrm{d}\mathbf{p}\left(\cos(k_x)-\cos(k_y)\right)\left(\cos(k_x-p_x)-\cos(k_y-p_y)\right)\Phi^{\mathrm{M},ph}_{00}(\mathbf{p})\right.\\ &\quad\left.+\int_{\mathrm{BZ}}\mathrm{d}\mathbf{k}\mathrm{d}\mathbf{p}\left(\cos(k_x)-\cos(k_y)\right)\left(\cos(q_x-k_x-p_x)-\cos(q_y-k_y-p_y)\right)\Phi^{\mathrm{M},\overline{ph}}_{00}(\mathbf{p})\right)\Pi^{\mathrm{SC}}_{11}(\mathbf{q})\\ &=-\Pi^{\mathrm{SC}}_{11}(\mathbf{q})\int_{\mathrm{BZ}}\mathrm{d}\mathbf{p}\left(\frac{1}{2}\left(\cos p_x+\cos p_y\right)+\cos\left(p_x-q_x\right)+\cos\left(p_y-q_y\right)\right)\Phi^{\mathrm{M}}_{00}(\mathbf{p})\Pi^{\mathrm{SC}}_{11}(\mathbf{q})\,, \end{aligned}\tag{D.4}$$

which reproduces Eq. (5.7).

D.3.2 Lowest-order diagram contributing to Φ^{SC}_{11}

The lowest-order vertex diagram from the magnetic channel contributing to the d-wave superconducting susceptibility reads

$$\begin{aligned}-[P^{\overline{ph}\to pp}\Phi^{\mathrm{M,lowest\ order}}_{00}]_{11}(\mathbf{q}) &= -U^2\left[P^{\overline{ph}\to pp}\Pi^{\mathrm{M}}\right]_{11}(\mathbf{q})\\ &= -U^2\int_{\mathrm{BZ}}\mathrm{d}\mathbf{k}\mathrm{d}\mathbf{p} f_1(\mathbf{k})f_1(\mathbf{p}-\mathbf{q}+\mathbf{k})\Pi^{\mathrm{M}}_{00}(\mathbf{p})\,. \end{aligned}\tag{D.5}$$

With the expressions for the form factors, we obtain

$$\begin{aligned} &= -\int_{\mathrm{BZ}} \mathrm{d}\mathbf{k}\mathrm{d}\mathbf{p}\,(\cos(k_x)-\cos(k_y))\,(\cos(p_x-q_x+k_x)-\cos(p_y-q_y+k_y))\,\Pi_{00}^{\mathrm{M}}(\mathbf{p}) \\ &= -\int_{\mathrm{BZ}} \mathrm{d}\mathbf{p}\,(\cos(p_x-q_x)+\cos(p_y-q_y))\,\Pi_{00}^{\mathrm{M}}(\mathbf{p}) \end{aligned} \tag{D.6}$$

and, inserted into $\chi^{\mathrm{SC},0}\Phi_{00}^{\mathrm{M}}\chi^{\mathrm{SC},0}$, gives

$$\begin{aligned} \chi^{\mathrm{SC},0}\Phi_{00}^{\mathrm{M,lowest\ order}}\chi^{\mathrm{SC},0}(\mathbf{q}) &= -U^2\left[P^{\overline{ph}\to pp}\Pi^{\mathrm{M}}\right]_{11}(\mathbf{q}) \\ &\approx -U^2\,\Pi_{11}^{\mathrm{SC}}(\mathbf{q})\Pi_{11}^{\mathrm{SC}}(\mathbf{q})\int_{\mathrm{BZ}}\mathrm{d}\mathbf{p}\,(\cos(p_x-q_x)+\cos(p_y-q_y))\,\Pi_{00}^{\mathrm{M}}(\mathbf{p}) \end{aligned} \tag{D.7}$$

as mixed pp-bubbles are very small and vanish exactly for $\mathbf{q}=(0,0)$. This lowest-order diagram exhibits the same momentum dependence as Eq. (D.1) and illustrates how features in the s-wave magnetic channel enter into χ_{11}^{SC}. In particular, we can trace how features at different transfer momenta in the magnetic channel enter into the maximum of χ_{11}^{SC} at zero transfer momentum in the d-wave superconducting channel, the main contribution being from (π,π)

$$\chi^{\mathrm{SC},0}\Phi_{00}^{\mathrm{M,lowest\ order}}\chi^{\mathrm{SC},0}(\mathbf{q}=0) = -U^2\,\Pi_{11}^{\mathrm{SC}}(0)\Pi_{11}^{\mathrm{SC}}(0)\,\frac{1}{2}\int_{\mathrm{BZ}}\mathrm{d}\mathbf{p}\,(\cos(p_x)+\cos(p_y))\,\Pi_{00}^{\mathrm{M}}(\mathbf{p}). \tag{D.8}$$

The $(\cos(p_x)+\cos(p_y))$ term acts as a weight, controlling how features at different $\mathbf{p}$ contribute. Commensurate AF features at $\mathbf{p}=(\pi,\pi)$ are the most favoured by the projection with a weight of -1, whereas incommensurate features are reduced by a factor of $(\cos(p_x-\delta_x)+\cos(p_y-\delta_y))$. Ferromagnetic features at $\mathbf{p}=(0,0)$ have a weight equal, but opposite in sign, to AF contributions.

Likewise, we obtain for

$$\Phi_{11}^{\mathrm{SC,lowest\ order}}(\mathbf{q}) = U^4\sum_{m'n'}\left[P^{\overline{ph}\to pp}\Pi^{\mathrm{M}}\right]_{1m'}(\mathbf{q})\,\Pi_{m'n'}^{\mathrm{SC}}(\mathbf{q})\,\left[P^{\overline{ph}\to pp}\Pi^{\mathrm{M}}\right]_{n'1}(\mathbf{q})\,, \tag{D.9}$$

with

$$\begin{aligned} &= U^4\sum_{m'n'}\left(\int_{\mathrm{BZ}}\mathrm{d}\mathbf{k}\mathrm{d}\mathbf{p}f_1(\mathbf{k})f_{m'}(\mathbf{p}-\mathbf{q}+\mathbf{k})\Pi_{00}^{\mathrm{M}}(\mathbf{p})\right)\Pi_{m'n'}^{\mathrm{SC}}(\mathbf{q}) \\ &\quad\left(\int_{\mathrm{BZ}}\mathrm{d}\mathbf{k}'\mathrm{d}\mathbf{p}'f_1(\mathbf{k}')f_{n'}(\mathbf{p}'-\mathbf{q}+\mathbf{k}')\Pi_{00}^{\mathrm{M}}(\mathbf{p}')\right) \\ &= U^4\left(\int_{\mathrm{BZ}}\mathrm{d}\mathbf{k}\mathrm{d}\mathbf{p}\,(\cos(k_x)-\cos(k_y))\,(\cos(p_x-q_x+k_x)-\cos(p_y-q_y+k_y))\,\Pi_{00}^{\mathrm{M}}(\mathbf{p})\right)\Pi_{11}^{\mathrm{SC}}(\mathbf{q}) \\ &\quad\left(\int_{\mathrm{BZ}}\mathrm{d}\mathbf{k}'\mathrm{d}\mathbf{p}'\,(\cos(k_x)-\cos(k_y))\left(\cos(p'_x-q_x+k_x)-\cos(p'_y-q_y+k_y)\right)\Pi_{00}^{\mathrm{M}}(\mathbf{p}')\right) \\ &= U^4\left(\int_{\mathrm{BZ}}\mathrm{d}\mathbf{p}\,(\cos(p_x-q_x)+\cos(p_y-q_y))\,\Pi_{00}^{\mathrm{M}}(\mathbf{p})\right)\Pi_{11}^{\mathrm{SC}}(\mathbf{q}) \\ &\quad\left(\int_{\mathrm{BZ}}\mathrm{d}\mathbf{p}'\left(\cos(p'_x-q_x)+\cos(p'_y-q_y)\right)\Pi_{00}^{\mathrm{M}}(\mathbf{p}')\right)\,, \end{aligned} \tag{D.10}$$

where we used the fact that the integral over $\mathbf{k}/\mathbf{k}'$ vanishes for $m'/n'=0$ and hence

$$\begin{aligned} &\chi^{\mathrm{SC},0}\Phi_{11}^{\mathrm{SC,lowest\ order}}\chi^{\mathrm{SC},0}(\mathbf{q}) \\ &\qquad= U^4\Pi_{11}^{\mathrm{SC}}(\mathbf{q})\left(\int_{\mathrm{BZ}}\mathrm{d}\mathbf{p}\,(\cos(p_x-q_x)+\cos(p_y-q_y))\,\Pi_{00}^{\mathrm{M}}(\mathbf{p})\right)\Pi_{11}^{\mathrm{SC}}(\mathbf{q}) \\ &\qquad\quad\left(\int_{\mathrm{BZ}}\mathrm{d}\mathbf{p}'\left(\cos(p'_x-q_x)+\cos(p'_y-q_y)\right)\Pi_{00}^{\mathrm{M}}(\mathbf{p}')\right)\Pi_{11}^{\mathrm{SC}}(\mathbf{q})\,. \end{aligned} \tag{D.11}$$

In fact, they represent the lowest-order contributions in the particle-particle ladder, with the insertion of $\left[P^{\overline{ph}\to pp}\Pi^{\mathrm{M}}\right]_{11}$ instead of the bare (local) interaction, as illustrated in Fig. D.2.

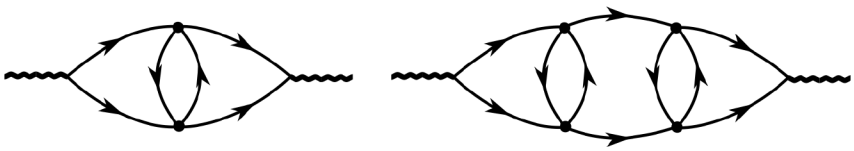

Figure D.2: First and second order diagrams of a ladder expansion in the pp-channel with $\left[P^{\overline{ph}\to pp}\Pi^{\mathrm{M}}\right]_{11}$ instead of the bare interaction.

E Personal contributions to publications

E.1 Single-boson exchange functional renormalization group application to the two-dimensional Hubbard model at weak coupling

Authors: Kilian Fraboulet, Sarah Heinzelmann, Pietro M. Bonetti, Aiman Al-Eryani, Demetrio Vilardi, Alessandro Toschi, and Sabine Andergassen
Kilian Fraboulet and I share first authorship. Published in: *Eur. Phys. J. B 95, 202 (2022)* `https://doi.org/10.1140/epjb/s10051-022-00438-2`
Sections 4.2-4.4 are adapted from the results section of this publication. My contribution consists in the numerical implementation of the flow equations, which has then been used by Kilian Fraboulet to generate the data and plots, which I adapted slightly for this thesis. The paragraph about bosonization of the multiboson rest function in the publication was provided by Pietro Bonetti and is not included in this work, whereas the sections on the SBEb were developed by me. The interpretation of the data and preparation of the manuscript was a joint effort by all authors under the supervision of Sabine Andergassen.

E.2 Entangled magnetic, charge, and superconducting pairing correlations in the two-dimensional Hubbard model: a functional renormalization-group analysis

Authors: Sarah Heinzelmann, Alessandro Toschi, and Sabine Andergassen
In preparation.
Chapter 5 is an adaption of this publication. The splitting of the susceptibilities into the individual components in the existing postprocessing code, the data production and plots were done by me. Interpretation of the data was done by me under the supervision of both Sabine Andergassen and Alessandro Toschi. The manuscript has been jointly prepared with Sabine Andergassen, with feedback from Alessandro Toschi.

Bibliography

[1] J. Hubbard, "Electron correlations in narrow energy bands," *Proceedings of the Royal Society of London. Series A, Mathematical and Physical Sciences*, vol. 276, no. 1365, pp. 238–257, (1963), ISSN: 00804630.

[2] S. S. P. J. M. D. Coey, *Handbook of Magnetism and Magnetic Materials*. Springer Cham, (2021). DOI: 10.1007/978-3-030-63210-6.

[3] J. G. Bednorz and K. A. Müller, "Possible high tc superconductivity in the ba-la-cu-o system," *Zeitschrift für Physik B Condensed Matter*, vol. 64, (1986). DOI: 10.1007/BF01303701.

[4] K. von Klitzing, "Quantum hall effect: Discovery and application," *Annual Review of Condensed Matter Physics*, vol. 8, no. 1, pp. 13–30, (2017). DOI: 10.1146/annurev-conmatphys-031016-025148.

[5] J. H. de Boer and E. J. W. Verwey, "Semi-conductors with partially and with completely filled 3d-lattice bands," *Proceedings of the Physical Society*, vol. 49, no. 4S, p. 59, (1937). DOI: 10.1088/0959-5309/49/4S/307.

[6] P. Grünberg, R. Schreiber, Y. Pang, M. B. Brodsky, and H. Sowers, "Layered Magnetic Structures: Evidence for Antiferromagnetic Coupling of Fe Layers across Cr Interlayers," *Phys. Rev. Lett.*, vol. 57, pp. 2442–2445, 19, (1986). DOI: 10.1103/PhysRevLett.57.2442.

[7] Y. Cao *et al.*, "Unconventional superconductivity in magic-angle graphene superlattices," *Nature*, vol. 556, (2018). DOI: 10.1038/nature26160.

[8] L. Savary and L. Balents, "Quantum spin liquids: A review," *Reports on Progress in Physics*, vol. 80, no. 1, p. 016 502, (2016). DOI: 10.1088/0034-4885/80/1/016502.

[9] J. Daughton, "GMR applications," *Journal of Magnetism and Magnetic Materials*, vol. 192, no. 2, pp. 334–342, (1999), ISSN: 0304-8853. DOI: 10.1016/S0304-8853(98)00376-X.

[10] M. Qin, T. Schäfer, S. Andergassen, P. Corboz, and E. Gull, "The hubbard model: A computational perspective," *Annual Review of Condensed Matter Physics*, vol. 13, no. 1, pp. 275–302, (2022). DOI: 10.1146/annurev-conmatphys-090921-033948.

[11] J. P. F. LeBlanc *et al.*, "Solutions of the Two-Dimensional Hubbard Model: Benchmarks and Results from a Wide Range of Numerical Algorithms," *Phys. Rev. X*, vol. 5, p. 041 041, 4, (2015). DOI: 10.1103/PhysRevX.5.041041.

[12] W. Metzner and D. Vollhardt, "Correlated lattice fermions in $d = \infty$ dimensions," *Phys. Rev. Lett.*, vol. 62, pp. 324–327, 3, (1989). DOI: 10.1103/PhysRevLett.62.324.

[13] E. Dagotto, "Correlated electrons in high-temperature superconductors," *Rev. Mod. Phys.*, vol. 66, pp. 763–840, 3, (1994). DOI: 10.1103/RevModPhys.66.763.

[14] A. N. Rubtsov, M. I. Katsnelson, A. I. Lichtenstein, and A. Georges, "Dual fermion approach to the two-dimensional Hubbard model: Antiferromagnetic fluctuations and Fermi arcs," *Phys. Rev. B*, vol. 79, p. 045 133, 4, (2009). DOI: 10.1103/PhysRevB.79.045133.

[15] N. Bickers and D. Scalapino, "Conserving approximations for strongly fluctuating electron systems. I. Formalism and calculational approach," *Annals of Physics*, vol. 193, no. 1, pp. 206–251, (1989), ISSN: 0003-4916. DOI: 10.1016/0003-4916(89)90359-X.

[16] N. Bickers, "Parquet equations for numerical self-consistent field theory," *Int. J. Mod. Phys. B*, p. 253, 5, (1991). DOI: 10.1142/S021797929100016X.

[17] C. Hille *et al.*, "Quantitative functional renormalization group description of the two-dimensional Hubbard model," *Phys. Rev. Research*, vol. 2, 3, (2020). DOI: 10.1103/PhysRevResearch.2.033372.

[18] F. Krien, A. Valli, and M. Capone, "Single-boson exchange decomposition of the vertex function," *Phys. Rev. B*, vol. 100, p. 155 149, 15, (2019). DOI: 10.1103/PhysRevB.100.155149.

[19] V. Harkov, A. I. Lichtenstein, and F. Krien, "Parametrizations of local vertex corrections from weak to strong coupling: Importance of the hedin three-leg vertex," *Phys. Rev. B*, vol. 104, p. 125 141, 12, (2021). DOI: 10.1103/PhysRevB.104.125141.

[20] F. Krien and A. Valli, "Parquetlike equations for the Hedin three-leg vertex," *Phys. Rev. B*, vol. 100, p. 245 147, 24, (2019). DOI: 10.1103/PhysRevB.100.245147.

[21] F. Krien, A. Kauch, and K. Held, "Tiling with triangles: Parquet and $GW\gamma$ methods unified," *Phys. Rev. Research*, vol. 3, p. 013 149, 1, (2021). DOI: 10.1103/PhysRevResearch.3.013149.

[22] F. Krien and A. Kauch, "The plain and simple parquet approximation: Single- and multi-boson exchange in the two-dimensional hubbard model," *Eur. Phys. J. B*, vol. 95, p. 69, (2022). DOI: 10.1140/epjb/s10051-022-00329-6.

[23] F. Krien, A. Valli, P. Chalupa, M. Capone, A. I. Lichtenstein, and A. Toschi, "Boson-exchange parquet solver for dual fermions," *Phys. Rev. B*, vol. 102, p. 195 131, 19, (2020). DOI: 10.1103/PhysRevB.102.195131.

[24] P. M. Bonetti, A. Toschi, C. Hille, S. Andergassen, and D. Vilardi, "Single-boson exchange representation of the functional renormalization group for strongly interacting many-electron systems," *Phys. Rev. Res.*, vol. 4, p. 013 034, 1, (2022). DOI: 10.1103/PhysRevResearch.4.013034.

[25] C. Husemann, K.-U. Giering, and M. Salmhofer, "Frequency-dependent vertex functions of the (t, t') Hubbard model at weak coupling," *Phys. Rev. B*, vol. 85, p. 075 121, 7, (2012). DOI: 10.1103/PhysRevB.85.075121.

[26] A. Eberlein, "Functional renormalization group study of fluctuation effects in fermionic superfluids," Ph.D. dissertation, Universität Stuttgart, (2014). DOI: 10.18419/opus-6837.

[27] F. B. Kugler and J. von Delft, "Derivation of exact flow equations from the self-consistent parquet relations," *New Journal of Physics*, vol. 20, no. 12, p. 123 029, (2018). DOI: 10.1088/1367-2630/aaf65f.

[28] M. Gievers, E. Walter, A. Ge, J. von Delft, and F. Kugler, "Multiloop flow equations for single-boson exchange fRG," *Eur. Phys. J. B*, vol. 95, p. 108, (2022). DOI: 10.1140/epjb/s10051-022-00353-6.

[29] N. Wentzell *et al.*, "High-frequency asymptotics of the vertex function: Diagrammatic parametrization and algorithmic implementation," *Phys. Rev. B*, vol. 102, p. 085 106, 8, (2020). DOI: 10.1103/PhysRevB.102.085106.

[30] A. Tagliavini, C. Hille, F. B. Kugler, S. Andergassen, A. Toschi, and C. Honerkamp, "Multiloop functional renormalization group for the two-dimensional Hubbard model: Loop convergence of the response functions," *SciPost Phys.*, vol. 6, p. 009, (2019). DOI: 10.21468/SciPostPhys.6.1.009.

[31] D. Gross, *Many-body quantum mechanis*, (2019). [Online]. Available: www.thp.uni-koeln.de/gross/aqm19_20/notes.pdf.

[32] L. F. Feiner, J. H. Jefferson, and R. Raimondi, "Effective single-band models for the high-T_c cuprates. I. Coulomb interactions," *Phys. Rev. B*, vol. 53, pp. 8751–8773, 13 (1996). DOI: 10.1103/PhysRevB.53.8751.

[33] A. Macridin, T. Maier, M. Jarrell, and G. Sawatzky, "Physics of cuprates with the two-band Hubbard model - The validity of the one-band Hubbard model," *Physical Review B*, vol. 71, (2004). DOI: 10.1103/PhysRevB.71.134527.

[34] N. Bulut, "D x 2 - y 2 superconductivity and the Hubbard model," *Advances in Physics*, vol. 51, no. 7, pp. 1587–1667, (2002). DOI: 10.1080/00018730210155142.

[35] T. Schäfer *et al.*, "Tracking the Footprints of Spin Fluctuations: A MultiMethod, MultiMessenger Study of the Two-Dimensional Hubbard Model," *Phys. Rev. X*, vol. 11, p. 011 058, 1, (2021). DOI: 10.1103/PhysRevX.11.011058.

[36] W. Metzner, M. Salmhofer, C. Honerkamp, V. Meden, and K. Schönhammer, "Functional renormalization group approach to correlated fermion systems," *Rev. Mod. Phys.*, vol. 84, pp. 299–352, 1, (2012). DOI: 10.1103/RevModPhys.84.299.

[37] N. Dupuis *et al.*, "The nonperturbative functional renormalization group and its applications," *Physics Reports*, vol. 910, p. 1, (2021). DOI: 10.1016/j.physrep.2021.01.001.

[38] A. Altland and B. Simons, *Condensed Matter Field Theory*. Cambridge University Press, (2006). DOI: 10.1017/CBO9780511804236.

[39] "The Hubbard model at half a century," *Nature Physics*, vol. 9, 9, (2013). DOI: 10.1038/nphys2759.

[40] D. P. Arovas, E. Berg, S. A. Kivelson, and S. Raghu, "The Hubbard Model," *Annual Review of Condensed Matter Physics*, vol. 13, no. 1, pp. 239–274, (2022). DOI: 10.1146/annurev-conmatphys-031620-102024.

[41] O. Andersen, A. Liechtenstein, O. Jepsen, and F. Paulsen, "LDA energy bands, low-energy hamiltonians, t', t", t⊥ (k), and J⊥," *Journal of Physics and Chemistry of Solids*, vol. 56, no. 12, pp. 1573–1591, (1995). DOI: 10.1016/0022-3697(95)00269-3.

[42] V. V. Mazurenko, I. V. Solovyev, and A. A. Tsirlin, "Covalency effects reflected in the magnetic form factor of low-dimensional cuprates," *Phys. Rev. B*, vol. 92, p. 245 113, 24, (2015). DOI: 10.1103/PhysRevB.92.245113.

[43] E. A. Stepanov, L. Peters, I. S. Krivenko, A. I. Lichtenstein, M. I. Katsnelson, and A. N. Rubtsov, "Quantum spin fluctuations and evolution of electronic structure in cuprates," *npj Quant. Mater.*, vol. 3, p. 54, (2018). DOI: 10.1038/s41535-018-0128-x.

[44] F. H. L. Essler, H. Frahm, F. Göhmann, A. Klümper, and V. E. Korepin, *The One-Dimensional Hubbard Model*. Cambridge University Press, (2005). DOI: 10.1017/CBO9780511534843.

[45] P. G. J. van Dongen, "Extended Hubbard model at strong coupling," *Phys. Rev. B*, vol. 49, pp. 7904–7915, 12, (1994). DOI: 10.1103/PhysRevB.49.7904.

[46] P. G. J. van Dongen, "Extended Hubbard model at weak coupling," *Phys. Rev. B*, vol. 50, pp. 14 016–14 031, 19, (1994). DOI: 10.1103/PhysRevB.50.14016.

[47] Y. Zhang and J. Callaway, "Extended Hubbard model in two dimensions," *Phys. Rev. B*, vol. 39, pp. 9397–9404, 13, (1989). DOI: 10.1103/PhysRevB.39.9397.

[48] J. Wahle, N. Blümer, J. Schlipf, K. Held, and D. Vollhardt, "Microscopic conditions favoring itinerant ferromagnetism," *Phys. Rev. B*, vol. 58, pp. 12 749–12 757, 19, (1998). DOI: 10.1103/PhysRevB.58.12749.

[49] Q. Si and J. L. Smith, "Kosterlitz-Thouless Transition and Short Range Spatial Correlations in an Extended Hubbard Model," *Phys. Rev. Lett.*, vol. 77, pp. 3391–3394, 16, (1996). DOI: 10.1103/PhysRevLett.77.3391.

[50] H. Terletska, T. Chen, and E. Gull, "Charge ordering and correlation effects in the extended Hubbard model," *Phys. Rev. B*, vol. 95, p. 115 149, 11, (2017). DOI: 10.1103/PhysRevB.95.115149.

[51] H. Terletska, T. Chen, J. Paki, and E. Gull, "Charge ordering and nonlocal correlations in the doped extended Hubbard model," *Phys. Rev. B*, vol. 97, p. 115 117, 11, (2018). DOI: 10.1103/PhysRevB.97.115117.

[52] M. Jiang, U. R. Hähner, T. C. Schulthess, and T. A. Maier, "*d*-wave superconductivity in the presence of nearest-neighbor Coulomb repulsion," *Phys. Rev. B*, vol. 97, p. 184 507, 18, (2018). DOI: 10.1103/PhysRevB.97.184507.

[53] J. Paki, H. Terletska, S. Iskakov, and E. Gull, "Charge order and antiferromagnetism in the extended Hubbard model," *Phys. Rev. B*, vol. 99, p. 245 146, 24, (2019). DOI: 10.1103/PhysRevB.99.245146.

[54] E. G. C. P. van Loon, A. I. Lichtenstein, M. I. Katsnelson, O. Parcollet, and H. Hafermann, "Beyond extended dynamical mean-field theory: Dual boson approach to the two-dimensional extended Hubbard model," *Phys. Rev. B*, vol. 90, p. 235 135, 23, (2014). DOI: 10.1103/PhysRevB.90.235135.

[55] G. Rohringer *et al.*, "Diagrammatic routes to nonlocal correlations beyond dynamical mean field theory," *Rev. Mod. Phys.*, vol. 90, p. 025 003, 2, (2018). DOI: 10.1103/RevModPhys.90.025003.

[56] P. Pudleiner, A. Kauch, K. Held, and G. Li, "Competition between antiferromagnetic and charge density wave fluctuations in the extended Hubbard model," *Phys. Rev. B*, vol. 100, p. 075 108, 7, (2019). DOI: 10.1103/PhysRevB.100.075108.

[57] A. Sushchyev and S. Wessel, "Thermodynamics of the metal-insulator transition in the extended Hubbard model from determinantal quantum Monte Carlo," *Phys. Rev. B*, vol. 106, p. 155 121, 15, (2022). DOI: 10.1103/PhysRevB.106.155121.

[58] R. A. Jishi, *Feynman Diagram Techniques in Condensed Matter Physics*. Cambridge University Press, (2013). DOI: 10.1017/CBO9781139177771.

[59] N. E. Bickers, "Self-consistent many-body theory for condensed matter systems," in *Theoretical Methods for Strongly Correlated Electrons*, D. Sénéchal, A.-M. Tremblay, and C. Bourbonnais, Eds., New York, NY: Springer New York, (2004), pp. 237–296. DOI: 10.1007/0-387-21717-7_6.

[60] C. De Dominicis and P. C. Martin, "Stationary Entropy Principle and Renormalization in Normal and Superfluid Systems. I. Algebraic Formulation," *J. Math. Phys.*, vol. 5, pp. 14–30, (1964). DOI: 10.1063/1.1704062.

[61] C. De Dominicis and P. C. Martin, "Stationary Entropy Principle and Renormalization in Normal and Superfluid Systems. II. Diagrammatic Formulation," *J. Math. Phys.*, vol. 5, no. 1, pp. 31–59, (1964). DOI: 10.1063/1.1704064.

[62] G. Rohringer, A. Valli, and A. Toschi, "Local electronic correlation at the two-particle level," *Phys. Rev. B*, vol. 86, p. 125 114, 12, (2012). DOI: 10.1103/PhysRevB.86.125114.

[63] C. Honerkamp, M. Salmhofer, N. Furukawa, and T. M. Rice, "Breakdown of the Landau-Fermi liquid in two dimensions due to Umklapp scattering," *Phys. Rev. B*, vol. 63, p. 035 109, (2001). DOI: 10.1103/PhysRevB.63.035109.

[64] G. Rohringer, "New routes towards a theoretical treatment of nonlocal electronic correlations," Ph.D. dissertation, TU Wien, (2013).

[65] C. Husemann and M. Salmhofer, "Efficient parametrization of the vertex function, Ω scheme, and the t, t' Hubbard model at van Hove filling," *Phys. Rev. B*, vol. 79, p. 195 125, 19, (2009). DOI: 10.1103/PhysRevB.79.195125.

[66] K.-U. Giering and M. Salmhofer, "Self-energy flows in the two-dimensional repulsive Hubbard model," *Phys. Rev. B*, vol. 86, p. 245 122, (2012). DOI: 10.1103/PhysRevB.86.245122.

[67] S. A. Maier, J. Ortloff, and C. Honerkamp, "Multiorbital effects in the functional renormalization group: A weak-coupling study of the Emery model," *Phys. Rev. B*, vol. 88, p. 235 112, (2013). DOI: 10.1103/PhysRevB.88.235112.

[68] J. Lichtenstein, D. Sánchez de la Peña, D. Rohe, E. Di Napoli, C. Honerkamp, and S. Maier, "High-performance functional Renormalization Group calculations for interacting fermions," *Computer Physics Communications*, vol. 213, pp. 100–110, (2017), ISSN: 0010-4655. DOI: 10.1016/j.cpc.2016.12.013.

[69] C. Hille, "The role of the self-energy in the functional renormalization group description of interacting fermi systems," Ph.D. dissertation, (2020).

[70] C. Hille, D. Rohe, C. Honerkamp, and S. Andergassen, "Pseudogap opening in the two-dimensional Hubbard model: A functional renormalization group analysis," *Phys. Rev. Res.*, vol. 2, p. 033 068, 3, (2020). DOI: 10.1103/PhysRevResearch.2.033068.

[71] P. Pudleiner, "One- and two-particle vertex functions within Monte Carlo and parquet calculations of correlated electron systems," Ph.D. dissertation, (2019).

[72] A. Tagliavini, "Response functions of correlated systems in the linear regime and beyond," Ph.D. dissertation, Universität Tübingen, (2018).

[73] F. B. Kugler and J. von Delft, "Multiloop Functional Renormalization Group That Sums Up All Parquet Diagrams," *Phys. Rev. Lett.*, vol. 120, p. 057 403, 5, (2018). DOI: 10.1103/PhysRevLett.120.057403.

[74] F. B. Kugler and J. von Delft, "Multiloop functional renormalization group for general models," *Phys. Rev. B*, vol. 97, p. 035 162, 3, (2018). DOI: 10.1103/PhysRevB.97.035162.

[75] A. A. Katanin, "Two-loop functional renormalization group approach to the one- and two-dimensional Hubbard model," *Phys. Rev. B*, vol. 79, p. 235 119, 23, (2009). DOI: 10.1103/PhysRevB.79.235119.

[76] G. Li, A. Kauch, P. Pudleiner, and K. Held, "The victory project v1.0: An efficient parquet equations solver," *Computer Physics Communications*, vol. 241, pp. 146–154, (2019), ISSN: 0010-4655. DOI: 10.1016/j.cpc.2019.03.008.

[77] M. Patricolo *et al.*, "Single-boson exchange formulation of the schwinger-dyson equation and its application to the functional renormalization group," *SciPost Phys.*, vol. 18, p. 078, (2025). DOI: 10.21468/SciPostPhys.18.3.078.

[78] K. Fraboulet *et al.*, "Single-boson exchange functional renormalization group application to the two-dimensional Hubbard model at weak coupling," *Eur. Phys. J. B*, vol. 95, no. 12, p. 202, (2022). DOI: 10.1140/epjb/s10051-022-00438-2.

[79] J.-P. Blaizot, J. M. Pawlowski, and U. Reinosa, "Functional renormalization group and 2PI effective action formalism," *Annals of Physics*, vol. 431, p. 168 549, (2021), ISSN: 0003-4916. DOI: 10.1016/j.aop.2021.168549.

[80] K. Held, *Lecture notes Autumn School Jülich, Beyond DMFT: Spin Fluctuations, Pseudogaps and Superconductivity*, (2022). [Online]. Available: www.cond-mat.de/events/correl22/manuscripts/held.pdf.

[81] E. A. Stepanov, V. Harkov, and A. I. Lichtenstein, "Consistent partial bosonization of the extended hubbard model," *Phys. Rev. B*, vol. 100, p. 205 115, 20, (2019). DOI: 10.1103/PhysRevB.100.205115.

[82] F. Krien, *Private communication*, (2022).

[83] A. Toschi, A. A. Katanin, and K. Held, "Dynamical vertex approximation: A step beyond dynamical mean-field theory," *Phys. Rev. B*, vol. 75, p. 045 118, 4, (2007). DOI: 10.1103/PhysRevB.75.045118.

[84] P. Chalupa-Gantner, F. B. Kugler, C. Hille, J. von Delft, S. Andergassen, and A. Toschi, "Fulfillment of sum rules and Ward identities in the multiloop functional renormalization group solution of the Anderson impurity model," *Phys. Rev. Research*, vol. 4, p. 023 050, 2, (2022). DOI: 10.1103/PhysRevResearch.4.023050.

[85] S. Heinzelmann, A. Toschi, and S. Andergassen, *Entangled magnetic, charge, and superconducting pairing correlations in the two-dimensional Hubbard model: A functional renormalization-group analysis*, (2023).

[86] O. Gunnarsson *et al.*, "Fluctuation Diagnostics of the Electron Self-Energy: Origin of the Pseudogap Physics," *Phys. Rev. Lett.*, vol. 114, p. 236 402, 23, (2015). DOI: 10.1103/PhysRevLett.114.236402.

[87] G. Rohringer, "Spectra of correlated many-electron systems: From a one- to a two-particle description," *Journal of Electron Spectroscopy and Related Phenomena*, vol. 241, p. 146 804, (2020), ISSN: 0368-2048. DOI: 10.1016/j.elspec.2018.11.003.

[88] T. Schäfer and A. Toschi, "How to read between the lines of electronic spectra: The diagnostics of fluctuations in strongly correlated electron systems," *Journal of Physics: Condensed Matter*, vol. 33, no. 21, p. 214 001, (2021). DOI: 10.1088/1361-648X/abeb44.

[89] C. J. Halboth and W. Metzner, "Renormalization-group analysis of the two-dimensional Hubbard model," *Phys. Rev. B*, vol. 61, pp. 7364–7377, 11, (2000). DOI: 10.1103/PhysRevB.61.7364.

[90] C. J. Halboth and W. Metzner, "*d*-Wave Superconductivity and Pomeranchuk Instability in the Two-Dimensional Hubbard Model," *Phys. Rev. Lett.*, vol. 85, pp. 5162–5165, 24, (2000). DOI: 10.1103/PhysRevLett.85.5162.

[91] H. Yamase, A. Eberlein, and W. Metzner, "Coexistence of Incommensurate Magnetism and Superconductivity in the Two-Dimensional Hubbard Model," *Phys. Rev. Lett.*, vol. 116, p. 096 402, 9, (2016). DOI: 10.1103/PhysRevLett.116.096402.

[92] A. Eberlein, "Fermionic two-loop functional renormalization group for correlated fermions: Method and application to the attractive Hubbard model," *Phys. Rev. B*, vol. 90, p. 115 125, (2014). DOI: 10.1103/PhysRevB.90.115125.

[93] H. Braun, S. Heinzelmann, F. Krien, and S. Andergassen, *Functional renormalization group analysis of the pseudogap opening in the two-dimensional hubbard model at finite doping*, (2023).

[94] F. Krien, P. Worm, P. Chalupa, A. Toschi, and K. Held, "Spin scattering turns complex at strong coupling: The key to pseudogap and Fermi arcs in the Hubbard model," *Communications Physics*, 2022. DOI: 10.1038/s42005-022-01117-5.

[95] A. Georges, G. Kotliar, W. Krauth, and M. J. Rozenberg, "Dynamical mean-field theory of strongly correlated fermion systems and the limit of infinite dimensions," *Rev. Mod. Phys.*, vol. 68, pp. 13–125, 1, (1996). DOI: 10.1103/RevModPhys.68.13.

[96] C. Taranto *et al.*, "From infinite to two dimensions through the functional renormalization group," *Phys. Rev. Lett.*, vol. 112, p. 196 402, 19, (2014). DOI: 10.1103/PhysRevLett.112.196402.

[97] D. Vilardi, C. Taranto, and W. Metzner, "Antiferromagnetic and d-wave pairing correlations in the strongly interacting two-dimensional Hubbard model from the functional renormalization group," *Phys. Rev. B*, vol. 99, p. 104 501, 10, (2019). DOI: 10.1103/PhysRevB.99.104501.

[98] J. Wang, A. Eberlein, and W. Metzner, "Competing order in correlated electron systems made simple: Consistent fusion of functional renormalization and mean-field theory," *Phys. Rev. B*, vol. 89, p. 121 116, 12 2014. DOI: 10.1103/PhysRevB.89.121116.

[99] P. M. Bonetti, "Accessing the ordered phase of correlated Fermi systems: Vertex bosonization and mean-field theory within the functional renormalization group," *Phys. Rev. B*, vol. 102, p. 235 160, 23, (2020). DOI: 10.1103/PhysRevB.102.235160.

[100] D. Vilardi, P. Bonetti, and W. Metzner, "Dynamical functional renormalization group computation of order parameters and critical temperatures in the two-dimensional Hubbard model," *Phys. Rev. B*, vol. 102, p. 245 128, (2020). DOI: 10.1103/PhysRevB.102.245128.